



HAL
open science

Robust reactive control of transition to turbulence of a supersonic boundary layer

Pierre Nibourel

► **To cite this version:**

Pierre Nibourel. Robust reactive control of transition to turbulence of a supersonic boundary layer. Fluid mechanics [physics.class-ph]. Institut Polytechnique de Paris, 2023. English. NNT : 2023IP-PAX022 . tel-04426257

HAL Id: tel-04426257

<https://theses.hal.science/tel-04426257v1>

Submitted on 30 Jan 2024

HAL is a multi-disciplinary open access archive for the deposit and dissemination of scientific research documents, whether they are published or not. The documents may come from teaching and research institutions in France or abroad, or from public or private research centers.

L'archive ouverte pluridisciplinaire **HAL**, est destinée au dépôt et à la diffusion de documents scientifiques de niveau recherche, publiés ou non, émanant des établissements d'enseignement et de recherche français ou étrangers, des laboratoires publics ou privés.



INSTITUT
POLYTECHNIQUE
DE PARIS

NNT : 2023IPPAX022

Thèse de doctorat



Robust reactive control of transition to turbulence of a supersonic boundary layer

Thèse de doctorat de l'Institut Polytechnique de Paris
préparée à l'École polytechnique

École doctorale n°626 École doctorale de l'Institut Polytechnique de Paris (EDIPP)
Spécialité de doctorat : Mécanique des fluides et des solides, acoustique

Thèse présentée et soutenue à Meudon, le 23/06/2023, par

PIERRE NIBOUREL

Composition du Jury :

| | |
|---|--------------------|
| Laurent Cordier Directeur de recherche, Université de Poitiers (Institut Pprime) | Président |
| Peter Jordan Directeur de recherche, Université de Poitiers (Institut Pprime) | Rapporteur |
| Georgios Rigas Senior Lecturer, Imperial College London (Department of Aeronautics) | Rapporteur |
| Aimee S. Morgans Professor, Imperial College London (Department of Mechanical Engineering) | Examineur |
| Eric Garnier Directeur de recherche, ONERA (DAAA) | Directeur de thèse |
| Colin Leclercq Ingénieur de recherche, ONERA (DAAA) | Encadrant de thèse |
| Fabrice Demourant Directeur de recherche, ONERA (DTIS) | Invité |
| Denis Sipp Directeur de recherche, ONERA (DAAA) | Invité |
| Franck Hervy Ingénieur, DGA | Invité |

Acknowledgements/Remerciements

After three years of intense research, I would like to thank all the people who supported me and made this work a success. I would first like to acknowledge the ‘Ministère des armées – Agence de l’innovation de défense (AID)’ for funding a part of this work as well as the ONERA for funding and welcoming me in the Département Aérodynamique, Aéroélasticité, Acoustique (DAAA).

I would like to express my gratitude to all the members who formed the thesis committee. In particular, I extend my appreciation to Mr. Laurent Cordier for the honor of chairing this committee. I thank Mr. Peter Jordan and Mr. Georgios Rigas for their interest in my work and for accepting the significant responsibility of being the reviewers. I also wish to thank Ms. Aimee S. Morgans, who agreed to be an examiner for this thesis, for all the valuable feedback and insightful discussions during the thesis defense. Finally, I thank Mr. Franck Hervy for giving his time to participate in the jury as a guest member.

Je souhaite exprimer mes remerciements particuliers à Eric Garnier pour avoir accepté de diriger cette thèse et pour le soutien qu’il m’a accordé tout au long de ces trois années.

Je tiens aussi à remercier le reste de l’équipe d’encadrement, constituée de Colin Leclercq, Fabrice Demourant et Denis Sipp, qui a contribué pour beaucoup à la réussite de ce travail. Sans leur expertise, leur énergie et leur enthousiasme, la thèse n’aurait évidemment pas été la même et ce fut un réel plaisir de travailler avec eux.

Je souhaite remercier l’ensemble des personnes présentes à l’ONERA, notamment les membres de l’unité Missiles, Aéronefs de combat, Stabilité, Hypersonique (MASH) pour m’avoir si bien accueilli, sans oublier également les membres de l’unité Modélisation et Simulation Avancée de la Turbulence (MSAT) ainsi que les doctorants avec qui j’ai partagé le temps de midi.

Plus particulièrement, un grand merci à Julien et Guillaume pour m’avoir accepté dans le AY-02-01 ; une pensée également pour Alexandre et Mathieu qui ont maintenant pris la place dans le bureau, m’éjectant ainsi vers le AY-02-06 où Rémi doit maintenant me supporter. Je tiens également à témoigner ma reconnaissance envers Lucas, Camille, Michele et Clément pour leur présence et leurs encouragements. Une pensée également pour Ilyès et Romain qui m’ont appris qu’il est parfois bon de ne pas se précipiter pour sortir du transilien. Merci à Arthur

et Xavier qui ont souffert en même temps que moi et qui viendront bientôt à bout de leur thèse.

Mes derniers remerciements intra-ONERA s'adressent à Jaime et Julian : je vous remercie infiniment tous les deux d'avoir toujours été là pour moi et de m'avoir permis de me changer les idées. Genau wie Julian kannst du nach all dieser Zeit immer noch kein Französisch lesen, und ich bin mir nicht sicher, ob du den vorherigen Satz verstanden hast. ChatGPT wiederholt ihn dir auf Deutsch: Ich danke dir unendlich dafür, immer für mich da gewesen zu sein.

Concernant mes remerciements extra-ONERA, mes premiers mots concernent Meuh-Meuh, entité aux idées diverses et variées qui a su, malgré quelques soubresauts ponctuels inhérents à toute vie bien remplie, garder sa droiture, son sens de l'humour, son unité et son sens du respect qui le caractérise si bien. En attendant de te revoir dans une villa niçoise ou à proximité d'une meule de Comté, je ne saurais que trop te conseiller de planter des navets plutôt que de pratiquer l'art délicat du putsch.

Je remercie également les douze autres membres du Groupe (ils se reconnaîtront) pour m'avoir accompagné depuis maintenant près de douze ans. Malgré les distances parfois importantes qui nous séparent, notre amitié demeure indéfectible et vous êtes pour moi comme une deuxième famille.

Mes derniers mots sont dédiés à ma famille (la vraie, héhé), et tout particulièrement à mon père, ma mère et mon frère qui m'ont supporté (à double sens ici) durant ces trois années difficiles et plus généralement depuis vingt-sept ans. Merci pour tout !

Contents

| | |
|--|------------|
| Nomenclature | VII |
| List of Figures | X |
| List of Tables | XX |
| Introduction | 1 |
| 1 Literature review: stability and transition of boundary layer flows | 6 |
| 1.1 Navier–Stokes equations | 8 |
| 1.2 Paths from receptivity to transition | 8 |
| 1.3 Linear stability theory | 10 |
| 1.3.1 Local linear stability theory | 10 |
| 1.3.2 Global linear stability theory | 11 |
| 1.3.3 Non-modal growth theory | 12 |
| 1.3.4 Resolvent analysis | 12 |
| 1.4 Linear mechanisms | 13 |
| 1.4.1 Modal growth in incompressible flow | 14 |
| 1.4.2 Modal growth in compressible flow | 15 |
| 1.4.3 Transient growth | 18 |
| 1.5 Non-linear mechanisms | 20 |
| 1.5.1 Non-linear mechanisms in incompressible flow | 20 |
| 1.5.2 First Mack mode oblique breakdown | 20 |
| 1.5.3 Second Mack mode fundamental and sub-harmonic breakdowns | 21 |
| 2 Literature review: controlling instabilities and transition | 23 |
| 2.1 Control strategies | 25 |
| 2.2 Purpose of reactive control depending on the flow nature | 27 |
| 2.3 Description of linear time-invariant systems | 28 |
| 2.4 Control formalism | 29 |
| 2.4.1 Nominal performance | 31 |
| 2.4.2 Stability robustness | 31 |
| 2.4.3 Performance robustness | 33 |

| | | |
|----------|--|-----------|
| 2.4.4 | Feedforward vs Feedback | 34 |
| 2.5 | Reduced-order models | 34 |
| 2.5.1 | Galerkin projections | 35 |
| 2.5.2 | Data-based approaches | 36 |
| 2.6 | Synthesis methods | 37 |
| 2.6.1 | LQR | 37 |
| 2.6.2 | LQG/LTR | 38 |
| 2.6.3 | Inverse feedforward/Wiener–Hopf framework | 38 |
| 2.6.4 | Classical loop-shaping | 39 |
| 2.6.5 | Modern optimal synthesis | 40 |
| 2.6.6 | Structured synthesis | 41 |
| 2.7 | Maintaining performance over several operating points | 41 |
| 3 | Numerical methods | 44 |
| 3.1 | Flow methods | 46 |
| 3.1.1 | Solvers and spatial schemes | 46 |
| 3.1.2 | Base flow | 46 |
| 3.1.3 | Local stability resolution | 47 |
| 3.1.4 | Global stability resolution | 48 |
| 3.1.5 | Unsteady simulations | 51 |
| 3.1.6 | Boundary-layer code | 52 |
| 3.2 | Control methods | 52 |
| 3.2.1 | Identification | 52 |
| 3.2.2 | Structured mixed H_2/H_∞ synthesis | 54 |
| 3.2.3 | Controller implementation | 55 |
| 4 | Control of 2D instabilities with modern robust synthesis tools: feedforward vs feedback | 57 |
| 4.1 | Flow configuration | 59 |
| 4.2 | Noise-amplifier behaviour | 60 |
| 4.2.1 | Local stability results | 60 |
| 4.2.2 | Global stability results | 61 |
| 4.3 | Control setup | 64 |
| 4.4 | Control settings | 66 |
| 4.4.1 | Estimation and performance sensors | 66 |
| 4.4.2 | Input disturbance | 66 |
| 4.4.3 | Actuator | 68 |
| 4.5 | Identification and synthesis methods | 71 |
| 4.5.1 | ROMs | 71 |
| 4.5.2 | General constrained minimization problem | 73 |
| 4.6 | Preliminary results | 74 |
| 4.6.1 | Position of the estimation sensor | 74 |
| 4.6.2 | Evolution of performance as a function of the number of sensors z_i used in the synthesis | 77 |
| 4.7 | Feedforward versus feedback control | 79 |
| 4.7.1 | Performance on the nominal case | 80 |
| 4.7.2 | Stability robustness | 84 |
| 4.7.3 | Performance robustness | 86 |

| | | |
|----------|---|------------|
| 5 | Maintaining low disturbances over a range of free-stream velocity variations | 92 |
| 5.1 | Input/output dynamics of the system after velocity variations | 94 |
| 5.2 | Combined feedforward/feedback configurations | 96 |
| 5.2.1 | Synthesis method | 96 |
| 5.2.2 | Performance on the design point | 97 |
| 5.2.3 | Performance robustness | 99 |
| 5.3 | Multi-model synthesis | 100 |
| 5.3.1 | ROMs and synthesis method | 100 |
| 5.3.2 | Performance on the design points | 103 |
| 5.3.3 | Performance robustness | 107 |
| 5.4 | Gain scheduling | 110 |
| 5.4.1 | Synthesis method | 110 |
| 5.4.2 | Performance on the design points | 111 |
| 5.4.3 | Performance robustness | 112 |
| 5.4.4 | Piecewise gain scheduled law | 113 |
| 6 | Robust control of 3D instabilities in a supersonic boundary layer | 117 |
| 6.1 | 3D Flow configuration | 119 |
| 6.2 | Control setup | 120 |
| 6.2.1 | MIMO transfers: centralized problem | 120 |
| 6.2.2 | SISO transfers: decentralized problem | 121 |
| 6.3 | Control settings | 124 |
| 6.3.1 | Input disturbances | 124 |
| 6.3.2 | Actuators | 129 |
| 6.3.3 | Sensors for the synthesis | 131 |
| 6.4 | Identification and synthesis methods | 134 |
| 6.4.1 | Reduced-order models | 134 |
| 6.4.2 | Constrained minimization problems | 137 |
| 6.5 | Analysis of the controlled flow in the linear regime | 138 |
| 6.5.1 | Performance on the ROMs | 138 |
| 6.5.2 | Performance on the full system | 140 |
| 6.5.3 | Performance robustness | 144 |
| 6.6 | Robustness to non-linearities | 148 |
| 6.7 | Transition to turbulence | 150 |
| | Conclusions and outlook | 157 |
| | Appendices | 164 |
| | A Inner product matrices | 166 |
| | B Validation of the temporal and spatial schemes | 168 |
| | C Sponge zone | 171 |
| | D Additional 2D global stability results | 173 |
| | E 3D: Controller based on velocity performance sensors only | 177 |
| | References | 183 |

Résumé en Français

195

Nomenclature

Acronyms

| | |
|--------|----------------------------------|
| CFL | Courant–Friedrichs–Lewy number |
| CMP | Constrained Minimization Problem |
| CP | Constrained Problem |
| CPSD | Cross Power Spectral Density |
| DNS | Direct Numerical Simulations |
| GM | Gain Margin |
| LLST | Local Linear Stability Theory |
| MIMO | Multiple Input Multiple Output |
| PM | Phase Margin |
| PSD | Power Spectral Density |
| ROM | Reduced-Order Model |
| r.m.s. | Root Mean Square |
| SISO | Single Input Single Output |
| TS | Tollmien–Schlichting |

Constants

| Symbol | Definition | Value | Unit |
|--------------------|--|------------------------|-------------------------------------|
| γ | Heat capacity ratio | 1.4 | [–] |
| μ_{ref} | Reference dynamic viscosity for Sutherland’s law | 1.716×10^{-5} | Pa.s |
| Pr | Prandtl number | 0.725 | [–] |
| r | Ideal gas constant for air | 287. | J.K ⁻¹ .kg ⁻¹ |
| S | Sutherland temperature | 110.4 | K |
| T_{ref} | Reference temperature for Sutherland’s law | 273.15 | K |

Control variables

| Symbol | Definition |
|--|---|
| $\mathbf{A}, \mathbf{B}, \mathbf{C}, \mathbf{D}$ | State, input, output and feedthrough matrix |
| Δ | Uncertainty block |
| η | Scheduling variable |
| K | Controller |
| \mathbf{n} | Noise corrupting the estimation sensors |
| s | Laplace variable |
| S | Sensitivity function |
| $T_{ba}(s)$ | Transfer function from a to b |
| τ_{ba} | Convective delay from a to b |
| W_G | Weighting function on transfer G |
| \mathbf{x} | State vector |
| $\ \cdot\ _2$ | H_2 norm for systems and euclidean norm for vectors |
| $\ \cdot\ _\infty$ | H_∞ norm for systems |

Greek symbols

| Symbol | Definition | Unit |
|-------------------------------------|---|-------------------|
| α_i/α_r | Streamwise growth rate and wavenumber from LLST | 1/m |
| $\tilde{\alpha}_i/\tilde{\alpha}_r$ | Streamwise growth rate and wavenumber from DNS/resolvent analysis | 1/m |
| β | Spanwise wavenumber | 1/m |
| δ | Boundary layer thickness | m |
| δ^* | Compressible displacement thickness | m |
| δ_0^* | Compressible displacement thickness at the inlet of the domain | m |
| ω | Angular frequency | rad/s |
| ρ | Density | kg/m ³ |

Roman symbols

| Symbol | Definition | Unit |
|----------------------|--|-----------------------------------|
| \mathcal{A} | Jacobian operator | [–] |
| \mathbf{B} | Spatial forcing field | m ⁻¹ |
| C_f | Skin friction coefficient | [–] |
| c_φ | Phase velocity in the direction of propagation from LLST | m/s |
| \tilde{c}_φ | Phase velocity in the direction of propagation from DNS | m/s |
| d_e | Energy density | J/m ² |
| E_{Chu} | Chu's energy | J |
| e | Volumic energy | J/m ³ |
| \mathbf{f} | Volumic force | N/m ³ |
| $\tilde{\mathbf{f}}$ | Complex volumic force eigenvector | N/m ³ |
| f | Frequency | Hz |
| F | Dimensionless frequency | [–] |
| \tilde{g}^2 | Optimal resolvent gain | m ³ s ² /kg |

| | | |
|----------------------------|--|-----------|
| \mathcal{I} | Identity tensor | [–] |
| L_{BLT} | Length scale of boundary layer thickness | m |
| L_x | Streamwise length of the computational domain | m |
| L_z | Spanwise length of the computational domain | m |
| M | Mach number | [–] |
| \widehat{M} | Relative Mach number | [–] |
| \mathcal{N} | Compressible Navier–Stokes operator | [–] |
| N | N -factor | [–] |
| \widetilde{N} | N -factor envelope | [–] |
| p | Static pressure | Pa |
| \mathbf{q} | State vector of conservative variables | [–] |
| $\bar{\mathbf{q}}$ | Laminar base-flow quantities | [–] |
| \mathbf{q}' | Fluctuating flow quantities | [–] |
| $\tilde{\mathbf{q}}$ | Complex state eigenvector | [–] |
| \mathcal{R} | Resolvent operator | [–] |
| Re | Reynolds number | [–] |
| $R = \sqrt{Re_x}$ | Root of the Reynolds number based on the plate abscissa | [–] |
| T | Static temperature | K |
| t | Time | s |
| τ_{wall} | Wall shear stress | Pa |
| u | Streamwise velocity | m/s |
| \mathbf{w}, \mathbf{u} | Exogenous disturbance and actuator signals | Pa |
| \mathbf{y}, \mathbf{z}_i | Estimation and performance signals | Pa or m/s |
| $\tilde{\mathbf{y}}$ | Estimation signals without control | Pa |
| y_g | Wall-normal position of the generalized inflection point | m |
| x, y, z | Streamwise, wall-normal and spanwise coordinates | m |
| $\ \cdot\ _E, \ \cdot\ _F$ | Energetic norms | [–] |

Subscripts

| Symbol | Definition |
|---------------------------|---------------------------------|
| \cdot_∞ | Free-stream value |
| \cdot_{fb} | Feedback |
| \cdot_{ff} | Feedforward |
| \cdot_{rms} | Root mean square value |
| $\langle \cdot \rangle_t$ | Averaging in time |
| $\langle \cdot \rangle_z$ | Averaging in spanwise direction |

Superscripts

| Symbol | Definition |
|---------------|--|
| \cdot^{a_k} | Transfer function associated with the wavenumber B_k |
| \cdot^c | Controlled variables |
| \cdot' | Fluctuating quantities |

List of Figures

| | | |
|------|--|----|
| 1 | Comparison of heat fluxes on a generic hypersonic fore-body in a quiet environment on the left and a noisy one on the right at $M = 6$ from [47]. | 1 |
| 1.1 | Description of the boundary layer transition process for an idealized flat plate flow from [201]. | 9 |
| 1.2 | Representation from [150] of the different paths from receptivity to transition established by Morkovin [125]. | 10 |
| 1.3 | Geometric representation of non-modal growth from [162]. | 12 |
| 1.4 | Visualisation of a Tollmien-Schlichting wave in a boundary layer from [199]. | 14 |
| 1.5 | Neutral curves obtained from experiments [166] (dashed) compared to theoretical curve according to [161, 189] (solid). | 15 |
| 1.6 | Transition to turbulence at $M_\infty = 6$ due to the (a) first Mack mode and (b) second Mack mode. Figures from [90] and [91] respectively. | 16 |
| 1.7 | Effect of Mach number M_∞ on the maximum temporal amplification rate by LLST (a) in 3D viscous flow for the first two modes at $R = \sqrt{Re_x} = 1500$ and (b) in 2D inviscid flow for the first four modes. Figures from [111]. | 17 |
| 1.8 | Effect of the Mach number on the transition Reynolds number for the first two modes. Transition is supposed to occur when a perturbation has been amplified by e^9 . Figure from [116]. | 17 |
| 1.9 | (a) Visualisation of streaks in an incompressible boundary layer flow from [117]. (b) Comparison of the linear transient growth (with and without the unstable mode) and of the growth of the unstable mode only at $M = 2.5$ from [71]. | 19 |
| 1.10 | Optimal forcing (left) and response (right) of the first oblique Mack mode at $M = 4.5$ from [24] by resolvent analysis. | 19 |
| 1.11 | Q-criterion isosurface colored by streamwise velocity for (a) fundamental (K-type) and (b) sub-harmonic (H-type) resonance mechanisms from [158]. | 20 |
| 1.12 | Streamwise velocity fluctuations for the first Mack mode oblique breakdown from [60]. The arrows refer to the beginning and the end of the transition process. | 21 |
| 1.13 | Streamwise velocity fluctuations for the second mode (a) fundamental and (b) sub-harmonic breakdown from [60]. The arrows refer to the beginning of transition, the saturation of the second Mack mode disturbances and the end of the transition, respectively. | 21 |

| | | |
|-----|--|----|
| 2.1 | Classification of flow control strategies from [63]. | 25 |
| 2.2 | Pressure fluctuation amplitudes above the wall from [186]. The authors employed an acoustic metasurface, which falls into the passive control category. | 26 |
| 2.3 | Effect of wall cooling (a) on the maximum amplification rates of the first two Mack modes at $R = 1500$ (numerical results from [113]) and (b) on the transition Reynolds number (experimental results from [142]). | 26 |
| 2.4 | Flow structures colored by streamwise velocity fluctuations for (a) an adiabatic case and (b) a controlled case by optimal wall heat flux calculation from [78]. | 27 |
| 2.5 | Schematic 2D views of the (a) feedforward and (b) feedback configurations. | 30 |
| 2.6 | Block diagram of noise-amplifier flows for feedforward and feedback configurations with an inverse multiplicative input uncertainty Δ . In a feedforward setup, $T_{\mathbf{y}\mathbf{u}} = \Delta = 0$. The quantity \mathbf{n} represents an additional noise source. | 31 |
| 2.7 | Classical stability margins for SISO closed-loop system. | 32 |
| 2.8 | Inter-connected M and Δ systems from [167]. | 33 |
| 2.9 | (a) Multi-model and (b) gain scheduling methods by multi-criteria structured mixed H_2/H_∞ synthesis. | 42 |
| 3.1 | Simplified diagram of the validation case from [109]. | 46 |
| 3.2 | Comparison of (a) wall-pressure distribution and (b) second wall-normal streamwise derivative velocity profile at $Re_x = 1 \times 10^6$ with results from [109]. In (b), lengths are made dimensionless using the length scale of the boundary-layer thickness $L_{BLT} = \sqrt{\frac{\mu_\infty x}{\rho_\infty U_\infty}}$ | 47 |
| 3.3 | Comparison of the growth rates $-\alpha_i$ from the in-house LLST python code used in this thesis (solid lines) and from the LLST results of Ma and Zhong [109] (circles) for two dimensionless frequencies $F_{Mz} = \frac{2\pi f \mu_\infty}{\rho_\infty U_\infty^2}$ (and $\beta = 0$). | 48 |
| 3.4 | 2D optimal combination of canonical basis vectors for the 5-cell-stencil spatial scheme used in this thesis. Figure from [16]. | 49 |
| 3.5 | Comparison of the 2D (a) optimal gains and profiles at $F_{Mz} = 2.26 \times 10^{-4}$ of the (b) optimal forcing at $Re_x = 9.9 \times 10^5$ and (c) response at $Re_x = 1.62 \times 10^6$ with results from [24] (circles). | 50 |
| 3.6 | Comparison of $-\alpha_i$ from LLST of our in-house code (red line) and of [109] (red circles) and $-\tilde{\alpha}_i = \frac{1}{ \tilde{p}(x,y=0) } \partial_x \tilde{p}(x,y=0) $ from our resolvent analysis (blue solid line) and from the Fourier transform of [109] on linearized DNS (blue circles) at $F_{Mz} = 1.6 \times 10^{-4}$ | 51 |
| 3.7 | Comparison of self-similar profiles at $M_\infty = 4$ of streamwise velocity (blue) and temperature (red) computed with CLICET (solid lines) and from [136] (circles). | 52 |
| 4.1 | (a) Diagram of the computational domain. Inputs and outputs of the control problem are in red and blue, respectively. (b) Boundary layer profile used for the inlet condition. (c) Mach number field of the laminar base flow. Solid, dotted and dashed lines represent the boundary layer thickness δ , the generalized inflection point y_g and the compressible displacement thickness δ^* , respectively. | 59 |
| 4.2 | (a) Stability diagram; red solid lines represent isolines $\alpha_i = 0$. (b) Calculation of the N -factors (black solid lines) for transition prediction based on LLST: transition occurs at x_t when $\tilde{N} > N_t$ (notional diagram). (c) Performance objective for closed-loop control based on the N -factor criterion. (d) Modification of the N -factor criterion using the H_2 norm, in order to reduce conservatism. The quantity $F = 2\pi f \delta_0^*/U_\infty$ represents the dimensionless frequency. | 61 |

- 4.3 (a) Optimal resolvent gain as a function of the dimensionless frequency F . According to LLST, red and green dashed areas represent the unstable frequency range of first and second Mack modes, respectively. The region where both modes are unstable corresponds to an area where the first mode is unstable over a tiny distance. Real part of the streamwise component of the optimal forcing (b) and its associated streamwise velocity response (c) at $F = 0.237$. (d) Evolution at $F = 0.237$ of the forcing density and the different contributions to the Chu's energy density normalized by their maximum values. The position of the branch I and II from LLST are symbolized by vertical dashed lines. (e) Comparison of $-\alpha_i$ and $-\tilde{\alpha}_i$ at $F = 0.237$. Profiles of the optimal forcing components at $x = 867.2\delta_0^*$ (f) and response at $x = 1766.7\delta_0^*$ (g) at $F = 0.237$. The black dashed and dashed-dotted lines in (b), (c), (f) and (g) represent respectively the generalised inflection point position and the limit of the region of supersonic instabilities ($\widehat{M} > 1$ below this line). 63
- 4.4 Block diagram of the supersonic boundary layer system in a ideal case (with quantities in black and blue) and in a realistic setup (with quantities in black and red). The quantities in black are shared by both the ideal and realistic setups. The red dotted zone represents the system used for the identification/synthesis step. In a feedforward configuration, $T_{yu} = \Delta = 0$ 65
- 4.5 Contour plot of (a) the streamwise and (b) wall-normal components of \mathbf{B}_w with streamlines in black. 67
- 4.6 Velocity wavepacket generated by an impulse triggered at $t = 0$ of the exogenous input w at times $tU_\infty/\delta_0^* = 55.7, 557.5, 1114.9, 1672.4$. The black dashed line represents the generalized inflection point position y_g 67
- 4.7 (a) Evolution of $F|T_{z(x)w}|^2$. (b) Variation of the frequency magnitude as a function of the plate abscissa. For each frequency, the green (resp. blue) dots represent branch I and branch II of the first (resp. second) Mack modes according to LLST. The vertical dotted line in (b) shows the streamwise location of the actuator \mathbf{B}_u (see section 4.4.3), denoted x_u 68
- 4.8 (a) Spatio-temporal response of wall-pressure fluctuation sensors after an impulse of u . The vertical dotted line shows the streamwise location of the actuator \mathbf{B}_u , denoted x_u . (b) Evolution of the ratio $|T_{z(x)u}|/|T_{z(x)w}|$ as a function of frequency F for several plate abscissa. 69
- 4.9 Comparison of (a,b) $-\alpha_i$ and $-\tilde{\alpha}_i$ and (c,d) c_φ and \tilde{c}_φ at (a,c) $F = 0.236$ and (b,d) $F = 0.277$. The vertical dotted line shows the position of the initial disturbance \mathbf{B}_u in the streamwise direction. The horizontal dashed line $u(x, y_g)/U_\infty$ represents the velocity at the generalised inflection point along the flat plate. 70
- 4.10 (a,b,c) Comparison between impulse responses (blue lines) and the ROMs (red circles) for the performance sensor z_6 and for the feedback estimation sensor y_{fb} . Note that for the ROMs of T_{z_6u} and $T_{z_6\tilde{y}_{fb}}$, the time axis of the impulse responses are shifted by $\frac{\tau_{z_i\tilde{y}}U_\infty}{\delta_0^*} \simeq 897$ (black dashed lines) which corresponds to the suppression of unnecessary dead times. (d) Comparison between the quantity $W_{\tilde{y}_{fb}}$ from the linear simulation (blue line) and the ROM (red circles). 72

4.11 (a) Evolution of the maximum performance achievable of the ROM of the sensor z_6 as a function of the position of the measurement sensor y . The dotted line represents the actuator position; feedforward and feedback designs are respectively to the left and right of this dotted line. Comparison of the gains of the controllers from the structured synthesis and those from ideal destructive interference case (denoted ‘DI’) for (b) feedforward and (c) feedback configurations. The grey shaded area represents the range of the dominant frequencies of the sensor z_6 75

4.12 Evolution of the maximum performance achievable of the ROM of the sensor z_6 as a function of the controller order. The feedback and feedforward estimation sensors are placed at $x_{fb} = 885.7\delta_0^*$ and $x_{ff} = 801.2\delta_0^*$, respectively. 77

4.13 (a) Evolution of the local H_2 norm of the transfer $T_{z(x)w}$ from upstream noise w to wall-pressure fluctuation probes $z(x)$. The vertical magenta and black dotted lines represent, respectively, the position of the actuator (with the sensors y_{fb} and y_{ff} nearby) and the performance sensors z_i that can be used for synthesis. The values are normalized by $\|T_{z_1w}\|_2$. (b) Comparison of T_{z_6w} (solid lines) and T_{z_1w} (dashed lines) for the uncontrolled (black lines), Fb1z (blue lines) and Ff1z (red lines) cases. (c) Comparison of S_{z_6w} for different control cases. Disturbance rejection is improved (respectively degraded) below (respectively above) the dotted line. Grey shaded area represents the frequency range to be controlled from the actuator to the end of the domain. 78

4.14 Blue, red and dashed lines represent the feedback case, the feedforward case and the constraints (inverse of the weighting functions) imposed for the control design, respectively. (a) Magnitude of S . (b) Magnitude of KS . (c) Evolution of the local H_2 norm of the transfer $T_{z(x)w}$ as obtained from the DNS simulation (those obtained with the ROMs are actually identical at $x = x_i$ since the ROMs are very accurate). The vertical magenta and black dotted lines represent, respectively, the position of the actuator (with the sensors y_{fb} and y_{ff} nearby) and the six performance sensors z_i used for synthesis. The values are normalized by $\|T_{z_1w}\|_2$. The horizontal black dotted line depicts the energy threshold $\|T_{z_1w}\|_2$ satisfied until x_6 following the minimization of the cost functional $\max_{i=1,\dots,6} (\|T_{z_iw}^c\|_2)$. 80

4.15 Evolution of the local H_∞ norm of the transfer $T_{z(x)w}$ as a function of the plate abscissa for the uncontrolled (black dashed lines), feedback (a) and feedforward (b) cases. The evolution of $|T_{z(x)w}^c(F)|$ for some frequencies is also shown for the controlled cases. For vertical lines, it is the same caption as in figure 4.14c. . . . 81

4.16 Temporal sequence of the inputs (w and u) and outputs (y and z_i) of the system when excited by a continuous white-noise signal w 82

4.17 Contours of T'_{rms} for the (a) uncontrolled, (b) feedback and (c) feedforward cases. The white solid lines and dashed lines respectively represent the boundary layer thickness δ and the generalised inflection point position y_g 83

4.18 Contours of u'_{rms} for the (a) uncontrolled, (b) feedback and (c) feedforward cases. The white solid lines and dashed lines respectively represent the boundary layer thickness δ and the generalised inflection point position y_g 84

4.19 Evolution of the (a) module and (b) phase of T_{yu} after a variation of $\pm 5\%$ of the inlet velocity. (c) Global view and (d) zoom near the critical point (-1,0) of the Nyquist plot of the loop gain $-T_{yu}K_{fb}$ (solid blue line) and $-T_{yu\pm 5\%}K_{fb}$ (dashed and dotted red lines). The black dotted line represents the modulus margin $\|S\|_\infty^{-1}$ (the minimal distance to instability). The black dashed line represents the gain difference before instability and is linked to the gain margin GM 85

| | | |
|------|--|-----|
| 4.20 | In all subplots, feedback and feedforward designs are in blue and red lines, respectively. Controlled systems with ideal and noisy estimation sensors are represented by solid and dashed lines, respectively. (a) Short sequence of y_{fb} corrupted by 50% of the r.m.s. value without control of y_{fb} . Comparison of the evolution of (b) PSD_y , (c) PSD_u and (d) $\max_y u'_{rms}$ for the controlled systems with ideal and noisy estimation sensors. For the vertical lines, the caption in (d) is the same as in figure 4.14c. | 87 |
| 4.21 | Solid lines and dashed lines represent the cases with ideal and noisy estimation sensors, respectively. Blue lines and red lines represent the feedback controller used in figure 4.14b and the one resulting from a synthesis with a larger $ 1/W_{KS} $, respectively. Comparison of (a) KS and (b) PSD_u . (c) Contours of u'_{rms} for the higher $ 1/W_{KS} $ case with noisy y_{fb} . (d) Comparison of $\max_y u'_{rms}$. For the vertical lines, the caption is the same as in figure 4.14c. | 88 |
| 4.22 | Velocity, temperature and density profiles used for the inlet condition (solid lines for the nominal case and dashed and dotted lines for the $\pm 5\%$ cases, respectively). All profiles are made dimensionless with the nominal free-stream values. (a) Density variations. (b) Velocity variations. Comparison of uncontrolled pressure wavepackets generated by an impulse of w (c) and their PSD (d) at x_6 after a variation of ρ_∞ and U_∞ of -5% | 89 |
| 4.23 | Evolution of the local H_2 norm of $T_{z(x)w}$ after a variation of (a) ρ_∞ and (b) U_∞ of $\pm 5\%$ (dotted and dashed lines). The nominal cases are in solid lines. For vertical lines, same caption as in figure 4.14c. | 89 |
| 5.1 | Evolution of (a) $ T_{z(x)w} $ and (b) $F T_{z(x)w} ^2$ for the nominal $M_\infty = 4.5$ and the $\pm 5\%$ cases. The vertical dotted line in (a) represents the streamwise position of the actuator. In (b), curves are spaced at a uniform streamwise interval of $66.8\delta_0^*$ | 94 |
| 5.2 | Contour plot of the streamwise component of \mathbf{B}_u with streamlines in black. The generalized inflection point y_g for the nominal, $+5\%$ and -5% cases are in black, red and blue dashed lines, respectively. | 95 |
| 5.3 | (a) Frequency spectrum (at $x_6 = 1766.7\delta_0^*$) and (b) spatio-temporal response of wall-pressure fluctuation sensors after an impulse of u | 95 |
| 5.4 | Block diagram of a combined feedforward/feedback configuration. | 97 |
| 5.5 | (a) Gain of KS and of the constraint $1/W_{KS}$ for the $M_\infty = 4.5$ case. For the combined configurations, the quantity $ KS $ of the feedback (respectively feedforward) controller is represented with dashed line (respectively dot-dashed line). The grey shaded area represents the frequency range to control from the actuator to the end of the domain. (b) Evolution of the local H_2 norm of $T_{z(x)w}$. For vertical and horizontal dotted lines, same caption as in figure 4.14c. (c) Gain of T_{z_6w} | 98 |
| 5.6 | Evolution of the local H_2 norm of $T_{z(x)w}$ for the (a) -5% and (b) $+5\%$ cases. For vertical and horizontal dotted lines, same caption as in figure 4.14c. Gain of T_{z_6w} for the (c) -5% and (d) $+5\%$ cases. | 100 |
| 5.7 | Comparison of the ROMs (circles) and impulse/frequency data (solid lines) for the $M_\infty = 4.5$ (in dark), the -5% (in blue) and $+5\%$ (in red) cases. (a) and (b) are displayed for a feedforward estimation sensor (with a shifted time axis for the suppression of the unnecessary dead times) while (c) and (d) stand for a feedback estimation sensor. | 101 |

5.8 (a) Gain of KS and of the constraint $1/W_{KS}$ for the $M_\infty = 4.5$ case. The grey shaded area represents the frequency range to control from the actuator to the end of the domain. Evolution of the local H_2 norm of $T_{z(x)w}$ for (b) the nominal $M_\infty = 4.5$, (c) the -5% and (d) the $+5\%$ cases. The horizontal black dotted lines show the energy thresholds $1.03\|T_{z_1w}\|_2$ imposed in the multi-model syntheses for some sensors z_i . Same caption as figure 4.14c for vertical lines. Gain of T_{z_6w} for (e) the -5% and (f) the $+5\%$ cases. 104

5.9 Evolution of the local H_2 norm of $T_{z(x)w}$ for the (a) $M_\infty = 4.5$, (b) -5% and (c) $+5\%$ cases. For vertical and horizontal dotted lines, same caption as in figure 5.8. 106

5.10 Same caption as in figure 5.9. Order 5 controllers and order 15 controllers are in dashed and dotted lines, respectively. 106

5.11 Evolution of the local H_2 norm of $T_{z(x)w}$ for (a) the -2.5% and (b) the $+2.5\%$ cases. The horizontal black dotted lines show the energy threshold $1.03\|T_{z_1w\pm 2.5\%}\|_2$. Same caption as in figure 4.14c for vertical lines. 107

5.12 (a) Gain of the ROMs for $a_g = 1$ (solid lines), $a_g = 0.5$ and $a_g = 1.5$ (dashed lines). (b) Phase of the ROMs for $a_\tau = 1$ (solid lines), $a_\tau = 0.85$ and $a_\tau = 1.15$ (dashed lines). Evolution of the performance of the ROM at x_6 as a function of (c) gain variations a_g and (d) phase variations a_τ . Vertical dashed lines represent the performance on the nominal $M_\infty = 4.5$ ROM. Below (respectively above) the horizontal dashed lines, the control action reduces (respectively increases) the amplitude of perturbations. The vertical solid line in (c) displays the stability limit of the Fb controller for gain variations. 109

5.13 Evolution of the local H_2 norm of $T_{z(x)w}$ for the two gain scheduling design points: (a) the -5% and (b) the $+5\%$ cases. The baseline Fb/Ff controllers $K_{0\%}$ are in solid lines for comparison. For vertical and horizontal dotted lines, same caption as in figure 4.14c. Gain of T_{z_6w} for (c) the -5% and (d) the $+5\%$ cases. 111

5.14 Actuator signals u following an impulse of w for the -5% case. The impulse of w defines the origin of time. (a) Feedforward controllers. (b) Feedback controllers. Ff and Fb designate baseline controllers $K_{0\%}$ 112

5.15 The baseline $K_{0\%}$ Fb/Ff controllers and the gain scheduled laws are in solid and dotted lines, respectively. Gain of (a) K (with in dashed lines $|K_{\pm 5\%}|$), (b) $|S|$ and (c) KS for the $M_\infty = 4.5$ case. (d) Evolution of the local H_2 norm for the $M_\infty = 4.5$ case (*i.e.* $\eta = 0.5$). At this point, the gain scheduled laws are off-design and the baseline $K_{0\%}$ Fb/Ff controllers are on-design. For (d), same caption as in figure 4.14c for vertical and horizontal dotted lines. 113

5.16 Evolution of the local H_2 norm of $T_{z(x)w}$ for two off-design points of the piecewise gain scheduled law: (a) the -2.5% and (b) the $+2.5\%$ cases. The baseline Fb/Ff controllers $K_{0\%}$ are in solid lines for comparison. For vertical and horizontal dotted lines, same caption as in figure 4.14c. 114

5.17 Evolution of the local H_2 norm of $T_{z(x)w}$ for the $+2.5\%$ case (*i.e.* $\eta = 0.75$). The gain scheduled cases with no error on η are in dotted lines while the cases with an imperfect scheduling sensor are plotted by triangular symbols. For vertical and horizontal dotted lines, same caption as in figure 4.14c. 114

6.1 Diagram of the 3D computational domain used for linearized DNS. The red shaded region represents the sponge zone. Inputs and outputs of the control problem are in red and blue, respectively. 119

6.2 Block diagram of the 3D supersonic boundary layer system for a spanwise mode k as $B_k = \frac{2\pi k}{L_z}\delta_0^*$ 123

| | | |
|------|---|-----|
| 6.3 | Velocity and pressure wavepackets generated by an impulse of the exogenous input w^0 at times $tU_\infty/\delta_0^* = 76$ (a), 455 (b), 834 (c) and 1365 (d). | 126 |
| 6.4 | (a) Profiles at $x = 1766.7\delta_0^*$ of r.m.s. variables averaged in the spanwise direction. (b) Evolution of $\arg_y \max$ of the r.m.s. variables averaged in the spanwise direction. Black solid, dashed and dotted lines represent the boundary layer thickness, the generalized inflection point and the compressible displacement thickness, respectively. | 127 |
| 6.5 | Normalized PSD of fluctuating variables at $x = 1775\delta_0^*$, $z = 0$, (a) y_g and (b) $y = 0.015\delta_0^*$ when the 3D boundary layer is excited simultaneously by the 35 uncorrelated white-noise signals w^j | 127 |
| 6.6 | Modules of $\hat{T}_{\mathbf{z}(x)\mathbf{w}}^k$ for (a) velocity fluctuation performance sensors at the generalized inflection point and (b) wall-pressure fluctuation performance sensors. . . | 128 |
| 6.7 | Evolution of $\ \hat{T}_{\mathbf{z}(x)\mathbf{w}}^k\ _\infty$ for some k (a,b) and number of spanwise modes k necessary to contain at least 90% of $\ T_{\mathbf{z}(x)\mathbf{w}}\ _2$ (c,d) for velocity fluctuation performance sensors at the generalized inflection point (a,c) and wall-pressure fluctuation performance sensors (b,d). The vertical dotted line represents the streamwise position $x_{\mathbf{u}}$ of the actuators. The spanwise modes equal or lower than $k = 5$ (below the horizontal dotted line in (c,d)) are those used in the identification and synthesis step. | 129 |
| 6.8 | (a) Profiles of the streamwise (in blue) and wall-normal components (in red) of \mathbf{B}_{u^0} at (x,y) coordinates associated with their respective maximum values. (b) Iso-surfaces of the streamwise component $\mathbf{B}_{u^0}^x$ at -10% (blue) and $+10\%$ (red) of the maximum absolute value. Both figures display \mathbf{B}_{u^0} only on the length L_z of the domain. | 130 |
| 6.9 | Comparison of the modules of (a,c) $\hat{T}_{\mathbf{z}(x)\mathbf{u}}^k$ and (b,d) $\hat{T}_{\mathbf{z}(x)\mathbf{w}}^k$ at $x = 1775\delta_0^*$ for velocity fluctuation performance sensors at the generalized inflection point (a,b) and wall-pressure fluctuation performance sensors (c,d). | 131 |
| 6.10 | Evolution of $F \times \text{PSD}_{\mathbf{z}(x)}$ for sensors at the center of the spanwise direction. . . | 132 |
| 6.11 | Module of $\hat{T}_{\mathbf{y}\mathbf{u}}^k$ | 133 |
| 6.12 | Comparison of the ROMs (circles) and frequency/impulse data (solid lines) for the $\hat{T}_{\mathbf{z}_i\tilde{\mathbf{y}}}^k$, $\hat{T}_{\mathbf{z}_i\mathbf{u}}^k$, $\hat{T}_{\mathbf{y}\mathbf{u}}^k$ and $\hat{W}_{\tilde{\mathbf{y}}}^k$ used in the synthesis. Black, blue, green, red, orange and magenta colors correspond to quantities associated with a spanwise mode $k = 0$, $k = 1$, $k = 2$, $k = 3$, $k = 4$ and $k = 5$, respectively. Figures (c,d) are plotted for the wall-pressure performance sensors $\mathbf{z}_{3,\mathbf{p}}$ while figures (g,h) are plotted for the velocity sensors $\mathbf{z}_{3,\mathbf{u}}$. For the ROMs of $\hat{T}_{\mathbf{z}_{3,\mathbf{p}}\tilde{\mathbf{y}}}^k$ and $\hat{T}_{\mathbf{z}_{3,\mathbf{u}}\mathbf{u}}^k$, the time axis of the impulse responses are shifted by $\tau_{\mathbf{z}_i\tilde{\mathbf{y}}}U_\infty/\delta_0^* \simeq 892$ which corresponds to the suppression of unnecessary dead times. | 136 |
| 6.13 | For colors, same caption as in figure 6.12. (a) Gain of $(\hat{K}\hat{S})^k$ for the two minimization steps. (b) Nyquist plot of the loop gain $-(\hat{T}_{\mathbf{y}\mathbf{u}}\hat{K})^k$. (c) Comparison for controlled and uncontrolled cases of $\ \hat{T}_{\mathbf{z}_{3,\mathbf{u}}\tilde{\mathbf{y}}}^k\hat{W}_{\tilde{\mathbf{y}}}^k\ _2$ and $\ \hat{T}_{\mathbf{z}_{3,\mathbf{p}}\tilde{\mathbf{y}}}^k\hat{W}_{\tilde{\mathbf{y}}}^k\ _2$ normalized by their respective uncontrolled values $\ T_{\mathbf{z}\mathbf{w}}\ _2$ approximated by the six spanwise modes used in the synthesis. | 139 |
| 6.14 | Spatio-temporal responses and frequency spectra of the spanwise modes are in the first and second columns, respectively. The uncontrolled case for the performance sensors $\mathbf{z}_{3,\mathbf{u}}$ (resp. $\mathbf{z}_{3,\mathbf{p}}$) is plotted in (a,b) (resp. (e,f)). The controlled case for the performance sensor $\mathbf{z}_{3,\mathbf{u}}$ (resp. $\mathbf{z}_{3,\mathbf{p}}$) is plotted in (c,d) (resp. (g,h)). | 141 |

- 6.15 Evolution of $\|\hat{T}_{\mathbf{z}(x)\mathbf{w}}^k\|_\infty$ for some k for (a) velocity fluctuation performance sensors at the generalized inflection point and (b) wall-pressure fluctuation performance sensors. The vertical dotted line represents the streamwise position of the actuators. For colors, same legend as in figures 6.7(a,b). 142
- 6.16 Contours of u'_{rms} averaged in the spanwise direction for the uncontrolled (a) and controlled (b) cases. The white solid and dashed lines represent the boundary layer thickness δ and the generalized inflection point position y_g , respectively. . . 142
- 6.17 Contours of p'_{rms} averaged in the spanwise direction for the uncontrolled (a) and controlled (b) cases. The white solid and dashed lines represent the boundary layer thickness δ and the generalized inflection point position y_g , respectively. . . 143
- 6.18 Evolution of $\max_y \langle \cdot \rangle_{\text{rms}} \rangle_z$ for (a) ρ' , (b) T' , (c) u' and (d) p' . The vertical magenta and black dotted lines represent, respectively, the streamwise positions of the actuators (with the sensors \mathbf{y} nearby) and the performance sensors \mathbf{z}_i used for synthesis. 143
- 6.19 In all subplots, controlled systems with ideal and noisy estimation sensors \mathbf{y} are represented by blue and red lines, respectively. PSD of (a) y^0 and (b) u^0 . Evolution of (c) $\max_y \langle u'_{\text{rms}} \rangle_z$ and (d) $\max_y \langle p'_{\text{rms}} \rangle_z$. For vertical lines in (c,d), same caption as in figure 6.18. 144
- 6.20 Estimation sensors \mathbf{y} are corrupted by different levels of colored noises. (a) Short sequence of y^0 . PSD of (b) y^0 and (c) u^0 . Evolution of (d) $\max_y \langle u'_{\text{rms}} \rangle_z$ and (e) $\max_y \langle p'_{\text{rms}} \rangle_z$. For vertical lines in (d,e), same caption as in figure 6.18. . . 145
- 6.21 Start of the time sequence for (a) $z_{3,u}^0$ and (b) $z_{3,p}^0$ for the on-design case (solid lines) and the $\pm 2.5\%$ (dotted and dashed lines) off-design cases. 147
- 6.22 Evolution of the PSD of (a) $z_{3,u}^0$ and (b) $z_{3,p}^0$ after a variation of U_∞ of $\pm 2.5\%$. Evolution of (c) $\max_y \langle u'_{\text{rms}} \rangle_z$ and (d) $\max_y \langle p'_{\text{rms}} \rangle_z$ after a variation of U_∞ of $\pm 2.5\%$. The nominal cases are in solid lines; the $\pm 2.5\%$ cases are in dotted and dashed lines. For vertical lines in (c,d), same caption as in figure 6.18. . . . 148
- 6.23 Short sequence of y^0 for different intensity levels of exogenous noises w^j in the uncontrolled case. 149
- 6.24 For exogenous noise sources with (a,b) $\text{Var}[w^j] = 1$ and (c,d) $\text{Var}[w^j] = 25$, evolution of (a,c) $\max_y \langle u'_{\text{rms}} \rangle_z$ and (b,d) $\max_y \langle p'_{\text{rms}} \rangle_z$. The linear cases (dashed lines) are rescaled by multiplying their results by $\sqrt{\text{Var}[w^j]/\text{Var}[w^j_{\text{linear}}]}$ for comparison. For vertical lines, same caption as in figure 6.18. 149
- 6.25 For exogenous noise sources with $\text{Var}[w^j] = 4$, evolution of (a) $\max_y \langle u'_{\text{rms}} \rangle_z$ and (b) C_f . The linear case (dashed line) in (a) is rescaled by multiplying its results by $\sqrt{\text{Var}[w^j]/\text{Var}[w^j_{\text{linear}}]}$ for comparison. The magenta vertical line represents the streamwise position of the actuators. The first and second black vertical dotted lines represent the streamwise position from which the non-linear effects are no longer negligible and the beginning of transition to turbulence, respectively. The black dashed curves in (b) represent the evolution of the skin friction coefficient for the fully laminar case (lower curve) and the turbulent case (upper curve). 150
- 6.26 Uncontrolled DNS results of transition visualized using a Q-criterion isosurface ($Q = 2 \times 10^{-7} U_\infty^2 / \delta_0^{*2}$) colored by streamwise velocity for different streamwise segments: (a) $0 < x < x_{\text{NI}}$, (b) $x_{\text{NI}} < x < x_{\text{Tr}}$ and (c) $x_{\text{Tr}} < x < 3820.4 \delta_0^*$ 151
- 6.27 Evolution of $\max_y \langle \cdot \rangle_{\text{rms}} \rangle_z$ for (a) ρ' , (b) T' , (c) u' and (d) p' for the transition case. For vertical lines, same caption as in figure 6.25. 152

| | | |
|------|---|-----|
| 6.28 | Short sequence of u' (a) and p' (b) at $(x, y, z) = (3281.6\delta_0^*, 15.1\delta_0^*, 0.)$ and $(x, y, z) = (3281.6\delta_0^*, 0., 0.)$, respectively. | 153 |
| 6.29 | Profiles of $\langle u'_{\text{rms}} \rangle_z$ at (a) $x = x_{\text{NI}}$, (b) $x = 1910.2\delta_0^*$, (c) $x = x_{\text{Tr}}$ and (d) $x = 3300.5\delta_0^*$ | 153 |
| 6.30 | 2D spectrum $ \hat{u}'(F, k) $ of the (a,b) uncontrolled and (c,d) controlled cases at (a,c) $(x, y) = (1904.8\delta_0^*, 11.5\delta_0^*)$ and (b,d) $(x, y) = (1904.8\delta_0^*, 0.015\delta_0^*)$ | 154 |
| 6.31 | Instantaneous contours of streamwise velocity (xz -plane at $y = 1.99\delta_0^*$) and numerical Schlieren visualisation (xy -plane at $z = 0$) between $2939.7\delta_0^* < x < 3820.4\delta_0^*$ for the (a) uncontrolled and (b) controlled cases. | 155 |
| 6.32 | Evolution of the friction coefficient C_f for the transition to turbulence case. The third black vertical dotted line represents the beginning of transition to turbulence for the controlled case. For other vertical lines, same caption as in figure 6.25. | 155 |
| B.1 | Comparison of the gain of $T_{z(x)w}$ from the linearized DNS (solid lines) and from the frequency-domain resolvent approach (circles) for $x = 866.6\delta_0^*$ (in blue) and $x = 1766\delta_0^*$ (in red). The quantity $F = 2\pi f\delta_0^*/U_\infty$ represents the dimensionless frequency. | 169 |
| B.2 | (a,b) Grid and (c,d) temporal convergences of the gain of $T_{z^0(x)w^0}$ at $x = 868.5\delta_0^*$ for (a,c) wall-pressure performance sensor and (b,d) velocity performance sensor at the generalized inflection point. | 169 |
| C.1 | Spatio-temporal response of wall-pressure fluctuation sensors after an impulse of w . The dashed line represents the sponge zone beginning. | 172 |
| D.1 | (a) Evolution at $F = 0.118$ of the forcing density and the different contributions to the Chu's energy density normalized by their maximum values. The position of the branch I from LLST is symbolized by vertical dashed line. Real part of the streamwise component at $F = 0.118$ of the (b) optimal forcing and its associated (c) streamwise velocity response. Profiles of the optimal forcing components at $x = 867.2\delta_0^*$ (d) and response at $x = 1766.7\delta_0^*$ (e) at $F = 0.118$. The black dashed and dashed-dotted lines in (b), (c), (d) and (e) represent respectively the generalised inflection point position and the limit of the region of supersonic instabilities ($ \widehat{M} > 1$ below this line). | 174 |
| D.2 | For $F = 0.118$ (a,b) and $F = 0.237$ (c,d), evolution of e_{Chu} (a,c) and $e_{u'}$ (b,d). The black dashed and dashed-dotted lines represent the generalised inflection point position and the limit of the region of supersonic instabilities ($ \widehat{M} > 1$ below this line), respectively. | 174 |
| D.3 | The results of the gain optimisation based on Chu's energy and kinetic energy are in solid lines and circles, respectively. (a) Optimal resolvent gain as a function of F . Evolution at (b) $F = 0.118$ and (c) $F = 0.237$ of the forcing density and the different contributions to the Chu's energy density normalized by their maximum values. The positions of the branch I and II from LLST are symbolized by vertical dashed lines. | 175 |
| D.4 | For $F = 0.118$ (a,b) and $F = 0.237$ (c,d), profiles of the optimal forcing components at $x = 867.2\delta_0^*$ (a,c) and response at $x = 1766.7\delta_0^*$ (b,d). Solid lines and circles represent the results for an optimisation of the Chu'energy and kinetic energy, respectively. The black dashed and dashed-dotted lines represent the generalised inflection point position and the limit of the region of supersonic instabilities ($ \widehat{M} > 1$ below this line), respectively. | 176 |

E.1 Evolution of (a) $\max_y \langle u'_{\text{rms}} \rangle_z$ and (b) $\max_y \langle p'_{\text{rms}} \rangle_z$ for the baseline controller (blue line) and the controller based solely on velocity performance sensors $\mathbf{z}_{\mathbf{3},\mathbf{u}}$ in the CMP (red line). The vertical magenta and black dotted lines represent, respectively, the streamwise positions of the actuators (with the sensors \mathbf{y} nearby) and the performance sensors $\mathbf{z}_{\mathbf{i}}$ used for the baseline synthesis. 178

E.2 Contours of p'_{rms} averaged in the spanwise direction for (a) the uncontrolled case, (b) the baseline controller and (c) the controller based solely on velocity performance sensors $\mathbf{z}_{\mathbf{3},\mathbf{u}}$ in the CMP. The white solid and dashed lines represent the boundary layer thickness δ and the generalized inflection point position y_g , respectively. 179

E.3 Comparison of $|\hat{p}'(F, k)|$ at $(x, y) = (1312.2\delta_0^*, 0)$ for (a) the uncontrolled case, (b) the baseline controller and (c) the controller based solely on velocity performance sensors $\mathbf{z}_{\mathbf{3},\mathbf{u}}$ in the CMP. 180

E.4 For exogenous noise sources with $\text{Var}[w^j] = 1$ (a,b) and $\text{Var}[w^j] = 25$ (c,d), evolution of $\max_y \langle u'_{\text{rms}} \rangle_z$ (a,c) and $\max_y \langle p'_{\text{rms}} \rangle_z$ (b,d). For vertical magenta lines, same caption as in figure E.1. 181

E.5 Comparison of $|\hat{u}'(F, k)|$ at $(x, y) = (1775\delta_0^*, 0.015\delta_0^*)$ for exogenous noise sources with $\text{Var}[w^j] = 25$: (a) the uncontrolled case, (b) the baseline controller and (c) the controller based solely on velocity performance sensors $\mathbf{z}_{\mathbf{3},\mathbf{u}}$ in the CMP. 182

List of Tables

| | | |
|-----|--|-----|
| 4.1 | Streamwise positions of the input perturbation, the actuator and the sensors used for the identification and synthesis steps. The position of the estimation sensor for feedforward and feedback configurations are denoted x_{ff} and x_{fb} , respectively, and are the ones allowing the best results in terms of perturbation amplitude reduction. | 71 |
| 4.2 | Evolution of the performance after the controllers are implemented in <i>elsA</i> as a function of the number of sensors z_i used in the synthesis step. Cases labelled ‘Fbkz’ (respectively ‘Ffkz’) stand for feedback designs (respectively feedforward designs) with k performance sensors used in the synthesis. The results are normalized by the local H_2 norm of the uncontrolled system at the position x_1 | 78 |
| 5.1 | Comparison of performance for the different cases. They are ranked from best to worst according to the performance metric $\max_{x_1 < x < x_6} \left(\frac{\ T_{z(x)w}^c\ _2}{\ T_{z_1 w}\ _2} \right)$ which is related to the minimization term in the CMP equation 5.2. | 98 |
| 5.2 | Comparison of performance for the different cases. As the energy threshold imposed in the multi-model syntheses is considered satisfied for the $M_\infty = 4.5$ case for all control configurations (<i>i.e.</i> $\max_{x_1 < x < x_6} \left(\frac{\ T_{z(x)w}^c\ _2}{\ T_{z_1 w}\ _2} \right) \lesssim 1.03$), they are ranked from best to worst according to the performance metric $\max_{x_1 < x < x_6} \left(\frac{\ T_{z(x)w \pm 5\%}^c\ _2}{\ T_{z_1 w \pm 5\%}\ _2} \right)$ | 103 |
| 6.1 | Summary of the control settings: exogenous noises \mathbf{w} , actuators \mathbf{u} , feedback estimation sensors \mathbf{y} and performance sensors \mathbf{z}_i used in identification and synthesis. | 134 |
| 6.2 | Nominal performance on the ROMs for each spanwise mode k normalized by the weightings used in step 1 of the algorithmic procedure: their respective uncontrolled values $\ T_{z\mathbf{w}}\ _2$ approximated by the six spanwise modes used in the synthesis. | 140 |
| 6.3 | Wind tunnel and typical free-stream conditions for different altitudes. | 162 |
| 6.4 | Requirements and performance of the control law for a 3D supersonic boundary layer at Mach 4.5 for different free-stream conditions. | 162 |

Overall positioning

Because of its ability to limit the undesirable effects of fluids that restrict the efficiency of many industrial applications, flow control has attracted increasing interest in recent years in research areas such as noise suppression, increased lift, improved mixing, postponed flow separation, or drag reduction [22]. In the latter case, reducing drag would reduce fuel consumption, which is a laudable objective from an ecological point of view, but also from a financial one, as fuel consumption represents one of the main areas of expenditure in the aeronautical and maritime transport sectors [86]. Drag is generated in part by parietal friction due to the boundary layer, a concept formalised by Prandtl [143], who breaks down the flow into two distinct regions: one very thin and close to the wall, called the boundary layer, in which viscosity plays an important role, and another, far away, where viscosity can be neglected. As long as viscosity effects dominate convection effects, the boundary layer has a stationary behaviour and is said to be laminar. However, small perturbations can cause a transition to a chaotic/unsteady state which is called turbulent. A turbulent boundary layer leads to higher wall friction compared to a laminar boundary layer; this wall friction represents for example around 50% of the total drag in the case of subsonic flights [165]. Moreover, by leading to a turbulent boundary layer, the instabilities will also generate an increase in heat transfer (see figure 1) which becomes a major constraint for the design of supersonic/hypersonic vehicles [47, 82]. Hence, we will seek to control the instabilities in a supersonic boundary layer to limit their magnitude and thus delay transition to turbulence.

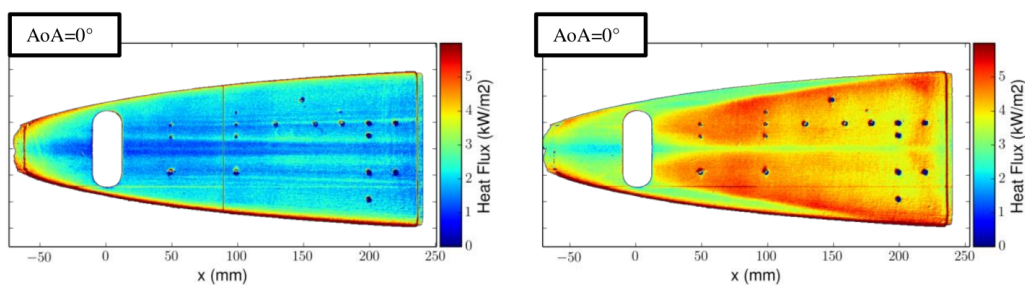


Figure 1: Comparison of heat fluxes on a generic hypersonic fore-body in a quiet environment on the left and a noisy one on the right at $M = 6$ from [47].

State of the art

Numerous studies addressed the problem of transition delay in the supersonic boundary layer flow: Gaponov and Smorodsky [64] injected heavy gas through porous wall to reduce surface friction and heat transfer, Sharma et al. [173] resorted to the generation of streaks to counter transient instabilities, Yao and Hussain [204] investigated the impact of spanwise wall oscillation on the drag of a supersonic turbulent boundary layer and Jahanbakhshi and Zaki [78] took advantage of the sensitivity of the Mack modes [111] to temperature to delay transition to turbulence. More recently, Celep et al. [29] combined both streak generation and wall heating/cooling effects to control oblique-breakdown in a supersonic boundary layer; Tian et al. [185, 186] managed to drastically decrease the linear growth rates of Mack modes thanks to ultrasonic absorptive coatings or to acoustic metasurfaces, which would potentially lead to delay transition. However, all the aforementioned studies employed passive or predetermined active strategies which do not exploit any real-time measurement and may therefore be less cost effective and robust to changes in operating conditions than a *reactive* control strategy [62]. Indeed, reactive control, due to its control action depending on measurements, is particularly well-suited to counteract hydrodynamic instabilities and therefore delay transition to turbulence. Nevertheless, to the best of our knowledge, reactive control of convective instabilities in a supersonic boundary layer has not yet been considered.

Noise-amplifier flows [38, 126, 153], like the supersonic boundary layer, are extremely sensitive to external disturbances, which are amplified downstream as they are convected by the flow. In this context, the purpose of reactive control is to cancel out noise-induced perturbations [10, 13] by producing destructive interferences with an actuator. This task is difficult for mainly two reasons: a) out of phase control actions respect to the incoming perturbations can be generated when variations of time-delay associated with the convection of perturbations occur, b) the wide spatially evolving range of amplified frequencies along the plate, from higher frequencies upstream to lower ones downstream.

The literature on noise-amplifier reactive control is dominated by the linear-quadratic-Gaussian (LQG) synthesis [13, 81, 153, 168, 188, and many others], a synthesis method dating back to the 1960s [83]. Despite being theoretically optimal with respect to a performance criterion (including a penalization of the control cost), this method comes with no guarantees on stability margins [43]. In other words, tiny errors in the model may end up in an unstable feedback loop when the estimation sensor is placed downstream of the actuator (*feedback* setup), which represents a major drawback for practical applications. Contrary to the feedback structure, the *feedforward* design (*i.e.* where the estimation sensor is placed sufficiently upstream of the actuator) is unconditionally stable and its implementation via LQG is not a problem. Therefore, feedforward configurations combined with LQG syntheses dominate the noise-amplifier flow control literature, particularly in the incompressible boundary layer control studies [10, 37, 38, 61, 126, 153, 156, 168–170].

However, the use of a feedforward setup raises the problem of performance robustness, which can be defined as the control law's ability to remain efficient in terms of perturbation amplitude reduction despite modelling errors or free-stream condition variations around the reference case. This problem has received little attention in the boundary layer control literature, with a few notable exceptions. To improve performance robustness compared to a simple fixed-structure LQG feedforward controller, Erdmann et al. [52] and Fabbiane et al. [54, 55] used an adaptive feedforward method for boundary layer control, based on the filtered-X least-mean-squares (FXLMS) algorithm, where the controller structure is adjusted according to the variations of the flow conditions through real-time measurements. However, this method is not robust to abrupt changes in inflow conditions because the controller coefficients are adjusted in a quasi-

static fashion. Due to its natural ability to be robust to unknown disturbances or uncertainties on the model [180], feedback design appears to be a promising alternative for performance robustness on short time scales. Barbagallo et al. [13] employed a feedback structure combined with an LQG synthesis to control instabilities over a backward-facing step. However, some of their feedback controllers turned out to be unstable on the real plant (the full linearized Navier–Stokes equations), because of the poor stability robustness of LQG to tiny errors in the model. Tol et al. [188] also obtained some unstable controllers when trying to control Tollmien–Schlichting (TS) waves in an incompressible two-dimensional boundary layer using LQG on a feedback setup. Belson et al. [14] are among the first to demonstrate the feasibility of a feedback setup with stability and performance robustness for the same flow, using a simple proportional-integral (PI) controller that was tuned by hand. A similar approach was used by Vemuri et al. [195], in order to cancel out TS waves in an experimental setup. The authors tuned a proportional controller by hand to optimise the controller gain in closed-loop while ensuring robust stability of their feedback configuration. Such loop-shaping approaches provide guarantees on stability robustness but are far from optimal from a performance viewpoint. And perhaps more importantly, they are very limited in the sense that they cannot be applied to more complex controller structures in a systematic way. In contrast, modern robust synthesis tools to optimize complex control laws, although available since the 1980s [45], are rarely employed in the case of noise-amplifier flows.

Motivations

To summarize, past studies were successful at delaying transition to turbulence in the supersonic boundary layer but they used passive or predetermined active strategies, potentially less effective and robust to changes in operating conditions than a reactive control strategy. Studies in incompressible flow with a reactive setup exist and succeed in delaying transition to turbulence of a boundary layer thanks to a feedforward configuration, which raises the problem of performance robustness (defined as the control law's ability to remain efficient in terms of perturbation amplitude reduction despite modelling errors or free-stream condition variations around the reference case). This fundamental issue has received little attention in the literature.

Objectives:

This is what justifies this study. It aims at creating a robust reactive control law to delay transition to turbulence of a supersonic boundary layer. Practically, the main objectives are to:

- ▷ Use a reactive setup to control instabilities in a supersonic boundary layer;
- ▷ Compare feedforward and feedback setups to mitigate the development of instabilities in noise-amplifier flows using modern robust synthesis methods;
- ▷ Present a generic methodology for the control of noise-amplifier flows to obtain a controller guaranteeing simultaneously nominal performance, stability robustness and performance robustness;
- ▷ Delay transition to turbulence in a 3D supersonic boundary layer based on the above-mentioned methodology.

Organisation of the manuscript

Chapters 1 and 2 are dedicated to a review of the literature concerning the stability/transition and control of boundary layer flows, respectively. The transition paths and the main results of linear stability and non-linear mechanisms as well as the control tools to mitigate the development of instabilities in noise-amplifier flows are detailed.

The aim of chapter 3 is to present the flow and control methods employed in the present work. The flow solvers and spatial/temporal schemes used are presented in this chapter. The local/global stability codes and the boundary-layer code used are also introduced along with validation elements. The algorithms of system identification and controller synthesis are also presented in this chapter, as well as the algorithm for the implementation of controllers in the fluid dynamics solvers.

Chapter 4 is dedicated to the construction of linear time-invariant (LTI) feedforward/feed-back controllers to control two-dimensional, *i.e.* spanwise invariant, and linear perturbations using modern robust synthesis tools. The 2D configuration simplifies the control problem and this chapter is a first step in learning how to design robust control laws to control convective instabilities. Firstly, the flow configuration and its noise-amplifier nature are introduced. Then, the control set-up and settings are presented, as well as the identified input-output models and constrained minimization problem for control. Finally, after some preliminary results about the position of the sensors, the results obtained on and off-design for the feedforward and feedback configurations are compared. Some of the results of this chapter have been presented at the 55th 3AF International Conference [127] and a paper has been published in Journal of Fluid Mechanics [131].

In order to maintain performance in terms of perturbation amplitude reduction over a wide range of free-stream velocity variations, advanced synthesis methodologies are investigated in chapter 5: LTI combinations of feedforward and feedback controllers, LTI controllers obtained by multi-model synthesis and gain scheduling controllers are considered, still for two-dimensional instabilities. Some of the results of this chapter have been presented at the GDR 2502 congress [128] and a paper has been submitted in AIAA Journal [129].

The aim of chapter 6 is to build a robust reactive law to control 3D instabilities. The purpose of this last chapter is to test the methodology developed in chapters 4 and 5 (resulting in a controller robust in stability and performance) first on a linear 3D configuration, but then also on a transitional configuration (*i.e.* with non-linear mechanisms) to verify that transition to turbulence can indeed be delayed. Firstly, the 3D configuration and the control setup/settings are presented. Then, the reduced-order models and the constrained minimization problem solved are explained. Finally, an analysis of the controlled flow in the linear and non-linear regimes (still laminar flow) is realized, before considering the results on a transitional case. Some of the results of this chapter have been presented at the 14th European Fluid Mechanics Conference [130] and a paper is in progress.

Conclusions and outlook are discussed in the last part of the manuscript, and additional results are left in appendices to facilitate the reading of the different chapters.

Literature review: stability and transition of boundary layer flows

| | | |
|------------|--|-----------|
| 1.1 | Navier–Stokes equations | 8 |
| 1.2 | Paths from receptivity to transition | 8 |
| 1.3 | Linear stability theory | 10 |
| 1.3.1 | Local linear stability theory | 10 |
| 1.3.2 | Global linear stability theory | 11 |
| 1.3.3 | Non-modal growth theory | 12 |
| 1.3.4 | Resolvent analysis | 12 |
| 1.4 | Linear mechanisms | 13 |
| 1.4.1 | Modal growth in incompressible flow | 14 |
| 1.4.2 | Modal growth in compressible flow | 15 |
| 1.4.3 | Transient growth | 18 |
| 1.5 | Non-linear mechanisms | 20 |
| 1.5.1 | Non-linear mechanisms in incompressible flow | 20 |
| 1.5.2 | First Mack mode oblique breakdown | 20 |
| 1.5.3 | Second Mack mode fundamental and sub-harmonic breakdowns | 21 |

Chapter foreword:

In this chapter, a review of the literature concerning the stability and transition of boundary layer flows is carried out. The Navier–Stokes equations are recalled in order to facilitate further reading. Then, the paths from receptivity to transition as well as the approaches that established the foundations of linear stability theory and the results derived from them are reviewed. As linear mechanisms do not lead directly to turbulence, we will briefly recall some results on the non-linear mechanisms that are necessary to initiate the transition process.

1.1 Navier–Stokes equations

The flow governing equations and the main dimensionless parameters used in this thesis are introduced at the beginning of the first chapter in order to facilitate the subsequent reading of the manuscript.

A three-dimensional compressible ideal gas is considered. The flow is governed by the Navier–Stokes equations:

$$\frac{\partial \rho}{\partial t} + \nabla \cdot (\rho \mathbf{u}) = 0, \quad (1.1a)$$

$$\frac{\partial \rho \mathbf{u}}{\partial t} + \nabla \cdot (\rho \mathbf{u} \otimes \mathbf{u}) = -\nabla p + \nabla \cdot \boldsymbol{\tau}, \quad (1.1b)$$

$$\frac{\partial \rho E}{\partial t} + \nabla \cdot (\rho E \mathbf{u}) = \nabla \cdot (-p \mathbf{u} + \boldsymbol{\tau} \cdot \mathbf{u} - \boldsymbol{\theta}), \quad (1.1c)$$

where ρ is the fluid density, \mathbf{u} the velocity vector, p the static pressure, $E = \frac{p}{\rho(\gamma-1)} + \frac{\mathbf{u} \cdot \mathbf{u}}{2}$ the total energy, $\boldsymbol{\tau}$ the viscous stress tensor and $\boldsymbol{\theta}$ the heat flux vector. Air being considered as a Newtonian fluid and Fourier's law for heat flux being considered applicable, the viscous stress tensor and the heat flux vector are given by:

$$\boldsymbol{\tau} = \mu(\nabla \otimes \mathbf{u} + (\nabla \otimes \mathbf{u})^T - \frac{2}{3}(\nabla \cdot \mathbf{u})\mathcal{I}), \quad (1.2)$$

$$\boldsymbol{\theta} = -k\nabla T, \quad (1.3)$$

with \mathcal{I} the identity tensor, k the thermal conductivity and μ the dynamic viscosity which is deduced from the local static temperature T via Sutherland's law,

$$\mu = \mu_{\text{ref}} \left(\frac{T}{T_{\text{ref}}} \right)^{\frac{3}{2}} \frac{T_{\text{ref}} + S}{T + S}. \quad (1.4)$$

The parameters of Sutherland's law are taken as: $\mu_{\text{ref}} = 1.716 \times 10^{-5}$ Pa.s, $T_{\text{ref}} = 273.15$ K and $S = 110.4$ K. The gas considered being air, $\gamma = 1.4$, $r = 287$ J.K⁻¹.kg⁻¹ and $Pr = \frac{\mu \gamma r}{k(\gamma-1)} = 0.725$.

The Reynolds and Mach numbers, representing respectively the ratio of inertial forces to viscous forces and the ratio of flow velocity to the local speed of sound, are defined as:

$$Re_L = \frac{\rho_{\infty} U_{\infty} L}{\mu_{\infty}}, \quad (1.5)$$

$$M = \frac{U}{\sqrt{\gamma r T}}, \quad (1.6)$$

with \cdot_{∞} denoting free-stream flow conditions and L a characteristic dimension.

1.2 Paths from receptivity to transition

The first observations of transition to turbulence in a flow are due to Reynolds [146] thanks to the injection of a dye in a circular pipe. For low velocities, the dye stream remains straight and stable: it is a laminar state. At higher velocities, the stream begins to diffuse and mix in the flow, which is considered characteristic of a turbulent state. In the case of the incompressible boundary layer on a smooth flat-plate with low amplitude external perturbations, the first experimental observations have shown a systematic evolution from an initially laminar to a

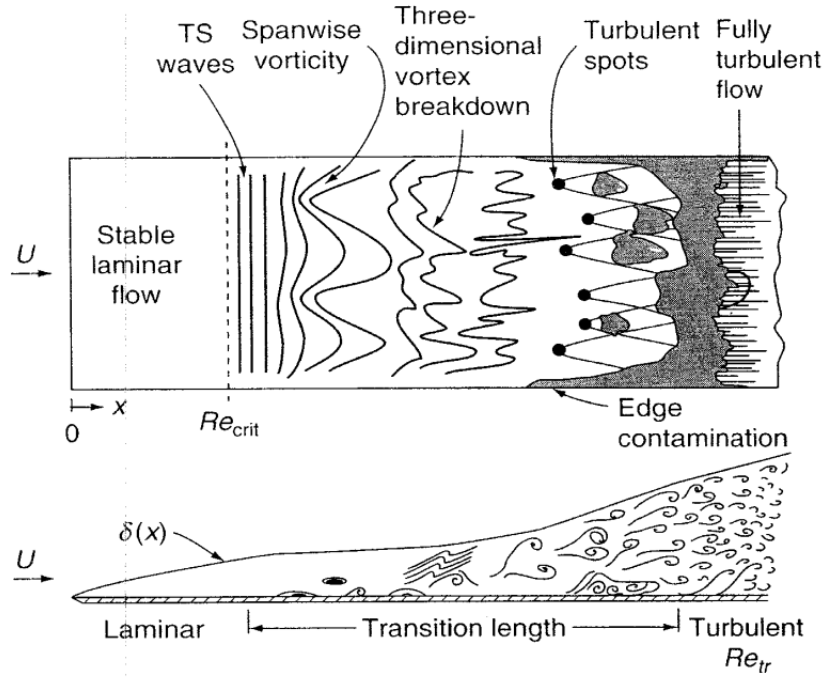


Figure 1.1: Description of the boundary layer transition process for an idealized flat plate flow from [201].

turbulent state. This natural transition process for a flow above an idealized flat plate is summarised in figure 1.1. The flow is initially laminar. From a certain plate abscissa x from the leading edge, the Reynolds number reaches a critical value (denoted Re_{crit}) for which the transition process starts: 2D propagating waves (*i.e.* spanwise invariant waves), called Tollmien–Schlichting (TS) waves, will form via a linear amplification process before giving rise to 3D waves and hairpin vortices. Subsequently, vortex breakdown appears in high shear regions and turbulent spots are formed and merge to form a fully turbulent flow.

Morkovin [125] has gathered the different mechanisms of transition to turbulence and the different processes are summarised in figure 1.2. The transition process starts with a receptivity phase which determines the characteristics (amplitude, nature, frequency, phase shift, etc.) of the disturbance which will be amplified along the boundary layer. Path *A* is the classical path of transition to turbulence when the external disturbances are of low amplitude. An infinitesimal perturbation leads to the exponential growth of unstable eigenmodes (*Primary modes*). The growth of each mode is considered independent. The amplitude of the modes increases until a threshold for which the linearity hypothesis (implying the non-interaction of the modes) is no longer valid, and three-dimensional non-linear mechanisms (*Secondary mechanisms*) appear before vortex breakdown (*Breakdown*) and a subsequent fully turbulent flow. However, it is possible that the superposition of stable but non-orthogonal eigenmodes (section 1.3.3) yields transient growth. It can then either be supported by modal growth if some modes are then unstable and if the amplitude of disturbances remains low at the end of the transient growth phase (path *B*), or be taken over by non-linear mechanisms for an initial disturbance of higher amplitude (path *C*), or bypass these two stages (path *D*) if the amplitude of the perturbation is strong enough to arrive directly at the vortex breakdown stage. The only difference between path *D* and *E* lies in the fact that the amplitude of the initial perturbation in the receptivity process is strong enough that the transient growth does not have time to take place and turbulent spots directly appear.

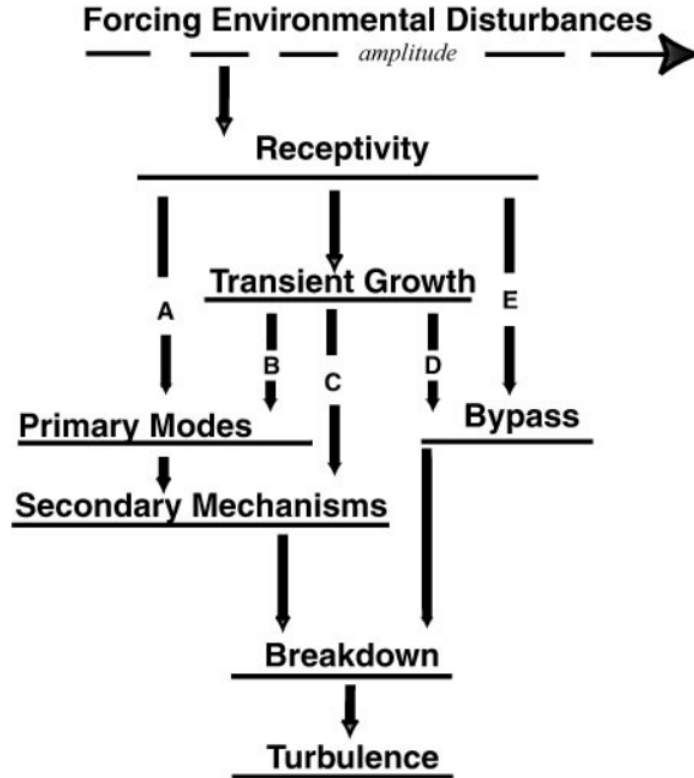


Figure 1.2: Representation from [150] of the different paths from receptivity to transition established by Morkovin [125].

1.3 Linear stability theory

As four of the five paths from receptivity to transition start with a linear growth phase (paths *A* to *D* in figure 1.2), it is important to review the different approaches that established the foundations of linear stability theory.

1.3.1 Local linear stability theory

The results of the modal growth phase (in path *A* of the figure 1.2) come from local linear stability theory (LLST). LLST studies the stability of a profile and cares about the development in time and/or space of an infinitesimal perturbation around the base state (also called fixed point), denoted $\bar{\mathbf{q}} = [\bar{\rho}, \bar{\rho\mathbf{u}}, \bar{\rho E}]^T$, which is a stationary solution of the Navier–Stokes equations (equation 1.1). The boundary-layer flow, which is homogeneous in the z -direction (spanwise direction), is assumed parallel and homogeneous in the x -direction (streamwise direction) in the LLST. The parallelism assumption in the case of a boundary layer flow, which is not a strictly parallel flow, implies that the characteristic dimension of the base flow evolution along the streamwise direction is sufficiently small compared to the wavenumber of the perturbation and that the characteristics of this perturbation are evolving very rapidly in the x -direction compared to the base flow [32]. At each streamwise position of the boundary layer, the base flow is assumed to be frozen in the x -direction for the stability analysis, therefore perturbations $\mathbf{q}' = \mathbf{q} - \bar{\mathbf{q}}$ can be sought in the form

$$\mathbf{q}' = \tilde{\mathbf{q}}(y)e^{i(\alpha x + \beta z - \omega t)}, \quad (1.7)$$

where in general the wavenumbers α/β and the angular frequency ω are complex numbers in the spatio-temporal framework. The quantity $\tilde{\mathbf{q}}(y)$ represents the eigenvector giving the structure

of the disturbance in the flow. Plugging this ansatz in the linearized Navier–Stokes equations with frozen base flow profile leads to a different dispersion relation $D(\alpha, \omega, \beta, x) = 0$ for each value of x .

In the case of the boundary-layer flow and with a spatial stability framework, real angular frequencies $\omega = 2\pi f$ and real wavenumbers β are considered; the dispersion relation is solved for the complex wavenumber $\alpha = \alpha_r + i\alpha_i$, where α_r is the streamwise wavenumber and $-\alpha_i$ is the spatial growth rate along x . When $-\alpha_i > 0$, the flow is locally spatially unstable. In the case of a temporal stability framework, real wavenumbers α/β and complex frequency $\omega = \omega_r + i\omega_i$ are considered; the flow is locally temporally unstable when $\omega_i > 0$.

A classical approach for relating instability to transition in boundary layer flows is based on the spatial framework of the LLST and is called the N -factor method [181]. A N -factor is defined as:

$$N(\omega, \beta, x) = \int_{x_c}^x -\alpha_i(\omega, \beta, x') dx' = \ln \left(\frac{|\phi'|}{|\phi'|_c} \right), \quad (1.8)$$

with x_c representing the position where the perturbation at the considered frequency ω and spanwise wavenumber β starts to be locally unstable and $|\phi'|_c$ the amplitude of one of the components of the vector \mathbf{q}' at this location. Transition is often assumed to occur when the quantity $\tilde{N}(x) = \max_{\omega, \beta} N(\omega, \beta, x)$ reaches at the position x_t a threshold value N_t . This criterion means that the transition process begins when a perturbation has been amplified by a factor of e^{N_t} , which defines an energy threshold depending on the disturbance environment and the receptivity process.

1.3.2 Global linear stability theory

The global approach consists in solving the spatial structure of the perturbations in all non-homogeneous directions [184], contrary to the local approach which was limited to the direction normal to the wall (y -direction). The global approach thus allows the capture of richer physics, but at a much higher numerical cost. The constraining assumptions of parallelism and homogeneity in the x -direction imposed by LLST are no longer necessary and the perturbation for boundary-layer flow is now written as \mathbf{q}' :

$$\mathbf{q}'(x, y, z, t) = \tilde{\mathbf{q}}(x, y)e^{i(\beta z - \omega t)}. \quad (1.9)$$

In the global approach, the Navier–Stokes equations (equation 1.1) can be written in condensed form:

$$\frac{\partial \mathbf{q}}{\partial t} = \mathcal{N}(\mathbf{q}), \quad (1.10)$$

with $\mathcal{N}(\mathbf{q})$ the compressible Navier–Stokes operator. By injecting the ansatz $\mathbf{q} = \bar{\mathbf{q}} + \mathbf{q}'$ into (1.10) and assuming \mathbf{q}' to be infinitesimal, we obtain:

$$\frac{\partial \mathbf{q}'}{\partial t} = \mathcal{A}(\bar{\mathbf{q}})\mathbf{q}', \quad (1.11)$$

where \mathcal{A} is the Jacobian matrix defined as $\mathcal{A} = \frac{d\mathcal{N}}{d\mathbf{q}}|_{\bar{\mathbf{q}}}$. Thus, the stability problem reduces to the following eigenvalue problem:

$$-i\omega\tilde{\mathbf{q}} = \mathcal{A}\tilde{\mathbf{q}}. \quad (1.12)$$

An eigenvalue decomposition of the Jacobian matrix can be performed to obtain information on the stability of the flow such as:

$$\mathcal{A} = \mathcal{V}\Lambda\mathcal{V}^{-1}, \quad (1.13)$$

with Λ and \mathcal{V} matrices containing respectively the eigenvalues $-i\omega$ and the spatial structure of the eigenvectors $\tilde{\mathbf{q}}$. As in the temporal framework of the LLST, the imaginary part ω_i of an eigenvalue corresponds to an amplification or attenuation in the time domain of the disturbance amplitude. If $\omega_i > 0$ for some eigenvalue, a global instability exists and the flow is referred to globally unstable or *oscillator*. Conversely, if $\omega_i < 0$ for all eigenvalues, the flow is globally stable. Although all eigenmodes are stable in this case, convective instabilities may exist (see section 1.3.3); the flow will be described in this case as convectively unstable or *noise-amplifier* and a disturbance will be convected and amplified downstream from its original source.

1.3.3 Non-modal growth theory

The modal analysis via local or global approach, although it has made it possible to obtain many stability results (see section 1.4), proves to be insufficient because being limited to the study of the eigenvalues amounts to being interested only in the behaviour of a disturbance when $t \rightarrow \infty$ and the behaviour of the disturbance at short time scale which could influence the dynamics of the flow is neglected [162]. Instead of studying the growth of each eigenmode independently, the matrix \mathcal{A} must be studied because information is contained in the eigenvectors of the matrix \mathcal{V} : when the eigenvectors are not orthogonal, their superposition can give a transient growth that is not detectable at long time scale (therefore not captured by a simple spectral analysis). The impact of the non-normality of the Jacobian matrix on the transient growth is illustrated in figure 1.3: the vectors Φ_1 and Φ_2 represent a basis of non-orthogonal eigenvectors associated to stable eigenvalues and \mathbf{f} a vector that decomposes in this eigenbasis such that $\mathbf{f} = \Phi_1 - \Phi_2$. Over the full time period considered, both $\|\Phi_1\|$ and $\|\Phi_2\|$ decrease. Although there is an attenuation of the norm of the eigenvectors due to the stability of the eigenvalues, $\|\mathbf{f}\|$ grows at short time scale before decreasing at long time scale. This illustration

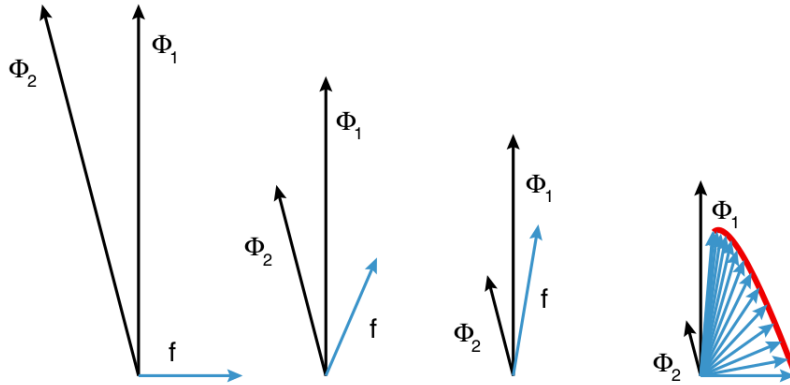


Figure 1.3: Geometric representation of non-modal growth from [162].

shows that the non-orthogonality of the eigenvectors and thus by extension the non-normality of the Navier–Stokes operator allows a transient growth which corresponds to the first stage from receptivity to transition of the paths B , C and D (see figure 1.2).

1.3.4 Resolvent analysis

Boundary-layer flow falls into the category of noise-amplifiers: all the eigenvalues of \mathcal{A} have a negative real part and the flow is therefore globally stable. As a result, all the global modes are stable and provide few information. An input/output analysis to reason in terms of amplification gain to characterize the convectively unstable behaviour of the flow from a

global point of view must be realized. By adding small-amplitude forcing \mathbf{f} to equation 1.11, we obtain:

$$\frac{\partial \mathbf{q}'}{\partial t} = \mathcal{A}\mathbf{q}' + \mathcal{P}\mathbf{f}. \quad (1.14)$$

The momentum forcing \mathbf{f} may either represent a noise source (naturally present in any real flow due to roughness, sound waves, free-stream turbulence, etc.) or the effect of an actuator. The matrix \mathcal{P} is a prolongation operator that transforms the momentum forcing into a full state-vector forcing by adding zero components. Switching to the frequency domain, a direct relation between the spatial structure of a harmonic forcing $\mathbf{f}(x, y, z, t) = \mathbf{f}(x, y)e^{i(\beta z - \omega t)}$ and its flow response $\mathbf{q}'(x, y, z, t) = \tilde{\mathbf{q}}(x, y)e^{i(\beta z - \omega t)}$ is established:

$$\tilde{\mathbf{q}} = \mathcal{R}\tilde{\mathbf{f}}, \quad (1.15)$$

where $\mathcal{R} = (-i\omega\mathcal{I} - \mathcal{A}(\beta))^{-1}\mathcal{P}$ is the resolvent operator. For a given real frequency ω and among all the possible forcings, the one which maximizes the gain

$$\tilde{g}^2(\omega) = \sup_{\tilde{\mathbf{f}} \neq 0} \frac{\|\tilde{\mathbf{q}}\|_E^2}{\|\tilde{\mathbf{f}}\|_F^2} \quad (1.16)$$

is examined, with $\|\cdot\|_E^2$ and $\|\cdot\|_F^2$ representing energetic norms. For a given frequency, the fields $\tilde{\mathbf{f}}$ and $\tilde{\mathbf{q}}$ corresponding to the optimal gain \tilde{g} are respectively called optimal forcing and response modes. In the spatially discretized framework, an inner product matrix can be defined such that:

$$\|\tilde{\mathbf{q}}\|_E^2 = \tilde{\mathbf{q}}^* \mathcal{Q}_e \tilde{\mathbf{q}}, \quad (1.17a)$$

$$\|\tilde{\mathbf{f}}\|_F^2 = \tilde{\mathbf{f}}^* \mathcal{Q}_f \tilde{\mathbf{f}}, \quad (1.17b)$$

with $\tilde{\mathbf{q}}^*$ denoting the conjugate transpose of $\tilde{\mathbf{q}}$. The Hermitian matrices \mathcal{Q}_e and \mathcal{Q}_f are respectively semi-definite-positive and positive-definite [151, 177]. Equation 1.16 becomes:

$$\tilde{g}^2(\omega) = \sup_{\tilde{\mathbf{f}} \neq 0} \frac{(\mathcal{R}\tilde{\mathbf{f}})^* \mathcal{Q}_e \mathcal{R}\tilde{\mathbf{f}}}{\tilde{\mathbf{f}}^* \mathcal{Q}_f \tilde{\mathbf{f}}} = \sup_{\tilde{\mathbf{f}} \neq 0} \frac{\tilde{\mathbf{f}}^* \mathcal{Q}'_e \tilde{\mathbf{f}}}{\tilde{\mathbf{f}}^* \mathcal{Q}_f \tilde{\mathbf{f}}}, \quad (1.18)$$

which amounts to a generalized Rayleigh quotient with $\mathcal{Q}'_e = \mathcal{R}^* \mathcal{Q}_e \mathcal{R}$ and where \tilde{g}^2 represents the largest eigenvalue of the following generalized eigen problem:

$$\mathcal{Q}'_e \tilde{\mathbf{f}} = \tilde{g}^2 \mathcal{Q}_f \tilde{\mathbf{f}}. \quad (1.19)$$

The optimal gain \tilde{g} provides information on the most amplified frequencies following a harmonic forcing and takes into account non-modal mechanisms and transient growth.

1.4 Linear mechanisms

The main linear growth results (first stage of paths A to D towards the transition) of boundary layer flows are presented in this section, first those related to modal growth (mostly from the LLST) in incompressible and compressible flows, then those related to transient/non-normal growth.

1.4.1 Modal growth in incompressible flow

For the hydrodynamic stability of parallel, incompressible and inviscid ($Re \rightarrow \infty$) shear flows, Rayleigh [145] demonstrated with the LLST that the existence of an inflection point ($\frac{\partial^2 u}{\partial y^2} = 0$ with u the streamwise velocity) is a necessary condition for instability. In the case of zero pressure gradient flat plate, this inflection point does not exist for incompressible flows and there can be no neutral ($\omega_i = 0$) or unstable waves. However, this inviscid approach and the Rayleigh's equation do not capture certain instabilities. Indeed, although viscous effects are traditionally associated with a stabilising effect, they are responsible for a viscous instability giving rise to Tollmien–Schlichting (TS) waves (see figure 1.4). These waves were demonstrated by the theoretical work of Tollmien [189] and Schlichting [161] during the inter-war period and were first observed experimentally in a low-speed wind tunnel by Schubauer and Skramstad [166].

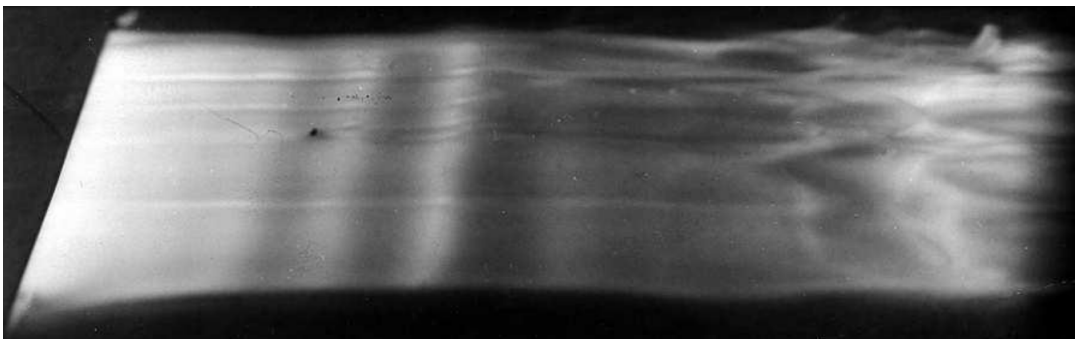


Figure 1.4: Visualisation of a Tollmien-Schlichting wave in a boundary layer from [199].

The equation used to describe the evolution of infinitesimal perturbations in the viscous framework is the Orr-Sommerfeld equation [163] and the existence of an inflection point is no longer a necessary condition for these viscous instabilities. Schubauer and Skramstad [166] neutral curve measurements are shown in figure 1.5. It is characterized by two distinct regions: one where a wave is amplified and one where a wave is damped. The instability domain for a given frequency is located between the lower branch, called branch I (convectively stable/unstable boundary) and the upper branch, called branch II (convectively unstable/stable boundary). Each frequency is therefore amplified only on a certain portion of the domain (the abscissa of figure 1.5 represents the square of Re_x): high-frequencies are amplified upstream of the plate while low-frequencies are found further downstream. In addition to these results, Squire's theorem [163] indicates that for any unstable oblique (3D) mode at a given Reynolds number, there is a 2D mode (*i.e.* spanwise invariant) which will be unstable further upstream. Furthermore, at any Reynolds number, the maximum amplification rate is found for 2D waves, so the N -factor instability threshold leading to transition will be related to 2D perturbations only [111].

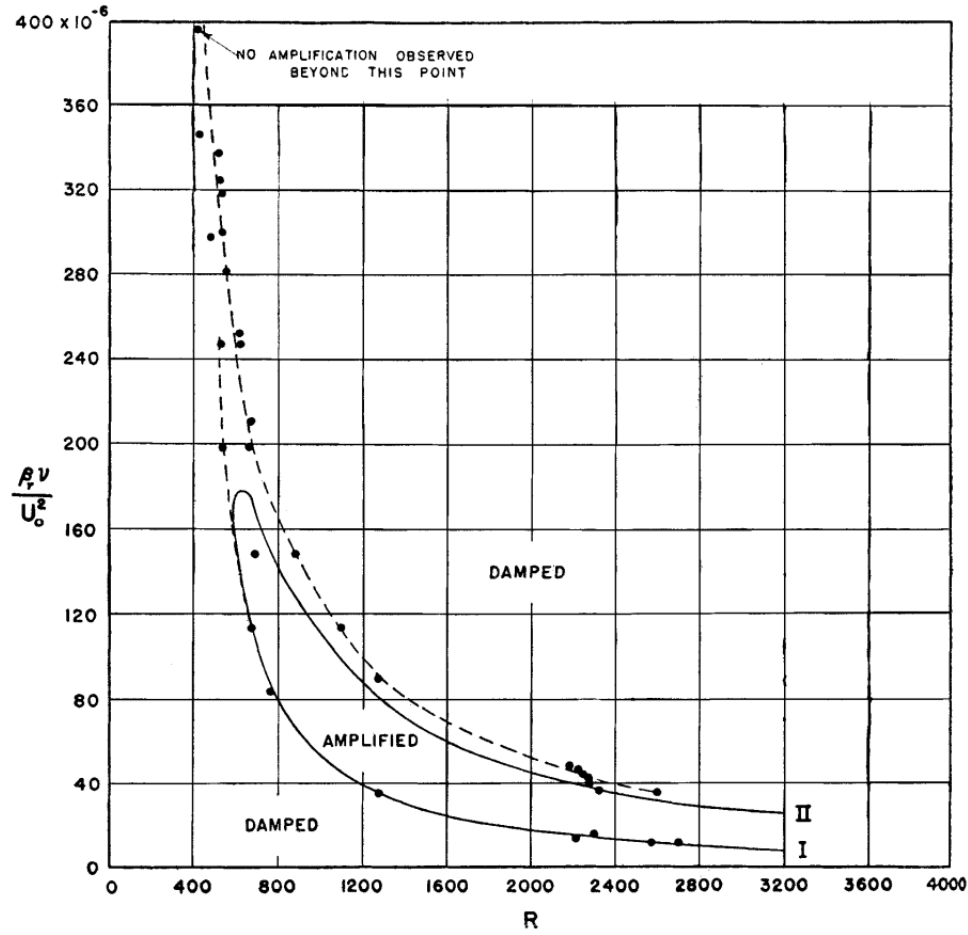


Figure 1.5: Neutral curves obtained from experiments [166] (dashed) compared to theoretical curve according to [161, 189] (solid).

1.4.2 Modal growth in compressible flow

As with the incompressible stability results, the general principles of compressible stability were obtained by LLST. After an initial classification of disturbances based on their phase velocities proposed by Lees and Lin [98], Mack [111] completed it by introducing a relative Mach number \widehat{M} , defined as follows [163]:

$$|\widehat{M}| = \frac{|\bar{u} - c_\phi|}{\sqrt{\gamma r T}}, \quad (1.20)$$

with $c_\phi = \omega_r / \sqrt{\alpha^2 + \beta^2}$ (in the temporal framework of the LLST) the phase velocity of the wave.

In the case where $|\widehat{M}| < 1$ in the entire flow field, a sufficient condition for the existence of a neutral/unstable wave in inviscid theory is that there exists a point $y_g > y_0$ where $\frac{\partial}{\partial y} \left(\frac{\rho \partial \bar{u}}{\partial y} \right) \Big|_{y_g} = 0$, called the generalized inflection point, with y_0 the point at which $\bar{u} = U_\infty (1 - 1/M_\infty)$. The phase velocity c_ϕ of the neutral wave (*i.e.* $\omega_i = 0$ with a temporal framework) is equal to the mean velocity at the generalized inflection point. This difference with the incompressible inflection point plays a predominant role in the case of a boundary-layer flow: contrary to the incompressible case where this inflection point does not exist, the generalized inflection point is present in the compressible adiabatic boundary layer, which may therefore be inviscidly unstable. When $|\widehat{M}| < 1$ in the entire flow field, there is only one unstable mode, called the *first Mack mode*. At low Mach number, this first mode is the compressible equivalent of TS waves

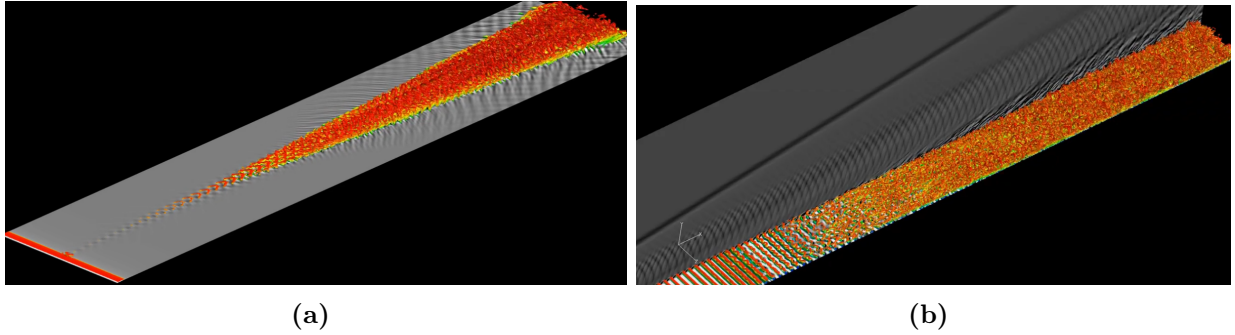


Figure 1.6: Transition to turbulence at $M_\infty = 6$ due to the (a) first Mack mode and (b) second Mack mode. Figures from [90] and [91] respectively.

and has a viscous nature. As the Mach number increases, the generalized inflection point moves out of the boundary layer and will exceed the point where $\bar{u} = U_\infty(1 - 1/M_\infty)$: the condition of inviscid instability $y_g > y_0$ is verified, the flow is unstable to inviscid perturbations (for $M_\infty > 2.2$ for 2D waves) and the nature of the first mode progressively changes from viscous instability to inviscid one [113]. For high Mach numbers ($M_\infty > 3$), the viscosity plays a stabilising role: the maximum amplification rates become lower in the viscous calculation than in the inviscid one. Conversely, as long as the viscous instability dominates the inviscid instability (*i.e.* for low Mach numbers) the viscosity helps to destabilise the system and the amplification rates are greater than in the inviscid case [111]. For incompressible flows, Squire's theorem [182] mentioned in section 1.4.1 indicates that the study of 2D perturbations is sufficient to establish a stability criterion. This criterion is no longer valid for compressible flows as the study of oblique disturbances (see figure 1.6a) is fundamental in the case of the first mode. Indeed, the amplification rates are maximal for 3D perturbations: for example, the most unstable first Mack mode is oblique and making an angle of 45° with the streamwise direction for $M_\infty = 1.3$ and up to 65° at $M_\infty = 3$ (see figure 1.7a).

Contrary to the case $|\widehat{M}| < 1$ where there is a unique wavenumber associated with the phase velocity of the neutral wave ($\omega_i = 0$) [98, 111], as soon as a portion of the fluid satisfies the condition $|\widehat{M}| > 1$, an infinite sequence of discrete wavenumbers corresponds to the phase velocity of the neutral wave [111, 116]. These additional modes appear in the inviscid theory when $M_\infty > 2.2$ in the case of a boundary-layer over an adiabatic flat plate. These additional modes are called *higher modes*. Mack [111] has shown that the first of these additional modes, called *second Mack mode*, is the most unstable of these higher modes in 2D (see figure 1.7b). Contrary to the first Mack mode which is the compressible equivalent of TS waves for low Mach values and whose inviscid instability mechanism at high Mach values is due to the presence of a generalized inflection point, the inviscid mechanism of the second Mack mode is only due the existence of a region where the streamwise base flow velocity relative to the disturbance phase velocity is supersonic (*i.e.* $|\widehat{M}| > 1$). Like the first mode for high Mach values, viscosity plays a stabilising role for the second Mack mode. Mack [111] has shown that the second mode has maximum amplification rates for 2D waves whatever the Mach number (see figure 1.7a) which is visually reflected in the simulation of Krishnan [91] by the upstream structures elongated in the spanwise direction (see figure 1.6b). Beyond the instability mechanism, several other distinctions exist between the first and second Mack modes: the unstable frequencies of the second Mack mode are higher and are associated with higher growth rates than those of the first Mack mode [109, 111] (see figure 1.7); it is said that the first mode is a vorticity mode in contrast to the second mode which is described as an acoustic mode [112]. Finally, with the *N*-factor method, the first Mack mode is responsible for transition to turbulence until $M_\infty = 7$

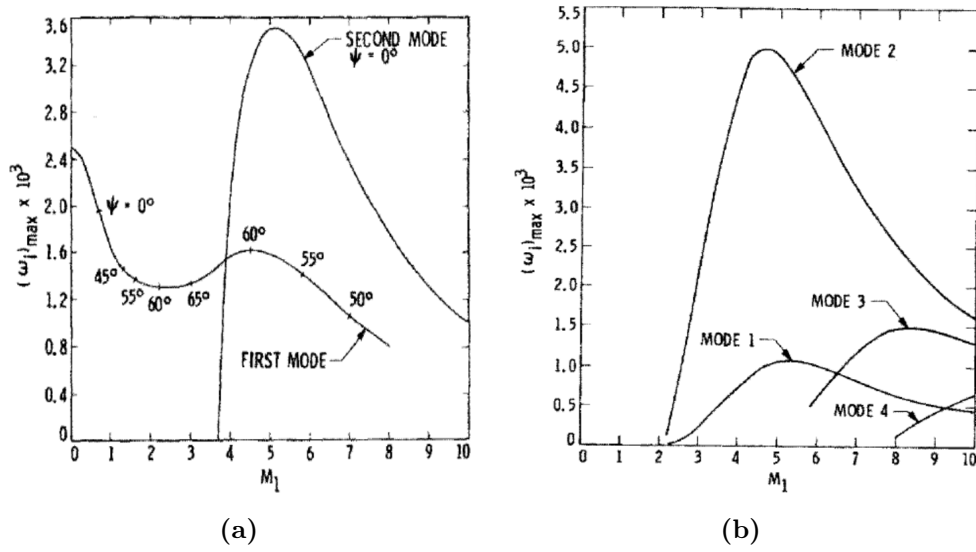


Figure 1.7: Effect of Mach number M_∞ on the maximum temporal amplification rate by LLST (a) in 3D viscous flow for the first two modes at $R = \sqrt{Re_x} = 1500$ and (b) in 2D inviscid flow for the first four modes. Figures from [111].

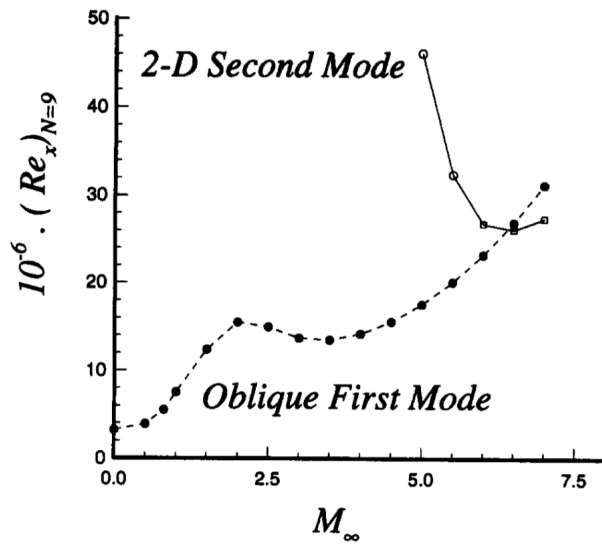


Figure 1.8: Effect of the Mach number on the transition Reynolds number for the first two modes. Transition is supposed to occur when a perturbation has been amplified by e^9 . Figure from [116].

(see figure 1.8), despite that the second Mack mode having higher growth rates than the first one as soon as $M_\infty > 4.5$ (see figure 1.7a); indeed, the energy of a disturbance depends on the local growth rate of the instability but also on the length over which it grows (*i.e.* the length of the instability domain, from the branch I to the branch II in LLST) [113, 116].

1.4.3 Transient growth

The phenomenon of transient growth exists when an energy growth is observed due to the stable mode superposition. This transient growth is associated with the non-normality of the Navier–Stokes operator and the non-orthogonality of the eigenvectors (see section 1.3.3). This phenomenon received a lot of attention in the 1990s, particularly in incompressible flows with the work of Trefethen et al. [190]. Hence, the consideration of linear transient growth explains that transition to turbulence in plane channel flow occurs well before the Re_{crit} found from the LLST [25]. Similarly, Couette flow is globally stable for all values of Re , whereas in reality, a transition appears due to transient growth [108]. For a boundary-layer flow, the flow being globally stable, the growth of disturbances is in reality only due to non-modal phenomena which are a consequence of the non-normality of \mathcal{A} [162]. The non-normal effects can be cast into two categories for open-flows: the *component-type non-normality* and the *convective-type non-normality* [177].

Component-type non-normality is characterized by a component-wise transfer of energy between the forcing and response fields and by the transport of the base flow by the disturbances [122] like in the lift-up or Orr mechanisms [24]. The lift-up effect results from the conservation of streamwise momentum when the particles are displaced vertically [137]. The lift-up effect was originally discovered in the 1970s by Ellingsen and Palm [51] in incompressible cases, and research on this phenomenon was then extended to compressible cases [71, 137, 191]. The appearance of streaks (see figure 1.9a), which is a purely 3D non-modal phenomenon as it cannot be predicted by classical spectral analysis, is explained by this lift-up mechanism. If the linear transient growth associated to the streaks is sufficiently important to create non-linear mechanisms, the local linear modal growth, which occurs further downstream of the flat plate, will be ignored (path C in figure 1.2) [122, 168]. These streaks have also been highlighted by Bugeat et al. [24] in a supersonic boundary layer at $M = 4.5$ through a resolvent analysis (see section 1.3.4). Starting with the LLST, Hanifi et al. [71] have also shown with an optimisation of a gain that the strongest linear transient growth is observed for very low longitudinal wavenumbers associated to streaks. Beyond this, they also showed that the superposition of the modes grew faster in the short term than the unstable mode (see figure 1.9b), thus justifying the importance of taking into account the non-orthogonality of the eigenvectors. Even without taking into account the unstable mode, the energy increases strongly over a certain period of time, which can lead to non-linear phenomena and then transition to turbulence. For the Orr mechanism [25, 134], Bugeat et al. [24] have shown that this mechanism impacts directly the Mack modes as the forcing and response fields are tilted in opposite direction (see figure 1.10), synonymous of the extraction of energy from the base flow.

Convective-type non-normality is governed by the transport of disturbances by the base flow and is caused by modal amplification on the local scale. It is characterized by a separation of the spatial supports of the forcing and response fields; for the boundary layer flows, the forcing field is localized upstream while the response field is localized further downstream (see figure 1.10). As this effect can be seen as the equivalent of a local modal instability but in a non-modal global framework, the principal results are the same as those developed in sections 1.4.1 and 1.4.2 and are not further detailed here.

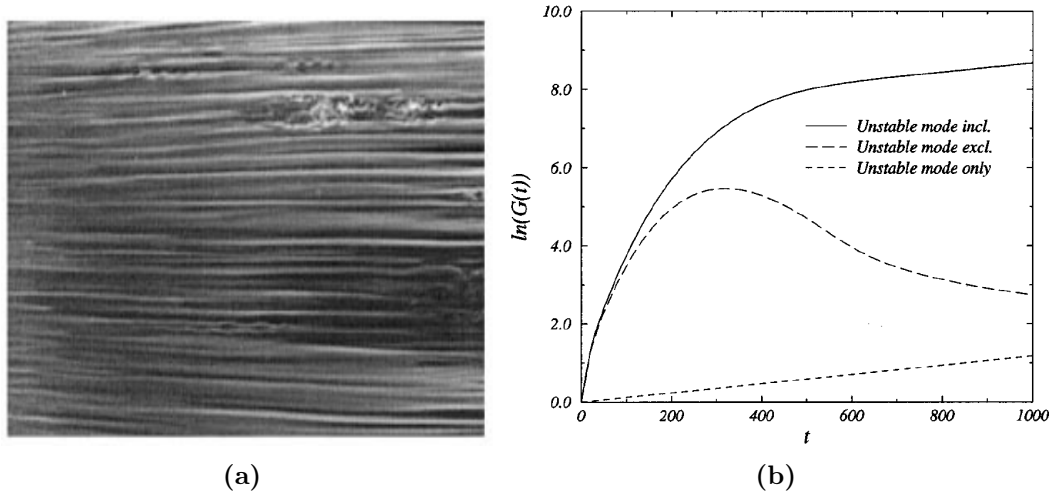


Figure 1.9: (a) Visualisation of streaks in an incompressible boundary layer flow from [117]. (b) Comparison of the linear transient growth (with and without the unstable mode) and of the growth of the unstable mode only at $M = 2.5$ from [71].

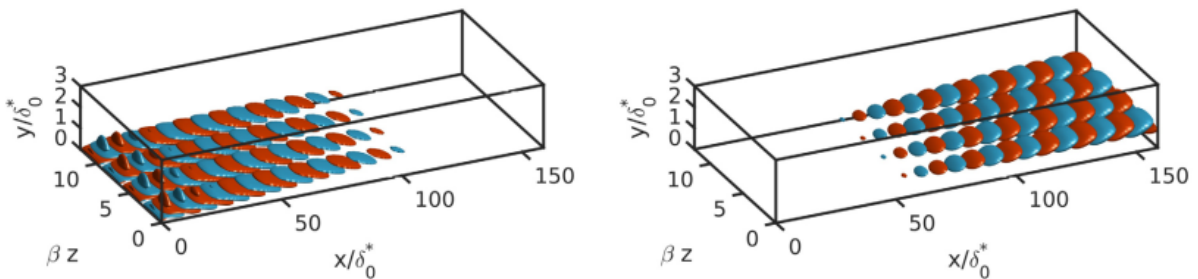


Figure 1.10: Optimal forcing (left) and response (right) of the first oblique Mack mode at $M = 4.5$ from [24] by resolvent analysis.

1.5 Non-linear mechanisms

The different mechanisms of linear growth (modal and non-modal) will not lead directly to turbulence, which will necessarily pass through a vortex breakdown stage, potentially due to secondary mechanisms leading to a growth by non-linear interactions (paths *A* to *C* in figure 1.2).

1.5.1 Non-linear mechanisms in incompressible flow

After the TS waves have reached a certain amplitude ($\sim 1/2\%$ of the free-stream velocity) and their growth saturate, secondary 3D instabilities start to develop in the flow. Klebanoff et al. [87] pointed out that a pair of oblique waves with the same angular frequency as the 2D fundamental TS waves can interact by non-linear mechanisms to create Λ -shaped vortices which will evolve in hairpin-shaped loops just before the onset of turbulence. In this scenario of fundamental transition (called *K-type*), the Λ structures are aligned (see figure 1.11a). In the case where the oblique waves have angular frequencies that are sub-harmonics of the fundamental 2D TS waves, the non-linear interactions will give the formation of staggered Λ vortices (see figure 1.11b); due to the work of Herbert [72] on this sub-harmonic breakdown scenario, it is referred as *H-type*.

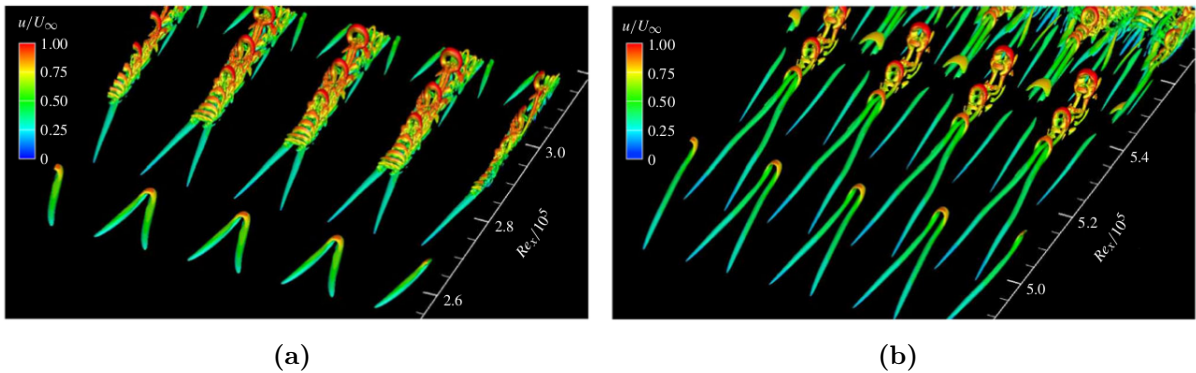


Figure 1.11: Q-criterion isosurface colored by streamwise velocity for (a) fundamental (*K-type*) and (b) sub-harmonic (*H-type*) resonance mechanisms from [158].

1.5.2 First Mack mode oblique breakdown

For supersonic boundary layer flows, as soon as the first Mack mode dominates, the first Mack mode oblique breakdown is considered to be a likely path from laminar to turbulent flow [60, 93, 118, 192, 206]. The non-linear interaction of two oblique Mack waves (with opposite wave angles) will form a wave-vortex triad with a steady streamwise structure [30, 118] showing that streaks play a fundamental role in the breakdown [93]. Franko and Lele [60] studied the laminar to transition process of a $M = 6$ flat-plate boundary layer and found that the first mode oblique breakdown leads to the shortest transition length compared to the second Mack mode fundamental/sub-harmonic breakdown (see section 1.5.3); figure 1.12 represents the growth and the breakdown of steady streaks with twice the spanwise wavenumber than the pairs of oblique waves that generated them.

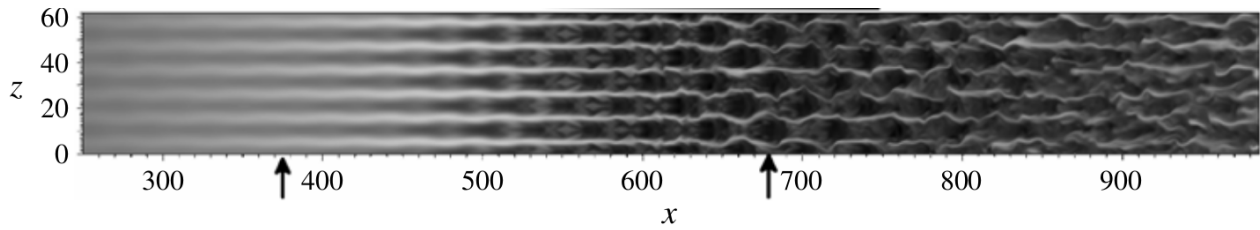


Figure 1.12: Streamwise velocity fluctuations for the first Mack mode oblique breakdown from [60]. The arrows refer to the beginning and the end of the transition process.

1.5.3 Second Mack mode fundamental and sub-harmonic breakdowns

Contrary to the first oblique breakdown which is highly documented, fewer studies exist about second Mack mode breakdown as both the amplification rates and unstable regions of the second mode oblique waves are small compared to the first Mack mode [206]. As in the incompressible case, two scenarios have been investigated for the second Mack mode breakdown: a fundamental one [70, 75, 179, 193] and a sub-harmonic one [1, 60, 193]. Both scenarios occur once the 2D wave grows sufficiently and saturates, leading to the growth of secondary oblique instabilities at either the same frequency (fundamental breakdown) or a sub-harmonic frequency (sub-harmonic breakdown) of the frequency of the 2D fundamental second Mack mode [60]. These secondary oblique instabilities lead to stationary streaks and then breakdown (see figure 1.13). Although the sub-harmonic resonance appears less strong than the fundamental resonance [60, 70, 75], this mechanism can play a role in the transition process [193, 206].

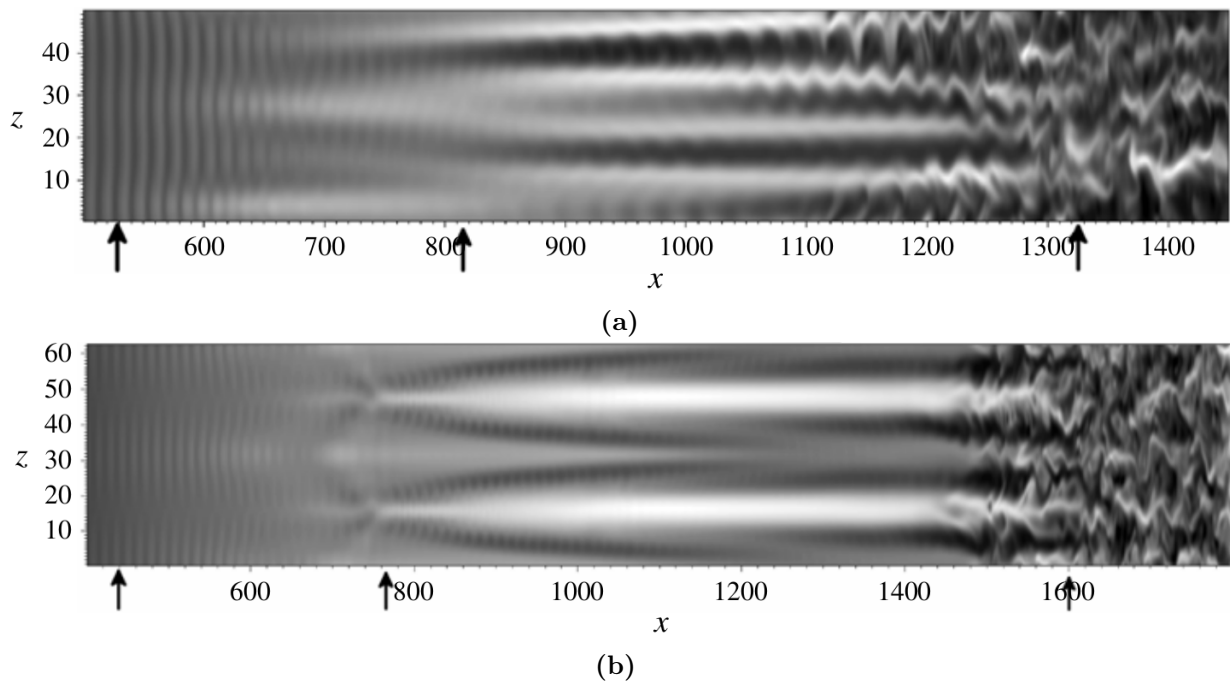


Figure 1.13: Streamwise velocity fluctuations for the second mode (a) fundamental and (b) sub-harmonic breakdown from [60]. The arrows refer to the beginning of transition, the saturation of the second Mack mode disturbances and the end of the transition, respectively.

Chapter outcome summary:

We saw in this chapter that transition to turbulence in boundary layers is initiated by amplification of external disturbances of various kinds (roughness, sound waves, free-stream turbulence, etc.) and several paths to transition are possible depending on the nature and intensity of incoming disturbances. For low levels of disturbances, which are at the beginning of four of the five paths from receptivity to transition, the disturbance growth is described by linear stability theory. For sufficiently high Mach number, a supersonic boundary layer is characterised by the presence of two convectively and inviscidly unstable modes: the first and the second Mack modes. The first Mack mode has a maximum amplification rate for 3D oblique perturbations while the second Mack mode has a maximum amplification rate for spanwise invariant perturbations. After this linear growth phase, first Mack mode or second Mack mode breakdowns are considered as likely path from laminar to turbulent flow, depending on which mode prevails. In this thesis, we will target transition to turbulence due to the linear growth of either the first or the second Mack modes, which we will try to reduce. For supersonic boundary layers, delaying transition will delay the increase in wall friction and the generated heat which are major concerns for the design of supersonic/hypersonic vehicles.

Literature review: controlling instabilities and transition

| | | |
|------------|---|-----------|
| 2.1 | Control strategies | 25 |
| 2.2 | Purpose of reactive control depending on the flow nature | 27 |
| 2.3 | Description of linear time-invariant systems | 28 |
| 2.4 | Control formalism | 29 |
| 2.4.1 | Nominal performance | 31 |
| 2.4.2 | Stability robustness | 31 |
| 2.4.3 | Performance robustness | 33 |
| 2.4.4 | Feedforward vs Feedback | 34 |
| 2.5 | Reduced-order models | 34 |
| 2.5.1 | Galerkin projections | 35 |
| 2.5.2 | Data-based approaches | 36 |
| 2.6 | Synthesis methods | 37 |
| 2.6.1 | LQR | 37 |
| 2.6.2 | LQG/LTR | 38 |
| 2.6.3 | Inverse feedforward/Wiener–Hopf framework | 38 |
| 2.6.4 | Classical loop-shaping | 39 |
| 2.6.5 | Modern optimal synthesis | 40 |
| 2.6.6 | Structured synthesis | 41 |
| 2.7 | Maintaining performance over several operating points | 41 |

Chapter foreword:

In this chapter, a review of the literature concerning the control of boundary layer flows is carried out. Firstly, a classification of the different control strategies is presented. Then, the purpose of control, reminders of control notions as well as the control formalism are detailed. Finally, various identification and synthesis methods necessary for the design of a control law are presented in order to choose the most suitable ones.

2.1 Control strategies

The terminology used in this thesis to classify the types of control is based on the work of Gad-el Hak [63]. His classification of control strategies is displayed in figure 2.1.

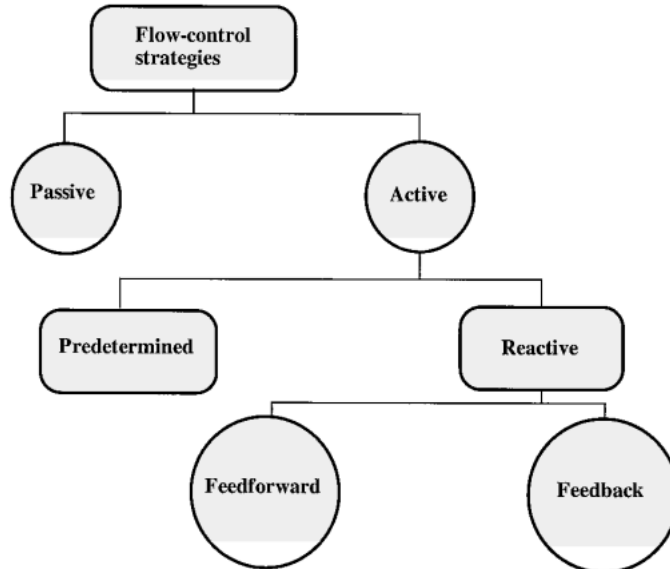


Figure 2.1: Classification of flow control strategies from [63].

The first main distinction is between a passive and an active strategy. Passive control does not require any auxiliary energy source. This category includes, for example, the use of chevrons in turbulent jets to limit large vortex structures in order to reduce acoustic noise [21, 94] or the use of riblets to limit turbulence and reduce drag [34]. More recently, Tian et al. [186] managed to drastically decrease the linear growth rate of the second Mack mode over a relatively wide frequency range thanks to an acoustic metasurface consisting of two layers of perforated plates, which would potentially delay transition (see figure 2.2). Some applications require the opposite effect, such as air intakes where a turbulent boundary layer is required to avoid separation, and roughness can be used to trigger transition to turbulence [99, 200].

An active strategy requires the use of an energy source and can be broken down into predetermined or reactive action. In the case of predetermined active action, the control acts in a predefined way regardless of the state of the flow; therefore, this method does not necessitate an estimation sensor which would inform in real time the actuator of the characteristics of the incoming disturbances (phase, bandwidth, etc.). The use of an isothermal flat plate to control transition to turbulence falls into this category and many studies exist for supersonic/hypersonic boundary layer flows. The purely modal numerical studies [111, 113, 116] have shown that cooling the plate leads to the stabilisation of the first Mack mode but destabilises the second one (see figure 2.3a). Conversely, heating the plate stabilises the second mode and destabilises the first one. This latter technique is rarely used because one of the main goals of delaying transition is to reduce heat flux as high temperatures may lead to material degradation. More recent numerical studies have also investigated the impact of wall temperature on transient growth. It was found that there is a particular plate temperature (lower than the adiabatic one) which optimally limits transient growth [20]. This optimal temperature effect has also been demonstrated experimentally by Potter [142]: cooling the plate allows the transition process to be delayed up to a certain wall temperature (see figure 2.3b); further cooling may have the opposite effect. Nevertheless, the effect on transition at high Mach number remains marginal (see figure 2.3b), which is in agreement with experimental results by Deem and Murphy [41]

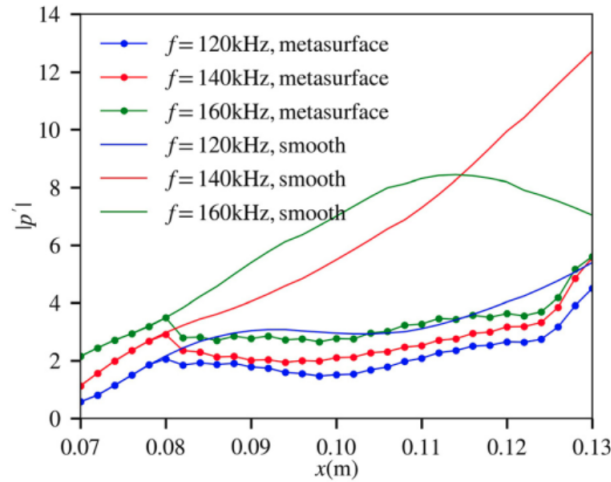


Figure 2.2: Pressure fluctuation amplitudes above the wall from [186]. The authors employed an acoustic metasurface, which falls into the passive control category.

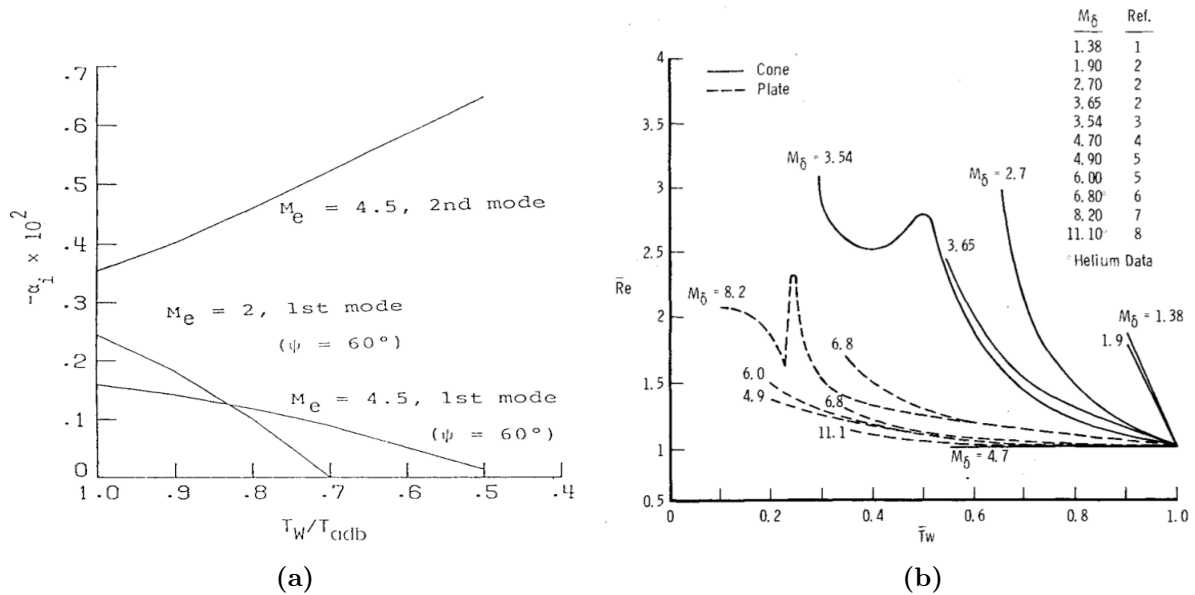


Figure 2.3: Effect of wall cooling (a) on the maximum amplification rates of the first two Mack modes at $R = 1500$ (numerical results from [113]) and (b) on the transition Reynolds number (experimental results from [142]).

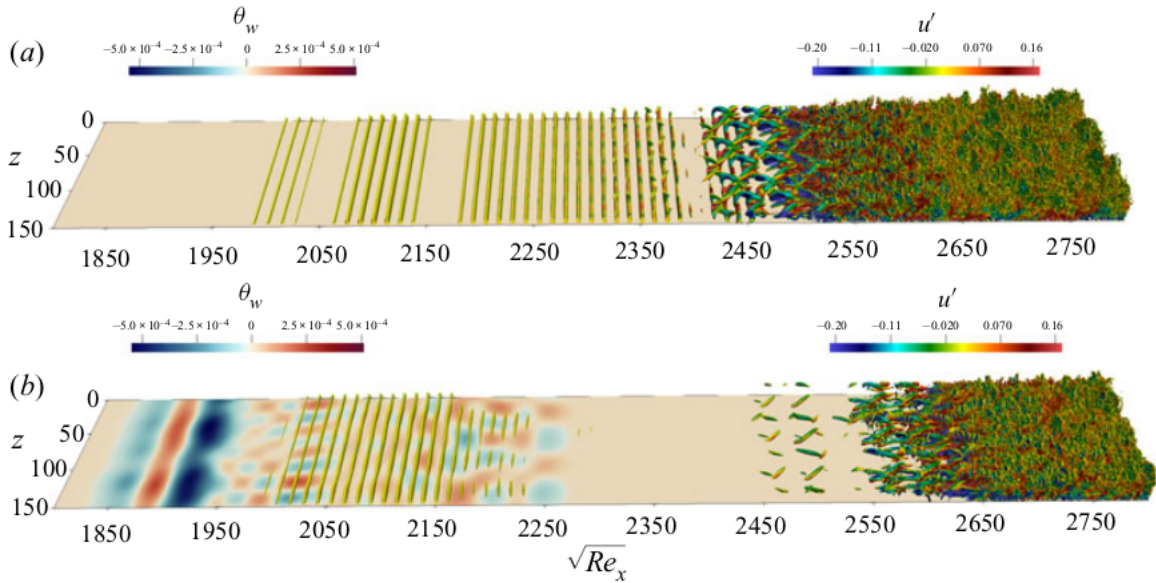


Figure 2.4: Flow structures colored by streamwise velocity fluctuations for (a) an adiabatic case and (b) a controlled case by optimal wall heat flux calculation from [78].

and Sanator et al. [149]. More recently and still using predetermined active control methods, Gaponov and Smorodsky [64] injected heavy gas through porous wall to reduce surface friction and heat transfer. Sharma et al. [173] resorted to the generation of streaks to counter transient instabilities while Yao and Hussain [204] investigated the impact of spanwise wall oscillation on the drag of a supersonic turbulent boundary layer. Jahanbakhshi and Zaki [78] took advantage of the sensitivity of the Mack modes to temperature to delay transition to turbulence (see figure 2.4).

However, all the aforementioned studies employed passive or predetermined active strategies which do not exploit any real-time measurement and may therefore be less cost effective and robust to changes in operating conditions than a *reactive* control strategy. The reactive strategy distinguishes two main categories: *feedforward* and *feedback* controls. The distinction between these two methods and the formalism of reactive control will be the subject of a whole section (see section 2.4), because of their importance in this thesis. The classical tools of control theory (identification, synthesis, etc.) generally only concern reactive control. These tools are well-established in a linear framework; despite the fact that the Navier–Stokes equations are strongly non-linear due to the convective term, they can be described in the linear approximation around the laminar base field (called the fixed point or equilibrium point), which is the stationary solution of equations 1.1 [177]. Seeking to control the perturbations around this equilibrium point amounts, from a physical point of view, to concentrating on perturbations of small amplitudes, being at the origin of the paths *A* to *D* from receptivity to transition (see figure 1.2). Therefore, one can seek to mitigate the modal and non-modal linear growths of the first and second Mack modes in order to delay transition in a supersonic boundary layer, using the classical tools of reactive control.

2.2 Purpose of reactive control depending on the flow nature

As explained in section 1.3.2, weakly non-parallel open shear flows can be classified into two categories: oscillator flows (by definition linearly globally unstable) and noise-amplifier flows

(by definition linearly convectively unstable). From a control point of view, these two flows are treated in a different way.

An oscillator flow has an intrinsic dynamic and the nature of the incoming disturbance has little influence from a control perspective. As the sensitivity to noise is low, the flow is dominated by a limited number of structures of well-defined frequencies [13]. For this type of flow, a necessary condition (but not sufficient if the flow is not in the vicinity of the fixed point) for the flow to be attracted to the fixed point is to suppress the global instability [164]. The control of a flow around a cylinder at $Re = 47$ [177] or a flow above a cavity at $Re = 7500$ [12] are the most common examples of oscillator flows where one seeks at least to stabilize the unstable pole(s). In the case where the flow is well beyond the critical equilibrium point, it is much more difficult to construct a control law based on linear tools because of the non-linearities that drive the system [164] but it is not impossible using an iterative approach [96].

Contrary to oscillator flows, noise-amplifier flows, in the absence of a dominant spatial structure, are extremely sensitive to external disturbances which are amplified downstream as they are convected by the flow. The backward-facing step [13] or the boundary-layer flow [10] fall into this category which constitutes the framework of our study. For this type of flow, the purpose of reactive control is to cancel out noise-induced perturbations [10, 13] by producing destructive interferences with actuators. This task is difficult for mainly two reasons: (a) out of phase control actions respect to the incoming perturbations can be generated when variations of time-delay associated with the convection of perturbations occur, (b) the spatially-evolving range of amplified frequencies along the domain, from higher frequencies upstream to lower ones downstream.

2.3 Description of linear time-invariant systems

To act on a system, it is necessary to know its behaviour, which is described by the link between the different inputs and outputs of the system. In the case of linear time-invariant (LTI) systems, the mathematical input/output model is:

$$\mathbf{y}(t) = G(t) * \mathbf{u}(t) = \int_{-\infty}^{+\infty} G(t - \tau) \mathbf{u}(\tau) d\tau, \quad (2.1)$$

with $\mathbf{y} \in \mathbb{R}^{n_y}$ and $\mathbf{u} \in \mathbb{R}^{n_u}$ representing arbitrary input and output signals, respectively. The matrix $G(t) \in \mathbb{R}^{n_y \times n_u}$ contains the impulse responses of the system (so the output signals for each of the inputs $u_i(t) = \delta(t)$ with δ the dirac delta function). An LTI system implies that relation between inputs and outputs are linear (*linearity*) and outputs do not depend on the particular time when inputs are applied (*time invariance*); outputs are not explicitly time-dependent but are input-dependent.

The Laplace transform of arbitrary causal signals (such as $\forall t < 0 \mathbf{u}(t) = 0$) is defined by:

$$\mathbf{u}(s) = \int_0^{+\infty} \mathbf{u}(t) e^{-st} dt, \quad (2.2)$$

with $s \in \mathbb{C}$. By taking the Laplace transform of (2.1), the mathematical relationship becomes:

$$\mathbf{y}(s) = G(s) \mathbf{u}(s), \quad (2.3)$$

where $G(s)$ is called the transfer function of the system. A transfer function is called *SISO* (Single Input Single Output) if the input/output are scalars and *MIMO* (Multiple Input Multiple Output) if the input/output are vectors. The numerator (respectively denominator) polynomial roots of the rational functions composing G are called *zeros* (respectively *poles*). The H_2

and H_∞ norms associated to stable, causal and strictly-proper (proper is enough for H_∞ norm) transfer functions are defined as:

$$\|G(s)\|_2 = \left(\frac{1}{2\pi} \int_{-\infty}^{+\infty} \text{Tr}(G^*(i\omega)G(i\omega)) d\omega \right)^{1/2} \stackrel{SISO}{=} \left(\frac{1}{2\pi} \int_{-\infty}^{+\infty} |G(i\omega)|^2 d\omega \right)^{1/2}, \quad (2.4a)$$

$$\|G(s)\|_\infty = \sup_{\omega \in \mathbb{R}} \sigma_{\max}(G(i\omega)) \stackrel{SISO}{=} \sup_{\omega \in \mathbb{R}} |G(i\omega)|. \quad (2.4b)$$

For a stable system, the square of the H_2 norm represents the sum of the variance output responses when excited by uncorrelated zero mean value unitary white noise inputs. For a SISO system, the H_2 norm is an integrated gain over all frequencies and the square of this norm directly corresponds to the signal energy of the impulse response of the system. The H_∞ norm is the maximum singular value over all frequencies (the maximum gain over all frequencies for a SISO system). This norm has also several time domain performance interpretations; one of them is that it represents the worst case steady state gain to sinusoids at any frequency [180]. The mathematical model describing the dynamics of the system can be written in a state-space representation where the inputs, outputs and state variables are related by first-order differential equations:

$$\dot{\mathbf{x}}(t) = \mathbf{A}\mathbf{x}(t) + \mathbf{B}\mathbf{u}(t), \quad (2.5a)$$

$$\mathbf{y}(t) = \mathbf{C}\mathbf{x}(t) + \mathbf{D}\mathbf{u}(t), \quad (2.5b)$$

where $\mathbf{x} \in \mathbb{R}^{n_x}$ is the *state vector*, $\mathbf{y} \in \mathbb{R}^{n_y}$ is the *output vector*, $\mathbf{u} \in \mathbb{R}^{n_u}$ is the *input vector*, $\mathbf{A} \in \mathbb{R}^{n_x \times n_x}$ is the *state matrix*, $\mathbf{B} \in \mathbb{R}^{n_x \times n_u}$ is the *input matrix*, $\mathbf{C} \in \mathbb{R}^{n_y \times n_x}$ is the *output matrix* and $\mathbf{D} \in \mathbb{R}^{n_y \times n_u}$ is the *feedthrough matrix*. The link between a transfer function $G(s)$ and a state-space representation is given by the relation:

$$G(s) = \mathbf{C}(s\mathcal{I} - \mathbf{A})^{-1}\mathbf{B} + \mathbf{D}. \quad (2.6)$$

2.4 Control formalism

The formalism of reactive control as well as the main distinctions between *feedforward* and *feedback* are introduced in this section, based mainly on results from noise-amplifier flow control.

As the boundary layer flow is convectively unstable, disturbances generated by exogenous noise will be amplified along the domain. The aim of control is to generate small-amplitude perturbations with the actuators that take advantage of the instability mechanisms to grow and eventually cancel the noise-induced perturbations to keep the flow as close as possible to its equilibrium position. This technique, where additional waves (from the actuators) of appropriate amplitude and phase oppose the waves generated by the noise, has been studied for decades [121].

The previous forcing field \mathbf{f} used in (1.14) is now decomposed into a volume forcing $\mathbf{B}_w(x, y, z)\mathbf{w}(t)$ modelling the impact of external noise sources (acoustic noises, roughness, free-stream turbulence, etc.) naturally present in realistic configurations and a volume forcing $\mathbf{B}_u(x, y, z)\mathbf{u}(t)$ modelling the actuators. Real-time measurements $\mathbf{y}(t)$ are necessary to estimate the phase and amplitude of the incoming disturbances. Performance measurements $\mathbf{z}(t)$ are also introduced to evaluate the control performance. To model these estimation and performance measurements, the fields $\mathbf{C}_y(x, y, z)$ and $\mathbf{C}_z(x, y, z)$ are introduced to extract from the state vector \mathbf{q}' the desired physical measurements. The semi-discretized state-space representation of the boundary

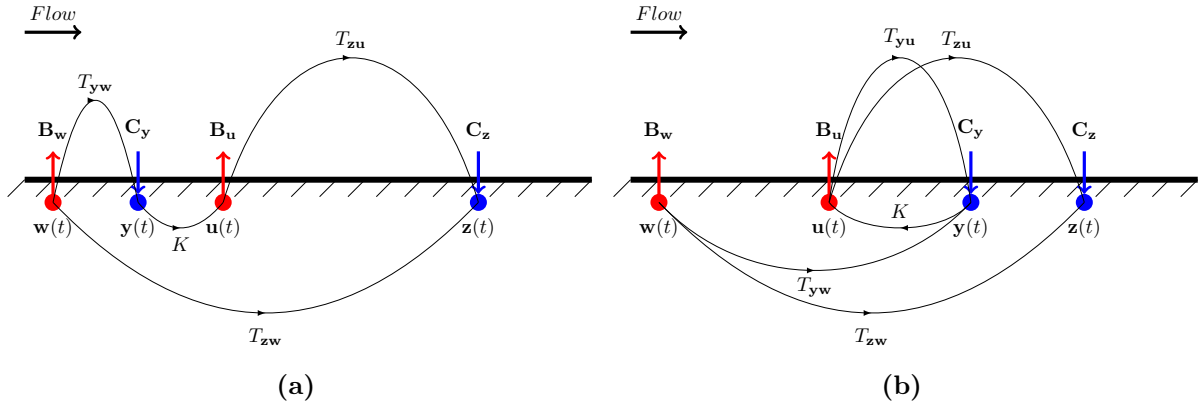


Figure 2.5: Schematic 2D views of the (a) feedforward and (b) feedback configurations.

layer system is thus written as follows:

$$\frac{d\mathbf{q}'}{dt} = \mathcal{A}\mathbf{q}' + \mathcal{P}(\mathbf{B}_w\mathbf{w}(t) + \mathbf{B}_u\mathbf{u}(t)), \quad (2.7a)$$

$$\mathbf{y}(t) = \mathbf{C}_y\mathbf{q}', \quad (2.7b)$$

$$\mathbf{z}(t) = \mathbf{C}_z\mathbf{q}'. \quad (2.7c)$$

Although we use a discretized formalism in space in this equation, we keep the same notations as for the continuous formalism for simplicity. By using the Laplace transform and the relation $s = i\omega$, we obtain:

$$\mathbf{q}'(s) = \mathcal{R}(\mathbf{B}_u\mathbf{u}(s) + \mathbf{B}_w\mathbf{w}(s)), \quad (2.8a)$$

$$\mathbf{y}(s) = \mathbf{C}_y\mathcal{R}(\mathbf{B}_u\mathbf{u}(s) + \mathbf{B}_w\mathbf{w}(s)), \quad (2.8b)$$

$$\mathbf{z}(s) = \mathbf{C}_z\mathcal{R}(\mathbf{B}_u\mathbf{u}(s) + \mathbf{B}_w\mathbf{w}(s)). \quad (2.8c)$$

The quantity \mathcal{R} is still the resolvent operator (see equation 1.15). Thus, $T_{yw} = \mathbf{C}_y\mathcal{R}\mathbf{B}_w$ and $T_{zw} = \mathbf{C}_z\mathcal{R}\mathbf{B}_w$ are the transfer function matrices from the set of inputs \mathbf{w} to the set of estimation outputs \mathbf{y} and performance outputs \mathbf{z} , respectively. These MIMO transfer functions represent, in the absence of control, the impact of the exogenous disturbances \mathbf{w} on the sensors \mathbf{y} and \mathbf{z} , respectively. The impact of the actuators on the sensors, in the absence of disturbances, is represented by the MIMO transfers $T_{yu} = \mathbf{C}_y\mathcal{R}\mathbf{B}_u$ and $T_{zu} = \mathbf{C}_z\mathcal{R}\mathbf{B}_u$. The last transfer function of the system is the one which transforms the estimation measurements \mathbf{y} into the actuation signals \mathbf{u} , denoted $K = T_{uy}$, and which represents the controller.

In noise-amplifier flows, there is no synchronization of the dynamics at the global scale, perturbations from actuators \mathbf{u} are rapidly damped in the upstream direction, hence the control setup changes fundamentally depending on the position of the estimation sensors \mathbf{y} relative to \mathbf{u} . When \mathbf{y} are placed upstream, actuator-induced perturbations are not observable and the configuration is termed *feedforward* (see figure 2.5a) [10, 73, 81, 126, 168]. On the other hand, when \mathbf{y} are placed downstream, the sensors measure the superposition of noise-induced and actuator-induced perturbations, hence the term *feedback* (see figure 2.5b) [13, 14, 170, 188, 195]. In this case though, there may be a significant time-delay before the effect of actuation may be seen by the sensors, because perturbations travel at the speed of the underlying base flow (plus or minus the speed of sound if the perturbation is acoustic): the farther downstream \mathbf{y} are, the longer the delay. In the context of fluidic control, the term *feedback* sometimes refers directly to reactive control, regardless of the relative position of estimation sensors/actuators [168]. To avoid this confusion, the notion feedforward/feedback will be used in the rest of this

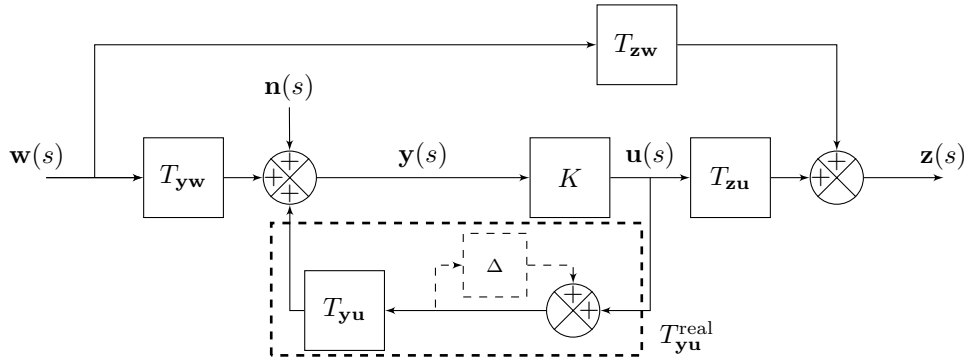


Figure 2.6: Block diagram of noise-amplifier flows for feedforward and feedback configurations with an inverse multiplicative input uncertainty Δ . In a feedforward setup, $T_{yu} = \Delta = 0$. The quantity \mathbf{n} represents an additional noise source.

thesis according to the relative position of \mathbf{y}/\mathbf{u} in accordance with the terminology defined by Gad-el Hak [62].

The fluidic specifications for noise-amplifier flow control can be described as follows: determine the control law K that reduces as much as possible the root-mean-square (r.m.s.) value of the disturbances propagating along the domain, while keeping the control law efficient and stable despite modelling errors, new noise sources or inflow condition variations. The closed-loop transfer functions that are usually tuned to meet these specifications are briefly detailed below.

2.4.1 Nominal performance

It is straightforward to show from the block diagram in figure 2.6 that the controlled transfer function from the set of exogenous inputs \mathbf{w} to the set of performance outputs \mathbf{z} is:

$$T_{\mathbf{z}\mathbf{w}}^c = T_{\mathbf{z}\mathbf{w}} + T_{\mathbf{z}\mathbf{u}}K(\mathcal{I} - T_{\mathbf{y}\mathbf{u}}K)^{-1}T_{\mathbf{y}\mathbf{w}}. \quad (2.9)$$

In a feedforward setup, $T_{\mathbf{y}\mathbf{u}} \approx 0$. From a control point of view, the reduction of the r.m.s. output responses following their excitations by white noise inputs translates into the minimization of the H_2 norm $\|T_{\mathbf{z}\mathbf{w}}^c\|_2$. The lower the ratio $\|T_{\mathbf{z}\mathbf{w}}^c\|_2/\|T_{\mathbf{z}\mathbf{w}}\|_2$, the better the nominal performance.

2.4.2 Stability robustness

Maintaining closed-loop performance in spite of modelling errors or inflow condition variations around the nominal case requires first and foremost stability robustness of the control law.

In order to ease the understanding of the stability robustness problem, this concept is introduced from the classical stability margins, which are defined for the SISO systems [167]. Therefore, the vectors \mathbf{u}/\mathbf{y} are now scalars u/y . For noise-amplifier flows, the transfer $-T_{\mathbf{y}\mathbf{u}}^{\text{real}}$, which represents the true/real transfer function and not the modelled one ($T_{\mathbf{y}\mathbf{u}}$ may not correspond to reality because of inflow condition variations or uncertainties and modelling errors), is stable as noise-amplifier flows are globally stable by nature. By considering a stable controller K , the quantity $-T_{\mathbf{y}\mathbf{u}}^{\text{real}}K$ has therefore no unstable pole for noise-amplifier flows. For this kind of configuration, the closed-loop system is stable if and only if the Nyquist plot of $-T_{\mathbf{y}\mathbf{u}}^{\text{real}}K$ does not encircle the critical point $(-1, 0)$ (see figure 2.7). The *gain* and *phase* margins respectively represent the minimum amount of gain and phase variations required on $T_{\mathbf{y}\mathbf{u}}$ to lose stability. For noise-amplifier flows, the gain and phase margins respectively allow for an estimation error

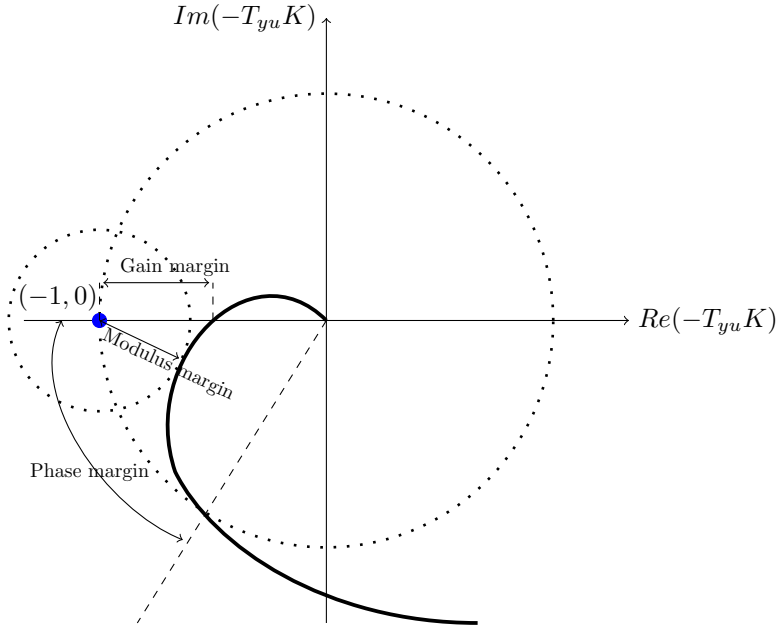


Figure 2.7: Classical stability margins for SISO closed-loop system.

in the instability's growth rate and convection speed which can lead to an instability of the feedback loop [176]. By directly measuring the minimal distance between the Nyquist plot and the critical point $(-1, 0)$ after which the closed-loop becomes unstable for a negative feedback loop, the *modulus* margin appears to be the most generic measure for quantifying the available stability margin [180]. This modulus margin is linked to the SISO sensitivity function:

$$S = (1 - T_{yu}K)^{-1}. \quad (2.10)$$

It is straightforward to show that the quantity $\|S\|_{\infty}^{-1}$ corresponds to the modulus margin. Unlike the gain and phase margins, which are easily interpreted for noise-amplifier flows in terms of errors in disturbance amplitude or phase velocity, the interpretation of the modulus margin requires the use of inverse multiplicative uncertainty Δ on T_{yu} . Indeed, for the block Δ represented in figure 2.6, if no upstream noise (n or w) is considered, we have for a SISO configuration $y = \frac{T_{yu}}{1-\Delta}u$, with $\Delta = \frac{T_{yu}^{\text{real}} - T_{yu}}{T_{yu}^{\text{real}}}$. Requiring that the Nyquist plot $-T_{yu}^{\text{real}}K$ does not encircle the critical point $(-1, 0)$ is equivalent [180] to:

$$\begin{aligned} |1 - T_{yu}K| &> |\Delta| \\ &\Leftrightarrow \\ |S| &< |\Delta|^{-1}. \end{aligned} \quad (2.11)$$

Therefore, from a control point of view, imposing the constraint $\|S\|_{\infty} < |\Delta|^{-1}$ guarantees the internal stability of the closed-loop up to a value $|\Delta|$ of relative model error on T_{yu} . Hence, the lower $\|S\|_{\infty}$, the better the stability robustness.

Contrary to the SISO case where stability robustness can be assessed graphically from the Nyquist diagram, it is not possible to do so directly in the MIMO case. For MIMO systems, the stability robustness is studied via the small-gain theorem [167, 180]:

Theorem. *Given two stable and invertible frequency weighting matrices W_i and W_o and a stable system M , the inter-connected system (M, Δ) (see figure 2.8) is stable for all stable transfer functions $\Delta(s)$ as $\Delta = W_i \tilde{\Delta} W_o$ with $\|\tilde{\Delta}\|_{\infty} < 1$ if and only if $\|W_o M W_i\|_{\infty} < 1$.*

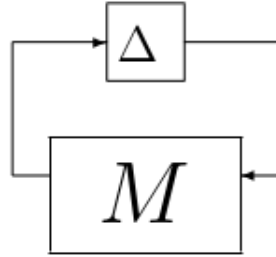


Figure 2.8: Inter-connected M and Δ systems from [167].

For an inverse multiplicative output (respectively input) uncertainty which can represent uncertainties on sensors (respectively actuators), $M = S = (\mathcal{I} - T_{\mathbf{y}\mathbf{u}}K)^{-1}$ (respectively $M = (\mathcal{I} - KT_{\mathbf{y}\mathbf{u}})^{-1}$). In the SISO case, both these inverse multiplicative uncertainties are equal as it is possible to swap the product of two transfer functions without changing the final result; applying this theorem to SISO systems is equivalent to the Nyquist graphical criterion. As it is no longer the case for MIMO systems, the impact of uncertainties at the input or output of the system may have a different impact on the stability of the system. Other types of uncertainty may be considered depending on the flow configuration. For example, when additive uncertainties $\Delta = T_{\mathbf{y}\mathbf{u}}^{\text{real}} - T_{\mathbf{y}\mathbf{u}}$ are considered, the small-gain theorem is applied on $M = KS$; when direct multiplicative input uncertainties $\Delta = T_{\mathbf{y}\mathbf{u}}^{-1}(T_{\mathbf{y}\mathbf{u}}^{\text{real}} - T_{\mathbf{y}\mathbf{u}})$ are considered, the small-gain theorem is applied on $M = (\mathcal{I} - KT_{\mathbf{y}\mathbf{u}})^{-1}KT_{\mathbf{y}\mathbf{u}}$; when direct multiplicative output uncertainties $\Delta = (T_{\mathbf{y}\mathbf{u}}^{\text{real}} - T_{\mathbf{y}\mathbf{u}})T_{\mathbf{y}\mathbf{u}}^{-1}$ are considered, the small-gain theorem is applied on $M = (\mathcal{I} - T_{\mathbf{y}\mathbf{u}}K)^{-1}T_{\mathbf{y}\mathbf{u}}K$. The small-gain theorem guarantees stability only when one form of uncertainty is considered at a time. To study the stability robustness in the case of different types of uncertainties occurring simultaneously, the uncertainties can be grouped into a single uncertainty matrix with an imposed form, called *structured uncertainty*; this generalization of the small-gain theorem is called the μ -analysis [6, 167, 180] but this tool is outside the scope of this thesis.

2.4.3 Performance robustness

In contrast to $T_{\mathbf{y}\mathbf{u}}$, model flaws and variations of the other transfer functions of noise-amplifier flows cannot destabilize the system and these modelling errors/uncertainties are only related to the concept of performance robustness. The concept of performance robustness consists in maintaining performance in terms of amplitude reduction despite differences between on-design and off-design operating conditions. For noise-amplifier flows, the lower the ratio $\|T_{\mathbf{z}\mathbf{w}}^c\|_2/\|T_{\mathbf{z}\mathbf{w}}\|_2$ despite for example free-stream variations or new noise sources, the better the performance robustness.

For the new noise source \mathbf{n} displayed in figure 2.6, the matrix transfer function from \mathbf{n} to \mathbf{y} corresponds to the sensitivity function $S = (\mathcal{I} - T_{\mathbf{y}\mathbf{u}}K)^{-1}$ which may desensitize or amplify the looped system to new external disturbances over a certain bandwidth. It is straightforward to see that for a SISO system, if $|S(s)| > 1$ (respectively $|S(s)| < 1$), the new disturbance will be amplified (respectively damped) by the closed-loop system.

To limit the actuator activity on certain bandwidth, a common practice is to constrain KS . This quantity represents the transfer function from \mathbf{n} to \mathbf{u} . Desensitizing the control outputs \mathbf{u} on certain frequency ranges allows for example to be robust to new noise sources such as noisy estimation sensors \mathbf{y} . As a matter of fact, measurement noise \mathbf{n} is strongly amplified in the case of high gain KS on their bandwidths, resulting in control signals \mathbf{u} of high amplitudes on these bandwidths. Even if these frequencies may be attenuated far downstream of actuators

(if they are convectively stable), strong injection of energy may occur in the direct vicinity of actuators, which may in turn provoke transition to turbulence.

2.4.4 Feedforward vs Feedback

The control of noise-amplifier flows has been fairly widely studied, either in feedforward [10, 73, 81, 126, 168] or in feedback [13, 14, 170, 188, 195].

The feedforward configuration has the advantage of being unconditionally stable. Indeed, a system composed of stable transfers (which is the case in noise-amplifier flows) with series topology (as in a feedforward setup) is stable; with a SISO point of view, it is straightforward to see that the critical point $(-1,0)$ is never encircled as $T_{yu} = 0$. Moreover, the feedforward design possesses excellent nominal performance in terms of disturbance rejection when the impact of disturbances on the system is perfectly modelled [10, 73, 153, 168]. For boundary-layer flows, although the control strategies were based on a linear approach, it has been possible to delay transition to turbulence in fully non-linear 3D incompressible boundary layer configurations [126, 156, 169] as small amplitude perturbations are at the origin of some paths from receptivity to transition. In addition to being robust to non-linearities not accounted for in the models, Sasaki et al. [153] have shown that a feedforward configuration could be robust to noisy estimation sensors. Nevertheless, Fabbiane [53] demonstrated that a feedforward controller may lose all its performance due to free-stream velocity variations.

In order to have equivalent nominal performance in terms of amplitude reduction as a feedforward configuration, a feedback setup needs the estimation sensors \mathbf{y} to be close enough to the actuators to avoid sending outdated information. The delay impacts the maximum achievable performance indeed [13, 14, 81]. For a transfer function $T_{\mathbf{y}\mathbf{u}}$ with a time delay $\tau_{\mathbf{y}\mathbf{u}}$, it is not possible to cancel out disturbances in a time scale shorter than $\tau_{\mathbf{y}\mathbf{u}}$ as a control at a time t has no effect until $t + \tau_{\mathbf{y}\mathbf{u}}$ [66]. Therefore, for non-minimum phase systems, characterized by zeros in the right half-plane (which necessarily appear with dead times such as convective-delays), the controllable bandwidth f_c is limited by $f_c \lesssim 1/\tau_{\mathbf{y}\mathbf{u}}$ [66, 180]. The feedback loop has the advantage to be inherently more robust in performance than a feedforward configuration thanks to the sensitivity function S [14, 180]. Indeed, for a feedforward setup, $T_{yu} = 0$ so for a SISO system $\forall s |S(s)| = 1$ and additional noise sources or free-stream condition variations not taken into account by the initial models will thus never be amplified (which explains the unconditional stability of the feedforward configuration contrary to a feedback design) nor damped (which explains its lower performance robustness compared to a feedback design). Hence, the sensitivity function S may limit the achievable nominal performance for noise-amplifier flows due to $\tau_{\mathbf{y}\mathbf{u}}$ and may destabilise the system but it also ensures a natural ability to be robust to unknown disturbances or uncertainties of the model. Note that for an oscillator flow, a feedback setup is automatically mandatory to cancel the unstable pole as $T_{\mathbf{y}\mathbf{u}} \neq 0$ regardless of the relative position of the actuators/estimation sensors due to the synchronisation of the dynamics at a global scale.

2.5 Reduced-order models

The synthesis step, which consists in designing the control law K , is only feasible for models of small dimensions (a few hundred state variables) due to the computational complexities and storage requirement of synthesis methods [144]. Fluidic problems have a typical range of 10^5 to 10^8 degrees of freedom (each conservative variable on a node of the mesh represents a degree of freedom); thus, most fluidic control problems go through the use of reduced-order models (ROMs) before the synthesis step. The control law is designed off-line on the ROMs and tested

a posteriori on the complete system. The main requirement in this *reduce-then-design* strategy is that the ROMs correctly capture the input/output dynamics; the entire state does not need to be approximated and only a fraction of the dynamics is needed, the one to establish the relationships between the input and output signals [5, 86].

The primordial states for the synthesis are the controllable and observable states. A dynamical system (see equation 2.5) is said to be state controllable if, for any initial state $\mathbf{x}(t=0) = \mathbf{x}_0$, any time $t_1 > 0$ and any final state \mathbf{x}_1 , there exists an input $\mathbf{u}(t)$ such that $\mathbf{x}(t_1) = \mathbf{x}_1$ [180]. A system is state controllable if and only if the controllability matrix

$$\begin{pmatrix} \mathbf{B} & \mathbf{AB} & \mathbf{A}^2\mathbf{B} & \dots & \mathbf{A}^{n_x-1}\mathbf{B} \end{pmatrix} \quad (2.12)$$

has rank n_x (with n_x the number of states). Roughly summarized, the controllable modes in noise-amplifier flows are those the most excited by the input parameters (\mathbf{w}, \mathbf{u}) [10, 14, 19]. In the same way, a dynamical system (see equation 2.5) is said to be state observable if, for any time $t_1 > 0$, the initial state $\mathbf{x}(t=0) = \mathbf{x}_0$ can be determined from the time history of the input $\mathbf{u}(t)$ and the output $\mathbf{y}(t)$ in the interval $[0, t_1]$ [180]. A system is state observable if and only if the observability matrix

$$\begin{pmatrix} \mathbf{C} \\ \mathbf{CA} \\ \mathbf{CA}^2 \\ \vdots \\ \mathbf{CA}^{n_x-1} \end{pmatrix} \quad (2.13)$$

has rank n_x . Roughly summarized, the observable modes in noise-amplifier flows are those which, taken as input conditions, will lead to the largest responses on the output parameters (\mathbf{y}, \mathbf{z}) [10, 14, 19].

In the case of oscillator flows, a small number of modes is required to reconstruct the whole dynamics of the system, unlike noise-amplifier flows where a larger number of modes is required due to the strongly convective nature of the system [54]. Indeed, the strong temporal delay in the detection of input-induced perturbations by the outputs results in the observable and controllable modes having quite distinct spatial supports: the observable modes are located upstream of the domain whereas the controllable modes are located further downstream, due to the convective-type non-normality effect (see section 1.4.3). As a result, oscillator flows can be described by models of order $O(10)$ [12, 175, 177] whereas noise-amplifier flows need up to a hundred degrees of freedom to be correctly approximated [13, 126, 168]. To obtain the ROMs, two main techniques stand out: model-based approaches via Galerkin projections and data-based approaches.

2.5.1 Galerkin projections

The Galerkin projection of the Navier–Stokes equations on a set of modes which correctly represents the input/output behaviour of the system is a possibility to obtain the ROMs. The ROMs are thus derived from physical principles and the choice of the projection basis is crucial.

One basis can be the set of global modes and consists in projecting the equations onto the least stable eigenvectors of equation 1.12. This method is frequently used in the case of globally unstable flows, whether for flow above a cavity [3, 12, 177] or for globally unstable separation bubble induced by a bump geometry [50]. Yet, Barbagallo et al. [12] have shown that the use of ROMs based on global modes only cannot be generalized to every oscillator flows as the global modes are inadequate to represent the input/output behaviour.

The POD (Proper Orthogonal Decomposition) basis, first introduced by Lumley [107], consists in projecting the equations onto a basis which is optimal with respect to an energy norm.

Indeed, the POD modes represent the most controllable structures of the system and allow to approximate with the least number of modes the energetic response of the system to the inputs. However, by taking into account only the most controllable modes and setting aside the observable modes, the POD basis may not correctly represent the input/output behaviour [73]. Most of the successful applications of ROMs based on the POD basis are thus found in the case of globally unstable flows, such as the flow around a cylinder [65, 174], where the exogenous inputs have little influence on the system, making the observable modes of little impact in a control perspective. Nevertheless, approaches for noise-amplifier flows such as the flow over a rounded backward-facing step have also been successfully implemented [13]. In addition to being taken as a basis of projection for the construction of the ROMs, the coefficients of the POD modes are sometimes used as performance sensors \mathbf{z} , which provides a global energy metric for the whole domain (output projection [10, 14, 168]).

One of the last and most commonly used basis is the BPOD (Balanced Proper Orthogonal Decomposition) basis. This basis, introduced by Moore [123], has the advantage of perfectly representing the input/output dynamics because its modes are equally controllable and observable, and it is therefore perfectly suited to a control perspective. It thus fills in one of the gaps of the POD basis which is only concerned with the most energetic structures without taking into account the inputs which led to these flow responses. To deal with large-dimensional fluidic systems, the method of snapshots, introduced by Sirovich [178], is required to obtain the BPOD basis and allows to considerably reduce the size of the eigenvalue problem. The BPOD modes as projection basis were used in some incompressible boundary-layer flow control problems [10, 168].

The advantage of these different projection bases lies in the fact that they are linked to the relevant structures of the flow and are based on physical considerations. However, these projections require the knowledge of the governing equations (forcing field of the exogenous inputs and actuators, adjoint simulations, Jacobian matrix, etc.) to construct the basis which makes them difficult to use in a realistic setup.

2.5.2 Data-based approaches

Data-based identification techniques solve this problem by building the ROMs only from input-output time/frequency data sets coming from simulations/experiments. The transfer functions of the system are identified purely from input-output data and these data-based approaches are sometimes called *black-box*, in contrast to the methods based on Galerkin projections and governing equations which derive from the interpretation of the structures of the system and which are said to be *grey-box* [22].

The vector-fitting method is one of these data-based techniques. Vector-fitting is based on a least-square fit to the response measurements by rational functions using an iterative reallocation of the poles of the approximant [68]. The model obtained appears in a transfer function form (not a state-space representation). Most of the vector-fitting algorithms use frequency data (the frequency response at each input frequency) instead of temporal one and some algorithms connect the least-square objective with a H_2 error measure to increase fidelity according to this norm [46].

The ARMAX (Auto-Regressive Moving-Average eXogenous) identification method is based only on temporal data. The output at a given time is given as a function of: its own previous values (Auto-Regressive part), a moving average term modelling the impact of a stochastic (imperfectly predictable) term (Moving-Average part) and a term representing the impact of the exogenous inputs of the system (eXogenous part). Both Hervé et al. [73] and Schmid and Sipp [164] have successfully used this identification technique for a flow over a backward facing

step by using only the temporal data of $\mathbf{z}/\mathbf{y}/\mathbf{u}$ that could all be obtained in an experimental configuration. Methods which do not take into account the moving average term can also be employed, either in a linear framework (called ARX) [74] or in a non-linear framework (NARX) to model non-linear dynamics [40].

Subspace identification techniques are another wide-spread data-based method for identification [81]. With a subspace identification method, the ROMs are searched in a state-space representation form (see equations 2.5) and the unknown coefficients of the matrices $\mathbf{A}/\mathbf{B}/\mathbf{C}/\mathbf{D}$ are identified from the sets of frequency or temporal data (depending on the subspace algorithm chosen). Subspace identification techniques are particularly well-suited for MIMO systems due to their state-space representation [69]. Indeed, in this framework, it is only necessary to add rows and columns to the matrices according to the number of inputs/outputs. The subspace algorithms are based on the use of Hankel matrices [69] and the main difference is the type of projection used on these matrices. The most commonly used algorithms for the subspace method are CVA [95], MOESP [196], N4SID [135] and ERA [80]. As regards the CVA, MOESP and N4SID algorithms in the context of noise-amplifier flows, Juillet et al. [81] verified that these three algorithms gave comparable ROMs during their study of flow over a backward facing step. The ERA (eigensystem realization algorithm), based on impulse response data, has also been used in many control studies for noise-amplifier flows [14, 37, 156, and many others]. One of the advantages of the ERA lies in the fact that the ROMs obtained are theoretically equivalent to those obtained using Galerkin projection on a reduced set of BPOD modes, which makes the ERA optimal to capture the input/output dynamics without the knowledge of the governing equations. One of the drawbacks of the ERA lies in the fact that the state variables of the ROMs represent fictitious variables which implies that one can no longer evaluate the physical state of the flow once the ROMs are obtained [154].

2.6 Synthesis methods

The synthesis step consists in designing a control law K which gives to the controlled system the specified performance. Several synthesis methods exist and their main principles will be briefly summarised in this section.

2.6.1 LQR

The linear-quadratic regulator (LQR) synthesis minimizes the quadratic cost function:

$$\mathcal{J} = \int_0^{\infty} (\mathbf{z}^*(t)\mathbf{Q}_{\text{LQR}}\mathbf{z}(t) + \mathbf{u}^*(t)\mathbf{R}_{\text{LQR}}\mathbf{u}(t)) dt, \quad (2.14)$$

with \mathbf{Q}_{LQR} and \mathbf{R}_{LQR} respectively semi-definite-positive and positive-definite penalizing matrices for the state and actuation. This synthesis method presents many advantages: this method has a cheap cost as only one Riccati equation is solved resulting in an optimal LQR gain matrix K ; there is no need for estimation sensors \mathbf{y} as the control signals $\mathbf{u}(t)$ are computed from the full-state, *i.e.* $\mathbf{u}(t) = K\mathbf{q}'(t)$ because $\mathbf{C}_{\mathbf{y}} = \mathcal{I}$ (hence, the name *full-state controller* commonly used in the literature [2, 203]) which avoids potential stability problems for feedback designs [61, 170]. Therefore, this synthesis method has been used in many fluid control problems [2, 61, 170, 176, 203] and gives an indication of the optimal performance that could be achieved in an ideal case where the full information is available.

2.6.2 LQG/LTR

As measuring the entire flow field (*i.e.* the full-state $\mathbf{q}'(t)$) to determine the actuator signals $\mathbf{u}(t)$ is impossible in realistic configurations, the LQR gain is associated with a Kalman filter which contains the dynamic part. This method dates from back to the 1960s [83] and is called LQG (linear-quadratic-Gaussian) synthesis. The Kalman filter is also obtained from the solution of a Riccati equation and estimates the state $\mathbf{q}'(t)$ from the measurements \mathbf{y} , so this LQG controller can be used in practice. Both LQR controller and Kalman filter are built independently thanks to the separation theorem which makes it a very simple to implement and inexpensive method of resolution. Despite being theoretically optimal with respect to the quadratic criterion based on performance and control cost (see equation 2.14), this method comes with no guarantees on stability margins [43]. In other words, tiny errors in the state estimation may end up with an unstable feedback loop when \mathbf{y} are placed downstream of \mathbf{u} (feedback setup), which represents a major drawback for practical applications.

Using the loop-transfer-recovery (LTR) method, it is in some cases possible to overcome this lack of stability robustness by overwhelming the control signal entering the estimator [44, 92]. This procedure has for example been successfully used by Sipp and Schmid [176] to improve the stability robustness of their controller in the case of a flow over an open square cavity (oscillator flow). The recovery procedure works by inverting the plant dynamics in order to obtain ultra-fast estimators: the Kalman filter dynamics becomes less prominent and the estimated state is closer to the real actual state. This procedure leads to an unstable closed-loop in the case of systems with time-delays, because they possess right half-plane zeros in the bandwidth to be controlled which are converted into right half-plane poles [176, 180, 205]. As a result, this method is not suitable for noise-amplifier flows in general, and in particular, the supersonic boundary layer flow.

Contrary to the feedback structure, the feedforward design is unconditionally stable and its implementation via LQG is not a problem. Therefore, feedforward configurations combined with LQG syntheses dominate the noise-amplifier flow control literature, particularly in the incompressible boundary layer control studies [10, 37, 38, 61, 126, 153, 156, 168–170]. As the feedback configuration is naturally more robust in performance than the feedforward design (see section 2.4.4), feedback configurations associated with LQG synthesis can be found in the literature. Barbagallo et al. [13] employed this combination to control instabilities over a backward-facing step. However, some of their feedback controllers turned out to be unstable on the real plant (the full linearized Navier–Stokes equations), because of the poor stability robustness of LQG to tiny errors in the ROM of T_{yu} . Tol et al. [188] also obtained some unstable controllers when trying to control TS waves in an incompressible two-dimensional boundary layer using LQG on a feedback setup.

2.6.3 Inverse feedforward/Wiener–Hopf framework

A very direct and simple way to obtain a controller K to reduce perturbation amplitude and to create perfect destructive interferences on the whole frequency spectrum is to use an inverse method. Indeed, with a SISO view, the ideal case would be to have for the controlled system $z(s) = 0$. From equation 2.9, a perfect wave cancellation for each frequency is obtained for:

$$\begin{aligned}
 0 &= (T_{zw} + T_{zu}K(1 - T_{yu}K)^{-1}T_{yw})w \\
 &\Leftrightarrow \\
 K &= -\frac{T_{zw}}{T_{yw}T_{zu} - T_{yu}T_{zw}}.
 \end{aligned} \tag{2.15}$$

This inverse method can also be employed in 3D configurations for periodic/homogeneous flows in the spanwise direction (as boundary-layer flows) by realizing a second Fourier transform in the spanwise direction [153, 156]; thus a multitude of controllers $K(s, \beta)$ are obtained (instead of one controller $K(s)$ in 2D configurations corresponding to the particular case $\beta = 0$). As no Riccati equations are solved, this method has the advantage of not requiring the identification of the transfer functions; the raw frequency data are directly exploited and the controller $K(i\omega)$ is constructed "frequency-by-frequency". This inversion may fail or lead to undesirable large control gain for small values of the denominator part for certain frequencies. Moreover, the inverses are generally non-causal for noise-amplifier flows and unstable due to the right half-plane zeros transforming in right half-plane poles [154] leading to controllers that are potentially unstable and unusable/infeasible in practice. Hence, penalizing weighting functions must be used to limit the controller activity, as in the LQR/LQG procedure [42]. Sasaki et al. [153, 154] employed this inverse method with a feedforward design to control Kelvin–Helmholtz and TS waves and have obtained equivalent results in terms of disturbance amplitude reduction to those obtained by a LQG feedforward controller. This inverse feedforward technique has also enabled to delay transition to turbulence in the case of a 3D incompressible boundary layer [126]. Nevertheless, this synthesis method is only employed in feedforward designs because feedback setups may be unstable as no consideration is given to stability robustness (the controller synthesis is just based on the objective $z = 0$) and performance robustness of these inverse feedforward controllers is therefore unclear.

It is also worth mentioning that strategies based on the Wiener–Hopf framework exist [114, 115] where both the flow state (possibly estimated from limited and noisy sensors) and control method are obtained on the full-rank system. As for the inverse feedforward, these methods do not require the use of ROMs and they permit an extension of LQG-like control strategies to systems of large dimension. The strategies based on the Wiener–Hopf framework can be used for example to avoid potential performance losses of ROM-derived controllers when applied to the full system or to improve the inverse feedforward strategy by minimizing the effect of kernel truncation when searching to obtain a causal controller. However, once again, the issue of robustness in terms of stability/performance with the Wiener–Hopf framework is not addressed.

2.6.4 Classical loop-shaping

Loop-shaping takes into account stability margins necessary for the construction of a robust feedback design contrary to the previous inverse/LQG procedures. The classical loop-shaping approach refers to a design procedure for SISO systems that shapes the magnitude of the open-loop transfer $T_{yu}K$ to achieve closed-loop specifications from frequency considerations [66, 180] (large loop gain in the frequency range to be controlled, small loop gain on certain bandwidths to ensure stability and robustness to unmodelled dynamics, etc.). Belson et al. [14] are among the first to demonstrate the feasibility of a feedback setup with stability and performance robustness for the incompressible boundary layer flow, using the loop-shaping method to manually tune the parameters of a simple proportional-integral (PI) controller: they chose parameters providing large phase margin and large loop gain at the low-frequencies of the TS waves. However, this tuning by hand did not allow to obtain a satisfactory performance for the chosen actuator/sensor pair, forcing the authors to change it to obtain large disturbance amplitude reduction with the loop-shaping approach, despite the good performance obtained with LQG on the ROMs with the same actuator/sensor pair. This phenomenon may have occurred because in their loop-shaping approach, there is no explicit H_2 norm minimization objective of the transfer T_{zw}^c in order to reduce the amplitude of the perturbations. A similar hand-tuning approach was used

by Vemuri et al. [195] to cancel out TS waves in an experimental setup. The authors tuned a proportional feedback controller thanks to the Nyquist plot to optimise the controller gain in closed-loop while ensuring robust stability of their feedback configuration. Such classical loop-shaping approaches provide guarantees on stability robustness but are far from optimal from a performance viewpoint. And perhaps more importantly, they are very limited in the sense that they cannot be easily applied to multi-criteria specifications and to more complex controller structures in a systematic way.

2.6.5 Modern optimal synthesis

In contrast, modern tools for multi-criteria/multi-objective synthesis allow to optimize complex control laws. These complex syntheses, introduced by Doyle et al. [45], satisfy several specifications by constraining several transfer functions simultaneously.

The H_2 optimal synthesis [45, 180] is one of these multi-objective syntheses. This synthesis computes, by solving Riccati equations, a stabilizing optimal controller in terms of H_2 minimization of a transfer function G_{H_2} . The LQG synthesis is a special case of the H_2 optimal synthesis. Indeed, minimizing the H_2 norm of

$$G_{H_2} = \begin{pmatrix} \mathbf{Q}_{\text{LQR}}^{1/2} T_{\text{zw}}^c & 0 \\ 0 & \mathbf{R}_{\text{LQR}}^{1/2} K S T_{\text{yw}} \end{pmatrix} \quad (2.16)$$

strictly amounts to minimize the quadratic cost function \mathcal{J} (see equation 2.14) by using the Parseval's identity [61, 180, 187]. Another example of the H_2 optimal synthesis is the mixed-sensitivity H_2 loop shaping which consists in finding a stabilizing controller K that minimizes the H_2 norm of:

$$G_{H_2} = \begin{pmatrix} W_1 S \\ W_2 K S \\ W_3 S T_{\text{yu}} K \end{pmatrix}, \quad (2.17)$$

with W_1, W_2, W_3 weighting functions. Therefore, with the H_2 optimal synthesis, it is no longer necessary to use a criterion based solely on the performance and cost of control as in LQG synthesis because every transfer functions can be constrained. However, the SISO stability via the Nyquist plot or the small gain theorem for MIMO systems corresponding to a H_∞ norm constraint, the H_2 optimal control synthesis is not appropriate to ensure stability robustness.

The H_∞ optimal synthesis [45, 167] solves this problem by computing a stabilizing optimal controller in terms of H_∞ minimization of a transfer function G_{H_∞} . The H_∞ optimal synthesis employs Riccati equations (as in LQG/ H_2 optimal syntheses) or LMIs (Linear Matrix Inequalities) convex solvers [159]. This H_∞ optimal synthesis is also called robust H_∞ synthesis as it minimizes H_∞ norms to ensure stability robustness of a feedback design. This robust synthesis has been mainly used in the case of oscillator flows to have some stability guarantees, because using a feedback setup is mandatory to stabilize a globally unstable flow. Dahan et al. [39] and Flinois and Morgans [58] employed the H_∞ loop-shaping technique, introduced by McFarlane and Glover [119], to control the flow over a bluff body with a blunt trailing edge and around a D-shaped body, respectively. The H_∞ loop-shaping technique generalizes and automates according to the minimization of a H_∞ criterion the classical SISO loop-shaping method based on Bode diagram of the open-loop gain $T_{\text{yu}} K$. The H_∞ loop-shaping technique first shapes the open-loop gain before optimizing the robustness of the controller by minimizing a H_∞ norm. Shaqarin et al. [172] and Kerstens et al. [85] exploited the mixed-sensitivity loop-shaping technique which consists in finding a stabilizing controller that minimizes the H_∞ norm of equation 2.17 to reduce the drag of a D-shaped bluff-body and to maintain a constant lift force on a low-aspect-ratio semicircular wing in a longitudinally gusting flow, respectively. Some studies

employing H_∞ techniques exist also for the control of linearly stable channel flows where the amplification of disturbances is due to transient growth [19, 79]. Nevertheless, the absence of an H_2 criterion in the H_∞ optimal synthesis can be restrictive for the control of noise-amplifier flows where one seeks to minimize the r.m.s. values of disturbances (thus passing through the minimisation of an H_2 norm, see section 2.4.1).

The mixed H_2/H_∞ synthesis [159, 160] solves this limitation by minimizing a trade-off criterion of the form $\|G_{H_2}\|_2^2 + \|G_{H_\infty}\|_\infty^2$ by employing LMI techniques. The possibility of working with both H_2 and H_∞ criteria for noise-amplifier flows ensures nominal performance, stability robustness and performance robustness (see section 2.4). Indeed, the use of H_∞ criteria on some transfer functions allows to satisfy stability margins on the feedback design (which was missing in the H_2 optimal framework) despite modelling errors and to desensitize the controller on certain frequency ranges, allowing optimal performance to be maintained despite the presence of, for example, noise on the estimation sensor. The use of H_2 criteria makes it possible to have a performance objective of r.m.s. value mitigation during the synthesis (which was sometimes lacking in previous feedback studies associated with loop-shaping or H_∞ optimal syntheses).

2.6.6 Structured synthesis

The optimal mixed H_2/H_∞ synthesis seems at first sight very suitable for the control of noise-amplifier flows. However, by solving Riccati equations or LMI, the modern optimal syntheses lead to high-order controllers (of the same order as the plant augmented by weighting functions). These are often too expensive to use in real-time applications and require reducing the controller order in a post-processing step. Performing this reduction optimally while maintaining stability and performance guarantees on the closed-loop remains an open problem [33, 67]. This important limitation has led the control community to develop the structured synthesis [7, 8]. A structured synthesis has the ability to limit the controller order and to impose its structure beforehand (*e.g.* state-space model of order 10, PID controller, etc.). These structured syntheses are solved via non-smooth/non-convex optimization techniques; non-smooth optimizations are computationally intensive (compared to an optimal synthesis) and several random controller initializations are required to deal with the non-convex nature of the optimization problem. Leclercq et al. [96] employed the structured H_∞ synthesis [7] to control a flow over a cavity (oscillator flow). For noise-amplifier flows, the structured mixed H_2/H_∞ synthesis [8] seems to be the most suitable synthesis as it has all the advantages of the previous methods: it constraints/minimizes both H_2 and H_∞ norms while imposing the structure of the controller which makes it a particularly powerful and flexible synthesis method.

2.7 Maintaining performance over several operating points

Controlling instabilities over several operating points can be seen as an extended performance robustness problem. Even if a simple feedback structure designed at one operating point has a natural ability to maintain performance in the presence of model uncertainty or external perturbations, it is not meant to be used in off-design conditions. Specific techniques may be used to extend performance robustness to additional operating points.

Erdmann et al. [52], Fabbiane et al. [54, 55] used an adaptive feedforward method for boundary layer control, based on the filtered-X least-mean-squares (FXLMS) algorithm, where the controller coefficients gradually adapt to free-stream variations to improve performance robustness compared to a simple LTI LQG feedforward controller. This method is only robust over long time-scales as the controller coefficients are adjusted in a quasi-static fashion.

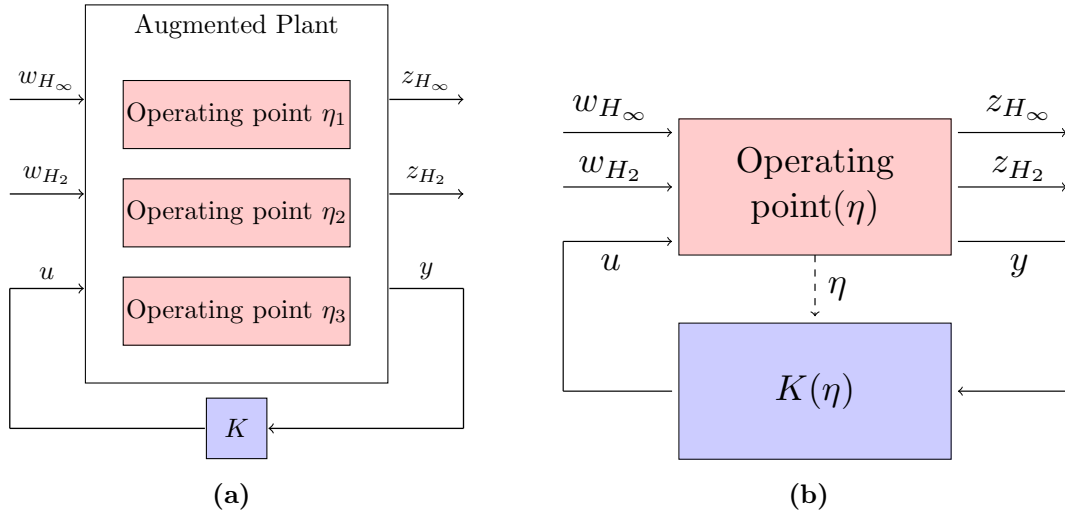


Figure 2.9: (a) Multi-model and (b) gain scheduling methods by multi-criteria structured mixed H_2/H_∞ synthesis.

Some methods, contrary to those which only used the ROMs of the nominal case and looked at the performance robustness in off-design conditions a posteriori [14, 54, 55, 188, and many others], directly exploit the ROMs at different operating points in the synthesis step. In multi-model synthesis [9, 88, 89], the use of the ROMs at different operating points allows to shape adequately the transfer functions to achieve specific design goals at each operating point simultaneously. The multi-model method may be combined with the structured mixed H_2/H_∞ synthesis (see figure 2.9a). The multi-model synthesis results in a LTI controller K with increased performance robustness (at the cost of a lower nominal performance) compared to a LTI controller built on a single operating point [104] and may therefore potentially allow to maintain performance in terms of perturbation amplitude reduction over a wide range of operating points, even with a feedforward structure. Gain scheduling is also a common approach for controlling systems whose dynamics change with operating conditions when a single set of controller parameters does not provide desired performance throughout the entire range of operating conditions [147]. The principle of the gain scheduling is to vary the controller parameters according to the value of a scheduling variable η , *e.g.* the free-stream velocity, which is assumed to be measured on-line (see figure 2.9b). The gain scheduled control law can be built from a family of LTI controllers designed at different operating points (*i.e.* at frozen values of the scheduling variable) [36, 76, 132] or from Linear Parameter-Varying (LPV) models where the analytical expression of the ROMs as a function of η is known (therefore, an explicit formulation of the controller can be obtained and it is no longer built from a family of LTI controllers) [11, 197]. The gain scheduling approach should not be confused with the FXLMS adaptive controllers where the controller parameters are updated on-line based on the information from performance sensors [54, 55]; in these adaptive methods, the controller parameters vary with the operating conditions, but are not known a priori and therefore remain subject to the convergence of the optimization method from one operating point to another. With the gain scheduling method, the parametrisation of the control law according to the scheduled variable is known in advance. Moreover, gain scheduling responds faster to changing operating conditions than adaptive methods because the law is automatically adapted as soon as η is modified [18, 147]. Finally, gain scheduling has the advantage of being based on powerful linear design tools as the structured mixed H_2/H_∞ synthesis ensuring stability and performance robustness, provided the scheduling parameter varies slowly enough in comparison with the control bandwidth (as the robustness properties are guaranteed in a local sense) [23, 147].

Chapter outcome summary:

Numerous studies addressed the problem of transition delay in the supersonic boundary layer flow but they used passive or predetermined active strategies making them less effective in terms of disturbance amplitude reduction and robust to modelling errors or inflow variations than a reactive control strategy. As four of the five paths from receptivity to transition involve small-amplitude perturbations, a reactive control strategy based on the classical linear tools of control theory (identification, synthesis, etc.), is perfectly suited to mitigate the linear growth of disturbances for transition delay. Such reactive control strategy has been employed many times in incompressible boundary layer flows to control disturbances and delay transition to turbulence.

For the identification step, necessary for most of the synthesis methods, data-based approaches such as ERA or vector-fitting methods have the advantage of building models only from input/output time or frequency data sets and can be used in a realistic setup unlike Galerkin projection methods. For the synthesis step, the limitations of a simple LQG LTI feedforward controller designed at one operating point in terms of performance robustness have been highlighted. For boundary-layer flow control, some feedback controllers, which are naturally more robust than the feedforward ones, have been successfully designed by a loop-shaping approach to handle the problem of stability robustness of a feedback configuration. However, modern robust synthesis tools such as the structured mixed H_2/H_∞ synthesis (which can be coupled with multi-model or gain scheduling methods) is a promising alternative to meet multi-criteria specifications and design complex controller structures in a systematic way in order to handle simultaneously the problems of nominal performance, stability and performance robustness for noise-amplifier flow control.

Numerical methods

| | | |
|------------|---|-----------|
| 3.1 | Flow methods | 46 |
| 3.1.1 | Solvers and spatial schemes | 46 |
| 3.1.2 | Base flow | 46 |
| 3.1.3 | Local stability resolution | 47 |
| 3.1.4 | Global stability resolution | 48 |
| 3.1.5 | Unsteady simulations | 51 |
| 3.1.6 | Boundary-layer code | 52 |
| 3.2 | Control methods | 52 |
| 3.2.1 | Identification | 52 |
| 3.2.1.1 | ERA | 52 |
| 3.2.1.2 | Vector-fitting method | 54 |
| 3.2.2 | Structured mixed H_2/H_∞ synthesis | 54 |
| 3.2.3 | Controller implementation | 55 |

Chapter foreword:

This chapter introduces the numerical methods used in this thesis and also provides elements of validation. Firstly, the solvers and spatial schemes employed to resolve the fully compressible Navier–Stokes equations are introduced. The validation of the spatial schemes in order to obtain the base flow is done by comparing with the results of Ma and Zhong [109]. Then, the in-house local and global stability codes are presented and validated from the results of Ma and Zhong [109] and Bugeat et al. [24]; the use of the global stability code allows also to validate the spatial numerical schemes for the 2D perturbation field. Next, the temporal schemes for the unsteady simulations and the in-house boundary-layer code are also introduced and validated. Finally, the ERA and the vector-fitting method for the identification of the useful transfer functions as well as the structured mixed H_2/H_∞ synthesis and the controller implementation in the flow solvers are presented in more detail.

3.1 Flow methods

3.1.1 Solvers and spatial schemes

The direct numerical simulations (DNS) of the fully compressible Navier–Stokes equations (see equations 1.1) are performed using the finite-volume codes *elsA* [27] and *FastS* [139]. The *elsA* solver is a powerful and flexible solver which is able to deal with both external flows around aircrafts or helicopters and with internal flows in turbomachinery. This reliable tool is employed for industrial applications by Airbus, Safran and MBDA. The 2D DNS, which are the first step to develop a methodology to delay transition to turbulence, are performed with this CFD software because of the ease of use as *elsA* is commonly employed at ONERA. The 3D DNS are performed with the in-house research solver *FastS*; *FastS* has less flexibility than *elsA* to handle complex cases but is much more efficient thanks to memory optimisation using cache blocking. As an example, *FastS* is 10 times faster than *elsA* for our 3D DNS. An upwind AUSM + scheme [102, 103] associated with a third-order MUSCL extrapolation method [97] is used for the spatial discretization of the convective fluxes both in *elsA* and *FastS*. The viscous fluxes are obtained by a second-order centered scheme.

3.1.2 Base flow

The laminar base-flow $\bar{\mathbf{q}}$, stationary solution of the Navier–Stokes equations 1.1 and defined as

$$\mathcal{N}(\bar{\mathbf{q}}) = 0, \quad (3.1)$$

is obtained by time-stepping the unsteady equations 1.10 with an implicit time-stepping method based on a local time step, up to convergence of the residuals. The ability of the AUSM scheme associated with a second-order centered scheme for viscous fluxes to accurately compute a base flow is evaluated by comparing with the results of Ma and Zhong [109]. This 2D test case is defined in figure 3.1 and consists of a uniform flow at $M_\infty = 4.5$ on an adiabatic flat plate. The numerical domain extends from $0 < Re_x \lesssim 4.1 \times 10^6$ in the streamwise direction and the wall-normal extent of the domain is taken to be $\sim 24\%$ of the streamwise length. A similar grid than the one of Ma and Zhong [109] is used: 3200 points uniformly spaced in the streamwise direction and 140 grid points in the boundary layer at the end of the domain (geometric distribution). A supersonic inlet condition is imposed at the upstream boundary with the same free-stream conditions as [109] (*i.e.* $T_\infty = 65.15$ K, $U_\infty = 728.2$ m.s⁻¹ and $p_\infty = 728.4$ Pa); a far-field [141] and a supersonic exit conditions are respectively applied at the top and at the outlet of the computational domain. Figure 3.2a presents the wall-pressure distribution along the

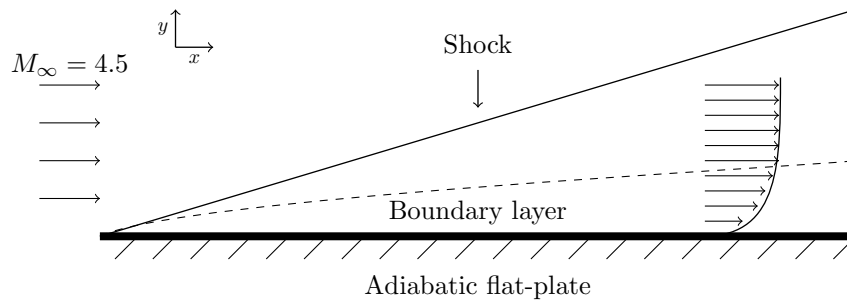


Figure 3.1: Simplified diagram of the validation case from [109].

domain. The second wall-normal derivative of the streamwise velocity $\partial_{yy}^2 u$ at $Re_x = 1 \times 10^6$ is also plotted in figure 3.2b; it is critical to describe correctly this quantity as it is related

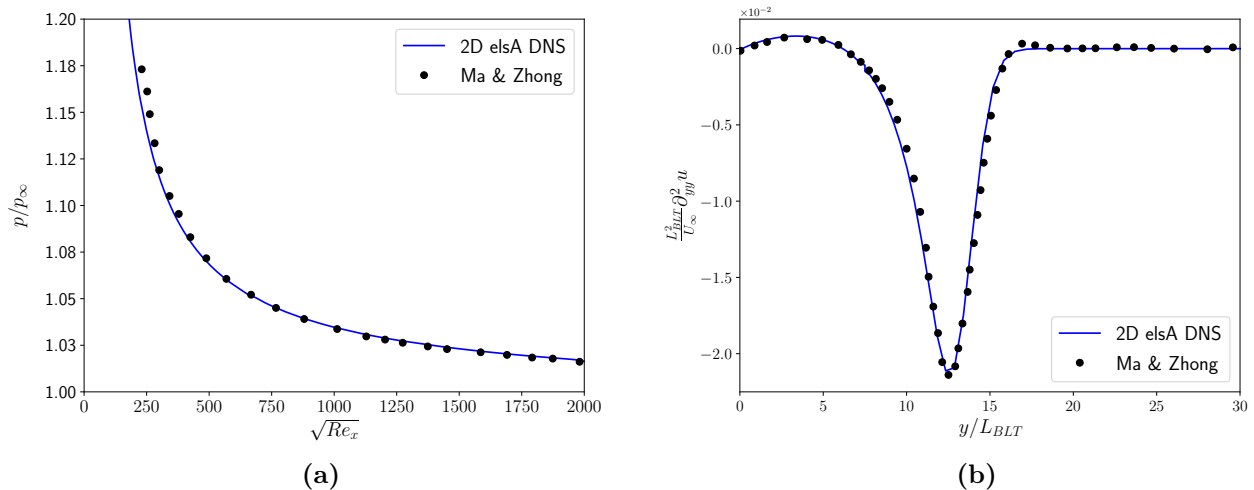


Figure 3.2: Comparison of (a) wall-pressure distribution and (b) second wall-normal streamwise derivative velocity profile at $Re_x = 1 \times 10^6$ with results from [109]. In (b), lengths are made dimensionless using the length scale of the boundary-layer thickness $L_{BLT} = \sqrt{\frac{\mu_\infty x}{\rho_\infty U_\infty}}$.

to the inflection point which is the cause of the inviscid instabilities. Despite the fact that Ma and Zhong [109] use much higher order schemes (5th order upstream scheme for convective fluxes and 6th order centred scheme for viscous fluxes), a good agreement is achieved for both wall-pressure distribution and $\partial_{yy}^2 u$ profile, which validates the spatial schemes used to compute a supersonic base flow.

3.1.3 Local stability resolution

The local stability analysis in this thesis is performed with an in-house python LLST code developed by Chanteux et al. [31]. This code is used in this thesis for the 2D analysis, and the dispersion relation $D(\alpha, \omega, \beta = 0, x) = 0$ for a frozen base flow profile is solved with a spatial stability framework (real angular frequencies $\omega = 2\pi f$ and complex wavenumber $\alpha = \alpha_r + i\alpha_i$, see section 1.3.1). All perturbations are assumed to vanish at the free-stream boundary $y \rightarrow \infty$ while on the bottom boundary $y = 0$, $\tilde{u} = \tilde{v} = 0$ and $d\tilde{\rho}/dy = d\tilde{T}/dy = 0$ (respectively $\tilde{T} = 0$) for an adiabatic (respectively isothermal) condition. The equations are discretized along the wall-normal direction y using a Chebyshev collocation method. The in-house LLST code follows the procedure resolution developed in Saint-James [148]: for a frequency ω that is known to be locally unstable at a position x , a generalized eigenvalue problem is solved, using the LAPACK library, in order to obtain the set of eigenvalues α and eigenvectors $\tilde{\mathbf{q}}(y)$; then, the unstable physical eigenvalue (which is independent of the wall-normal grid, contrary to the spurious numerical eigenvalues) is used as initialization eigenvalue for a pseudo-temporal shooting method [148] to determine for any x and ω the physical eigenvalue α . The spacing dx between two base flow profiles and $d\omega$ between two frequencies must be low enough to converge step by step the shooting method to the correct physical value α . The code is validated here by comparing with the 2D linear local growth rates of the supersonic boundary layer from [109] (see figure 3.1). The adiabatic base flow profiles, validated in section 3.1.2, are used and the LLST code is performed with an isothermal or adiabatic boundary condition as in [109]. According to [111], the use of an isothermal wall-boundary condition for the infinitesimal perturbations whereas the steady base flow is subject to an adiabatic condition may be justified as the high-frequency temperature disturbances will not penetrate deep into the solid boundary

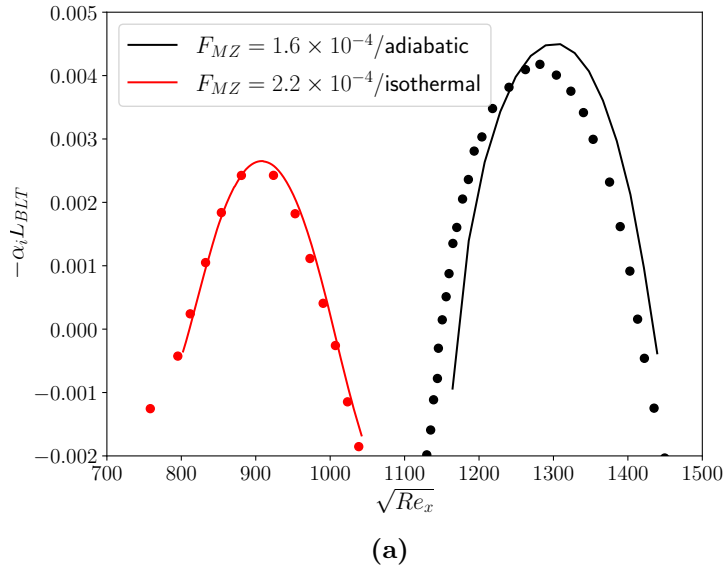


Figure 3.3: Comparison of the growth rates $-\alpha_i$ from the in-house LLST python code used in this thesis (solid lines) and from the LLST results of Ma and Zhong [109] (circles) for two dimensionless frequencies $F_{MZ} = \frac{2\pi f \mu_\infty}{\rho_\infty U_\infty^2}$ (and $\beta = 0$).

due to its thermal inertia. For two dimensionless frequencies $F_{MZ} = \frac{2\pi f \mu_\infty}{\rho_\infty U_\infty^2}$ (and $\beta = 0$), a good agreement is achieved between the evolution along x of the growth rates $-\alpha_i$ from our in-house LLST python code and those from [109] for both isothermal and adiabatic conditions (see figure 3.3), which validates our in-house LLST code.

3.1.4 Global stability resolution

The resolvent analysis in this thesis is performed using a python tool developed by Beneddine et al. [17]. This code is used in this thesis for 2D analysis. To solve the optimal gain problem (see equation 1.18), the Jacobian matrix $\mathcal{A} = \frac{d\mathcal{N}}{d\tilde{\mathbf{q}}}$ has to be obtained. It is calculated using a second-order finite-difference method:

$$\mathcal{A}(\tilde{\mathbf{q}})\mathbf{v} \simeq \frac{\mathcal{N}(\tilde{\mathbf{q}} + \epsilon\mathbf{v}) - \mathcal{N}(\tilde{\mathbf{q}} - \epsilon\mathbf{v})}{2\epsilon}, \quad (3.2)$$

with $\mathbf{v} = [0, \dots, 0, 1, 0, \dots, 0]^T$ a canonical basis vector and ϵ a scalar. The unitary vector \mathbf{v} determines one of the columns of \mathcal{A} . Hence, the combination of every unitary vectors yields the full operator. In practice, \mathbf{v} is a combination of unitary vector to limit the number of calls of the equation 3.2 and speed up the determination of \mathcal{A} . Indeed, particular linear combinations of canonical basis vectors lead to independent responses in the flow as the stencil of the solver is limited in space; a disturbed cell can only impact a limited number of neighbouring cells (see figure 3.4). For the parameter ϵ , a compromise must be found between the numerical error for ϵ too small and the linearisation error for ϵ too large. The choice of the matrices \mathcal{Q}_f and \mathcal{Q}_e featured in equation 1.19 depends on the quantity one seeks to optimise. In this manuscript, the positive-definite matrix \mathcal{Q}_f is defined such that $\|\tilde{\mathbf{f}}\|_F^2 = \tilde{\mathbf{f}}^* \mathcal{Q}_f \tilde{\mathbf{f}}$ corresponds to the energy of the momentum forcing. For the semi-definite-positive matrix \mathcal{Q}_e , it is defined such that $\|\tilde{\mathbf{q}}\|_E^2 = \tilde{\mathbf{q}}^* \mathcal{Q}_e \tilde{\mathbf{q}}$ corresponds to the total kinetic perturbation energy $\frac{1}{2} \int_V \bar{\rho}(|u'|^2 + |v'|^2) dV$

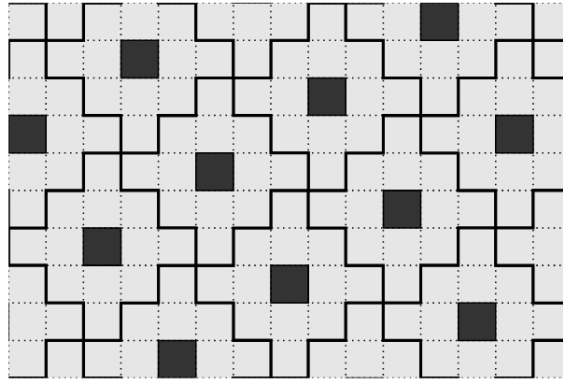


Figure 3.4: 2D optimal combination of canonical basis vectors for the 5-cell-stencil spatial scheme used in this thesis. Figure from [16].

[140, 152] or the total Chu's energy [35]. The Chu energy norm is defined as

$$E_{\text{Chu}} = \frac{1}{2} \int_{\mathcal{V}} \underbrace{(\bar{\rho}(|u'|^2 + |v'|^2))}_{e_{u'}} + r \underbrace{\frac{\bar{T}}{\bar{\rho}} |\rho'|^2}_{e_{\rho'}} + \underbrace{\frac{r}{\gamma - 1} \frac{\bar{\rho}}{\bar{T}} |T'|^2}_{e_{T'}} dV. \quad (3.3)$$

It is commonly used for compressible flows as it contains terms relative to thermodynamic perturbations in addition to the kinetic one [24, 71]. The explicit expressions of \mathcal{Q}_f and \mathcal{Q}_e for these energetic norms are provided in appendix A. Determining the optimal gain \tilde{g} amounts to computing the largest eigenvalue of the generalised eigenvalue problem 1.19; this problem is solved with the Arnoldi algorithm [ARPACK library, 100] using a sparse LU solver [MUMPS library, 4] for linear system solution.

This global analysis tool is validated on the 2D supersonic boundary layer results from Bugeat et al. [24]. This validation configuration is similar to that described in section 3.1.2 (see figure 3.1); contrary to the simulations of [109] for the base flow validation, the domain only extends to $Re_x = 2 \times 10^6$. The spatial schemes validated in section 3.1.2 are kept for this validation case. Following Bugeat et al. [24], the Chu energy norm for the response is employed for the gain optimisation; the optimisation domain (for both forcing and response) for the calculation of \tilde{g} is restricted to $Re_x \in [0; 1.75 \times 10^6]$ in the streamwise direction and to $y \in [0; 9\delta_{Bugeat}^*]$ (with δ_{Bugeat}^* the compressible displacement thickness at $Re_x = 1.75 \times 10^6$, defined as $\delta^* = \int_0^\infty (1 - \frac{\rho u}{\rho_\infty u_\infty}) dy$) in the wall-normal direction, for computational savings. For the same mesh grid as Bugeat et al. [24] in the streamwise direction (2400 points), good agreement is obtained between the optimal gains \tilde{g} from our in-house global code and those obtained by [24] (see figure 3.5a). The comparison of the gains only gives a global indication (the gains result from volume integration over the domain), and it may be interesting to have a more local validation. Hence, the profiles of the optimal forcing at $Re_x = 9.9 \times 10^5$ (see figure 3.5b) and response at $Re_x = 1.62 \times 10^6$ (see figure 3.5c) are compared for the peak gain (at $F_{MZ} = 2.26 \times 10^{-4}$). Our results coincide with those of [24] for both the optimal forcing and response profiles, which validates the optimal gain algorithm and the resolvent operator \mathcal{R} obtained by our in-house global code.

In addition to the validation of the global stability tool, the ability of spatial schemes to correctly capture the perturbation field \mathbf{q}' is evaluated. It is assessed by comparing the spatial growth rate $-\tilde{\alpha}_i = \frac{1}{|\tilde{p}(x,y=0)|} \partial_x |\tilde{p}(x,y=0)|$ from the response field of the resolvent analysis (solid line) and from Fourier transform results of Ma and Zhong [109] on linearized DNS (blue circles) (see figure 3.6). The quantity $-\tilde{\alpha}_i$ represents the slope of $\ln |\tilde{p}|$ with respect to x and

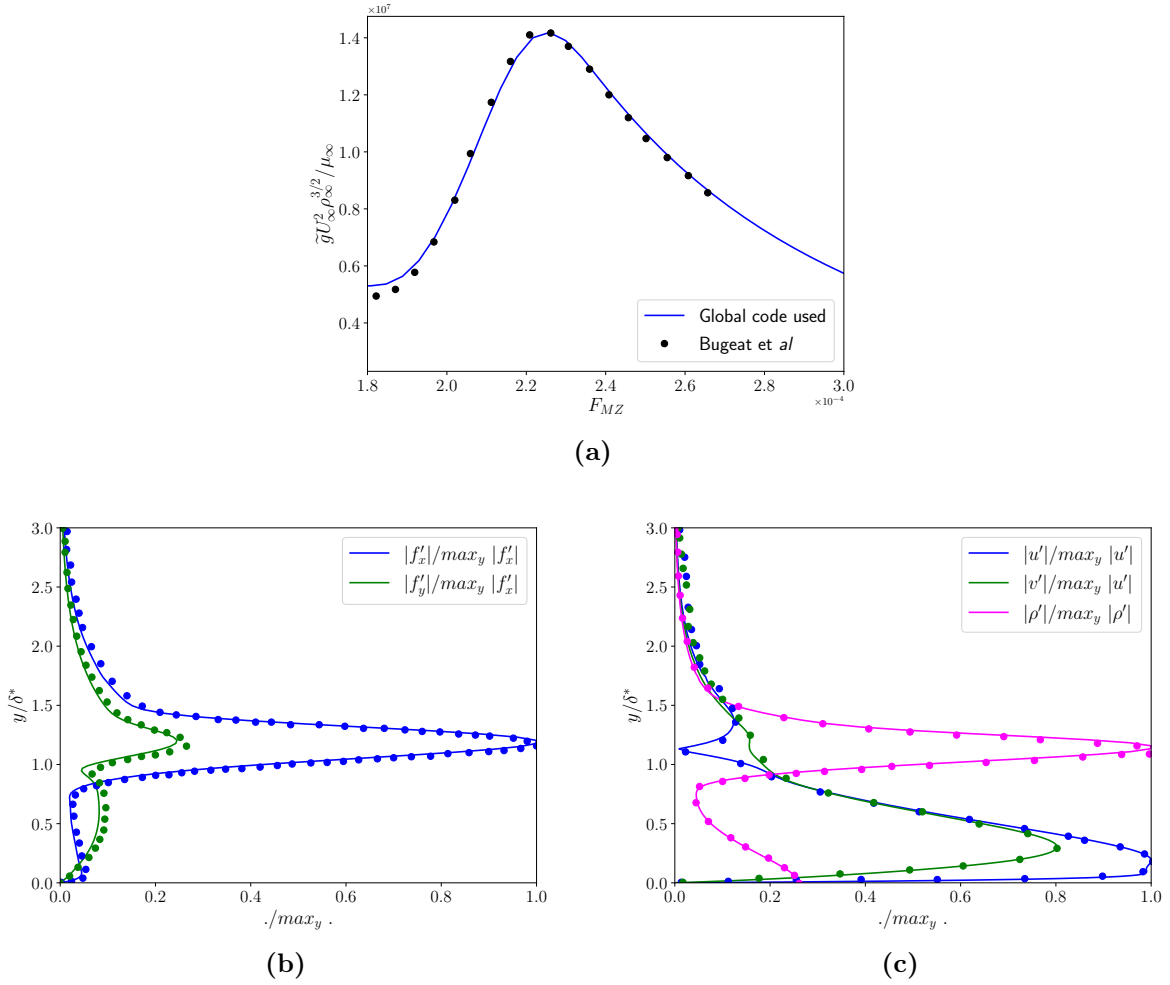


Figure 3.5: Comparison of the 2D (a) optimal gains and profiles at $F_{MZ} = 2.26 \times 10^{-4}$ of the (b) optimal forcing at $Re_x = 9.9 \times 10^5$ and (c) response at $Re_x = 1.62 \times 10^6$ with results from [24] (circles).

can therefore be interpreted as a local spatial growth rate. Indeed, in regions where transient growth is dominated by the convective-type non-normality effects (between branch I and branch II of the LLST), the quantity $-\tilde{\alpha}_i$ is nearly independent of the choice of y and primitive variable and $-\tilde{\alpha}_i$ is very close to the quantity $-\alpha_i$ computed with LLST [48, 49, 109]. The validation case corresponds to the one described in section 3.1.2, with the adiabatic condition for the perturbation field. For their linearized DNS, Ma and Zhong [109] force waves from the inlet boundary condition by specifying the flow as the superposition of the steady base flow and a temporal fluctuation of flow variables at frequency $F_{MZ} = 1.6 \times 10^{-4}$. Hence, to compare their results to the global stability approach, the forcing field \mathbf{f} for the resolvent optimisation problem is constrained to a thin strip $\sqrt{Re_x} \in [476.67, 483.3]$ localized (via a prolongation operator, see appendix A) far upstream of the locally unstable region. This streamwise restriction is sufficiently far upstream to ensure that the component-type non-normality effects no longer dominate in the modal instability domain to compare with Ma and Zhong [109]. The domain involved in the streamwise direction for the Chu energy optimisation of the response field is $\sqrt{Re_x} \in [476.67, 1998.1]$. In the wall-normal direction, no restriction is applied for the domains involved in the definition of $\|\cdot\|_E^2$ and $\|\cdot\|_F^2$. Good agreement is achieved between the evolution along x of the quantity $-\tilde{\alpha}_i$ from our resolvent analysis and the one from linearized DNS of [109]. The growth rates $-\alpha_i$ from LLST are also plotted and exhibit similar values to $-\tilde{\alpha}_i$ in the LLST instability region. As the configuration of [109] is very similar to the one that will

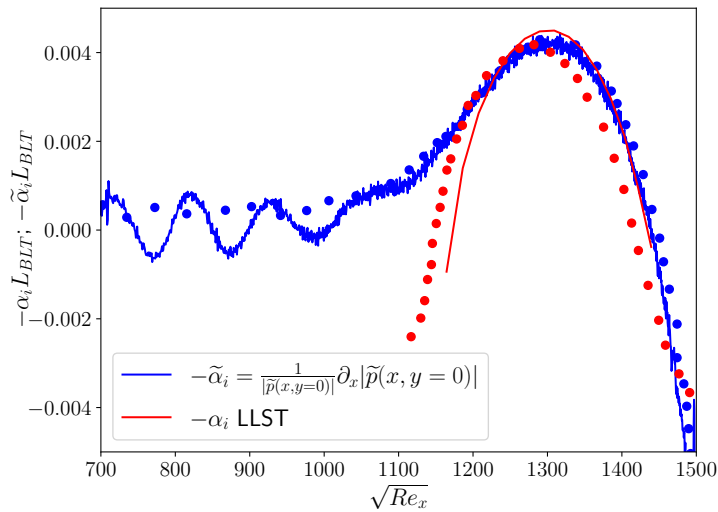


Figure 3.6: Comparison of $-\alpha_i$ from LLST of our in-house code (red line) and of [109] (red circles) and $-\tilde{\alpha}_i = \frac{1}{|\tilde{p}(x,y=0)|} \partial_x |\tilde{p}(x,y=0)|$ from our resolvent analysis (blue solid line) and from the Fourier transform of [109] on linearized DNS (blue circles) at $F_{MZ} = 1.6 \times 10^{-4}$.

be used in chapters 4, 5 and 6, it validates the spatial schemes used in this thesis (see section 3.1.1) to describe the 2D perturbation field of our configuration.

3.1.5 Unsteady simulations

The 2D unsteady simulations performed with *elsA* for the development of instabilities are performed with an implicit second-order Gear scheme with 4 sub-iterations and a time-step dt ensuring a Courant-Friedrichs-Lewy (CFL) number lower than 1.4 in the whole domain. The time step and the number of sub-iterations of the temporal method have been validated by comparing transfer functions from the linearized DNS and those determined from the frequency-domain resolvent approach (see section 2.4). As this validation requires the introduction of the transfers used in chapter 4, it is left to appendix B in order to facilitate the reading of the manuscript.

The 3D unsteady simulations performed with *FastS* use an explicit third-order 3-steps low-storage Runge–Kutta scheme [202] (to have accurate solutions when simulating transition to turbulence) with a time-step ensuring a CFL number lower than 0.7 (respectively 0.4) in the whole domain for the linearized DNS (respectively the non-linear DNS that lead to transition to turbulence). The time-step of the fully non-linear DNS that lead to transition is lower compared to the one of the linearized DNS for stability reasons. Contrary to the 2D case, a global stability analysis has not been carried out on the 3D configuration; hence, the validation of the schemes for unsteady 3D simulations is performed by temporal and grid convergences (see appendix B).

For the linearized 2D/3D unsteady simulations, the amplitude of the forcing \mathbf{f} is chosen sufficiently small to ensure that the induced perturbation \mathbf{q}' remains in the linear regime until the end of the computational domain.

3.1.6 Boundary-layer code

In the 2D/3D simulations of chapters 4, 5 and 6, the inlet condition matches a zero-pressure gradient laminar boundary layer profile computed with the in-house ONERA boundary layer code CLICET (see for instance Olazabal-Loumé et al. [133]). This code solves the boundary-layer equations with a finite-volume method. The system of equations is integrated using a forward-marching method; the knowledge of the boundary layer profiles at an initial position and wall/free-stream boundary conditions is sufficient to calculate the profiles at downstream positions. The initial profile corresponds to a local self-similar solution near the stagnation point. The validation is carried out in comparison with the self-similar results of Ozgen and Kiricali [136] for a laminar boundary layer at $M_\infty = 4$ above an adiabatic flat-plate (see figure 3.7); the velocity and temperature profiles match, which validates the calculations.

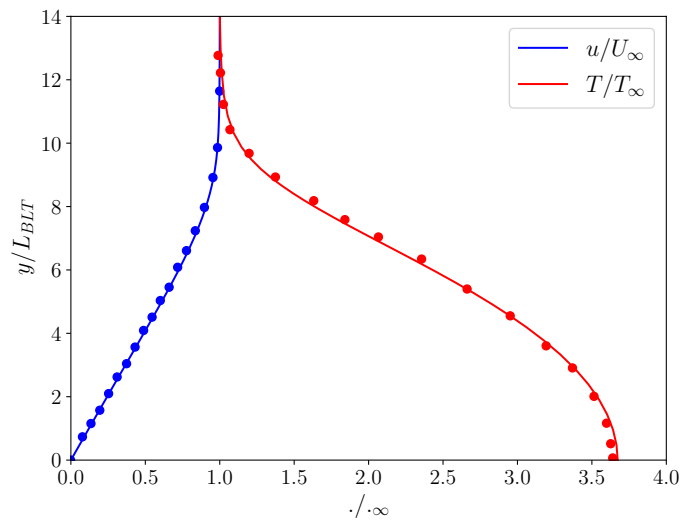


Figure 3.7: Comparison of self-similar profiles at $M_\infty = 4$ of streamwise velocity (blue) and temperature (red) computed with CLICET (solid lines) and from [136] (circles).

3.2 Control methods

3.2.1 Identification

The identification methods employed in this manuscript in order to obtain models of small dimensions are briefly detailed in this section. Both the ERA and the vector-fitting method are data-based approaches and do not require the knowledge of the governing equations. They need only the input-output time/frequency data sets to build the ROMs and can therefore be used in realistic setups (see section 2.5.2).

3.2.1.1 ERA

The ERA is a popular tool, introduced by Juang and Pappa [80], used many times in noise-amplifier flow control studies [14, 126, 153, and many others]. This subspace identification technique is based on a discrete framework; in this framework, a state-space model (see

equations 2.5) is written as:

$$\mathbf{x}_{k+1} = \mathbf{A}\mathbf{x}_k + \mathbf{B}\mathbf{u}_k, \quad (3.4a)$$

$$\mathbf{y}_k = \mathbf{C}\mathbf{x}_k + \mathbf{D}\mathbf{u}_k. \quad (3.4b)$$

The ERA exploits the set of impulse responses of all the outputs for each of the inputs. Thus, an input matrix $\mathbf{U}_k = \mathbf{I}u_k \in \mathbb{R}^{n_u \times n_u}$ is introduced with $u_0 = 1$ and $u_k = 0$ for $k \geq 1$:

$$\mathbf{X}_{k+1} = \mathbf{A}\mathbf{X}_k + \mathbf{B}\mathbf{U}_k, \quad (3.5a)$$

$$\mathbf{Y}_k = \mathbf{C}\mathbf{X}_k + \mathbf{D}\mathbf{U}_k, \quad (3.5b)$$

with $\mathbf{X}_k \in \mathbb{R}^{n_x \times n_u}$ and $\mathbf{Y}_k \in \mathbb{R}^{n_y \times n_u}$. The i^{th} column of these matrices corresponds to the state vector and output vector at time k following the impulse of the i^{th} input of vector \mathbf{u} . By assuming zero initial conditions $\mathbf{x}_0 = 0$ and a feedthrough matrix $\mathbf{D} = 0$ (as the direct influence of the actuations signals on the measurements is negligible because the speed of sound and the speed of convection have finite values), we obtain:

$$\mathbf{X}_1 = \mathbf{B}$$

$$\mathbf{Y}_0 = \mathbf{0}$$

$$\mathbf{X}_2 = \mathbf{A}\mathbf{X}_1 = \mathbf{A}\mathbf{B}$$

$$\mathbf{Y}_1 = \mathbf{C}\mathbf{X}_1 = \mathbf{C}\mathbf{B}$$

$$\mathbf{X}_3 = \mathbf{A}\mathbf{X}_2 = \mathbf{A}^2\mathbf{B}$$

$$\mathbf{Y}_2 = \mathbf{C}\mathbf{X}_2 = \mathbf{C}\mathbf{A}\mathbf{B}$$

⋮

$$\mathbf{X}_{n+1} = \mathbf{A}\mathbf{X}_n = \mathbf{A}^n\mathbf{B}$$

$$\mathbf{Y}_n = \mathbf{C}\mathbf{X}_n = \mathbf{C}\mathbf{A}^{n-1}\mathbf{B}$$

Therefore, the impulse response of a discrete state-space model can be summarized as:

$$\mathbf{Y}_n = \begin{cases} \mathbf{0}, & n = 0 \\ \mathbf{C}\mathbf{A}^{n-1}\mathbf{B}, & n > 0 \end{cases} \quad (3.6)$$

The impulse response terms $\mathbf{Y}_n = \mathbf{C}\mathbf{A}^{n-1}\mathbf{B}$ are called the Markov parameters. These Markov parameters are used to assemble two Hankel matrices \mathbf{H} and \mathbf{H}' , defined by:

$$\mathbf{H} = \begin{pmatrix} \mathbf{C}\mathbf{B} & \mathbf{C}\mathbf{A}\mathbf{B} & \dots & \mathbf{C}\mathbf{A}^n\mathbf{B} \\ \mathbf{C}\mathbf{A}\mathbf{B} & \mathbf{C}\mathbf{A}^2\mathbf{B} & \dots & \mathbf{C}\mathbf{A}^{n+1}\mathbf{B} \\ \vdots & \vdots & \ddots & \vdots \\ \mathbf{C}\mathbf{A}^n\mathbf{B} & \mathbf{C}\mathbf{A}^{n+1}\mathbf{B} & \dots & \mathbf{C}\mathbf{A}^{2n}\mathbf{B} \end{pmatrix}, \quad (3.7)$$

and

$$\mathbf{H}' = \begin{pmatrix} \mathbf{C}\mathbf{A}\mathbf{B} & \mathbf{C}\mathbf{A}^2\mathbf{B} & \dots & \mathbf{C}\mathbf{A}^{n+1}\mathbf{B} \\ \mathbf{C}\mathbf{A}^2\mathbf{B} & \mathbf{C}\mathbf{A}^3\mathbf{B} & \dots & \mathbf{C}\mathbf{A}^{n+2}\mathbf{B} \\ \vdots & \vdots & \ddots & \vdots \\ \mathbf{C}\mathbf{A}^{n+1}\mathbf{B} & \mathbf{C}\mathbf{A}^{n+2}\mathbf{B} & \dots & \mathbf{C}\mathbf{A}^{2n+1}\mathbf{B} \end{pmatrix}. \quad (3.8)$$

Not all time steps of the DNS are required to obtain a good representation of the impulse response and the Markov parameters can be separated by several time steps (as long as the Nyquist-Shannon sampling theorem is satisfied) to reduce the size of the matrices for computational saving (and enhance the conditioning of the matrices). Then, a singular value decomposition $\mathbf{H} = \mathbf{U}\mathbf{\Sigma}\mathbf{V}^*$, where \mathbf{U} and \mathbf{V} are unitary and $\mathbf{\Sigma}$ diagonal, is performed. Only a limited number of singular values is required to correctly describe the input-output dynamics. Hence, to compress the state and select the order r of the reduced-order model, the matrices are truncated and the first r columns of \mathbf{U} and \mathbf{V} and the first r rows and columns of $\mathbf{\Sigma}$ are only conserved. Finally, the matrices $\mathbf{A}/\mathbf{B}/\mathbf{C}$ of the reduced-order state-space representation are obtained by the following relations:

$$\mathbf{A} = \mathbf{\Sigma}_r^{-1/2} \mathbf{U}_r^* \mathbf{H}' \mathbf{V}_r \mathbf{\Sigma}_r^{-1/2}, \quad (3.9)$$

$$\mathbf{B} = \text{the first } n_u \text{ columns of } \mathbf{\Sigma}_r^{1/2} \mathbf{V}_r^*, \quad (3.10)$$

$$\mathbf{C} = \text{the first } n_y \text{ rows of } \mathbf{U}_r \mathbf{\Sigma}_r^{1/2}. \quad (3.11)$$

This algorithm has been implemented in a python format. The discrete-time models obtained by the ERA are then converted to continuous-time models by first-order hold method [Matlab function *d2c*, 59] to be usable in the synthesis step.

3.2.1.2 Vector-fitting method

The vector-fitting method employed in this thesis uses the *tfest* function of the software Matlab. This method estimates continuous-time transfer functions to fit frequency data. For a SISO system G , the algorithm performs S-K iterations [46] to solve a nonlinear least-square problem:

$$\text{minimize } \sum_{k=1}^{n_f} |G(iw_k) - \tilde{G}(iw_k)|^2, \quad (3.12)$$

with \tilde{G} the estimate model designed to fit the data of G . For a given number of poles, the estimate model is searched in a rational form $\tilde{G} = \frac{\tilde{N}}{\tilde{D}}$ with \tilde{N} and \tilde{D} the numerator and denominator of the transfer function model. Models using frequency-data may be unstable (contrary to models using time-data). To avoid unstable models that are unusable for synthesis of noise-amplifier flows, an iterative reallocation step of the poles of the approximant is performed: the unstable poles of \tilde{G} are reflected with respect to the imaginary axis inside the stability region (by reversing the sign of the real part of the unstable poles to place them in the left half-plane). This last step changes the phase of the approximant, which is not a problem when trying to fit real frequency data (as $G(iw_k) = |G(iw_k)|$).

3.2.2 Structured mixed H_2/H_∞ synthesis

The structured mixed H_2/H_∞ synthesis is used in this thesis as it appears as the most flexible and powerful synthesis tool (see section 2.6.6). The syntheses of the chapters 4, 5 and 6 are performed using the Matlab function *systune*. The algorithm of *systune* solves the general problem:

$$\begin{aligned} &\text{minimize } f(x) \\ &\text{subject to } g(x) < 1, \end{aligned} \quad (3.13)$$

with $x \in \mathbb{R}^n$ is the decision vector consisting of tunable parameters of the structured controllers. The functions f and g may capture several requirements f_i and g_i at the same time and are

written as $f = \max_{i=1,\dots,n_f} f_i(x)$ and $g = \max_{i=1,\dots,n_g} g_i(x)$. Each positive function f_i or g_i may correspond to an H_2/H_∞ norm of a closed-loop transfer function weighted by an appropriate frequency template [180]. Weighting functions act as frequency domain constraints in order to shape adequately the transfer functions to achieve specific design goals. Furthermore, weighting functions allow to normalize the different requirements f_i and g_i to be able to balance them during the constrained minimization problem (CMP) in equation 3.13. Mathematically, a weighting function needs to be at least stable. In practice, it is easier to use a minimum-phase weighting function where the system (the weighting function) and its inverse (the constraint) are causal and stable (all the poles and zeroes are in the left half-plane of the s-plane representation) to be able to work independently on the weighting function or on its inverse (the constraint).

The CMP in equation 3.13 is non-smooth by nature because of the max aggregates of the functions f and g ; moreover, some of the individual requirements f_i/g_i may themselves be maxima of non-smooth functions (*e.g.* an H_∞ requirement). Without the structural constraint on the controller, this multi-criteria problem could be solved using convex optimization with LMI constraints. As soon as structurally constrained controllers are required, the CMP becomes a non-convex problem and a new algorithmic strategy is necessary. The *syntune* algorithm approaches the CMP in equation 3.13 by solving a sequence of unconstrained subproblems of the form:

$$\text{minimize } \max(f(x), \alpha_g g(x)), \quad (3.14)$$

in order to converge to the solution of the original CMP [9]. More precisely, α_g is adjusted by a bisection scheme based on constraint feasibility: α_g is increased (respectively decreased) when the constraint g is violated (respectively satisfied). For a given α_g , the subproblem in equation 3.14 is solved by a descent method: the descent directions are computed by solving quadratic programs and a line search is then employed [7]. The CMP in equation 3.13 is a non-smooth and non-convex problem and its resolution may be computationally intensive: non-smooth algorithms are more complex and have higher computational costs than smooth algorithms (which presume certain differentiability and strong regularity assumptions) and several initializations of the controller parameters are needed to deal with the non-convex nature of the problem.

3.2.3 Controller implementation

The controllers obtained from the structured mixed H_2/H_∞ synthesis are in a continuous state-space representation. Therefore, their implementation in the DNS solvers (*elsA* or *FastS*) consists in solving the first-order differential equations 2.5 at different time steps of the simulations to update the control vector signal $\mathbf{u}(t)$ (seen as the output vector of the state-space representation of the controller) from the estimation measurements $\mathbf{y}(t)$ (seen as the input vector of the state-space representation of the controller). At a time t_i , the controller state $\mathbf{x}(t_i)$ is obtained with a backward differentiation method of the second order:

$$\begin{aligned} \dot{\mathbf{x}}(t_i) &= \mathbf{A}\mathbf{x}(t_i) + \mathbf{B}\mathbf{y}(t_i) \\ \mathbf{x}(t_i) &\simeq (1.5\mathcal{I} - dt\mathbf{A})^{-1}(2\mathbf{x}(t_{i-1}) - 0.5\mathbf{x}(t_{i-2}) + dt\mathbf{B}\mathbf{y}(t_i)). \end{aligned} \quad (3.15)$$

Finally, since the controllers obtained are strictly-proper *i.e.* $\mathbf{D} = 0$ (see chapters 4, 5 and 6), the control vector signal $\mathbf{u}(t)$ is obtained:

$$\mathbf{u}(t_i) = \mathbf{C}\mathbf{x}(t_i). \quad (3.16)$$

Chapter outcome summary:

The main numerical methods used in this thesis have been presented in this chapter. The ability of the spatial schemes to obtain a supersonic base flow have been verified in comparison with the results of [109]; the in-house python local and global stability algorithms have been validated from the results of [109] and [24], respectively. Moreover, thanks to the global stability code, the spatial schemes used in this thesis are validated to describe the 2D perturbation field. The procedure employed for the unsteady simulations have been also introduced, as well as the boundary layer code used to generate the inlet profiles of the simulations. Finally, the main algorithms used for the creation of control laws, *i.e.* the ERA and the vector-fitting method for the identification step and the structured mixed H_2/H_∞ method for the synthesis step, are presented, as well as the controller implementation algorithm in the flow solvers.

Control of 2D instabilities with modern robust synthesis tools: feedforward vs feedback

| | |
|--|-----------|
| 4.1 Flow configuration | 59 |
| 4.2 Noise-amplifier behaviour | 60 |
| 4.2.1 Local stability results | 60 |
| 4.2.2 Global stability results | 61 |
| 4.3 Control setup | 64 |
| 4.4 Control settings | 66 |
| 4.4.1 Estimation and performance sensors | 66 |
| 4.4.2 Input disturbance | 66 |
| 4.4.3 Actuator | 68 |
| 4.5 Identification and synthesis methods | 71 |
| 4.5.1 ROMs | 71 |
| 4.5.2 General constrained minimization problem | 73 |
| 4.6 Preliminary results | 74 |
| 4.6.1 Position of the estimation sensor | 74 |
| 4.6.2 Evolution of performance as a function of the number of sensors z_i used in the synthesis | 77 |
| 4.7 Feedforward versus feedback control | 79 |
| 4.7.1 Performance on the nominal case | 80 |
| 4.7.2 Stability robustness | 84 |
| 4.7.3 Performance robustness | 86 |
| 4.7.3.1 Noisy sensors | 86 |
| 4.7.3.2 Off-design operating conditions | 87 |

Chapter foreword:

In the present chapter, we will consider a supersonic boundary layer at $M_\infty = 4.5$ and focus on the control of two-dimensional, i.e. spanwise invariant, and linear perturbations. We will not be dealing with oblique modes or finite-amplitude perturbations, even if they often do play a significant role in the transition process in practice. Hence this chapter is only a first step in learning how to design robust control laws for the problem of transition in the supersonic boundary layer and more generally on the control of instabilities for noise-amplifier flows. One key question we wish to address before introducing more physical complexity is how do the feedforward and feedback setups compare on this noise-amplifier flow, using modern robust synthesis tools? With the help of multi-criteria structured H_2/H_∞ controller synthesis, can we design a feedback setup which outperforms the often-used feedforward one with regards to performance robustness to realistic changes in operating conditions, *e.g.* velocity and density variations? Answering these questions is a first step in developing a control methodology that results in a robust control.

The chapter is organized as follows. Firstly, a description of the flow configuration is provided. Secondly, local and global linear stability tools are used to characterize the noise-amplifier behavior of our configuration and define appropriate closed-loop specifications, *i.e.* determining the actuators, sensors and performance criterion to be optimized. Then, the ROM identification (with special emphasis on the problem of time-delays in such noise-amplifier flows) and the constrained minimization problem solved by the structured mixed H_2/H_∞ synthesis are presented. Finally, after some preliminary results about the position of the sensors, the results obtained on and off-design for the feedforward and feedback configurations are compared.

4.1 Flow configuration

A two-dimensional compressible ideal gas flowing over a flat plate is considered. The flow is governed by the Navier–Stokes equations 1.1. The parameters of Sutherland’s law are taken as: $\mu_{\text{ref}} = 1.716 \times 10^{-5}$ Pa.s, $T_{\text{ref}} = 273.15$ K and $S = 110.4$ K. The gas considered being air, $\gamma = 1.4$, $r = 287$ J.K $^{-1}$.kg $^{-1}$ and $Pr = \frac{\mu\gamma r}{k(\gamma-1)} = 0.725$. The free-stream flow conditions are very close to those used experimentally by Kendall [84] and in the simulations of Ma and Zhong [109], *i.e.*: $T_{\infty} = 65.149$ K, $U_{\infty} = 728.191$ m.s $^{-1}$ and $p_{\infty} = 728.312$ Pa. Thus, the free-stream Mach number of the simulation is $M_{\infty} = \frac{U_{\infty}}{\sqrt{\gamma r T_{\infty}}} = 4.5$.

The computational domain is represented in figure 4.1a: it consists of a rectangular domain where the lower boundary is an adiabatic flat plate of length $L_x = 2002.1\delta_0^*$, with $\delta_0^* = 3.2656 \times 10^{-4}$ m the compressible displacement thickness at the inlet of the domain (defined as $\delta_0^* = \int_0^{\infty} (1 - \frac{\rho u}{\rho_{\infty} u_{\infty}}) dy$), which results in $Re_{\delta_0^*} = \frac{\rho_{\infty} U_{\infty} \delta_0^*}{\mu_{\infty}} \simeq 2121$.

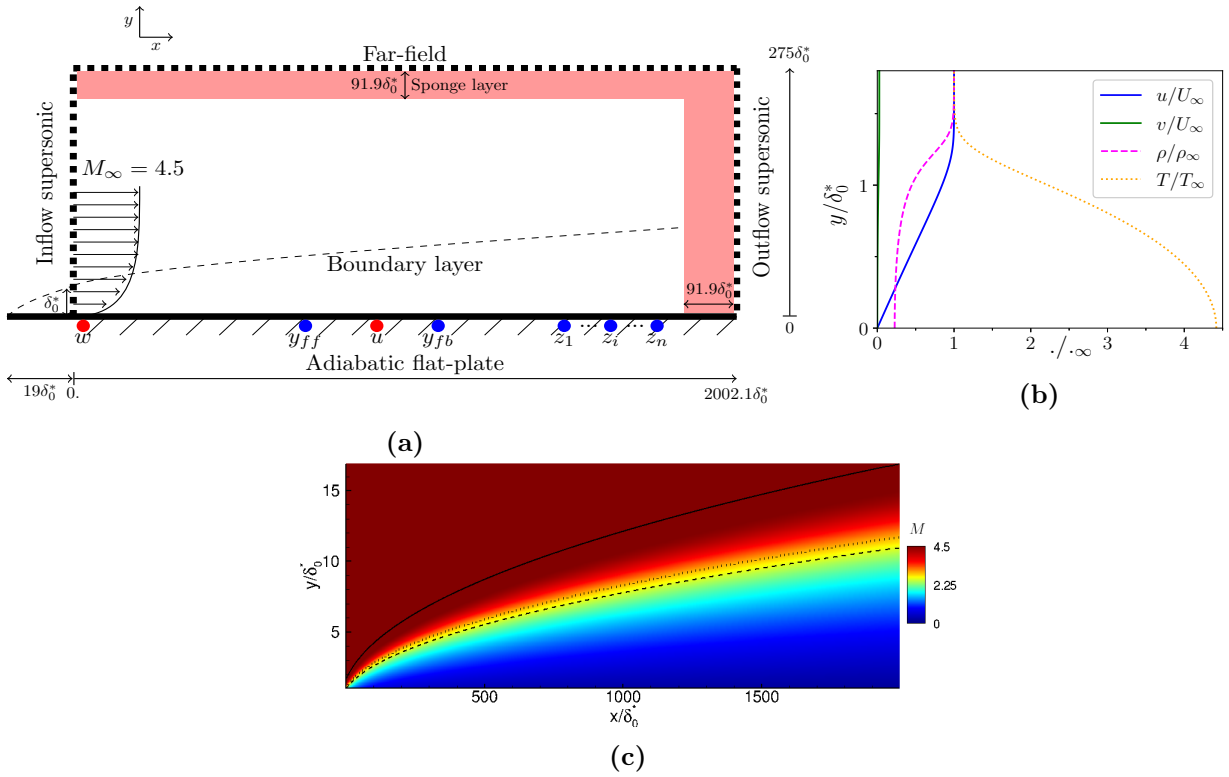


Figure 4.1: (a) Diagram of the computational domain. Inputs and outputs of the control problem are in red and blue, respectively. (b) Boundary layer profile used for the inlet condition. (c) Mach number field of the laminar base flow. Solid, dotted and dashed lines represent the boundary layer thickness δ , the generalized inflection point y_g and the compressible displacement thickness δ^* , respectively.

A far-field and a supersonic exit conditions are respectively applied at the top ($y = 275\delta_0^*$) and at the outlet of the computational domain. Furthermore, a sponge zone is used downstream and in the upper part of the domain to minimize reflections. This sponge zone has a length of $L_{\text{sponge}} = 91.9\delta_0^*$ in both streamwise and wall-normal directions; it consists in adding a source term in (1.1) on the last 10 cells closest to the boundaries to bring the flow back to its equilibrium point. In addition, the mesh is stretched in the longitudinal direction for the downstream boundary (30 cells in the streamwise direction). The source term of the sponge zone and the impact of the sponge zone on the flow are discussed in appendix C. A supersonic inlet condition is imposed at the upstream boundary where the complete state is prescribed and matches a zero-pressure gradient laminar boundary layer profile (see figure 4.1b) computed

with the ONERA boundary layer code CLICET (see section 3.1.6). It corresponds to a profile taken at a distance of $19\delta_0^*$ from the leading edge. The beginning of the numerical domain has been chosen to be in a stable area for all frequencies according to local linear stability theory (see section 4.2). The boundary layer thickness (denoted δ) at the end of the domain of interest leads to $Re_\delta \simeq 35081$. Overall, the useful numerical domain (i.e. excluding the length of the sponge zone) extends from $4 \times 10^4 < Re_x = \frac{\rho_\infty U_\infty x}{\mu_\infty} < 4.1 \times 10^6$.

DNS are performed using the finite volume code *elsA*. A resolution of 3200×220 cells for the useful domain is chosen. The mesh is uniform in the x direction while a geometric law is used in the y direction to resolve strong gradients near the wall. The spatial and temporal schemes used for the base flow and 2D unsteady simulations have been given and validated on the configuration of Ma and Zhong [109] (which is close to the one of the figure 4.1a) in section 3.1. The Mach number field for the laminar base flow is represented in figure 4.1c.

4.2 Noise-amplifier behaviour

For purposes of controlling instabilities, the noise-amplifier behaviour of our configuration is characterized by local and global analysis, which allows to define appropriate closed-loop specifications and help in choosing the placement of sensors/actuator.

4.2.1 Local stability results

The in-house LLST code described and validated in section 3.1.3 is employed with the adiabatic boundary condition. The local spatial stability diagram of spanwise-invariant perturbations is displayed in figure 4.2a, with $F = 2\pi f\delta_0^*/U_\infty$ the dimensionless frequency. It is characterized by two distinct instability regions (i.e. where the spatial growth rate is positive $-\alpha_i > 0$): one for the first Mack mode and one for the second Mack mode. For each mode, the instability domain (depicted by the red solid line) for a given frequency is located between branch I (convectively stable/unstable boundary) and branch II (convectively unstable/stable boundary). Each frequency is therefore amplified only on a certain portion of the domain: high-frequencies are amplified upstream while low-frequencies are found further downstream. Compared to the first mode, the unstable frequencies of the second mode are higher and are associated with higher growth rates. Transition to turbulence is often predicted from LLST using the N -factor (see equation 1.8). The N -factors for different frequencies are represented in figure 4.2b. Although the instability range of the first Mack mode is larger, the N -factors of the second mode are greater all along the domain due to their higher growth rates. Transition is often assumed to occur when the quantity $\tilde{N}(x) = \max_{\omega} N(\omega, x)$ (red solid lines in figures 4.2(b,c)) reaches at the position x_t a threshold value N_t (dashed lines in figures 4.2(b,c), arbitrarily placed for the explanation). Thus, in order to delay transition to turbulence, when $x > x_t$, a control action should transform the quantity \tilde{N} obtained without control into the quantity \tilde{N}^c (blue line in figure 4.2c) with control, such that $\tilde{N}^c < N_t$ as long as possible (see figure 4.2c). The dominant frequency being different at each streamwise location of the domain, a large frequency range needs to be controlled, which complicates the design of the control law. The $\tilde{N}^c < N_t$ criterion could be directly translated into a H_∞ criterion, because this would mean that the maximum amplification over the entire frequency spectrum must not exceed a threshold over the entire domain, exactly as in the N -factor method. However, this method may be considered conservative as it is based on the worst perturbation, which is purely harmonic and therefore not quite realistic [110]. Fedorov and Tumin [57] recommended to use a criterion based on both the N -factors and the entire frequency spectrum of the incoming disturbance

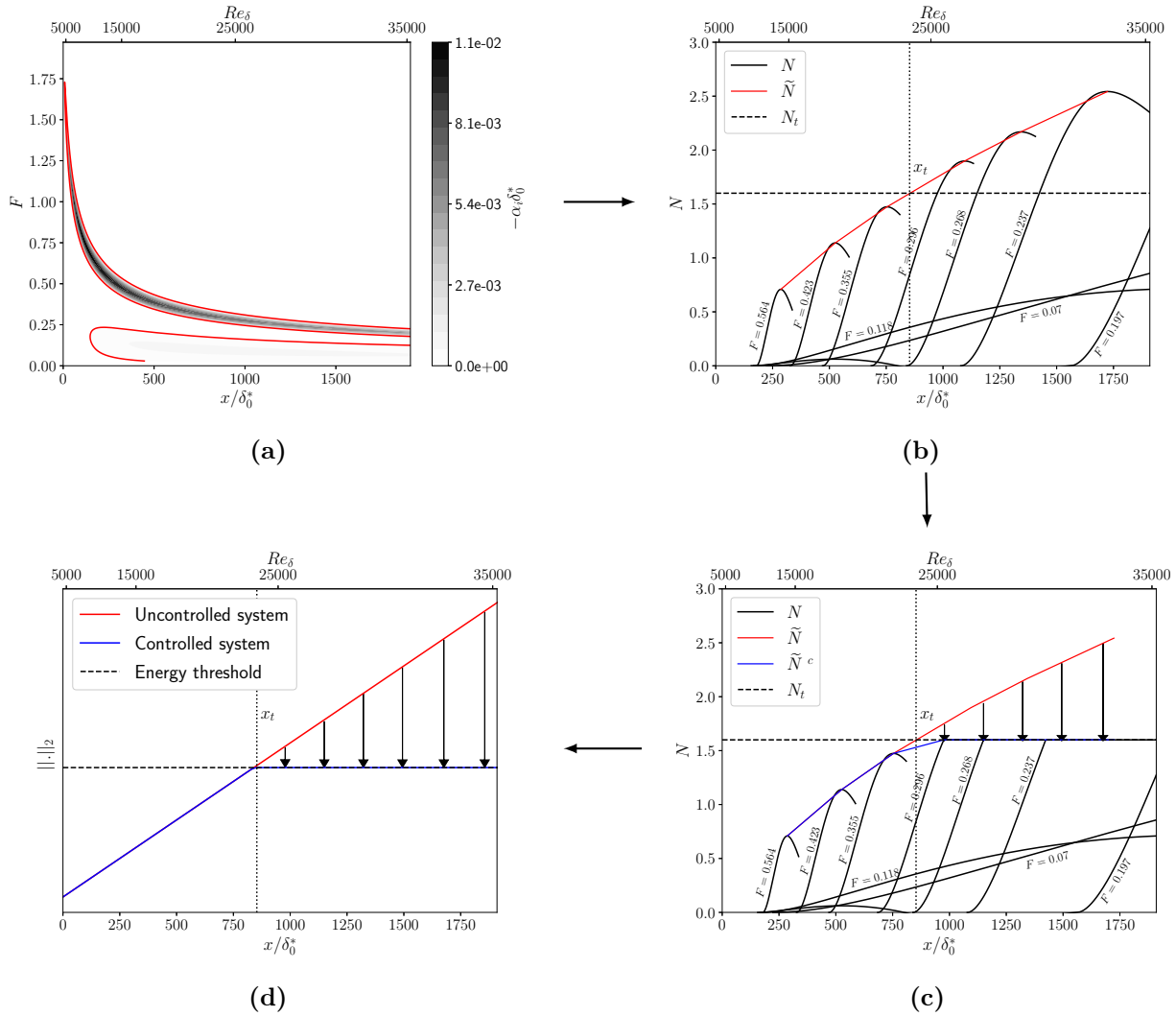


Figure 4.2: (a) Stability diagram; red solid lines represent isolines $\alpha_i = 0$. (b) Calculation of the N -factors (black solid lines) for transition prediction based on LLST: transition occurs at x_t when $\tilde{N} > N_t$ (notional diagram). (c) Performance objective for closed-loop control based on the N -factor criterion. (d) Modification of the N -factor criterion using the H_2 norm, in order to reduce conservatism. The quantity $F = 2\pi f \delta_0^*/U_\infty$ represents the dimensionless frequency.

$|\phi|_c$, which amounts to considering an H_2 norm rather than an H_∞ norm. We follow this recommendation and choose a performance objective based on an H_2 norm and which represents the r.m.s of the perturbations when excited by white noise. More precisely, our objective will be to maintain the spatially-integrated amplification below a given threshold along the plate, and this integrated amplification will be quantified using an H_2 norm (see figure 4.2d).

4.2.2 Global stability results

For the purpose of controlling instabilities, the choice of the type and position of the actuator/sensors will play an essential role. This choice is guided by resolvent analysis, which characterizes the noise-amplifier behaviour from an input-output viewpoint. In this study, the domains involved in the definition of $\|\cdot\|_E^2$ and $\|\cdot\|_F^2$ is restricted to $x \in [0; 1910.2\delta_0^*]$ and $y \in [0; 92\delta_0^*]$. The optimisation is realized with an inner product matrix $\|\tilde{\mathbf{q}}\|_E^2 = \tilde{\mathbf{q}}^* \mathbf{Q}_e \tilde{\mathbf{q}}$ corresponding to the Chu's energy (see section 3.1.4).

The optimal energy gain \tilde{g} as a function of the forcing frequency F is represented in figure

4.3a. This curve displays two peaks at $F \approx 0.118$ and $F \approx 0.237$, which correspond respectively to the first and second Mack modes identified in LLST. Global resolvent analyses are consistent with those of the local approach, since the optimal energy gain is closely related to N -factors [17, 177].

For the frequency $F = 0.237$ leading to the highest gain, the real parts of the streamwise optimal forcing and velocity response are shown in figures 4.3(b,c). The spatial structure of the forcing is located upstream of the domain while that of the response is located further downstream. This separation of the spatial supports, related to the convective-type non-normality of the Jacobian operator, implies a time-delay between actuation upstream and sensing downstream, making the design of a robust control law even more complex. Figure 4.3d shows that the peak of the forcing density $d_{e_f}(x) = \int_0^{y=92\delta_0^*} \|\tilde{\mathbf{f}}\|^2 dy$ (resp. Chu's energy density $d_{e_{\text{Chu}}}(x) = \int_0^{y=92\delta_0^*} e_{\text{Chu}} dy$) is not very far from the position of branch I (resp. II) from LLST [177]. The energy of the response is dominated at each abscissa by the thermodynamic quantities $e_{T'}$ and $e_{\rho'}$, while quantity $e_{u'}$ has a smaller contribution. Note that the most amplified frequencies depend on the extent of the domain used in the optimisation problem (not shown here): the longer the domain, the lower the dominant frequency. The gain of the frequencies that already reach their peak of forcing density and Chu's energy density (linked to the position of branch I and II, respectively) does not vary with an increase of the domain size in the streamwise direction as these frequencies can no longer be amplified. For all the other frequencies (that are lower), the phenomenon of amplification continues, leading to higher gains for a wider area.

A comparison between the spatial amplification rates $-\alpha_i$ from LLST (red dashed line) and $-\tilde{\alpha}_i = \frac{1}{|\tilde{u}(x,y=1.7\delta_0^*)|} \partial_x |\tilde{u}(x,y=1.7\delta_0^*)|$ from resolvent analysis (black dashed line) is depicted in figure 4.3e. The quantity $-\tilde{\alpha}_i$ represents the slope of $\ln |\tilde{u}|$ with respect to x (black solid line) and can therefore be compared to a growth rate. The growth of the resolvent mode within $x \in [0; 1078\delta_0^*]$ is due to the optimal forcing that is non-zero in this region (see figure 4.3d) and that induces the response. The inclined pattern in the forcing field (see figure 4.3b) indicates that the response also takes advantage of the Orr mechanism [134] and more generally of non-modal local interactions. After this initial growth region induced by the forcing, both $-\alpha_i$ and $-\tilde{\alpha}_i$ exhibit similar values in the region between $x \in [1200\delta_0^*; 1730\delta_0^*]$, which indicates that transient growth is then dominated by the convective instability associated with the second Mack mode.

To maximize the amplification of the second Mack mode, the forcing field (see figures 4.3(b,f)) must be localised near the generalised inflection point y_g (denoted in figures 4.3(b,c,f,g) with a dashed line). A region of supersonic instabilities (below the dashed-dotted line in figures 4.3(b,c,f,g)), where $\widehat{M} = \frac{|\bar{u} - \frac{\omega}{\alpha_r}|}{\sqrt{\gamma r \bar{T}}} > 1$ with $\tilde{\alpha}_r$ the global resolvent streamwise wavenumber computed as $\tilde{\alpha}_r = \partial_x \arg(\tilde{u})$ where \arg stands for the argument of a complex number [see 17], is detected close to the wall (see figure 4.3c). This confirms that the optimal response mode at $F = 0.237$ corresponds to a second Mack mode (see section 1.4.2). Note that the critical layer, where $\bar{u} = \frac{\omega}{\alpha_r}$, is not shown here as it is similar to the generalised inflection point; indeed, the phase velocity of an inflectional neutral wave in the LLST is equal to the mean velocity at y_g [111].

Finally, we observe in figure 4.3g that the different components of the second Mack mode peak at different locations in the wall-normal direction y . Hydrodynamic perturbations (velocity and pressure) peak close to the wall and seem trapped in the region $\widehat{M} > 1$ whereas thermodynamic quantities (density and temperature) peak near the generalised inflection point. This observation is in complete agreement with the qualitative results of Bugeat et al. [24].

As the second Mack mode largely dominates the first one in terms of optimal energy gain,

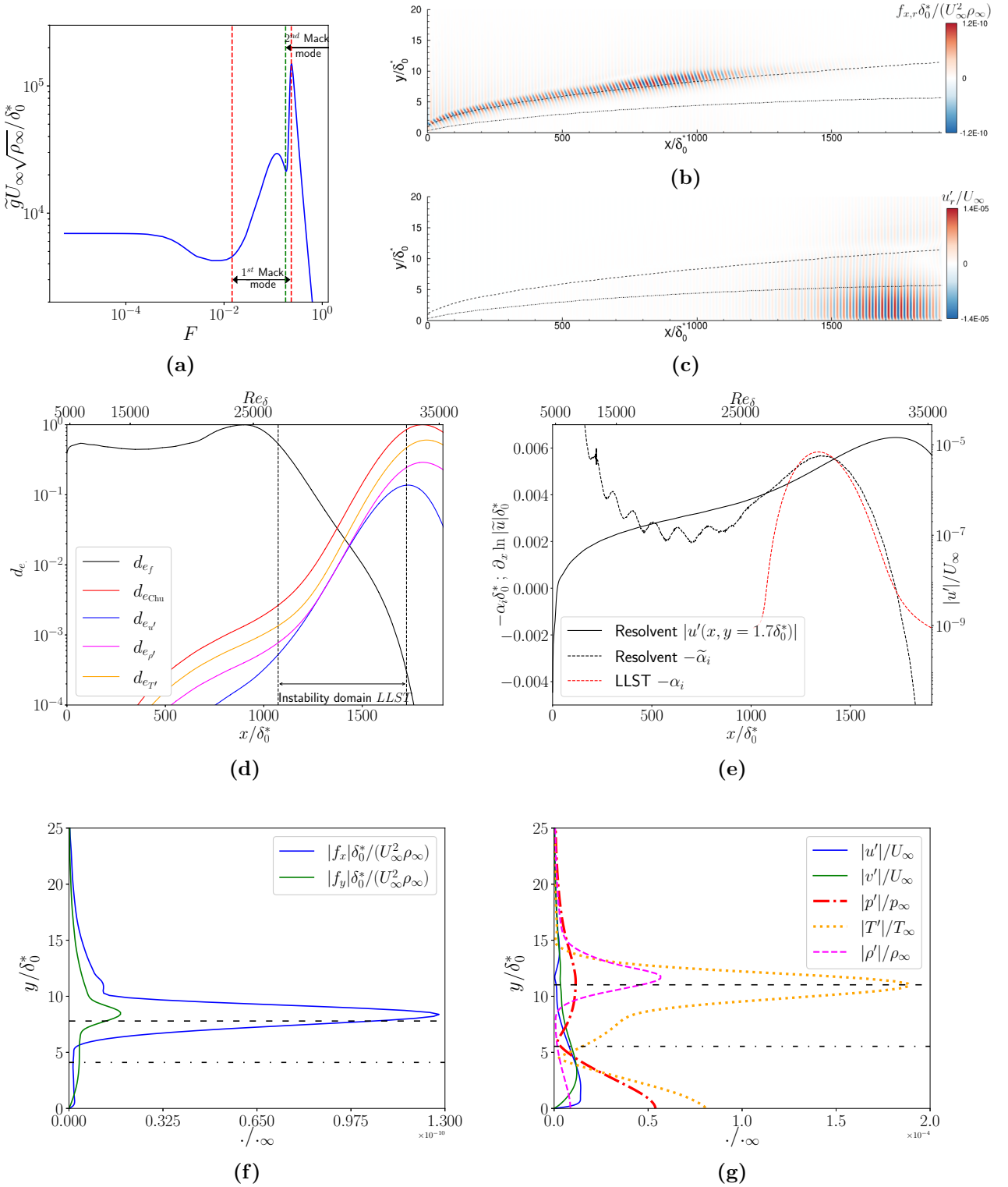


Figure 4.3: (a) Optimal resolvent gain as a function of the dimensionless frequency F . According to LLST, red and green dashed areas represent the unstable frequency range of first and second Mack modes, respectively. The region where both modes are unstable corresponds to an area where the first mode is unstable over a tiny distance. Real part of the streamwise component of the optimal forcing (b) and its associated streamwise velocity response (c) at $F = 0.237$. (d) Evolution at $F = 0.237$ of the forcing density and the different contributions to the Chu's energy density normalized by their maximum values. The position of the branch I and II from LLST are symbolized by vertical dashed lines. (e) Comparison of $-\alpha_i$ and $-\tilde{\alpha}_i$ at $F = 0.237$. Profiles of the optimal forcing components at $x = 867.2\delta_0^*$ (f) and response at $x = 1766.7\delta_0^*$ (g) at $F = 0.237$. The black dashed and dashed-dotted lines in (b), (c), (f) and (g) represent respectively the generalised inflection point position and the limit of the region of supersonic instabilities ($\widehat{M} > 1$ below this line).

the analysis of the frequency $F = 0.118$ corresponding to the peak of the first Mack mode is let in appendix D. Briefly, for the first Mack mode, the optimal forcing is also located at the generalized inflection point and one of the main differences compared to the second Mack mode is that the velocity field is no more trapped in the region $\widehat{M} > 1$ but takes important values near the generalized inflection point. It is also verified in this appendix D that the results (dominant frequencies, location of the optimal forcing, optimal response profiles, etc.) do not vary according to the energy norm chosen in the gain optimization and the analysis is conducted with an inner product matrix $\|\tilde{\mathbf{q}}\|_E^2 = \tilde{\mathbf{q}}^* \mathcal{Q}_e \tilde{\mathbf{q}}$ corresponding to the kinetic energy in the optimization problem.

4.3 Control setup

The control formalism and important transfer functions to be constrained for noise-amplifier flows have already been described in section 2.4 for a general purpose. The control setup of our particular 2D supersonic boundary layer configuration is detailed in this section and includes elements mentioned earlier in the literature review chapter.

The block diagram of the supersonic boundary layer system is depicted in figure 4.4. An exogenous disturbance w excites the boundary layer; the instabilities created will develop along the domain and be detected by an estimation sensor y . This measurement signal is transformed by a controller K into a control signal u which is used by the actuator to generate small-amplitude perturbations that take again advantage of the instability mechanisms to grow and to cancel the fluctuations at the downstream measurements z_i by destructive interferences (see figure 4.1a). The input/output dynamics are represented by the different transfer functions. In the absence of control, the SISO transfers $T_{yw} = y(s)/w(s)$ and $T_{z_iw} = z_i(s)/w(s)$ (with $s \in \mathbb{C}$ the Laplace variable) represent the impact of the disturbances on the sensors y and z_i , respectively. The impact of the actuator on the sensors, in the absence of disturbances, is represented by the SISO transfers $T_{yu} = y(s)/u(s)$ and $T_{z_iu} = z_i(s)/u(s)$. In a realistic setup, the transfers T_{yw} and T_{z_iw} cannot be determined as the exogenous noise w is unknown. Therefore, an artificial transfer function $T_{z_i\tilde{y}}$ is introduced; the quantity $\tilde{y} = T_{yw}w$ is the new exogenous input of the system and this leads to the modified block diagram framed by the red dotted zone in figure 4.4, where in case of actuation, the upstream measurement is: $y = \tilde{y} + T_{yu}u$ (+ n , which is a measurement noise). The artificial transfer $T_{z_i\tilde{y}}$ aims at predicting the downstream measurements z_i from the upstream measurement y in the absence of control [73]. This artificial transfer $T_{z_i\tilde{y}}$ can be obtained using uncontrolled temporal y/z_i data [126, 156]. In this study, for convenience, this artificial transfer function is computed from $T_{z_i\tilde{y}} = T_{z_iw}T_{yw}^{-1}$ as in [153, 154], using the transfers T_{z_iw} and T_{yw} which can be obtained from impulses of w instead of having to go through white noise simulations which require several convective times to converge statistics. The controlled transfer function of the new system, denoted with the superscript c , is:

$$T_{z_i\tilde{y}}^c = T_{z_i\tilde{y}} + T_{z_iu}K(1 - T_{yu}K)^{-1}, \quad (4.1)$$

with $T_{yu} = 0$ in a feedforward configuration (as the actuator in this configuration is placed sufficiently downstream of the estimation sensor y so that actuator-induced perturbations are not observable).

In the following, we will suppose that w is a white noise and we will seek to reduce the root-mean-square (r.m.s.) of the measurements z_i to white noise-input w . From a control point of view, this objective translates to reduce the H_2 norms of the controlled transfers:

$$\|W_{\tilde{y}}T_{z_i\tilde{y}}^c\|_2 = \left(\frac{1}{2\pi} \int_{-\infty}^{+\infty} |W_{\tilde{y}}T_{z_i\tilde{y}}^c|^2 d\omega \right)^{1/2}, \quad (4.2)$$

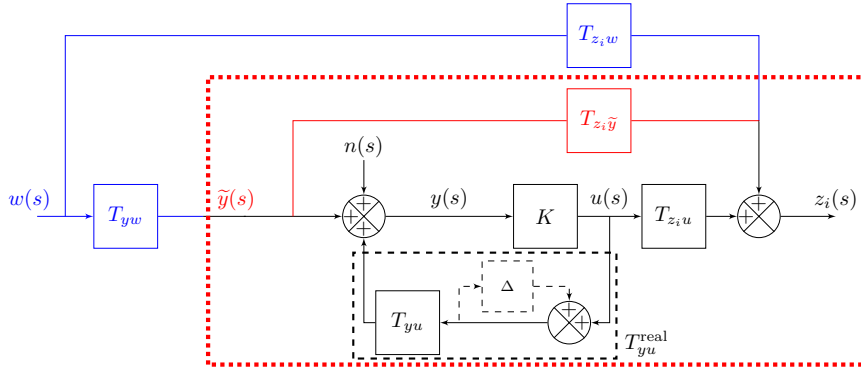


Figure 4.4: Block diagram of the supersonic boundary layer system in an ideal case (with quantities in black and blue) and in a realistic setup (with quantities in black and red). The quantities in black are shared by both the ideal and realistic setups. The red dotted zone represents the system used for the identification/synthesis step. In a feedforward configuration, $T_{yu} = \Delta = 0$.

with $W_{\tilde{y}}$ a weighting function which module corresponds to $\sqrt{PSD_y(\omega)}$ (where PSD_y is the power spectral density of the estimation sensor y in the absence of control); it represents the fact that the new system input \tilde{y} is no longer a white noise as w but a colored noise. Indeed, the ideal and realistic control schemes shown in figure 4.4 are related through:

$$\|T_{z_i w}^c\|_2 = \| |T_{yw}| T_{z_i \tilde{y}}^c \|_2. \quad (4.3)$$

with $T_{z_i w}^c = T_{z_i w} + T_{z_i u} K (1 - T_{yu} K)^{-1} T_{yw}$. By replacing $|T_{yw}|$ with $W_{\tilde{y}}$ (which can be obtained in a realistic setup), there is no loss of generality because the linear minimization problem is defined to within one amplitude. Therefore, the four quantities needed for the synthesis are $T_{z_i u}$, T_{yu} , $T_{z_i \tilde{y}}$ and $W_{\tilde{y}}$. They can all be obtained in a realistic setup as the temporal data of z_i , u and y would be available and will be the ones used for identification (see section 4.5.1) and controller synthesis (see section 4.5.2) where we will seek to reduce $\|W_{\tilde{y}} T_{z_i \tilde{y}}^c\|_2$. For the sake of clarity and to simplify notations, the quantity $\|W_{\tilde{y}} T_{z_i \tilde{y}}^c\|_2$ will be replaced in the rest of the chapter by $\|T_{z_i w}^c\|_2$.

Contrary to the feedforward setup which is unconditionally stable (as soon as K is stable), the feedback configuration may be unstable [14, 43, 180]. From a control design point of view, this implies considering uncertainty Δ representing a model error on T_{yu} that can lead to the instability of the feedback loop. For example, for the block Δ represented in figure 4.4, if no upstream noise is considered, $y = \frac{T_{yu}}{1-\Delta} u$, so that Δ represents an inverse multiplicative uncertainty on T_{yu} such that $\Delta = \frac{T_{yu}^{\text{real}} - T_{yu}}{T_{yu}^{\text{real}}}$. This type of uncertainty has the advantage of representing a relative error, which facilitates its interpretation. Since $-T_{yu}^{\text{real}} K$ does not exhibit any unstable pole (T_{yu}^{real} is stable because the supersonic boundary layer flow is globally stable while K is stable by design), the closed-loop system is stable if and only if the Nyquist plot of $-T_{yu}^{\text{real}} K$ does not encircle the critical point $(-1, 0)$, which is equivalent to $|1 - T_{yu} K| > |\Delta|$ [180]. Therefore, the stability of the closed-loop can be guaranteed by working on the sensitivity function

$$S = (1 - T_{yu} K)^{-1}. \quad (4.4)$$

By keeping $\|S\|_\infty = \sup_{\omega \in \mathbb{R}} |S(i\omega)|$ below a threshold $|\Delta|^{-1}$, the system will be guaranteed stable up to a value $|\Delta|$ of a relative model error on T_{yu} .

Finally, maintaining optimal performance despite uncertainties on a certain frequency range of the measurement y means minimizing the H_∞ norm of the transfer function

$$\frac{u}{n} = KS. \quad (4.5)$$

This allows to limit flow perturbations triggered by erratic actuator signal fluctuations due to the amplification of sensor noise by the controller.

In summary, with a view of a realistic fluidic specification, H_2 and H_∞ norms will be used to minimize/constrain certain transfers: $W_{\tilde{y}}T_{z_i\tilde{y}}^c$ which is associated with nominal performance in terms of amplitude reduction as its H_2 norm corresponds to that of $T_{z_iw}^c$, S which is associated with stability robustness and KS which is associated with performance robustness despite noisy estimation sensors. The constrained minimization problem (CMP) for our specific study will be formulated in section 4.5.2.

4.4 Control settings

The choice of the input/output of the system will be made in order to facilitate the observability and the controllability of the second Mack mode as it is the dominant mode in the noise-amplifier behaviour (see section 4.2).

4.4.1 Estimation and performance sensors

For the sensors, in order to have strong observability of the disturbances, we choose y and $z(x)$ to be wall-pressure fluctuation sensors. This choice is supported by the fact that second Mack modes exhibit strong pressure fluctuations close to the wall, as shown by the optimal response profiles in figure 4.3g. Also, that kind of sensors is commonly used in supersonic experimental studies [106]. The evolution of performance as a function of the position and the number of performance sensors z_i used in the identification/synthesis step (as well as the position of the estimation sensor y) will be assessed in section 4.6.

4.4.2 Input disturbance

The input perturbation, representing an external disturbance (acoustic noise, roughness, free-stream turbulence, etc.) is modelled by a volume forcing $w(t)\mathbf{B}_w(x, y)$ in the right-hand-side of the momentum equations (1.1b), where the noise $w(t)$ is chosen Gaussian white (with a variance sufficiently small for the perturbation to remain in the linear regime) and $\mathbf{B}_w(x, y)$ is divergence-free and compact in space [10, 14, 168]:

$$\mathbf{B}_w = \mathbf{h} \left(\frac{10.66}{\delta_0^{*2}}, 4.1\delta_0^*, \delta_0^*, 1.5\delta_0^*, 0.15\delta_0^* \right), \quad (4.6)$$

with

$$\mathbf{h}(A_h, x_0, y_0, \sigma_x, \sigma_y) = A_h \begin{pmatrix} (y - y_0)\sigma_x/\sigma_y \\ -(x - x_0)\sigma_y/\sigma_x \end{pmatrix} \exp^{-\left(\frac{x-x_0}{\sigma_x}\right)^2 - \left(\frac{y-y_0}{\sigma_y}\right)^2}. \quad (4.7)$$

It is centred near the generalised inflection point in the wall-normal direction in order to maximize the receptivity process by exciting the optimal mechanisms of the second Mack mode (and also those of the first one), as shown by the resolvent analysis results in section 4.2.2. The position of \mathbf{B}_w in the streamwise direction is upstream of branch I (locally stable regions) for all frequencies according to the LLST. As shown in figure 4.5, the lines of force of such a noise source form a vortex. The evolution of the velocity wavepacket generated by an impulse of the exogenous noise w is depicted in figure 4.6. This velocity wavepacket is convected downstream and takes its most important value near the wall and below the generalized inflection point (black dashed line), which means a predominance of the second Mack mode over the first Mack mode (see section 4.2.2). As the disturbance propagates downstream at a group velocity of

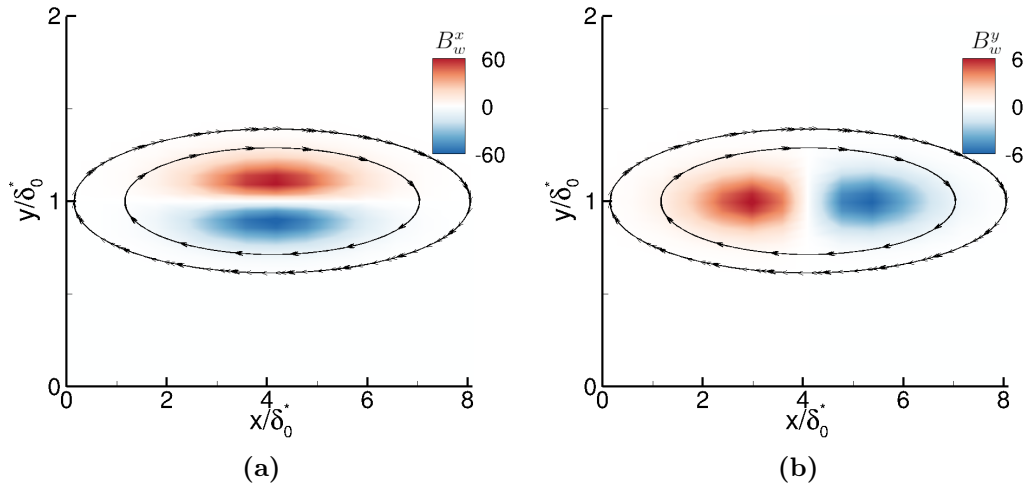


Figure 4.5: Contour plot of (a) the streamwise and (b) wall-normal components of \mathbf{B}_w with streamlines in black.

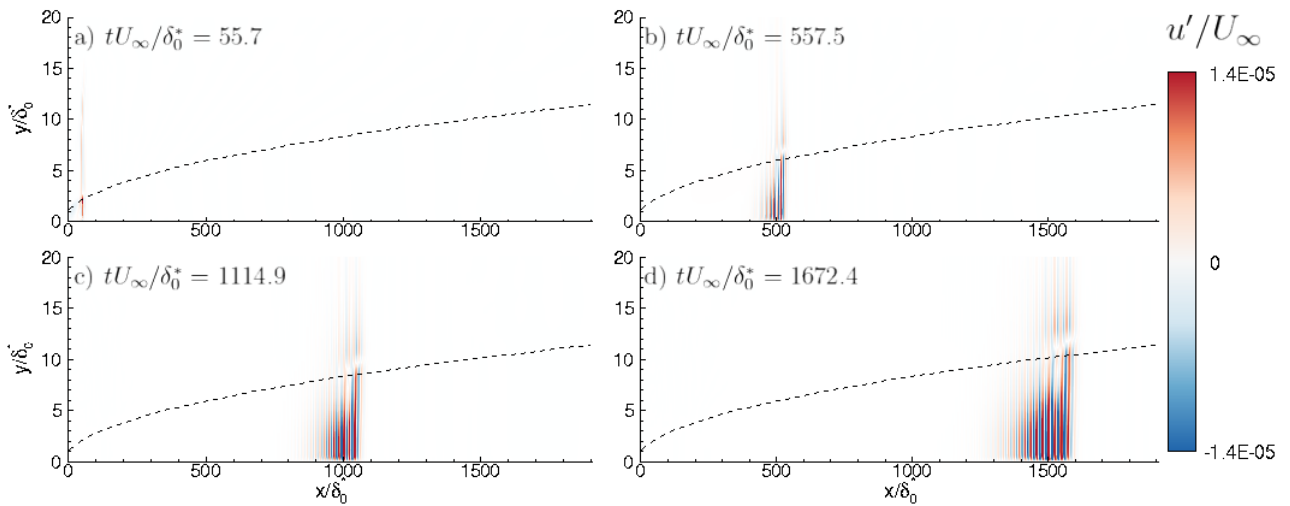


Figure 4.6: Velocity wavepacket generated by an impulse triggered at $t = 0$ of the exogenous input w at times $tU_\infty/\delta_0^* = 55.7, 557.5, 1114.9, 1672.4$. The black dashed line represents the generalized inflection point position y_g .

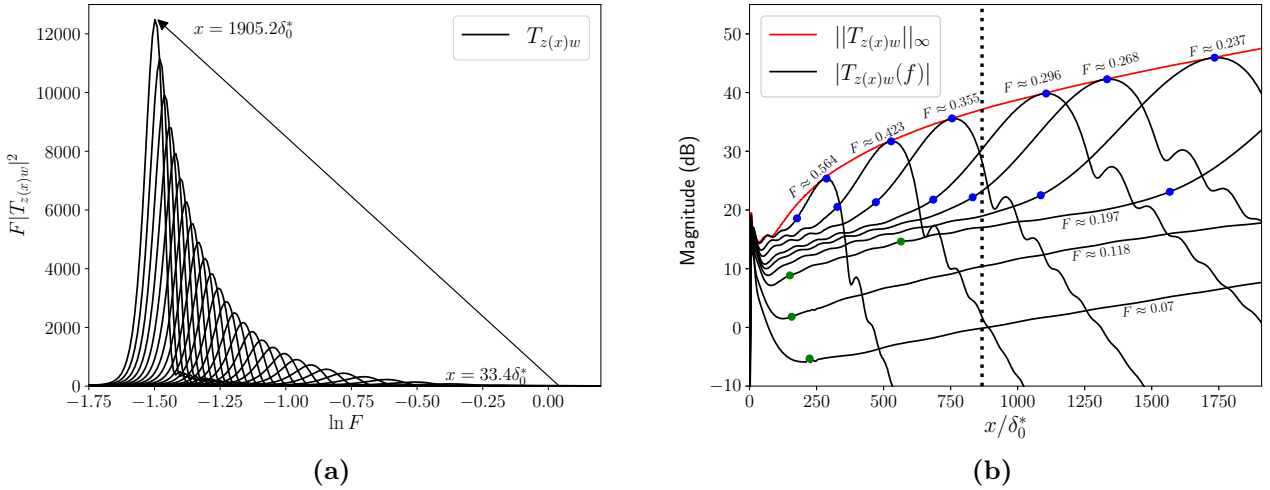


Figure 4.7: (a) Evolution of $F|T_{z(x)w}|^2$. (b) Variation of the frequency magnitude as a function of the plate abscissa. For each frequency, the green (resp. blue) dots represent branch I and branch II of the first (resp. second) Mack modes according to LLST. The vertical dotted line in (b) shows the streamwise location of the actuator \mathbf{B}_u (see section 4.4.3), denoted x_u .

approximately $0.92U_\infty$, the wave grows in amplitude and spreads in the streamwise direction, the boundary layer being a dispersive system.

In figure 4.7a, the quantity $F|T_{z(x)w}|^2$ is represented as a function of $\ln F$, where F is the frequency, such that the integral of this quantity is proportional to the square of $\|T_{z(x)w}\|_2$ (quantity that we seek to minimize). The module of $|T_{z(x)w}|$ is obtained by Fourier transform of the signals from an impulse response. At each abscissa x of the plate, the energy contribution to the sensor $z(x)$ is only due to a certain frequency range. Indeed, after reaching a peak, the magnitude associated with a frequency rapidly decreases, as can be seen in figure 4.7b. Therefore, for control, several performance sensors z_i are needed in the synthesis to obtain a suitable frequential representation at different streamwise positions and capture the entire amplified bandwidth. As the spectrum of $F|T_{z(x)w}|^2$ is narrow (especially downstream of the domain), reducing $\|T_{z_i w}^c\|_2$ should also lead to a significant reduction in $\|T_{z_i w}^c\|_\infty$. Sufficiently far downstream from \mathbf{B}_w , the most amplified frequency at each abscissa of the domain (red line in figure 4.7b) is similar to the one that could be found with the N -factors (see figure 4.2b). As the magnitude of the perturbations increases for all frequencies in spatially stable regions upstream of branch I (see first dot symbols in figure 4.7b), the perturbations seem to be subject first to a growth due to the non-modal Orr mechanism, before being dominated by the "modal" growth of the unstable Mack mode. The highest value of $|T_{z(x)w}|$ is found at the end of the domain of interest, at a frequency of $F = 0.223$, close to the frequency leading to the highest gain in the global resolvent analysis ($F = 0.237$). Therefore, the optimal response mechanisms already observed in section 4.2 are well triggered by the chosen disturbance \mathbf{B}_w , which is therefore representative of a more general transition scenario due to the second Mack mode.

4.4.3 Actuator

The control goal is to create a destructive interference by generating a second wave of appropriate amplitude and phase, which will oppose the one generated by the upstream noise $w(t)$ [73, 153]. Thus, in order to maximize the impact of control, the perturbations generated by

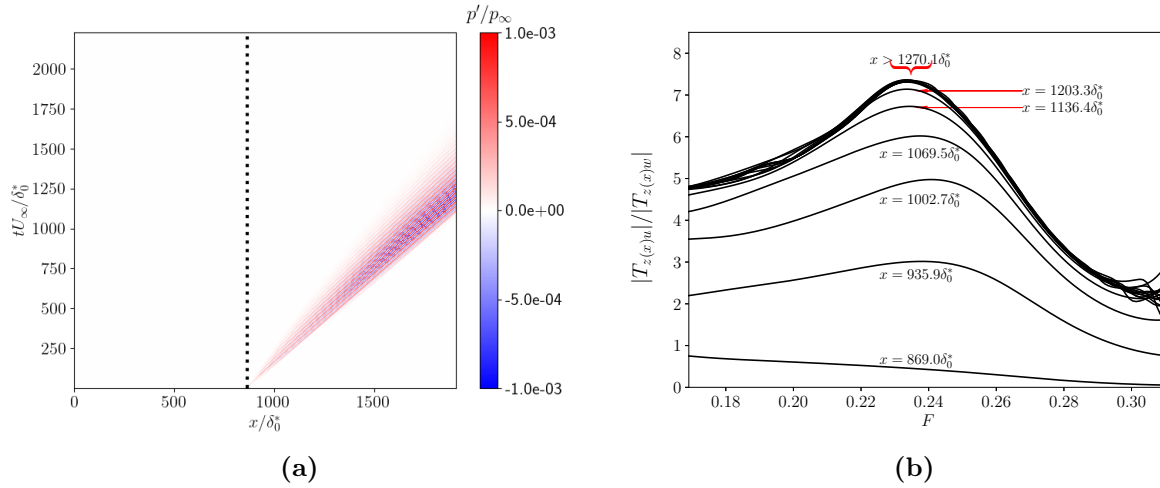


Figure 4.8: (a) Spatio-temporal response of wall-pressure fluctuation sensors after an impulse of u . The vertical dotted line shows the streamwise location of the actuator \mathbf{B}_u , denoted x_u . (b) Evolution of the ratio $|T_{z(x)u}|/|T_{z(x)w}|$ as a function of frequency F for several plate abscissa.

the actuator must match those induced by the upstream noise source. The incoming disturbance being mainly due to second Mack mode instabilities, an efficient actuator can be obtained with a volume forcing around the generalised inflection point in the wall-normal direction. This wall-normal actuator location is potentially far from a real experiment implementation but the modelling of a realistic actuator is beyond the scope of the study. We just select this wall-normal position to ease the control of the instabilities by maximizing the receptivity process. We therefore consider $\mathbf{B}_u u(t)$ in the right-hand-side of equations (1.1b) to model the actuator, with the same divergence free spatial support as for the disturbance \mathbf{B}_w :

$$\mathbf{B}_u = \mathbf{h} \left(\frac{10.66}{\delta_0^{*2}}, 867.2\delta_0^*, 7.79\delta_0^*, 1.5\delta_0^*, 0.5\delta_0^* \right). \quad (4.8)$$

The actuator is placed sufficiently far downstream of \mathbf{B}_w ($x_u = 867.2\delta_0^*$) for two reasons. The first one is to allow disturbances to strengthen sufficiently to be easily detected by the estimation sensor y (which is close to the actuator), which in an experimental configuration would mean placing the actuator a little upstream of the beginning of the transition process. The second reason is to limit the bandwidth of the frequencies to be controlled (see figure 4.7b) in order to keep the complexity of the control problem reasonable. Hence, for the chosen streamwise position of the actuator, the frequency range to be controlled is around $F \in [0.225, 0.324]$; a more upstream actuator should have controlled a wider bandwidth. The streamwise position of the actuator remains sufficiently upstream so that incoming perturbations are controlled over a sufficiently long domain (~ 0.34 m) representative of an experimental configuration (the plate of the experimental tests of Kendall [84] measured 0.35 m).

The evolution of the wall-pressure wavepacket generated by an impulse of u is depicted in figure 4.8a. A comparison of $|T_{z(x)w}|$ and $|T_{z(x)u}|$ is shown in figure 4.8b. It can be noted that in the vicinity of the actuator, the ratio $|T_{z(x)u}|/|T_{z(x)w}|$ evolves with the x abscissa. As this phenomenon no longer appears for abscissas further away from the actuator and the ratio becomes constant, it could be attributed to a non-modal transient behaviour. Indeed, we have:

$$\frac{|T_{z(x)u}|}{|T_{z(x)w}|} \propto \frac{e^{\int_{x_u}^x -(\tilde{\alpha}_i)_u dx}}{e^{\int_{x_u}^x -(\tilde{\alpha}_i)_w dx}}, \quad (4.9)$$

where $-(\tilde{\alpha}_i)_u$ and $-(\tilde{\alpha}_i)_w$ represent the slope of $\ln |T_{z(x)u}|$ and $\ln |T_{z(x)w}|$ with respect to x , respectively. Therefore, a constant ratio implies having the same slope from a certain distance

x . This distance x represents the non-modal distance due to the receptivity of multiple modes to the volume forcing of the actuator on the flow. This non-modal distance is associated with a

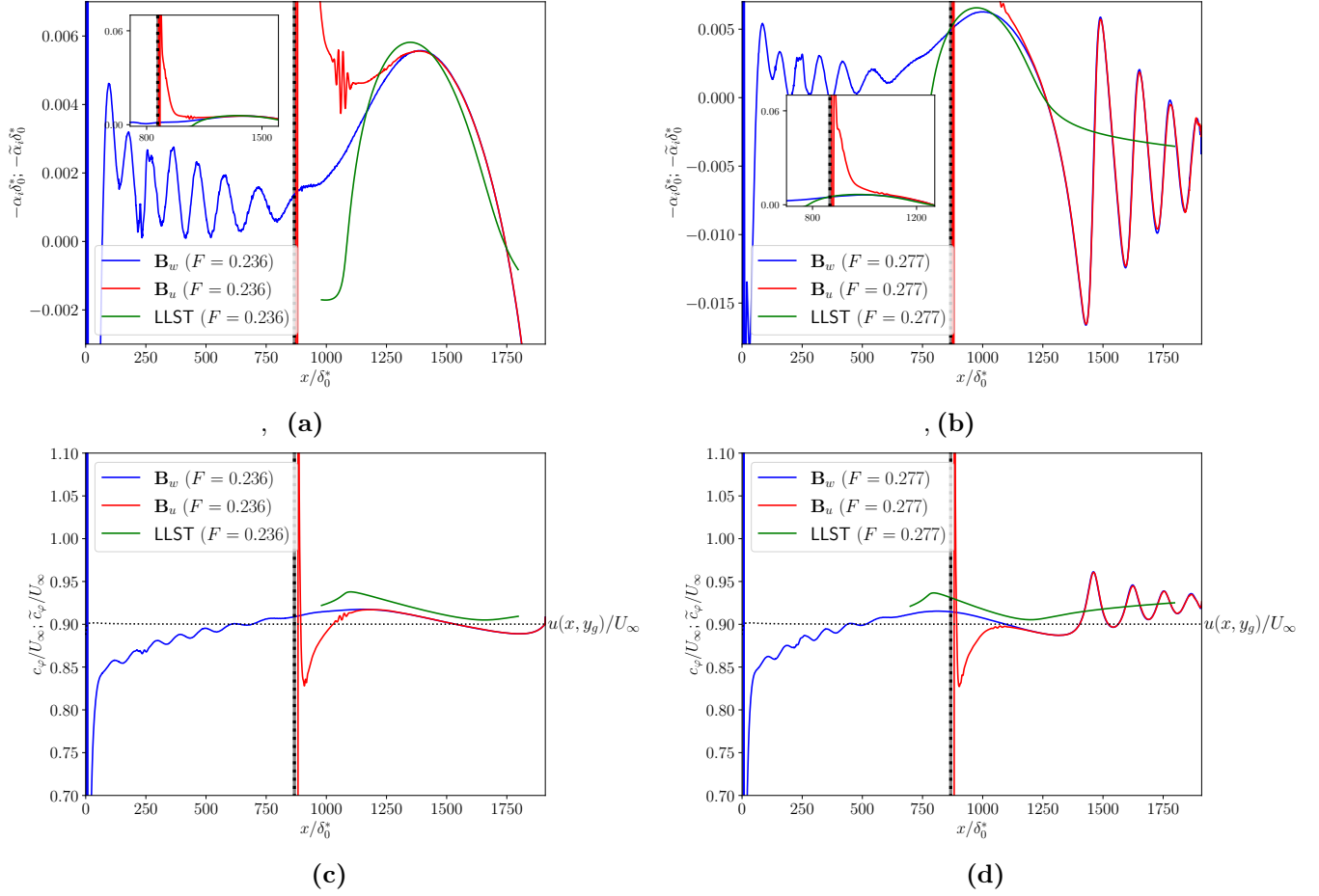


Figure 4.9: Comparison of (a,b) $-\alpha_i$ and $-\tilde{\alpha}_i$ and (c,d) c_φ and \tilde{c}_φ at (a,c) $F = 0.236$ and (b,d) $F = 0.277$. The vertical dotted line shows the position of the initial disturbance \mathbf{B}_u in the streamwise direction. The horizontal dashed line $u(x, y_g)/U_\infty$ represents the velocity at the generalised inflection point along the flat plate.

transient growth (in the local sense), as seen on the non-modal growth rate $-\tilde{\alpha}_i = \partial_x \ln |T_z(x)|$ (see figures 4.9a, 4.9b). Regarding the growth rates $-\tilde{\alpha}_i$ induced by an impulse of the actuator (red lines), the values of $-\tilde{\alpha}_i$ from w (blue lines) are only found far from the streamwise actuator position x_u (vertical dotted lines); the vicinity of the actuator appears to be subject to an important transient spatial growth, attributed to the Orr mechanism. The convective-type non normality effects dominate only in the region where the behaviour of $-\tilde{\alpha}_i$ is similar to the one we could obtain by LLST for a dominant unstable mode (green lines). For the frequency $F = 0.277$, shortly after crossing the branch II, $-\tilde{\alpha}_i$ starts to oscillate and causes the wave packet to grow again at certain locations. This behavior is similar to that noted by [109] and is attributed to the fact that the second Mack mode no longer dominates, there is a modulation between this Mack mode and other modes. Regarding the non-modal phase velocity $\tilde{c}_\varphi = \frac{\omega}{\tilde{\alpha}_r}$ (with $\tilde{\alpha}_r = \partial_x \arg(T_z(x))$) (see figures 4.9c, 4.9d), a transient behaviour is also observed: the phase velocities of the waves generated by w and u are only equal far from the actuator position. In the modal growth region, \tilde{c}_φ fluctuates around a value equal to the base flow velocity at the generalised inflection point (horizontal dashed line), recalling the fact that the phase velocity of an inflectional neutral wave in the LLST is equal to the mean velocity at y_g [111]. In this region, the behaviour of c_φ computed with LLST is similar to that of the

non-modal \tilde{c}_φ ; the difference in the value of the phase velocity between LLST and DNS in this zone is about 2%. For the frequency $F = 0.277$, after crossing the branch II, \tilde{c}_φ generated by w and u oscillates, following the example of non-modal $-\tilde{\alpha}_i$.

4.5 Identification and synthesis methods

As explained in section 4.4.1, it was found by numerical simulations that performance depends of the position and number of y/z_i sensors. Nevertheless, for the sake of clarity and to ease the understanding of the identification and synthesis section, the streamwise positions of the estimation and performance sensors to achieve the best results in terms of perturbation amplitude reduction along all the domain are given in table 4.1; six probes z_i are required to achieve nearly uniform performance along the domain. The streamwise positions of the input perturbation and the actuator are also summarized in this table.

| | B_w | B_u | y | z_i |
|---------------------|-----------------------|-------------------------|----------------------------|--------------------------|
| | | | | $x_1 = 933.2\delta_0^*$ |
| | | | | $x_2 = 1029.4\delta_0^*$ |
| Streamwise position | $x_w = 4.1\delta_0^*$ | $x_u = 867.2\delta_0^*$ | $x_{ff} = 801.2\delta_0^*$ | $x_3 = 1125.6\delta_0^*$ |
| | | | $x_{fb} = 885.7\delta_0^*$ | $x_4 = 1317.9\delta_0^*$ |
| | | | | $x_5 = 1510.2\delta_0^*$ |
| | | | | $x_6 = 1766.7\delta_0^*$ |

Table 4.1: Streamwise positions of the input perturbation, the actuator and the sensors used for the identification and synthesis steps. The position of the estimation sensor for feedforward and feedback configurations are denoted x_{ff} and x_{fb} , respectively, and are the ones allowing the best results in terms of perturbation amplitude reduction.

4.5.1 ROMs

Most synthesis methods require the use of state-space ROMs corresponding to the transfers involved in the controller synthesis. For the model reduction step, some of the input/output delays linked to the convective nature of the flow may be discarded due to the fact that the H_2 norm is not modified by delays. In a feedback configuration (u, y, z_i) , the delays verify $\tau_{z_i u} = \tau_{z_i \tilde{y}} + \tau_{yu}$, so that

$$\begin{aligned} \|T_{z_i w}^c\|_2 &= \| e^{-\tau_{z_i \tilde{y}} s} W_{\tilde{y}}(T'_{z_i \tilde{y}} + e^{-\tau_{yu} s} T'_{z_i u} K S) \|_2 \\ &= \| W_{\tilde{y}}(T'_{z_i \tilde{y}} + e^{-\tau_{yu} s} T'_{z_i u} K S) \|_2, \end{aligned} \quad (4.10)$$

where $T'(s)$ designates the "dead-time-free" transfer function associated with $T(s)$. The same idea can be applied also to a feedforward design (y, u, z_i) with the result below:

$$\|T_{z_i w}^c\|_2 = \| W_{\tilde{y}}(e^{-\tau_{uy} s} T'_{z_i \tilde{y}} + T'_{z_i u} K) \|_2. \quad (4.11)$$

Thus, the only remaining delay is the one between the actuator and the estimation sensor, τ_{yu} or τ_{uy} , which is reasonably small (compared to the delays involving z_i .) Removing unnecessary delays (for example $\tau_{z_i \tilde{y}}$ in the feedback case) leads to a significant reduction in the size of the ROMs when the dead-time scale is important compared to the time scale of the physical phenomenon to be captured (the period of the second Mack mode). This reduction in the order of the ROMs is beneficial both for the identification and the synthesis step: the higher the

order, the more difficult the identification and the larger the cost of the controller synthesis. Moreover, in case of syntheses which solve Riccati equations which lead to controller of the same order as the plant (although this is not the case here thanks to the structured synthesis used), having a low-order model will avoid the need for a post-processing step to reduce the number of states of the controller to make it usable; it is therefore always beneficial to do without useless dynamics for the synthesis.

The quantities required for the synthesis are obtained by impulse responses of w and u ; impulse responses are employed for convenience instead of having to go through simulations which require several convective times to converge statistics (*e.g.* white noise simulations). The state-space ROMs associated with the transfer functions $T_{z_i u}$, $T_{y u}$ and $T_{z_i \tilde{y}}$ are obtained by the subspace identification method ERA, which requires impulse responses for each of the inputs (see section 3.2.1.1). The ERA is applied after removing (just by shifting the time axis) either $\tau_{z_i \tilde{y}}$ (in the feedback case) or $\tau_{z_i u}$ (in the feedforward case) within the impulses from y and u to z_i . The impulse responses from y to z_i are obtained by inverse Fourier transform of $T_{z_i w} T_{y w}^{-1}$, each individual transfer function being obtained by Fourier transform of an impulse from w . The sampling time for ERA is $5 \times dt$. As shown in figures 4.10(a,b,c) for the performance sensor z_6 and for the feedback estimation sensor y_{fb} , the constructed ROMs capture most of the dynamics. Note that even if the impulse responses of the flow are not easily available in an

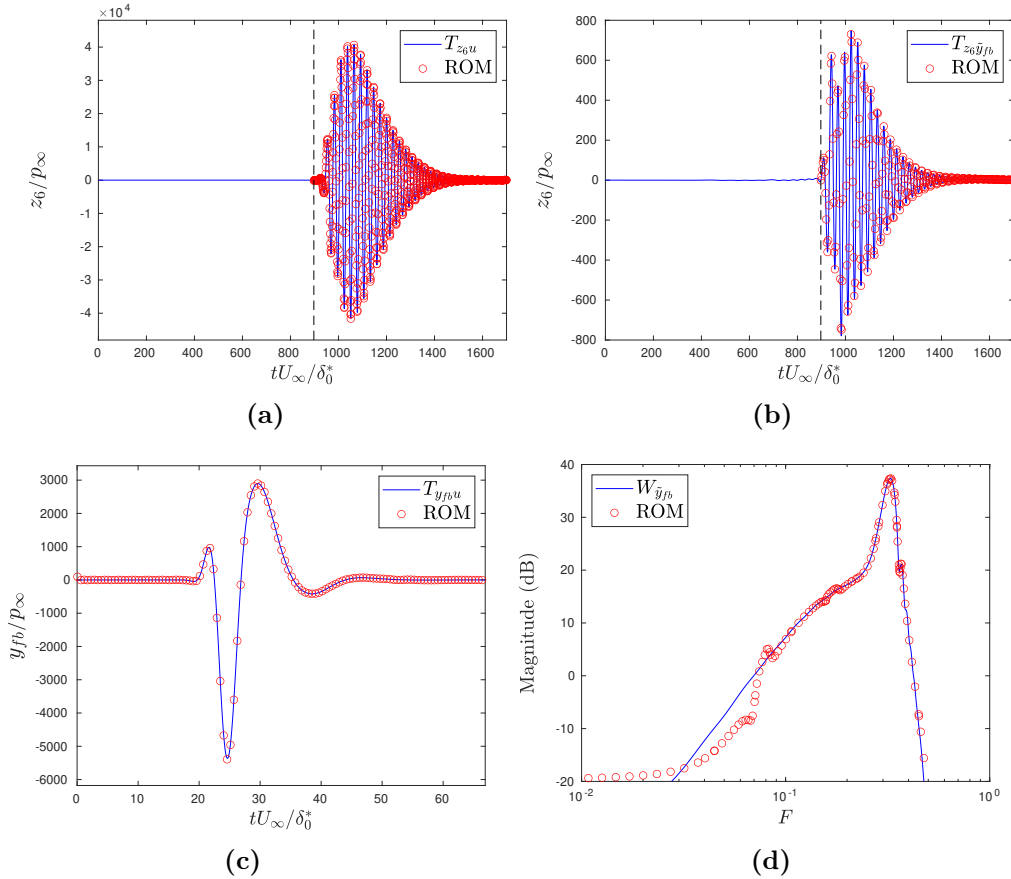


Figure 4.10: (a,b,c) Comparison between impulse responses (blue lines) and the ROMs (red circles) for the performance sensor z_6 and for the feedback estimation sensor y_{fb} . Note that for the ROMs of $T_{z_6 u}$ and $T_{z_6 \tilde{y}_{fb}}$, the time axis of the impulse responses are shifted by $\frac{\tau_{z_i \tilde{y}} U_\infty}{\delta_0^*} \simeq 897$ (black dashed lines) which corresponds to the suppression of unnecessary dead times. (d) Comparison between the quantity $W_{\tilde{y}_{fb}}$ from the linear simulation (blue line) and the ROM (red circles).

experiment, it is always possible to get them as soon as the frequency data (gain and phase)

of the quantities to be identified are available: it is sufficient to perform an inverse Fourier transform to build the impulse response in order to use the ERA for identification (as realized for $T_{z_i\tilde{y}}$) [126].

The identification of the quantity $W_{\tilde{y}}$ is obtained by a vector-fitting method designed to fit frequency response measurements (see section 3.2.1.2). For this quantity, there is no uniqueness of the identified model as the phase can vary from one model to another without impacting the results of the synthesis (see equation 4.3); the ROM just needs to be stable and causal. Hence, we simply choose to define $W_{\tilde{y}}$ such as its module fits with $\sqrt{PSD_y(\omega)}$ where y is the response from an impulse in w . A good agreement is achieved between $W_{\tilde{y}_{fb}}$ and the ROM in the case of the feedback estimation sensor y_{fb} (see figure 4.10d).

For the current application and with the six performance sensors z_i , the sum of the orders of each ROM is 130 for the case of the feedback configuration and 115 for the feedforward one. By comparison, identifying the single transfer function T_{z_6u} (corresponding to the farthest performance sensor downstream) without suppressing the dead time leads to a ROM of order 220, which is already greater than the sum of the orders of each ROM without their unnecessary dead-times.

In the control result sections 4.6.2 and 4.7, because the models are of excellent quality (see figure 4.10), the distinction between ROMs and real transfer functions is not deemed necessary and the depicted results are those on the complete system after implementation of the controllers in the CFD solver *elsA*.

4.5.2 General constrained minimization problem

Control laws are designed following a structured mixed H_2/H_∞ synthesis (see section 3.2.2). The structure of the controller K is imposed beforehand in the following way: (1) the controller K is searched in a state-space representation form; (2) the controller K must be stable; (3) we impose a tridiagonal state matrix which has significantly fewer parameters to determine than the full matrix given that any real square matrix is similar to a real tridiagonal form [120]; (4) we impose a strictly-proper controller involving a natural roll-off of the high-frequencies of -20 dB per decade in order to neglect dynamics in high-frequencies and to be robust to high-frequency noise on the estimation sensor y naturally present in every experimental setup; (5) we limit the controller order to 5. The choice of the order will be justified in section 4.6.1.

For the controller structure imposed above, the algorithm then solves the following constrained minimization problem:

$$\begin{aligned} & \text{minimize } \max_{z_i \in z_{used}} (\|T_{z_i w}^c\|_2) \\ & \text{subject to } \|W_S S\|_\infty < 1 \text{ and } \|W_{KS} K S\|_\infty < 1. \end{aligned} \quad (4.12)$$

This CMP is the transcription of the fluidic specifications established throughout the section 4.2.

Firstly, the minimization of H_2 norms of $T_{z_i w}^c$ directly allows the reduction of the expected power for the performance sensors z_i used in the synthesis (denoted z_{used}) when they are excited by white-noise perturbation w and sensed by the estimation sensor y . A multi-objective synthesis approach is necessary for our problem by minimizing the expected power of sensors at different abscissa of the flat plate instead of minimizing an overall energy. Indeed, the disturbance energy growing as it is convected downstream, an overall energy would then essentially account for the fluctuating energy downstream of the domain, leaving aside the structures further upstream in the case of a very large computational domain. Transition to turbulence appearing locally above a certain perturbation energy threshold (see section 4.2.1),

we advocate the need for minimizing the largest H_2 norm of the controlled system over the set of performance sensors z_i used to assess the local character of transition to turbulence.

Secondly, the H_∞ constraint on $W_S S$ maintains adequate stability margins. To prevent the closed-loop from being unstable in a feedback design, a frequent choice is to ensure that $\|S\|_\infty < 2$ [14, 180]. Thus, the weighting function W_S has a constant frequency template such as $W_S(s) = 0.5$ because the H_∞ constraint on $W_S S$ is equivalent to $|S| < 1/|W_S| \forall \omega \in \mathbb{R}$. This means that the system will be guaranteed stable up to 50% of relative model errors Δ on T_{yu} (see section 4.3). In the case of a feedforward design, $S(s) = 1$ (because $T_{yu} = 0$) and this H_∞ constraint is always satisfied, which explains the unconditional stability of the feedforward configuration.

Finally, the H_∞ constraint on $W_{KS} K S$ is here to desensitize the controller to new noise sources on a certain frequency range. Our controller being already robust to high-frequency uncertainties due to the strictly-proper structure imposed, W_{KS} is just designed to limit low-frequency actuator activity in case, for example, of low-frequency noise on the estimation sensor y .

By minimizing the maximum value between several transfer functions and using H_∞ norm constraints, a non-smooth optimization is performed. As non-smooth optimization is computationally intensive (compared to LQG), it is all the more important to obtain ROMs with the least possible states (see section 4.5.1). Indeed, a hundred random controller initializations are required when six z_i are used to deal with the non-convex nature of the optimization problem, giving in this case computations of several tens of minutes with a parallel computation on 12 CPU cores (Intel(R) Xeon(R) CPU E5-2650 v3 @ 2.30GHz).

4.6 Preliminary results

The performance of the controllers depends on the position of the estimation sensor y as well as the number of performance sensors z_i used in the synthesis. In order to obtain the best performance in terms of amplitude reduction along the domain, preliminary tests are performed.

4.6.1 Position of the estimation sensor

The impact of the position of the estimation sensor y has been already extensively studied in the noise-amplifier flow control literature [13, 14, 61, 81] because it plays an important role in the performance, particularly in a feedback design. For a feedback design, the estimation sensor y has to be close enough to the actuator to avoid sending outdated information and limit the effective delay impacting the maximum achievable performance (see section 2.4.4). For a feedforward design where the impact of the actuator on the estimation sensor y is assumed to be negligible in the synthesis step ($T_{yu} = 0$), the estimation sensor has to be located sufficiently upstream of the actuator for the hypothesis to be valid.

To obtain the quantitative position of the sensor y in our supersonic boundary layer study for both feedforward and feedback configurations, a quick analysis is carried out; it consists in looking at the impact of the actuator/measurement sensor distance on the maximum achievable performance in terms of H_2 norm reduction on the performance sensor z_6 regardless of the desensitization to low-frequency disturbances. We only consider the performance sensor z_6 because it is the furthest downstream of the domain; the further downstream we are, the more we have to reduce the local H_2 norm in order not to exceed a given threshold (see the principle diagram in figure 4.2d). This performance sensor therefore plays a central role and the position of the estimation sensor y must allow a consequent reduction of the energy of the sensor z_6 . Since this analysis is only done off-line on the ROMs and the resulting controller

is not implemented on the real complete system, the $\|W_{KS}KS\|_\infty$ constraint which was only useful in case of new noise sources (as noisy estimation sensor) is disabled.

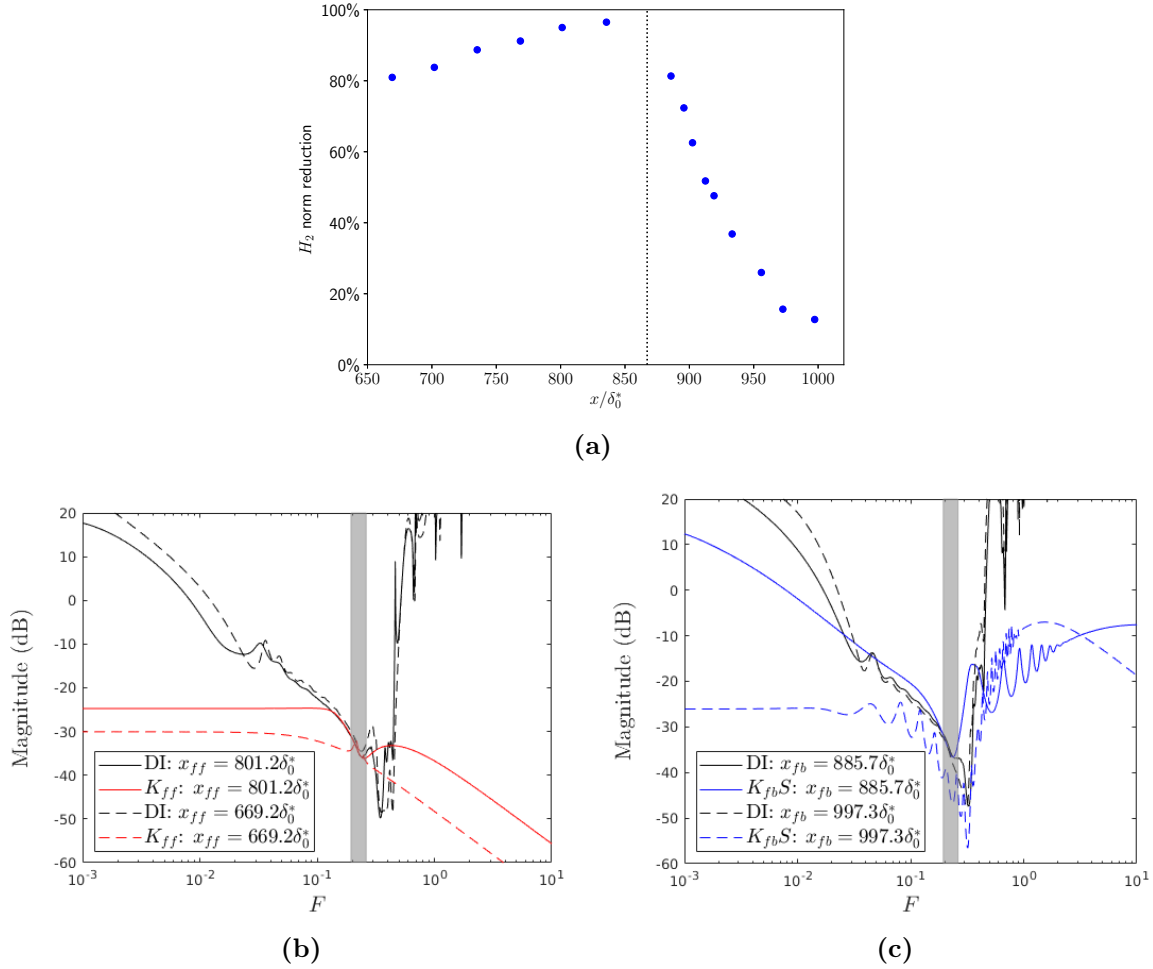


Figure 4.11: (a) Evolution of the maximum performance achievable of the ROM of the sensor z_6 as a function of the position of the measurement sensor y . The dotted line represents the actuator position; feedforward and feedback designs are respectively to the left and right of this dotted line. Comparison of the gains of the controllers from the structured synthesis and those from ideal destructive interference case (denoted ‘DI’) for (b) feedforward and (c) feedback configurations. The grey shaded area represents the range of the dominant frequencies of the sensor z_6 .

For the controller structure developed in section 4.5.2, the general CMP (4.12) is therefore written as

$$\begin{aligned} & \text{minimize } \|T_{z_6 w}^c\|_2 \\ & \text{subject to } \|W_S S\|_\infty < 1. \end{aligned} \quad (4.13)$$

Figure 4.11a shows the evolution of the maximum performance achievable of the ROM of the performance sensor z_6 as a function of the actuator/measurement sensor distance. The H_2 norm reduction represents the quantity $(\|T_{z_6 w}^c\|_2 - \|T_{z_6 w}\|_2)/\|T_{z_6 w}\|_2$. On the one hand, the actuator/measurement sensor distance influences very strongly the maximum performance achievable for feedback designs (to the right of the dotted line). On the other hand, feedforward designs (to the left of the dotted line) are relatively unaffected by this distance over a certain range and they perform better than feedback ones, which is consistent with the results of the incompressible literature [14, 61, 81]. Controllers from the structured synthesis are compared

with those which would have created perfect destructive interferences (denoted ‘DI’) on the whole frequency spectrum at x_6 (see figures 4.11(b,c)); indeed, a perfect wave cancellation at x_6 for each frequency is obtained for

$$\begin{aligned} z_6^c = 0 &= (T_{z_6\tilde{y}} + T_{z_6u}KS)\tilde{y} \\ KS &= -T_{z_6\tilde{y}}/T_{z_6u}. \end{aligned} \quad (4.14)$$

To get rid of the problems of stability and causality that occur when T_{z_6u} is directly inverted, the ratio $-T_{z_6\tilde{y}}/T_{z_6u}$ is constructed frequency-by-frequency. Hence, this ideal DI quantity just allows to evaluate how close the controllers obtained by structured synthesis are to the perfect cancellation (without taking into account feasibility, stability and robustness principles). The gain of K computed with the structured synthesis for a feedforward estimation sensor y placed at $x_{ff} = 801.2\delta_0^*$ (red solid line) overlaps the ideal DI one (black solid line) in the range of the dominant frequencies of the sensor z_6 (grey shaded area); for a feedforward estimation sensor y placed at $x_{ff} = 669.2\delta_0^*$ (red dashed line), the gain is also very similar in the area of interest to the ideal DI gain. For a feedback configuration, the closer an estimation sensor is to the actuator, the more similar the controller resulting from the structured synthesis is to the DI case in the range of the dominant frequencies of the sensor z_6 , which allows for large reduction of the H_2 norm. For a feedback sensor placed at $x_{fb} = 997.3\delta_0^*$ (blue dashed line), the resulting controller does not allow to create perfect destructive interferences, which explains the low performance obtained for this position. The rapid drop in performance in the feedback cases is largely due to the delay in T_{yu} [14], which is the time it takes for the wave generated by the actuator to reach the estimation sensor. Intuitively, to counteract efficiently disturbances of a wavelength $2\pi/\tilde{\alpha}_r$, the actuator/measurement sensor distance must be less than $2\pi/\tilde{\alpha}_r$. As a result, the frequency spectrum of the performance sensor z_6 containing a significant amount of energy up to $F \approx 0.282$ and by approximating a wavelength by $2\pi/\tilde{\alpha}_r \sim U_\infty/f$, this requires actuator/sensor distance of less than $2\pi\delta_0^*/F \sim 20\delta_0^*$ in this case. Then, to obtain significant performance in terms of amplitude reduction, it is decided to place the sensor y_{fb} for the feedback configuration at a distance of $18.5\delta_0^*$ from the streamwise position of the actuator ($x_{fb} = 885.7\delta_0^*$). For the feedforward design, the sensor y_{ff} is placed at a distance of $66\delta_0^*$ from the streamwise position of the actuator ($x_{ff} = 801.2\delta_0^*$) in such a way as to ensure that it is possible to disregard T_{yu} in the synthesis while having an optimal performance. These feedback and feedforward positions will not be modified anymore in the rest of the manuscript for the 2D configuration.

To validate the choice of a controller order of 5, the CMP equation 4.13 is solved with different controller orders. As the controllers are searched in a state-space representation form with a strictly-proper structure and a tridiagonal state matrix, the number of decision variables to be optimized for each controller is equal to $5n - 2$ (with n the order of the controller). As long as the controller order is at least 5, the H_2 norm reduction is nearly constant (see figure 4.12); some low order controllers have even slightly better performance than higher order controllers. This is due to the non-convex nature of the synthesis method (even if a hundred random controller initialization is performed); the higher the order of the controller, the higher the number of decision variables to optimize, which can greatly complicate the possibility of determining the optimal controller for the algorithm. For example, the number of decision variables increases from 23 (order 5 controller) to 198 (order 40 controller). Hence, the structured mixed H_2/H_∞ is adapted when a few decision variables need to be optimized. Note that for an order 1 controller, feedback configuration is more efficient than a feedforward configuration. To summary, as increasing the controller order to more than 5 does not bring any improvement for both feedforward and feedback designs, the structure of order 5 will be kept until the end of this chapter.

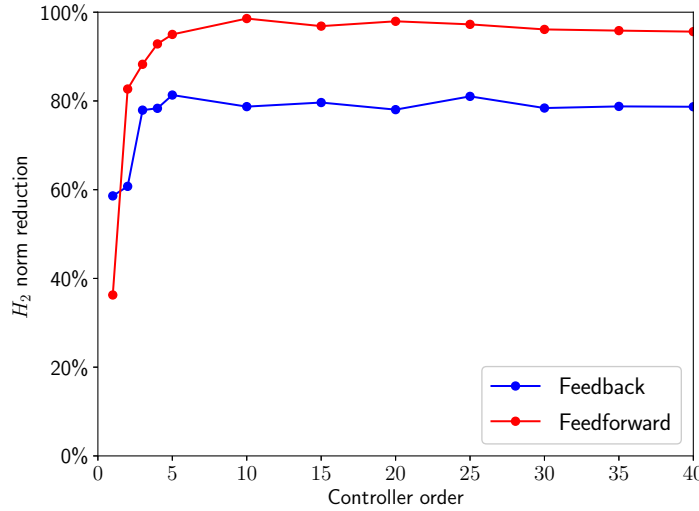


Figure 4.12: Evolution of the maximum performance achievable of the ROM of the sensor z_6 as a function of the controller order. The feedback and feedforward estimation sensors are placed at $x_{fb} = 885.7\delta_0^*$ and $x_{ff} = 801.2\delta_0^*$, respectively.

4.6.2 Evolution of performance as a function of the number of sensors z_i used in the synthesis

For the two sensor positions x_{fb} and x_{ff} determined previously, the CMP in equation 4.12 is solved. Not all the six performance sensors are necessarily used for the minimisation problem and the evolution of performance as a function of the number of sensors z_i (and by extension their positions) employed in the synthesis is assessed. The set of sensors z_i used in the synthesis is denoted z_{used} . In table 4.2, the different configurations tested are listed: the cases labelled ‘Fbkz’ (respectively ‘Ffkz’) stand for feedback designs (respectively feedforward designs) with k performance sensors used in the synthesis; the performance sensors used for each case are also given. Assuming that transition to turbulence process begins shortly after the streamwise position of the actuator, it is chosen to scale the results by the local H_2 norm of the uncontrolled system at the performance sensor z_1 , which is the closest performance sensor to the actuator. The maximum local H_2 norm between the position of the sensors z_1 and z_6 (respectively the most upstream and the most downstream performance sensors used in some syntheses) for the controlled system is denoted $\max_{x_1 < x < x_6} \|T_{z(x)w}^c\|_2$.

The resulting controllers are then implemented in *elsA* and we focus on the evolution of the local H_2 norm of the transfers $T_{z(x)w}$ at each abscissa of the plate. The evolution of the local H_2 norm of the transfers $T_{z(x)w}$ for the case without control and the different feedback cases is depicted in figure 4.13a (for feedforward cases, these results are summarised in table 4.2). For the Fb1z and Ff1z cases, where the controller is designed to minimize the energy of the performance sensor z_6 , this results in a strong reduction of the local H_2 norm at the end of the domain; in the feedback (respectively feedforward) configuration, $\|T_{z_6w}^c\|_2$ is even about 4.78 (respectively 14.) times lower than $\|T_{z_6w}\|_2$. However, this significant decrease in energy downstream of the domain was accompanied by a strong increase in the local H_2 norm upstream in the domain (blue dashed line in figure 4.13a for the feedback case). The quantity $\max_{x_1 < x < x_6} \|T_{z(x)w}^c\|_2$ for both feedforward and feedback configurations appears greater than the uncontrolled case; this increase of the local H_2 norm may then lead to a faster transition to turbulence in a 3D setup, which is the opposite of the desired objective.

| Case | Sensors z used for synthesis | $\max_{z_i \in z_{used}} \left(\frac{\ T_{z_i w}^c\ _2}{\ T_{z_1 w}\ _2} \right)$ | $\max_{x_1 < x < x_6} \left(\frac{\ T_{z(x)w}^c\ _2}{\ T_{z_1 w}\ _2} \right)$ |
|-----------------|---|--|---|
| Without control | - | 1.96 | 1.96 |
| Fb1z | $z_{used} = \{z_6\}$ | 0.41 | 9.03 |
| Fb3z | $z_{used} = \{z_1, z_4, z_6\}$ | 0.67 | 1.98 |
| Fb4z | $z_{used} = \{z_1, z_2, z_3, z_6\}$ | 0.90 | 1.06 |
| Fb6z | $z_{used} = \{z_1, z_2, z_3, z_4, z_5, z_6\}$ | 0.92 | 0.92 |
| Ff1z | $z_{used} = \{z_6\}$ | 0.14 | 2.48 |
| Ff6z | $z_{used} = \{z_1, z_2, z_3, z_4, z_5, z_6\}$ | 0.67 | 0.73 |

Table 4.2: Evolution of the performance after the controllers are implemented in *elsA* as a function of the number of sensors z_i used in the synthesis step. Cases labelled ‘Fbkz’ (respectively ‘Ffkz’) stand for feedback designs (respectively feedforward designs) with k performance sensors used in the synthesis. The results are normalized by the local H_2 norm of the uncontrolled system at the position x_1 .

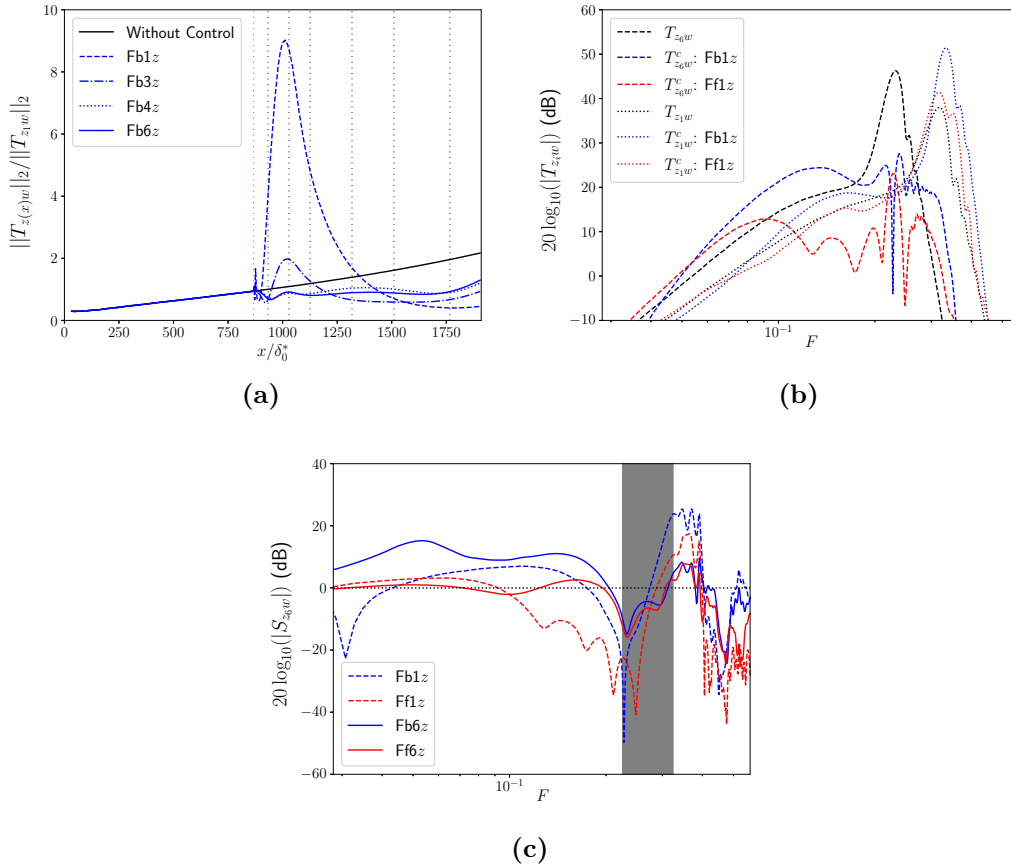


Figure 4.13: (a) Evolution of the local H_2 norm of the transfer $T_{z(x)w}$ from upstream noise w to wall-pressure fluctuation probes $z(x)$. The vertical magenta and black dotted lines represent, respectively, the position of the actuator (with the sensors y_{fb} and y_{ff} nearby) and the performance sensors z_i that can be used for synthesis. The values are normalized by $\|T_{z_1 w}\|_2$. (b) Comparison of $T_{z_6 w}$ (solid lines) and $T_{z_1 w}$ (dashed lines) for the uncontrolled (black lines), Fb1z (blue lines) and Ff1z (red lines) cases. (c) Comparison of $S_{z_6 w}$ for different control cases. Disturbance rejection is improved (respectively degraded) below (respectively above) the dotted line. Grey shaded area represents the frequency range to be controlled from the actuator to the end of the domain.

This increase of the local H_2 norm can be explained from figure 4.13b, which represents the module of T_{z_6w} (dashed lines) and T_{z_1w} (dotted lines) for the uncontrolled (black lines), Fb1z (blue lines) and Ff1z (red lines) cases. On the one hand, the amplitudes of the dominant frequencies of the uncontrolled system for the sensor z_6 (which is the only one used in the synthesis for these cases) are significantly reduced both in feedback and feedforward cases, which partly explains the significant reduction in the H_2 norm for this transfer. On the other hand, the amplitudes of the dominant frequencies for the sensor z_1 are amplified by both feedback and feedforward designs, leading to an increase of the H_2 norm for this transfer and thus an amplification upstream of the domain.

Indeed, reducing the amplitude of disturbances in one part of the frequency spectrum can lead to increasing it in the other part, which could predominate in other abscissas of the domain. Figure 4.13c shows the frequency spectrum of $S_{z_iw} = \frac{T_{z_iw}^c}{T_{z_iw}}$. For a sensor z_i , disturbance rejection is achieved at frequencies where $|S_{z_iw}| < 1$. An effect similar to the waterbed effect [180] appears: for the Fb1z and Ff1z cases, the significant disturbance rejection at frequencies around $F = 0.225$ is accompanied by an amplification for higher and lower frequencies. The frequency range to be controlled being around $F \in [0.225, 0.324]$ (see figure 4.7b), amplifying lower frequencies is not a problem in our case as these will be found further downstream of z_6 and therefore not taken into account in the computational domain. However, amplifying frequencies around $F = 0.324$ will directly impact performance on the sensor z_1 which is dominated by these frequencies. This translates into the need to use several sensors z_i in the synthesis to obtain a suitable frequency representation in different abscissas of the domain to avoid an unwanted waterbed effect. Both Fb6z and Ff6z cases have lower disturbance rejection at frequencies around $F = 0.225$ but the waterbed effect on high-frequencies is mitigated compared to Fb1z and Ff1z cases (see figure 4.13c). By taking more and more performance sensors along the plate for the synthesis, a wider spectrum of amplified frequencies is covered. The larger the frequency range to be rejected, the more complicated obtaining very high attenuation on the spectrum. This is why the quantity $\max_{z_i \in z_{used}} \|T_{z_iw}^c\|_2$ increases with the number of performance sensors used in the synthesis (see table 4.2). Nevertheless, due to the better coverage of amplified frequencies by increasing the number of z_i used in the synthesis, a more uniform performance along the plate is obtained (see table 4.2 and figure 4.13a).

By taking three performance sensors (one near the actuator, one near the end of the domain and an other in between) and thus covering a wider frequency spectrum, the Fb3z case (dash-dot line in figure 4.13a) significantly reduces the local H_2 norm increase near the actuator compared to the Fb1z. However, immediately after the position of the sensor z_1 (first vertical black dotted line), yet taken into account in this synthesis, the local H_2 norm increases and a slight bump appears at $x \approx 1020\delta_0^*$. It is associated with strong non-modal effects in the vicinity of the actuator (see section 4.4.3). For frequencies around $F = 0.296$, those dominant in the vicinity of the actuator, the modal behaviour is only found for $x \gtrsim 1136.4\delta_0^*$ (see figure 4.8b). Therefore, the area from the actuator to the end of the transient non-modal region has to be discretised with several performance sensors as in the Fb4z and Fb6z cases. Because $\max_{x_1 < x < x_6} \|T_{z(x)w}^c\|_2$ is lower in the Fb6z case than in the Fb4z one due to a better coverage of the amplified frequency spectrum along the plate, the controllers resulting from the syntheses with six performance sensors are kept to evaluate the results in more detail in section 4.7.

4.7 Feedforward versus feedback control

For the two controllers derived from the Fb6z and Ff6z synthesis, which provide the most uniform performance along the plate for wall-pressure fluctuation sensors for feedback and

feedforward designs, the results are evaluated in more detail. To lighten the notations, the Fb6z and Ff6z cases are now denoted Fb and Ff, respectively.

4.7.1 Performance on the nominal case

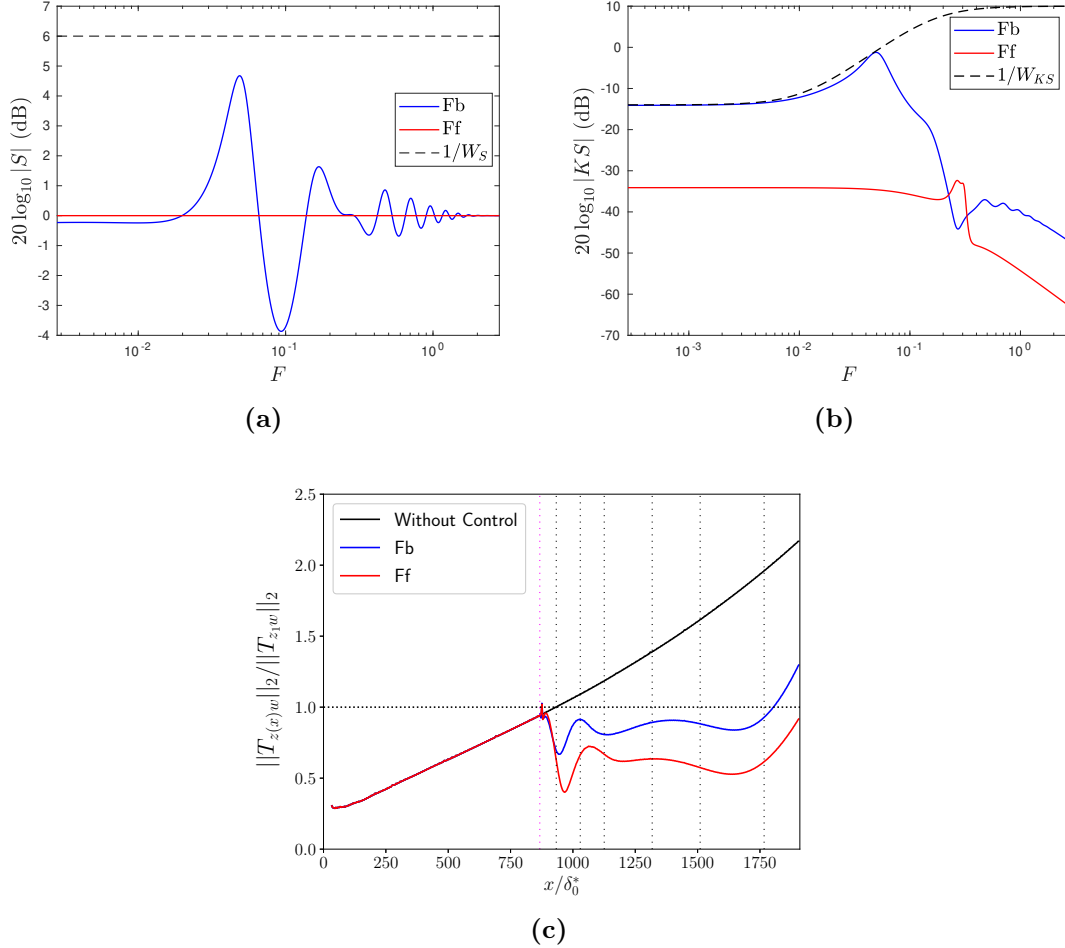


Figure 4.14: Blue, red and dashed lines represent the feedback case, the feedforward case and the constraints (inverse of the weighting functions) imposed for the control design, respectively. (a) Magnitude of S . (b) Magnitude of KS . (c) Evolution of the local H_2 norm of the transfer $T_{z(x)w}$ as obtained from the DNS simulation (those obtained with the ROMs are actually identical at $x = x_i$ since the ROMs are very accurate). The vertical magenta and black dotted lines represent, respectively, the position of the actuator (with the sensors y_{fb} and y_{ff} nearby) and the six performance sensors z_i used for synthesis. The values are normalized by $\|T_{z_1 w}\|_2$. The horizontal black dotted line depicts the energy threshold $\|T_{z_1 w}\|_2$ satisfied until x_6 following the minimization of the cost functional $\max_{i=1,\dots,6} (\|T_{z_i w}^c\|_2)$.

Figure 4.14a shows the sensitivity function S for the feedback design which respects the H_∞ constraint on the sensitivity function (*i.e.* $|S| < 1/|W_S| = 6$ dB) imposed in the CMP (4.12) (represented by the black dashed line). As previously explained, for the feedforward design, $|S| = 1$ (red line) and the constraint is automatically satisfied. Figure 4.14b represents $|KS|$ for both the feedforward and feedback cases. The weighting function W_{KS} , which limits actuator activity in case of low-frequency disturbances, is also shown and we verify that $|KS| < 1/|W_{KS}| \forall \omega \in \mathbb{R}$. For the feedback design, $|KS|$ is close to $1/|W_{KS}|$ at low-frequencies, meaning that there is a trade-off between minimizing H_2 norms and desensitizing the controller in the low-frequency range. We notice the natural roll-off of the controllers of -20 dB per decade at

high-frequencies related to the strictly-proper structure imposed in the synthesis.

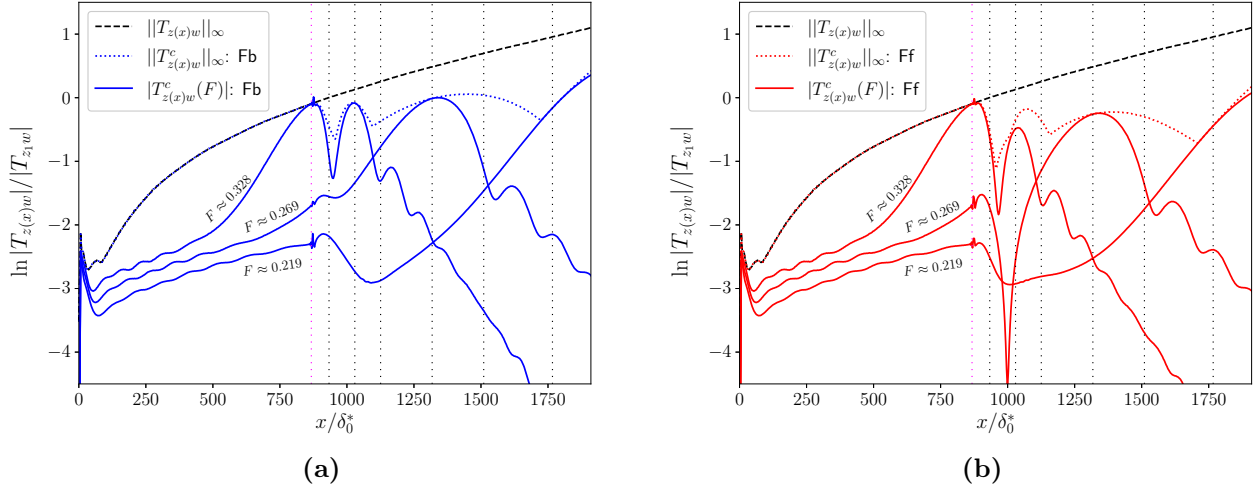


Figure 4.15: Evolution of the local H_∞ norm of the transfer $T_{z(x)w}$ as a function of the plate abscissa for the uncontrolled (black dashed lines), feedback (a) and feedforward (b) cases. The evolution of $|T_{z(x)w}^c(F)|$ for some frequencies is also shown for the controlled cases. For vertical lines, it is the same caption as in figure 4.14c.

The control results in a significant reduction in the local H_2 norm of the transfers $T_{z(x)w}$ at each abscissa of the plate (see figure 4.14c) for both the feedforward and feedback configurations. As expected from the literature [14, 81, 170, 188], the feedforward design minimizes even more the local H_2 norm than the feedback one. Nevertheless, for both configurations, the minimization of the cost functional $\max_{i=1,\dots,6} (\|T_{z_iw}^c\|_2)$ allowed the local H_2 norm of $T_{z(x)w}$ not to exceed, before $x = x_6$, a threshold given by the H_2 norm at $x = x_1$. Thus both configurations successfully achieve the control strategy set forth in figure 4.2. The use of an H_2 performance criterion alongside the H_∞ criterion on stability margin allows to address both performance in terms of disturbance rejection and stability robustness in the design of the feedback loop.

In addition to the reduction of the local H_2 norm along the plate, the local H_∞ norm $\|T_{z(x)w}\|_\infty$ has also decreased for both the feedforward and feedback designs (see figure 4.15); this variation may related to the N -factor envelope \tilde{N} by:

$$\max_{x_1 < x < x_6} \ln \|T_{z(x)w}\|_\infty - \max_{x_1 < x < x_6} \ln \|T_{z(x)w}^c\|_\infty = \max_{x_1 < x < x_6} \tilde{N} - \max_{x_1 < x < x_6} \tilde{N}^c. \quad (4.15)$$

More precisely, feedforward and feedback designs respectively “save” 1.13 and 0.89 points of N -factor. One might ask which is the most effective setup for delaying transition, between minimizing $\max_i (\|T_{z_iw}^c\|_2)$ or minimizing $\max_i (\|T_{z_iw}^c\|_\infty)$, but answering the question is beyond the scope of this study.

Beyond these results on wall-pressure fluctuation sensors computed with impulse responses, results when the boundary layer is excited by a continuous white-noise signal w are considered. A temporal sequence of the inputs (w and u) and outputs (y and z_i) of the system is represented in figure 4.16. The global root-mean-square (r.m.s.) temperature field (denoted T'_{rms}) and streamwise velocity field (denoted u'_{rms}) are represented in figures 4.17 and 4.18, respectively. For T'_{rms} , whose high values are located around the generalised inflection point (white dashed line) in the uncontrolled case (see figure 4.17a), the control reduces the amplitude of the perturbations (see figures 4.17b and 4.17c). For the field u'_{rms} in the uncontrolled case (see figure 4.18a), high level regions are localized close to the wall. These levels are drastically

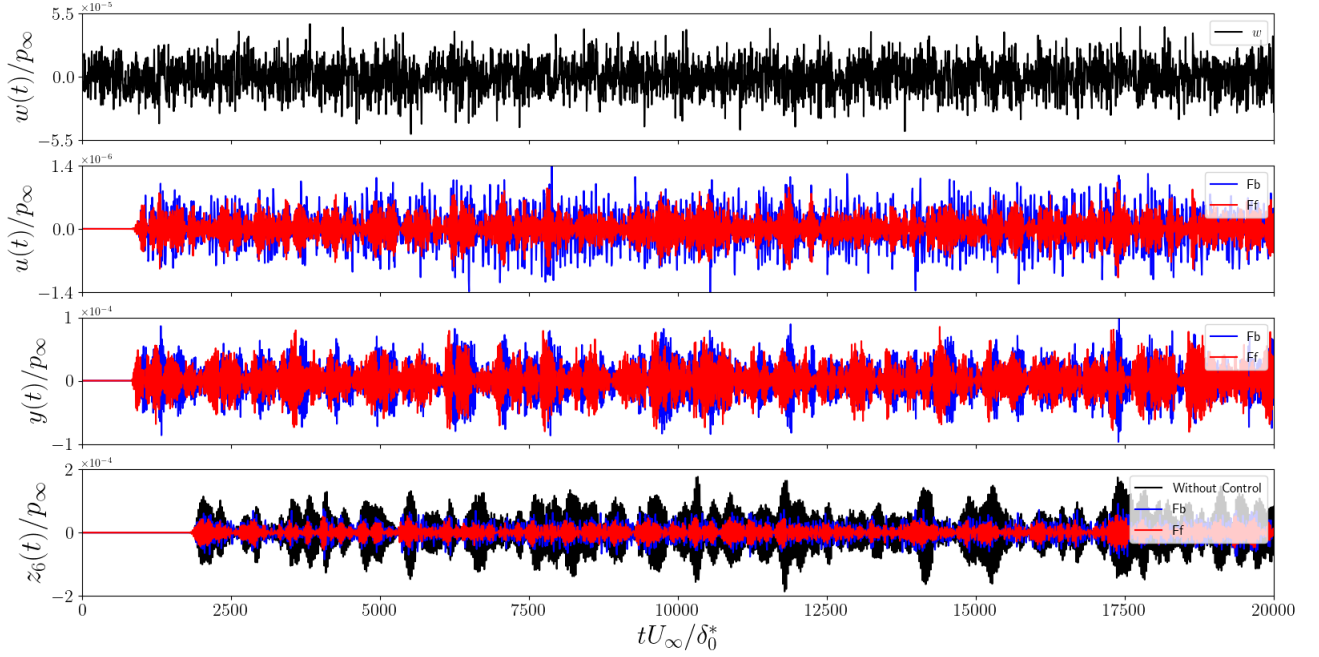


Figure 4.16: Temporal sequence of the inputs (w and u) and outputs (y and z_i) of the system when excited by a continuous white-noise signal w .

decreased when control is present (see figures 4.18b and 4.18c). The feedforward design further reduces the amplitude of disturbances. Nevertheless, by drastically reducing the amplitude of velocity disturbances in both feedforward and feedback configurations, while the controllers were built from wall pressure fluctuation performance sensors only, one may hope to strongly delay transition to turbulence due to the second Mack mode in a 3D setup.

The control efficiency is also assessed by looking at the coefficient:

$$\Phi = \frac{\int_{\partial\Omega} \frac{1}{2} \langle e_{\text{Chu}} - e_{\text{Chu}}^c \rangle_t \bar{\mathbf{u}} \cdot \mathbf{n} \, ds}{\int_{\Omega} \langle u(t) \mathbf{B}_u \cdot \mathbf{u}^c \rangle_t \, d\Omega}. \quad (4.16)$$

As mean kinetic perturbation energy flux difference between the uncontrolled and controlled simulations is sometimes used in incompressible case [13], a mean Chu's energy flux difference $\int_{\partial\Omega} \frac{1}{2} \langle e_{\text{Chu}} - e_{\text{Chu}}^c \rangle_t \bar{\mathbf{u}} \cdot \mathbf{n} \, ds$ is chosen for our compressible boundary layer to compute the gain. The term $\int_{\Omega} \langle u(t) \mathbf{B}_u \cdot \mathbf{u}^c \rangle_t \, d\Omega$ represents the mean power spent by the user during the control effort [13, 56]. For Ω , the right boundary stops at x_6 while the left boundary is taken sufficiently upstream of the actuator position so that the uncontrolled and controlled flux at this boundary are identical. Moreover, the line integrals along the wall and the upstream boundary yield zero contributions, so the gain just represents the mean Chu's energy flux difference at x_6 . For the feedforward and feedback designs, $\Phi_{ff} = 555.5$ and $\Phi_{fb} = 109.1$, respectively. The feedforward design has a better energy-efficiency than the feedback one as one would expect because the feedforward controller reduces more the perturbation amplitude (see figures 4.18(b,c)) and has lower control signal amplitude (see figure 4.16) than the feedback one. Both configurations have a largely positive efficiency, which is due to the fact the control takes advantage of the instability mechanism to cancel perturbations, leading to a low control effort [13]. This coefficient Φ based on mean Chu's energy flux would be underestimated compared to realistic 3D configurations where non-linearities and transition start to occur at the end of Ω : delaying transition in Ω would lead to large gain while keeping low control effort as the actuator would be placed in a weakly non-linear area at its streamwise position to stay close to the linear on-design point. Nevertheless, the coefficient Φ may also be considered as overestimated because the forcing of

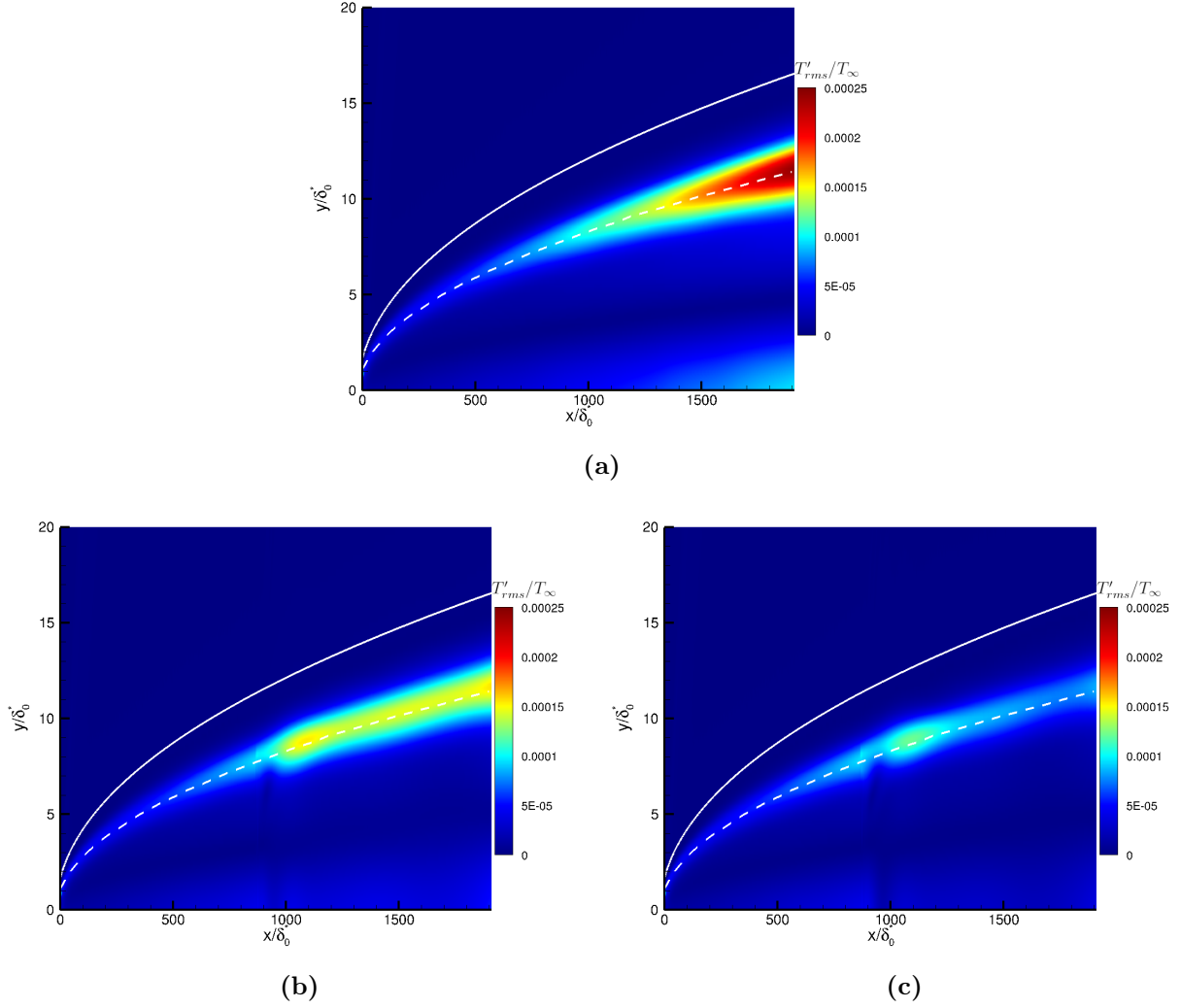


Figure 4.17: Contours of T'_{rms} for the (a) uncontrolled, (b) feedback and (c) feedforward cases. The white solid lines and dashed lines respectively represent the boundary layer thickness δ and the generalised inflection point position y_g .

the actuator would not necessarily be optimal in a realistic configuration (*i.e.* not centered around the generalized inflection point) and there would be also electro-mechanical conversion losses. Indeed, the control cost between an ideal actuator (modelled by a volume forcing) and a realistic one (*e.g.* plasma actuator) may be very different [56]. Lastly, in 3D configurations where transition occurs, the gain would no longer be related to a mean Chu's energy flux but would be computed in terms of saved drag [56, 183], which makes the conclusions of a 2D ideal numerical study difficult to exploit in terms of control efficiency.

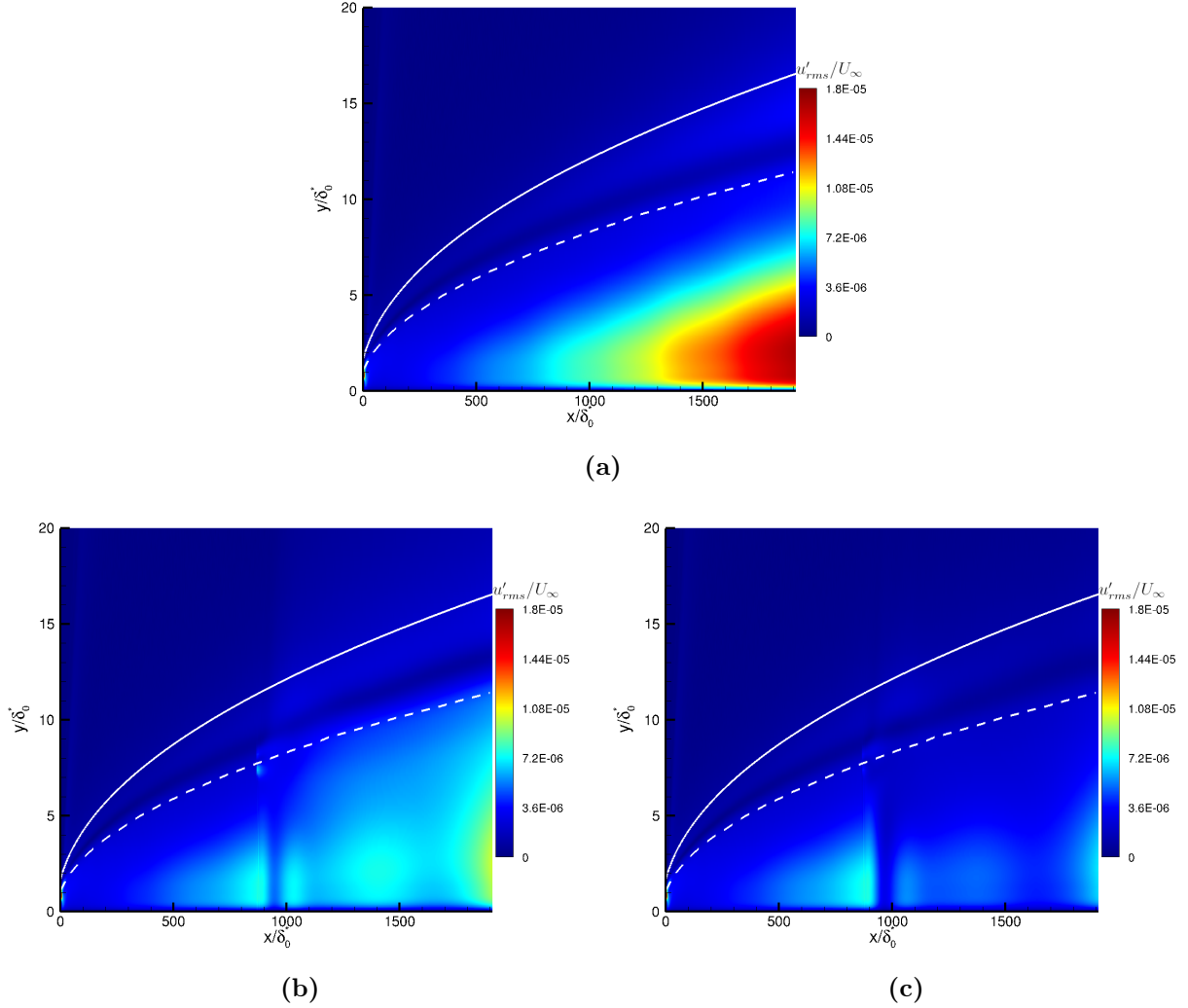


Figure 4.18: Contours of u'_{rms} for the (a) uncontrolled, (b) feedback and (c) feedforward cases. The white solid lines and dashed lines respectively represent the boundary layer thickness δ and the generalised inflection point position y_g .

4.7.2 Stability robustness

In the case of the feedback design, the configuration can be unstable and it is necessary to quantify the evolution of the stability margins following inflow condition variations or uncertainties. The closed-loop system is stable if and only if the Nyquist plot of the loop gain $-T_{yu}^{\text{real}}K$ (which is stable) does not encircle the critical point $(-1, 0)$. As already discussed in sections 2.4.2 and 4.3, the Nyquist plot of $-T_{yu}K$ therefore allows to quantify the available stability margins. The modulus margin corresponds to the minimal distance between the Nyquist plot and the critical point $(-1, 0)$ (so the maximum amount of error $|\Delta|$ admissible) before instability sets in. The phase margin PM (respectively gain margin GM) represents the minimal additive (respectively multiplicative) error on the phase (respectively gain) of T_{yu} before instability sets in.

Inlet velocity variation is considered here to be the most problematic variation (compared to other primitive variable variations) as it involves multiple changes: (i) variation in time delays due to change in convection velocity; (ii) modification of the Reynolds number Re_x implying that for a given abscissa on the domain, the dominant frequencies are higher (respectively lower) after an increase (respectively decrease) of Re_x ; (iii) variation of the Mach number M_{∞}

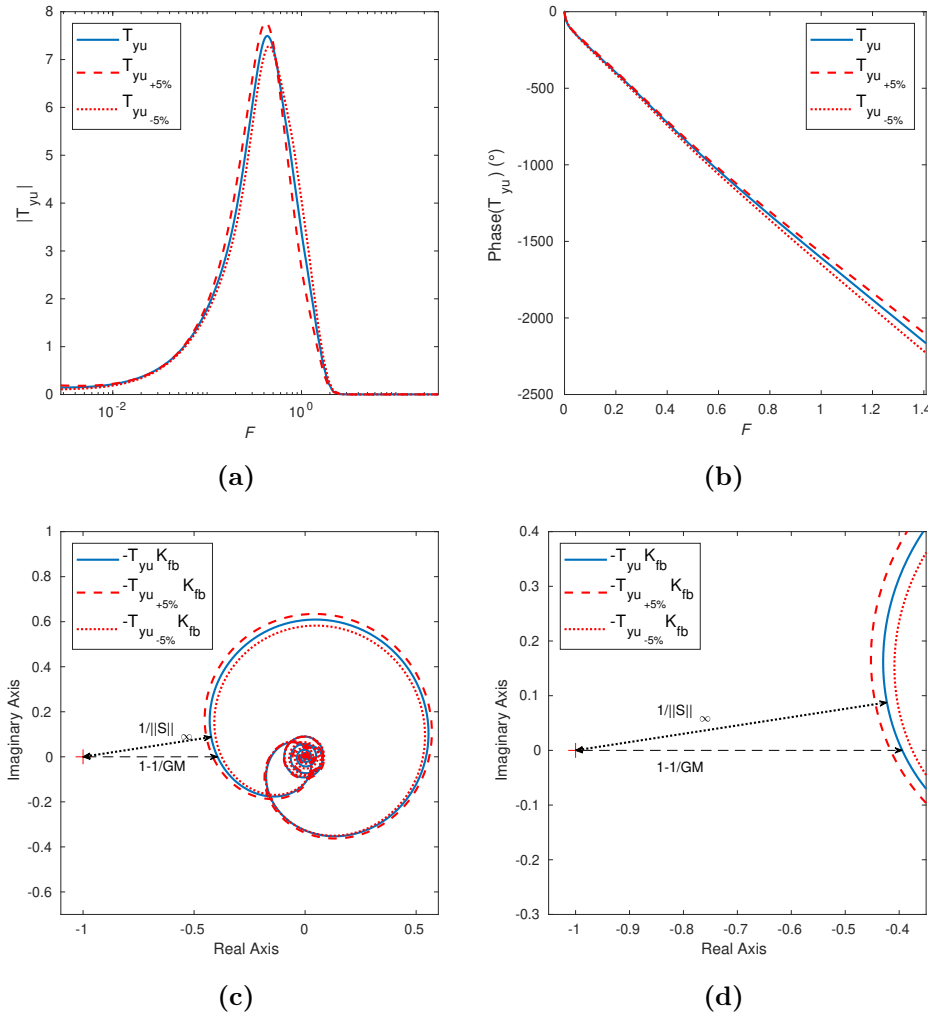


Figure 4.19: Evolution of the (a) module and (b) phase of T_{yu} after a variation of $\pm 5\%$ of the inlet velocity. (c) Global view and (d) zoom near the critical point $(-1, 0)$ of the Nyquist plot of the loop gain $-T_{yu}K_{fb}$ (solid blue line) and $-T_{yu\pm 5\%}K_{fb}$ (dashed and dotted red lines). The black dotted line represents the modulus margin $||S||_{\infty}^{-1}$ (the minimal distance to instability). The black dashed line represents the gain difference before instability and is linked to the gain margin GM .

implying a modification of the neutral curves and by extension a modification of the growth rates.

For a variation of the upstream velocity at the entry of the domain U_{∞} of $\pm 5\%$, which induces $M_{\infty} \in [4.275, 4.725]$, the new transfer functions $T_{yu\pm 5\%}$ are compared with the reference one T_{yu} in figures 4.19a and 4.19b. The greatest variations for the module appear to be around $F = 0.423$; we notice that a 5% increase of the upstream velocity implies a greater maximum value for the module at a slightly lower frequency whereas a 5% decrease in velocity implies a smaller maximum value for the module at a slightly higher frequency (see figure 4.19a). The variation of $\pm 5\%$ of the inlet velocity leads to the modification of the delays, represented by the slope of the phase versus frequency plot (see figure 4.19b): for the 5% increase of the upstream velocity, the absolute value of the slope is less and the delay is therefore shorter (with a relative variation for the delay of 3.4% compared to the reference case), whereas the opposite is obtained in the case -5% (with a relative variation of 3.9% for the delay).

Figures 4.19c and 4.19d show the Nyquist plot of the loop gains $-T_{yu}K_{fb}$ and $-T_{yu\pm 5\%}K_{fb}$. The variations of the upstream velocity slightly alter the stability margins compared to those

obtained in the reference case: the phase margin stays infinite, while the gain margin GM (black dashed lines) and the modulus margin $\|S\|_{\infty}^{-1}$ (black dotted lines) fluctuate respectively by a maximum of 3.6% and 5.1%, while remaining far from the critical point. Given the small impact of the inflow velocity variations of $\pm 5\%$ on all margins, the feedback design may be stable for even greater velocity variation. Therefore, unlike previous feedback studies using LQG [13, 188], the stability robustness for a feedback design obtained with a robust synthesis method is not a problem. Next, performance robustness is examined, which is a different issue.

4.7.3 Performance robustness

Performance robustness is evaluated by checking that the control laws remain efficient in terms of expected power reduction of the different performance sensors z_i despite new noise sources or differences between on-design and off-design operating conditions.

4.7.3.1 Noisy sensors

Noisy estimation sensors are modelled by adding white Gaussian noise on both y_{fb} and y_{ff} (see figure 4.20a). Both estimation sensors are corrupted by the same amount of noise (50% of the r.m.s. value without control of y_{fb}), which models an intrinsic defect of the sensor, such as electronic noise, that does not depend on its position along the domain. Nevertheless, the streamwise position of y_{ff} being quite close to that of y_{fb} , the ideal signal-to-noise ratio remains very similar for both configurations and only varies by a few percents. The PSD of the corrupted estimation sensors remain unchanged in the frequency band of the second Mack mode but exhibit much larger values in low and high frequencies (see figure 4.20b). This is because the PSD of white noise being constant, the ideal signal-to-noise ratio is particularly low for frequencies where the ideal signal energy is low. The signal y is given to the controller K , which generates the actuator signal u ; the control signal PSD for corrupted signals y becomes stronger on the previously mentioned low and high frequency bands, compared to the PSD of u for ideal signals y (see figure 4.20c). Nevertheless, thanks to the strictly-proper structure and the filter W_{KS} imposed in the synthesis step, $|KS|$ has been constrained in these frequency bands. Thus, the actuator activity remains limited in these regions despite the important added noise and, if we consider the evolution of the maximum along the wall-normal direction of u'_{rms} (denoted $\max_y u'_{rms}$), we keep a performance close to the ideal case (see figure 4.20d). Both feedback and feedforward configurations stay below the velocity energy threshold until x_6 and these two designs are robust to noise on the estimation sensors. If even noisier sensors were used, it would suffice to decrease the amplitude of the constraint $1/W_{KS}$ to recover performance robustness (especially in low-frequencies for the feedback configuration).

To illustrate the impact of the weighting function W_{KS} on the performance, the CMP (4.12) is solved but with an higher $|1/W_{KS}|$ compared to the one use in figure 4.14b. The feedback controller resulting from this synthesis (red lines) is shown in figure 4.21a and is compared to the previous one (*i.e.* the one which is robust to signal to noise ratio of 2 at y_{fb} , blue lines). The two controllers have globally the same behaviour in the bandwidth of the second Mack mode, but the new controller has higher gain in low-frequency range. In the case where the estimation sensors are corrupted, it follows that the u -PSD for a corrupted signal y becomes more important in low-frequencies for the controller resulting from the synthesis with an higher $|1/W_{KS}|$ than for the previous controller (see figure 4.21b). For the noisy estimation sensor case, the new controller leads to a strong energy injection in the vicinity of the actuator (see the red square in figure 4.21c) which could trigger the transition to turbulence in a 3D configuration. As these injected low-frequencies are convectively stable, they attenuate very quickly but the maximum along the wall-normal direction of u'_{rms} clearly exceeds the energy threshold before

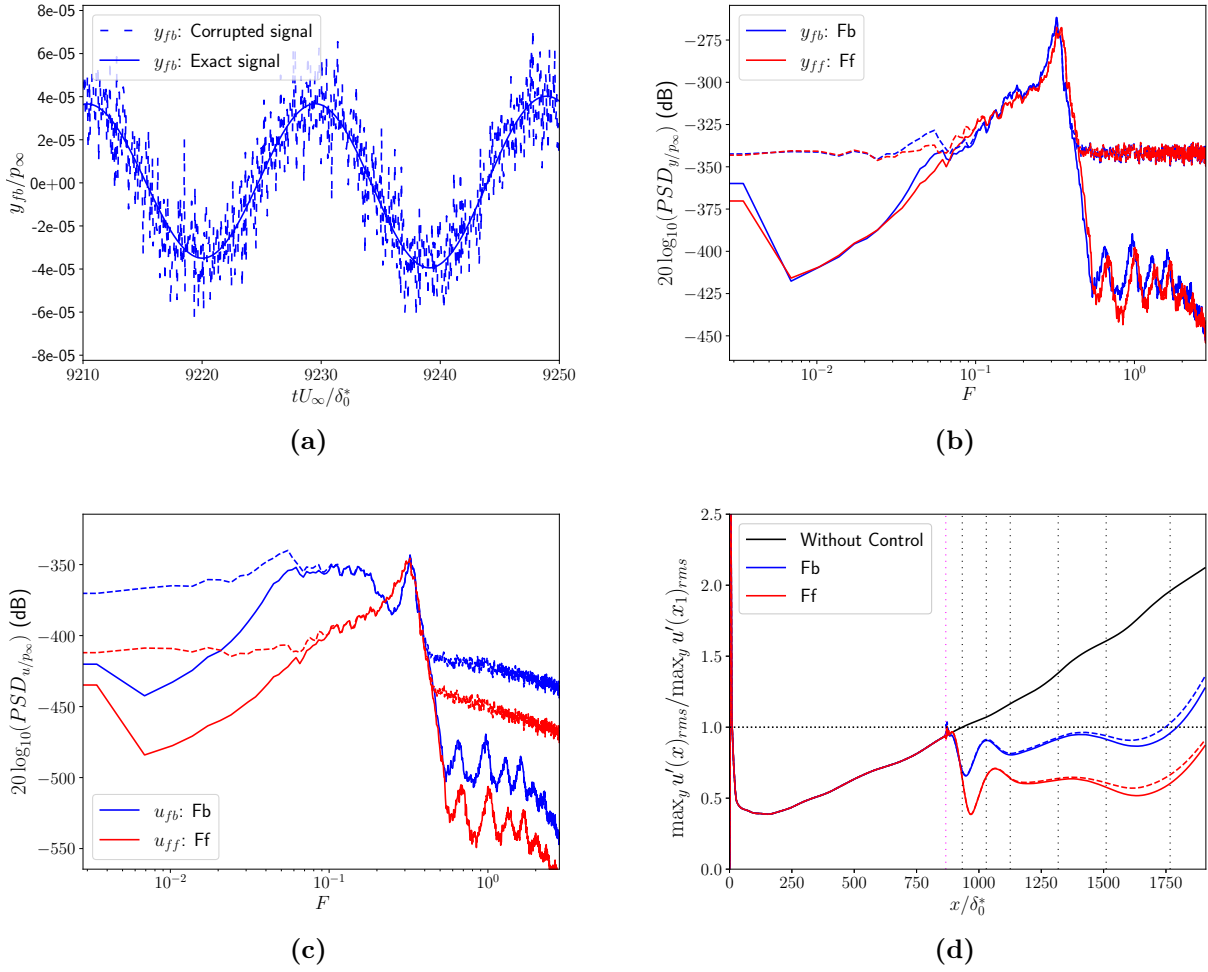


Figure 4.20: In all subplots, feedback and feedforward designs are in blue and red lines, respectively. Controlled systems with ideal and noisy estimation sensors are represented by solid and dashed lines, respectively. (a) Short sequence of y_{fb} corrupted by 50% of the r.m.s. value without control of y_{fb} . Comparison of the evolution of (b) PSD_y , (c) PSD_u and (d) $\max_y u'_{rms}$ for the controlled systems with ideal and noisy estimation sensors. For the vertical lines, the caption in (d) is the same as in figure 4.14c.

the last performance sensor z_i used in the synthesis, contrary to the previous controller (see dashed lines in figure 4.21d). It should be noted that in the case of ideal estimation sensors, the controller resulting from the synthesis with an higher $|1/W_{KS}|$ minimizes slightly more the velocity fluctuations compared to the previous feedback controller used in figure 4.14b (see solid lines in figure 4.21d) because the constraint on W_{KS} is less important. There is therefore a trade-off between minimizing H_2 norms and desensitize the controller in the low-frequency range during the synthesis.

4.7.3.2 Off-design operating conditions

Performance robustness to off-design operating conditions is assessed by considering the evolution of the local H_2 norm of $T_{z(x)w}$ after a variation of free-stream density ρ_∞ and velocity U_∞ of $\pm 5\%$, for both feedback and feedforward controllers of the section 4.7.1. New boundary layer profiles at a distance of $19\delta_0^*$ from the leading edge are therefore used as inlet conditions (see figures 4.22(a,b)). The density variation may correspond in practice to a change in altitude

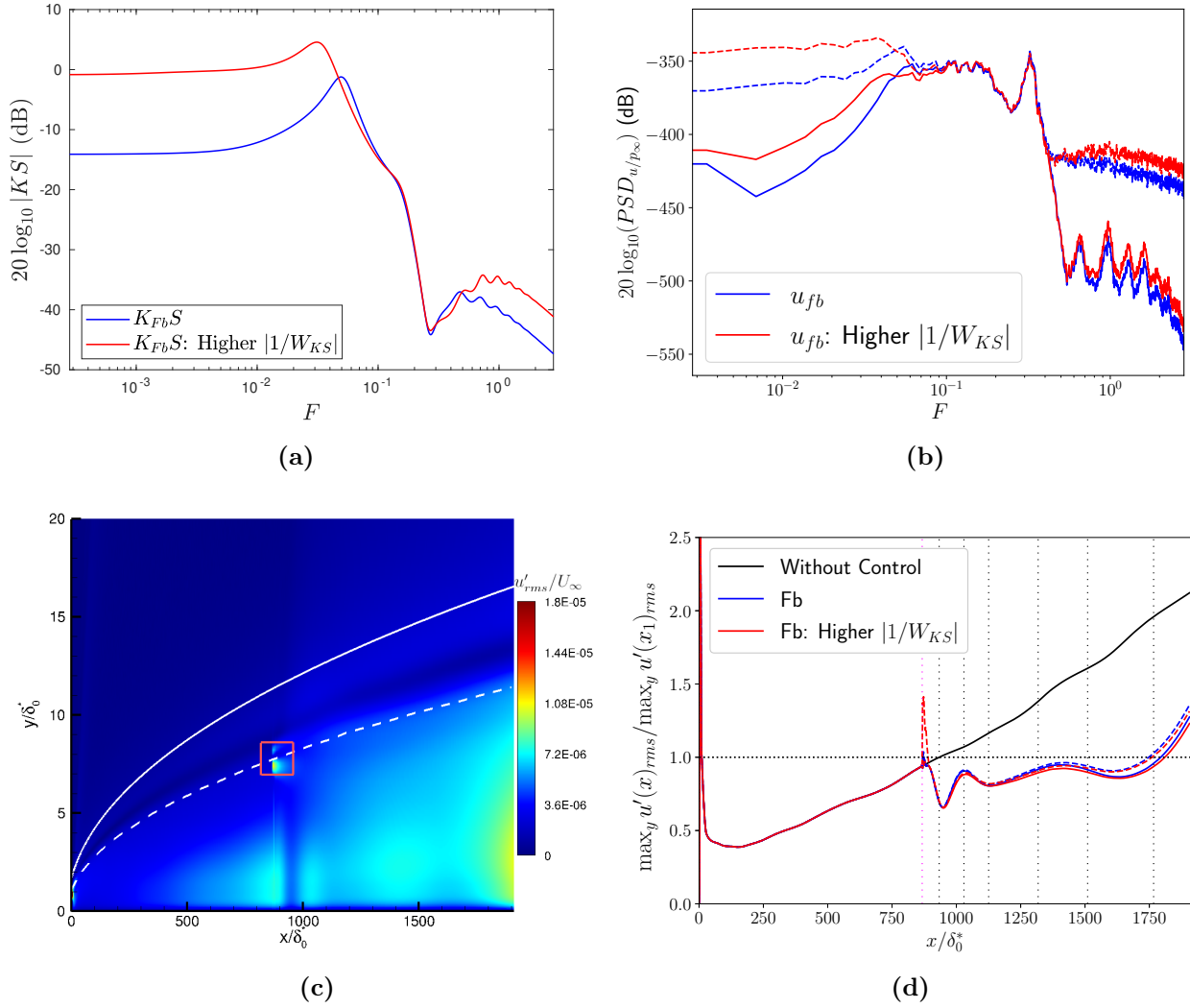


Figure 4.21: Solid lines and dashed lines represent the cases with ideal and noisy estimation sensors, respectively. Blue lines and red lines represent the feedback controller used in figure 4.14b and the one resulting from a synthesis with a larger $|1/W_{KS}|$, respectively. Comparison of (a) KS and (b) PSD_u . (c) Contours of u'_{rms} for the higher $|1/W_{KS}|$ case with noisy y_{fb} . (d) Comparison of $\max_y u'_{rms}$. For the vertical lines, the caption is the same as in figure 4.14c.

whereas the velocity variation may correspond to a change in cruise speed. When ρ_{∞} is modified, the temperature and velocity inlet values are kept constant, which means that M_{∞} and hydrodynamic delays related to the convective behaviour are maintained (see green dashed line figure 4.22c) while only Re_x is modified (which implies a change in the dominant frequencies at a given abscissa as seen in figure 4.22d). A modification of U_{∞} on the other hand implies variations of hydrodynamic delays (see purple dashed line figure 4.22c). It will also impact the values of Re_x and M_{∞} , which modify the base flow profiles. Changing the base flow impacts the stability characteristics of the boundary layer, and, in turn, the dominant frequencies along the plate, as seen in figure 4.22d.

With density variations of $\pm 5\%$ (see figure 4.23a), despite degraded off-design performance, both feedback and feedforward controllers manage to reduce the local H_2 norm compared to the case without control over a fairly large distance on the flat plate. However, while the feedforward design minimized the local H_2 norm more than the feedback one for the nominal case (solid lines), it seems that this is no longer necessarily the case in off-design situations

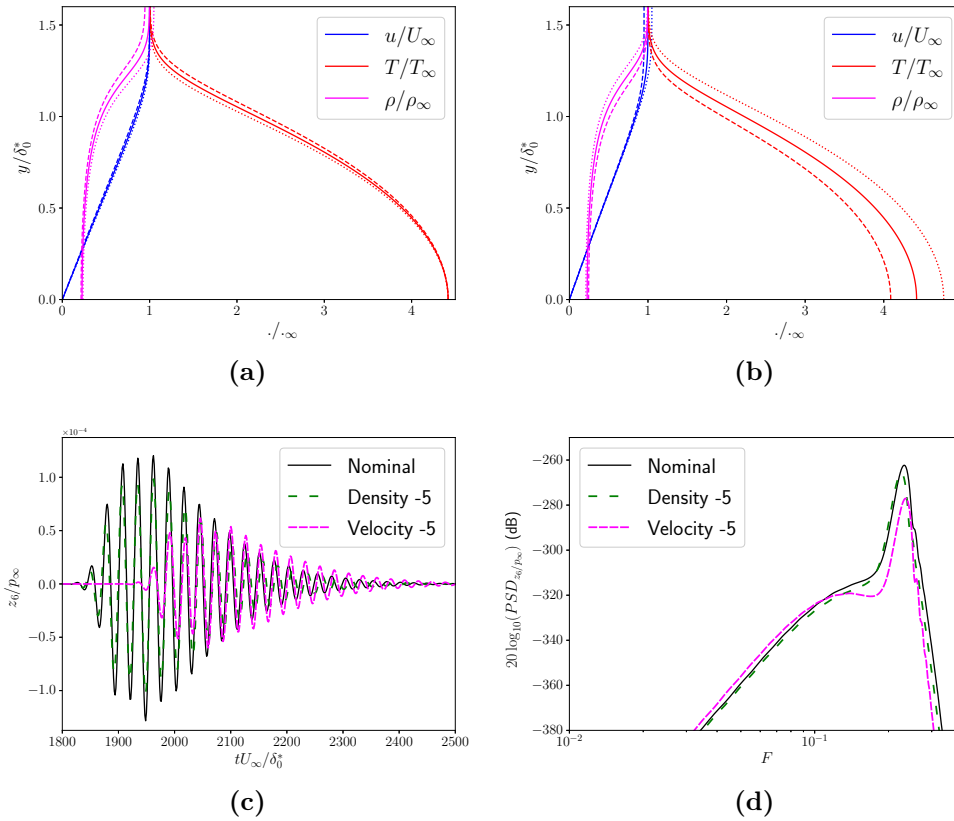


Figure 4.22: Velocity, temperature and density profiles used for the inlet condition (solid lines for the nominal case and dashed and dotted lines for the $\pm 5\%$ cases, respectively). All profiles are made dimensionless with the nominal free-stream values. (a) Density variations. (b) Velocity variations. Comparison of uncontrolled pressure wavepackets generated by an impulse of w (c) and their PSD (d) at x_6 after a variation of ρ_∞ and U_∞ of -5% .

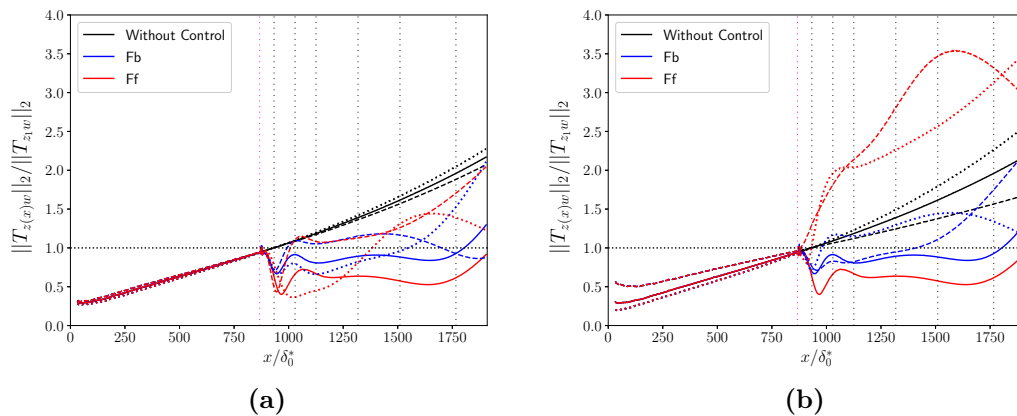


Figure 4.23: Evolution of the local H_2 norm of $T_{z(x)w}$ after a variation of (a) ρ_∞ and (b) U_∞ of $\pm 5\%$ (dotted and dashed lines). The nominal cases are in solid lines. For vertical lines, same caption as in figure 4.14c.

(dotted and dashed lines). The variation in performance between the nominal and off-design cases in the feedback configuration appears less pronounced than in the feedforward setup, which is allowed by the sensitivity function S . Although this transfer function, because of the delay due to the actuator/estimation sensor distance, limits the achievable performance on the

nominal case for a feedback setup (see section 4.6.1), it desensitizes the system to modelling errors or to variations in system characteristics over a certain bandwidth (see section 2.4.4). Even if both designs exceed the H_2 norm threshold at some point, they have some performance robustness with respect to density variations by staying below the uncontrolled system H_2 norm all along the domain.

The real strength and superiority of the feedback design over the feedforward one lies in its ability to maintain correct performance during velocity variations (see figure 4.23b). While the feedback setup manages to maintain some performance in off-design conditions by staying below the local H_2 norm of the uncontrolled system over a fairly long distance along the plate, the feedforward design fails to maintain the performance requirement by amplifying the local H_2 norm. This increase in the feedforward setup may then lead to a faster transition to turbulence, which is the opposite of the desired objective. Thus, in the case of noise-amplifier flows, we underline the importance to assess the performance robustness with respect to velocity variations, that appear to be the most problematic ones, as in Fabbiane et al. [55]. As soon as variations or uncertainties on the inflow velocity are present and that controllers are built from a single operating point, the best trade-off between performance and robustness is a feedback configuration.

Chapter outcome summary:

A robust reactive control method has been developed in order to control the linear growth of the second Mack mode in a 2D boundary layer over a flat plate at Mach 4.5.

The choice of the type and position of the actuator and sensors are based on the study of the noise-amplifier behaviour of our flow, in order to trigger the optimal growth mechanisms and ensure efficient flow control. During the identification step, some unnecessary dead times related to the convective nature of the flow are removed, allowing a significant reduction in the size of the ROMs, which is beneficial both for the identification and synthesis steps. Moreover, we strive to identify only quantities that could be obtained in an experimental setup.

After identifying these useful transfers through data-driven methods, the synthesis of the controllers is achieved with a structured mixed H_2/H_∞ synthesis. This robust synthesis method allows to limit the order of the controller, to impose its structure upfront and to constrain simultaneously several transfer functions to obtain at the same time performance and robustness. Instead of simply minimizing a global energy, the constrained minimization problem is posed in such a way that a shaping of the spatial evolution of different local energy measures is realized, which seems a more suitable approach to delay transition to turbulence. Multiple performance sensors in the streamwise direction are therefore needed in this study to cover the entire spectrum of amplified frequencies along the domain and to counteract the non-modal transient growth in the vicinity of the actuator.

After implementing the control laws in the *elsA* solver, we find that feedforward and feedback designs both manage not to exceed a certain energy threshold on the nominal case. Moreover, the stability robustness for the feedback design is not a problem thanks to the robust synthesis and the constraints imposed. Regarding performance robustness, both feedforward and feedback designs manage to reduce the amplitude of disturbances compared to the uncontrolled case despite noisy estimation sensors or inflow density variations. By changing the inflow velocity, it appears that the feedforward setup is completely unable to follow inflow condition variations while the feedback setup keeps reasonable performance over a large velocity variation of $\pm 5\%$. Therefore, the best trade-off between performance and robustness requires a feedback configuration when LTI controllers are built from a single operating point.

Nevertheless, modern synthesis tools allow the construction of more complex synthesis schemes (*e.g.* combining a feedforward and a feedback controller) or to exploit the ROMs at different operating points in the synthesis step instead of building the controller on a single operating point and checking robustness to performance in off-design conditions a posteriori. Hence, an improvement in performance robustness regarding velocity variations, which appeared as the most problematic ones, can be expected and it is the subject of the next chapter.

Maintaining low disturbances over a range of free-stream velocity variations

| | | |
|------------|--|------------|
| 5.1 | Input/output dynamics of the system after velocity variations | 94 |
| 5.2 | Combined feedforward/feedback configurations | 96 |
| 5.2.1 | Synthesis method | 96 |
| 5.2.1.1 | Control setup | 96 |
| 5.2.1.2 | Constrained minimisation problem | 96 |
| 5.2.2 | Performance on the design point | 97 |
| 5.2.3 | Performance robustness | 99 |
| 5.3 | Multi-model synthesis | 100 |
| 5.3.1 | ROMs and synthesis method | 100 |
| 5.3.1.1 | Identification | 100 |
| 5.3.1.2 | Constrained minimisation problem | 101 |
| 5.3.2 | Performance on the design points | 103 |
| 5.3.2.1 | Multi-model feedforward and feedback | 103 |
| 5.3.2.2 | Multi-model combined configuration | 105 |
| 5.3.2.3 | Effect of controller order | 105 |
| 5.3.3 | Performance robustness | 107 |
| 5.3.3.1 | Off-design operating points | 107 |
| 5.3.3.2 | Gain versus phase uncertainties | 108 |
| 5.4 | Gain scheduling | 110 |
| 5.4.1 | Synthesis method | 110 |
| 5.4.2 | Performance on the design points | 111 |
| 5.4.3 | Performance robustness | 112 |

| | |
|--|-----|
| 5.4.4 Piecewise gain scheduled law | 113 |
|--|-----|

Chapter foreword:

While stability robustness in a feedback setup is not an issue thanks to modern synthesis methods, performance robustness to velocity variations has emerged as the major issue for noise-amplifier flows. A simple feedforward controller based on a single operating point is completely unable to follow inflow velocity variations of 5% while the feedback setup keeps reasonable performance.

The present chapter is dedicated to optimized control law synthesis to maintain performance in terms of perturbation amplitude reduction over a range of $\pm 5\%$ of free-stream velocity variations around $M_\infty = 4.5$ for the 2D supersonic boundary layer. Hence, it is only a first step in order to delay transition over a wider range of operating points more representative of changes in flight conditions. We will evaluate the ability of combining feedforward and feedback, multi-model synthesis and gain scheduling methods to cover several operating points and compare their performance with the previous baseline LTI controllers designed at a single operating point. Through this objective, one key question we wish to address is whether the feedforward setup can be made robust to velocity variations. If so, does the benefit of using a feedback design completely vanishes? Answering these questions allows to know which control strategies are the most effective for the performance robustness issue and to advance in the construction of a methodology leading to a robust control law over a range of inflow velocities.

The chapter is organized as follows. Firstly, we come back in more detail to the implication of free-stream velocity variations on instability characteristics. Then, for each of the new configurations tested (*i.e.* combination of a feedforward and feedback controller, multi-model synthesis and gain scheduling methods), the synthesis method (ROMs used and CMP solved) is introduced and the results in terms of disturbance amplitude reduction on-design and off-design are compared to those of the baseline feedforward and feedback controllers.

5.1 Input/output dynamics of the system after velocity variations

This section elaborates on some of the elements briefly discussed in section 4.7.3.2 in order to clarify the impact of free-stream velocity variations on the characteristics (phase, bandwidth, amplitude, etc.) of both noise-induced and actuator-induced disturbances.

The configuration studied in this chapter is the one described in section 4.1 with the same boundary conditions; the case at $M_\infty = 4.5$ is called the nominal operating point. For the cases after free-stream velocity variations of $\pm 5\%$ around $M_\infty = 4.5$, which may correspond in practice to a small change in cruise speed, $T_\infty^{\pm 5\%}$ and $p_\infty^{\pm 5\%}$ are equal to the values at the nominal operating point and only $U_\infty^{\pm 5\%}$ varies, as $U_\infty^{\pm 5\%} = U_\infty \pm 0.05U_\infty$. The range of operating points studied is within $M_\infty \in [4.275, 4.725]$. The inputs w/u and the outputs y/z_i are those described in section 4.4 with their streamwise positions given in table 4.1. The streamwise and wall-normal positions of the inputs/outputs are the same for the nominal and $\pm 5\%$ cases; the compressible displacement thickness δ_0^* refers only to the one at the inlet of the domain for the nominal case. The six performance sensors z_i will be systematically employed for all the syntheses of this chapter.

For the noise-induced perturbations, the evolution of the magnitude of some frequencies as a function of the plate abscissa is displayed in figure 5.1a. The module of $T_{z(x)w}$ is obtained by Fourier transform of the temporal signals from the impulse responses. Each frequency is amplified only on a certain portion of the domain: the further downstream, the lower the dominant frequency. For each frequency, the evolution of its amplitude is decomposed in three steps: first the amplitude increases due to the non-modal local Orr growth, then modal growth in the instability zone of the second Mack mode, before finally decreasing (see section 4.4.2). For the $+5\%$ (respectively -5%) case, the most amplified frequency at each abscissa of the domain has a higher (respectively lower) magnitude $\|T_{z(x)w}\|_\infty$ (dashed lines) than the one of the nominal case; moreover, the maximum amplitude along the domain for any given dimensionless frequency $F = 2\pi f\delta_0^*/U_\infty$ is found further upstream (respectively downstream) than in the nominal case. These differences in terms of instability amplitude and dominant

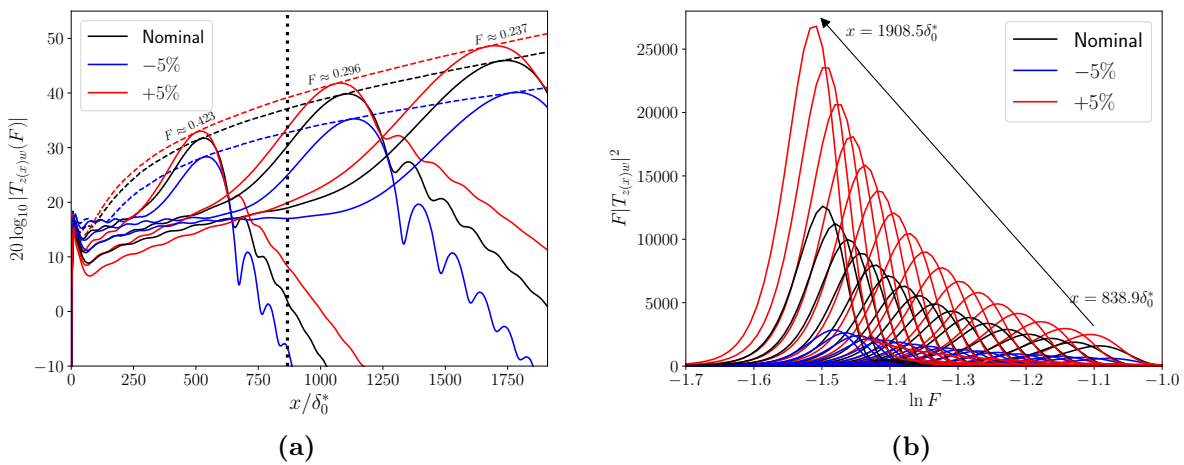


Figure 5.1: Evolution of (a) $|T_{z(x)w}|$ and (b) $F|T_{z(x)w}|^2$ for the nominal $M_\infty = 4.5$ and the $\pm 5\%$ cases. The vertical dotted line in (a) represents the streamwise position of the actuator. In (b), curves are spaced at a uniform streamwise interval of $66.8\delta_0^*$.

frequency position between the nominal and $\pm 5\%$ cases are also found in figure 5.1b. It shows

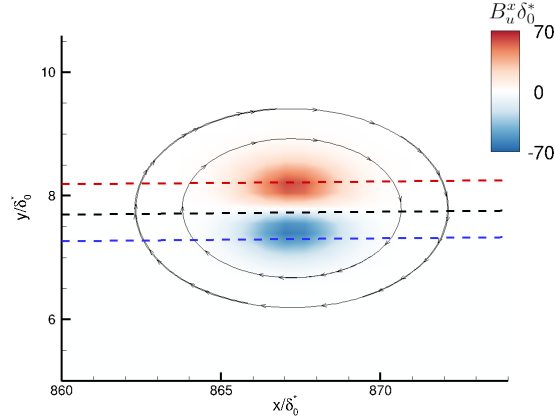


Figure 5.2: Contour plot of the streamwise component of \mathbf{B}_u with streamlines in black. The generalized inflection point y_g for the nominal, +5% and -5% cases are in black, red and blue dashed lines, respectively.

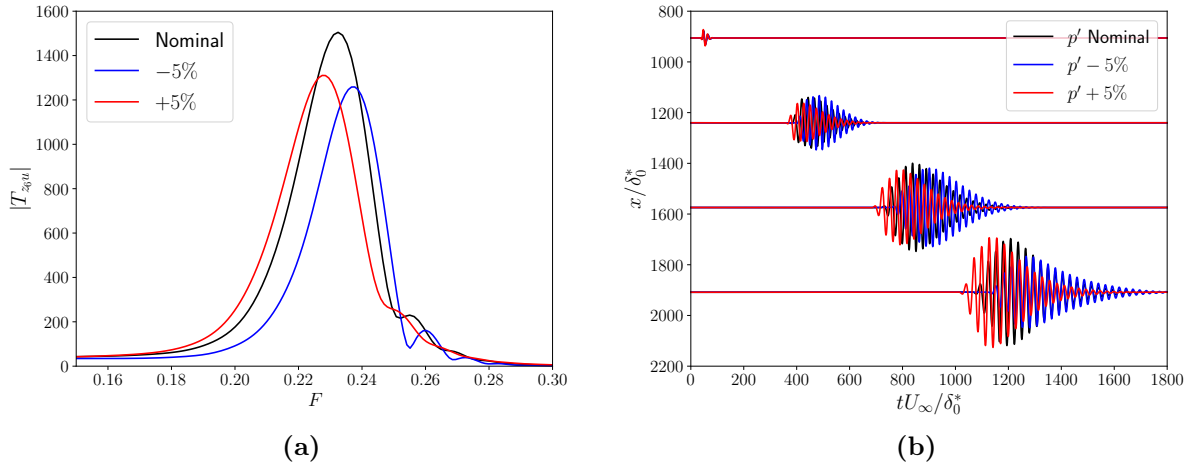


Figure 5.3: (a) Frequency spectrum (at $x_6 = 1766.7\delta_0^*$) and (b) spatio-temporal response of wall-pressure fluctuation sensors after an impulse of u .

$F|T_{z(x)w}|^2$ as a function of $\ln F$. As for the nominal case, the spectrum of $F|T_{z(x)w}|^2$ is quite narrow downstream of the domain for the $\pm 5\%$ cases, which means that the energy contribution of a sensor $z(x)$ for these cases is also mainly due to a restricted frequency range.

The position of the actuator u is kept constant when the free-stream velocity is varied and the actuator forcing field is therefore no longer centered around the generalized inflection point at $\pm 5\%$ as y_g moves with the base flow modifications (see figure 5.2). Thus, for the $\pm 5\%$ cases, the receptivity process to maximize the growth of the second Mack mode is less efficient than in the nominal case. This observation may explain why the most amplified frequency has a higher magnitude for the nominal case than for the $\pm 5\%$ cases after an impulse of u (see figure 5.3a), contrary to the case after an impulse of w (see figure 5.1a). The free-stream velocity variations of $\pm 5\%$ around $M_\infty = 4.5$ also induce a modification of the convective times, thus a modification of the transfer-function phase; a wave packet will arrive sooner (respectively later) with an increase (respectively a decrease) of the free-stream velocity (see figure 5.3b).

Therefore, although the range $M_\infty \in [4.275, 4.725]$ may seem restricted at first sight, it will be qualified as "wide" in this chapter because variations of $\pm 5\%$ of the free-stream velocity lead to important variations on the characteristics of both noise-induced and actuator-induced

disturbances.

5.2 Combined feedforward/feedback configurations

We saw in section 4.7 that although both the feedforward and feedback configurations were able to stay below an energy threshold (meaningful to delay transition to turbulence) in the nominal case until x_6 (position of the most downstream performance sensor used in the synthesis), the feedforward configuration has a greater potential by further reducing the local H_2 norm. However, this advantage is completely lost when velocity variations are considered and the feedback design appears at first sight to be the best compromise between performance and performance robustness. A first approach is therefore to try to take advantage of both the nominal performance of the feedforward configuration and the robust performance of the feedback configuration by combining the two in a single synthesis scheme to achieve the best trade-off regarding both aspects [188].

5.2.1 Synthesis method

5.2.1.1 Control setup

The block diagram of this configuration is represented in figure 5.4 with only transfer functions that can be obtained from observable inputs (namely, not the noise w but a measurement of it \tilde{y}_{ff}). The transfers K_{fb} and K_{ff} respectively represent the controllers of the feedback and feedforward parts of the combined design. These two controllers lead to a single actuator signal u . The transfer $T_{\tilde{y}_{fb}\tilde{y}_{ff}}$ predicts the measurement \tilde{y}_{fb} from the upstream measurement \tilde{y}_{ff} in the same way as in section 4.3. It is recalled that the tilde notation refers to the signal of the estimation sensor in the absence of the control: for the feedforward sensor $y_{ff} = \tilde{y}_{ff}$ but for the feedback sensor $y_{fb} = \tilde{y}_{fb} + T_{yu}u$. The transfer $T_{\tilde{y}_{fb}\tilde{y}_{ff}}$ is an artificial transfer function because it models a relation between two outputs of the system; the estimation sensors are not inputs of the boundary-layer system. For convenience, this transfer is computed as $T_{\tilde{y}_{fb}\tilde{y}_{ff}} = T_{y_{fb}w}T_{y_{ff}w}^{-1}$ from impulse responses instead of $T_{\tilde{y}_{fb}\tilde{y}_{ff}} = CPD_{\tilde{y}_{fb},\tilde{y}_{ff}}PSD_{\tilde{y}_{ff}}^{-1}$ (with CPD the cross power spectral density) [126, 155, 156] which requires several convective times to converge statistics.

As in equations 4.10 and 4.11, some delays may be discarded:

$$\|T_{z_i w}^c\|_2 = \|W_{\tilde{y}_{ff}}(T'_{z_i \tilde{y}_{ff}} e^{-\tau_{uy_{ff}}s} + T'_{z_i u}S(K_{fb}T'_{\tilde{y}_{fb}\tilde{y}_{ff}} e^{-\tau_{\tilde{y}_{fb}\tilde{y}_{ff}}s} + K_{ff}))\|_2. \quad (5.1)$$

with T' the transfer associated with $T(s)$ but without the input/output delay τ linked to the convective nature of the flow. The required delays $\tau_{uy_{ff}}$ and $\tau_{\tilde{y}_{fb}\tilde{y}_{ff}} = \tau_{y_{fb}u} + \tau_{uy_{ff}}$ are the same as in equations 4.10 and 4.11 and are linked to the actuator/estimation sensors distances. The impulse response from \tilde{y}_{ff} to \tilde{y}_{fb} is obtained by inverse Fourier transform of $T_{\tilde{y}_{fb}\tilde{y}_{ff}}$ and identified by the ERA; the ROMs of the other quantities are those of section 4.5.1.

5.2.1.2 Constrained minimisation problem

The CMP in equation 4.12 for this two-controller structure becomes:

$$\begin{aligned} & \text{minimize } \max_{i=1,\dots,6} (\|T_{z_i w}^c\|_2) \\ & \text{subject to } \|W_S S\|_\infty < 1, \|W_{KS} K_{ff}\|_\infty < 1 \text{ and } \|W_{KS} K_{fb} S\|_\infty < 1, \end{aligned} \quad (5.2)$$

with the controller structures developed in section 4.5.2. This CMP only includes ROMs of the nominal $M_\infty = 4.5$ case as before. In this combined feedforward/feedback configuration, two

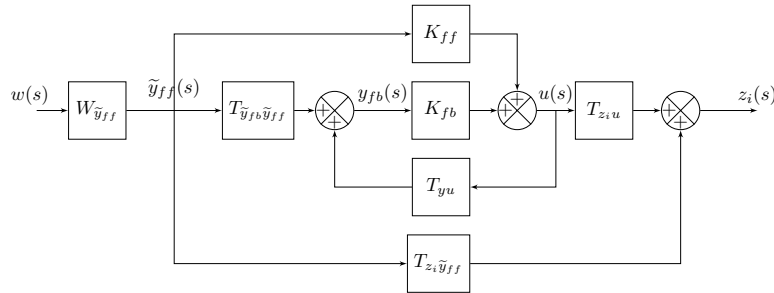


Figure 5.4: Block diagram of a combined feedforward/feedback configuration.

solutions are tested. The first solution is to obtain the feedforward and feedback controllers sequentially (denoted ‘Fb+Ff_Sequ’); this means taking the feedback controller of section 4.7 and then solving the CMP in equation 5.2 with the feedforward controller K_{ff} as the only unknown. The second solution is to obtain the feedforward and feedback controllers simultaneously (denoted ‘Fb+Ff_Simu’) and the CMP in equation 5.2 is solved with both K_{ff} and K_{fb} as unknowns.

The resulting combined configurations are implemented in the DNS solver *elsA*. These controllers satisfy the same constraints in terms of stability margins ($\|W_S S\|_\infty < 1$) and performance robustness to noisy estimation sensors ($\|W_{KS} K S\|_\infty < 1$) as the baseline LTI feedforward/feedback controller designed at a single operating point which performed well with regard to these two criteria. Therefore, we will focus on the ability of the controllers to maintain performance in terms of amplitude reduction over the entire range of free-stream velocity fluctuations. The baseline feedforward and feedback controllers of section 4.7 are denoted ‘Ff’ and ‘Fb’, respectively.

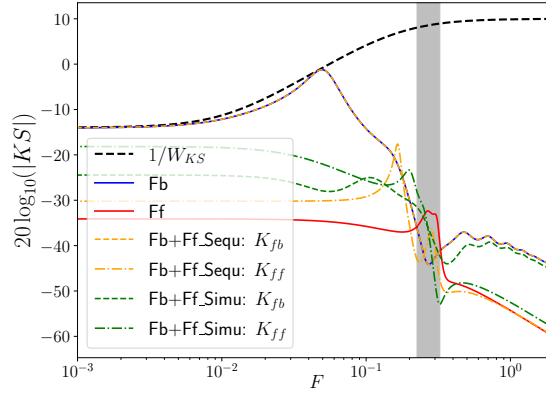
5.2.2 Performance on the design point

For the on-design $M_\infty = 4.5$ case, the quantity $|KS|$ is plotted in figure 5.5a for both Fb+Ff_Sequ (orange dashed lines) and Fb+Ff_Simu (green dashed lines); for these combined configurations, the feedforward controller K_{ff} is plotted in dot-dashed lines while the feedback controller K_{fb} is represented by dashed lines. All these controllers obviously obey the template $1/|W_{KS}|$ and roll-off at high-frequencies. In the frequency range of the amplification of the second Mack mode from the actuator to the end of the domain ($F \in [0.225, 0.324]$, see figure 5.1), symbolized by the grey shaded area in figure 5.5a, the dynamics of $|KS|$ of the combined configurations are far from those of the baseline Fb (blue solid line) and Ff (red solid line) controllers (except for K_{fb} of the Fb+Ff_Sequ and Fb cases which are equal by design). Note that the frequency spectrum of the actuator signal is $|u| = |KS\tilde{y}| = |KS W_{\tilde{y}} w|$; so even if the controllers have high gains at low-frequency, the actuator activity is moderate/low in this range as $|W_{\tilde{y}}|$ is high in the second Mack mode frequency range and low elsewhere (see figure 4.20).

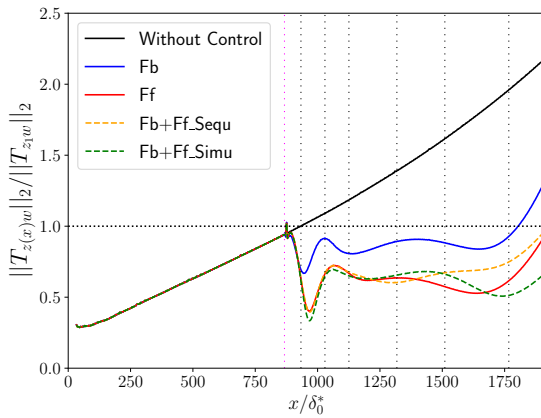
The evolution of the local H_2 norm of $T_{z(x)w}$ is represented in figure 5.5b and summarized in table 5.1. Like the baseline Fb and Ff controllers, the Fb+Ff_Sequ and Fb+Ff_Simu cases stay below the energy threshold $\|T_{z_1 w}\|_2$ at least up to x_6 thanks to the minimization of $\max_{i=1,\dots,6} (\|T_{z_i w}^c\|_2)$ in the synthesis. The Fb+Ff_Sequ case reduces the local H_2 norm more than the baseline Fb all along the domain, but reduces slightly less than the baseline Ff configuration, which has only one controller. The Fb+Ff_Simu configuration has the best results in terms of reduction of local H_2 norm but remains relatively close to the Ff design; indeed, compared to the Ff case, the Fb+Ff_Simu case decreases $\max_{x_1 < x < x_6} \left(\frac{\|T_{z(x)w}^c\|_2}{\|T_{z_1 w}\|_2} \right)$ from 0.73 to 0.70 which represents a relative improvement of $\sim 4\%$. In terms of meeting the specifications of the CMP

| Case | $\max_{x_1 < x < x_6} \left(\frac{\ T_{z(x)w}^c\ _2}{\ T_{z_1 w}\ _2} \right)$ |
|-----------------|---|
| Without control | 1.96 |
| Fb+Ff_Simu | 0.70 |
| Ff | 0.73 |
| Fb+Ff_Seq | 0.75 |
| Fb | 0.92 |

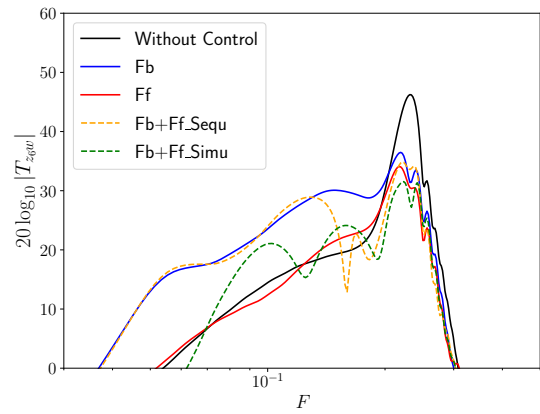
Table 5.1: Comparison of performance for the different cases. They are ranked from best to worst according to the performance metric $\max_{x_1 < x < x_6} \left(\frac{\|T_{z(x)w}^c\|_2}{\|T_{z_1 w}\|_2} \right)$ which is related to the minimization term in the CMP equation 5.2.



(a)



(b)



(c)

Figure 5.5: (a) Gain of KS and of the constraint $1/W_{KS}$ for the $M_\infty = 4.5$ case. For the combined configurations, the quantity $|KS|$ of the feedback (respectively feedforward) controller is represented with dashed line (respectively dot-dashed line). The grey shaded area represents the frequency range to control from the actuator to the end of the domain. (b) Evolution of the local H_2 norm of $T_{z(x)w}$. For vertical and horizontal dotted lines, same caption as in figure 4.14c. (c) Gain of $T_{z_6 w}$.

in equation 5.2, the best configuration is the Fb+Ff_Simu (see table 5.1) because it meets all the constraints and reduces more $\max_{i=1,\dots,6} (\|T_{z_{iw}}^c\|_2)$ than the Fb+Ff_Sequ and baseline controllers. For all the controlled cases, the reduction of the local H_2 norm arises from the reduction of the dominant frequencies (see figure 5.5c); indeed, an H_2 norm corresponds to a integrated gain over all frequencies. The Fb+Ff_Sequ case has the same behaviour as the baseline Fb at low-frequencies, *i.e.* amplification, and it has a similar behaviour as the baseline Ff only in the dominant frequencies of the second Mack mode. The quantity $|T_{z_{6w}}^c|$ is comparable on the entire frequency range between the Fb+Ff_Simu and the baseline Ff cases.

In summary, the combined feedforward/feedback configurations provides similar nominal performance as the baseline feedforward controller. It remains to check that the combined configurations are as robust in performance as the baseline feedback controller to obtain an optimized strategy maintaining performance in terms of disturbance amplitude reduction over the entire range of free-stream velocities.

5.2.3 Performance robustness

For the off-design $\pm 5\%$ points, the evolution of the local H_2 norm is plotted in figures 5.6(a,b). Both Fb+Ff_Simu and Fb+Ff_Sequ cases fail to maintain performance over this wide free-stream velocity variations of $\pm 5\%$ and increase the amplitude of the instabilities compared to the uncontrolled case on a wide portion of the domain. The Fb+Ff_Simu has the same behaviour as the baseline Ff at low-frequencies but amplifies the dominant frequencies even more (see figures 5.6(c,d)); the Fb+Ff_Sequ amplifies the low-frequencies as the baseline Fb but amplifies more the dominant frequencies. Hence, combining a feedforward controller to the baseline Fb (which is the case in the Fb+Ff_Sequ design) "spoils" the performance robustness of the feedback. The Fb+Ff_Sequ has better performance robustness than the Fb+Ff_Simu, which may be explained by the fact that the baseline Fb composing the Fb+Ff_Sequ is robust to velocity variations; the addition of a feedforward controller, although improving the performance on the nominal case due to the CMP solved, will deteriorate the performance of the baseline Fb on the off-design conditions as a feedforward controller has no robustness when velocity variations are considered. For the Fb+Ff_Simu design, the feedback controller of this configuration has potentially no nominal performance and performance robustness, which amounts to a pure feedforward structure as the baseline Ff one. Indeed, the specifications of the CMP in equation 5.2 only concern the nominal case; as the strongest minimization of $\max_{i=1,\dots,6} (\|T_{z_{iw}}^c\|_2)$ is obtained for a feedforward structure for a one controller architecture, the *syntune* algorithm may favor the feedforward controller over the feedback one when both are optimized simultaneously in the Fb+Ff_Simu design.

According to Tol et al. [188], the combined feedforward/feedback configuration (where both controllers are optimized simultaneously) gave the best trade-off between robust performance and robust stability because their simple feedback controller (equivalent to our Fb case) could be unstable due to LQG synthesis, contrary to their combined configuration. With modern robust synthesis methods though, stability robustness being not an issue, the baseline feedback controller appears as the best solution to ensure both nominal and robust performance if only the ROMs of the nominal case are used in the synthesis as the combined configurations cannot maintain performance over the wide range of free-stream velocity variations.

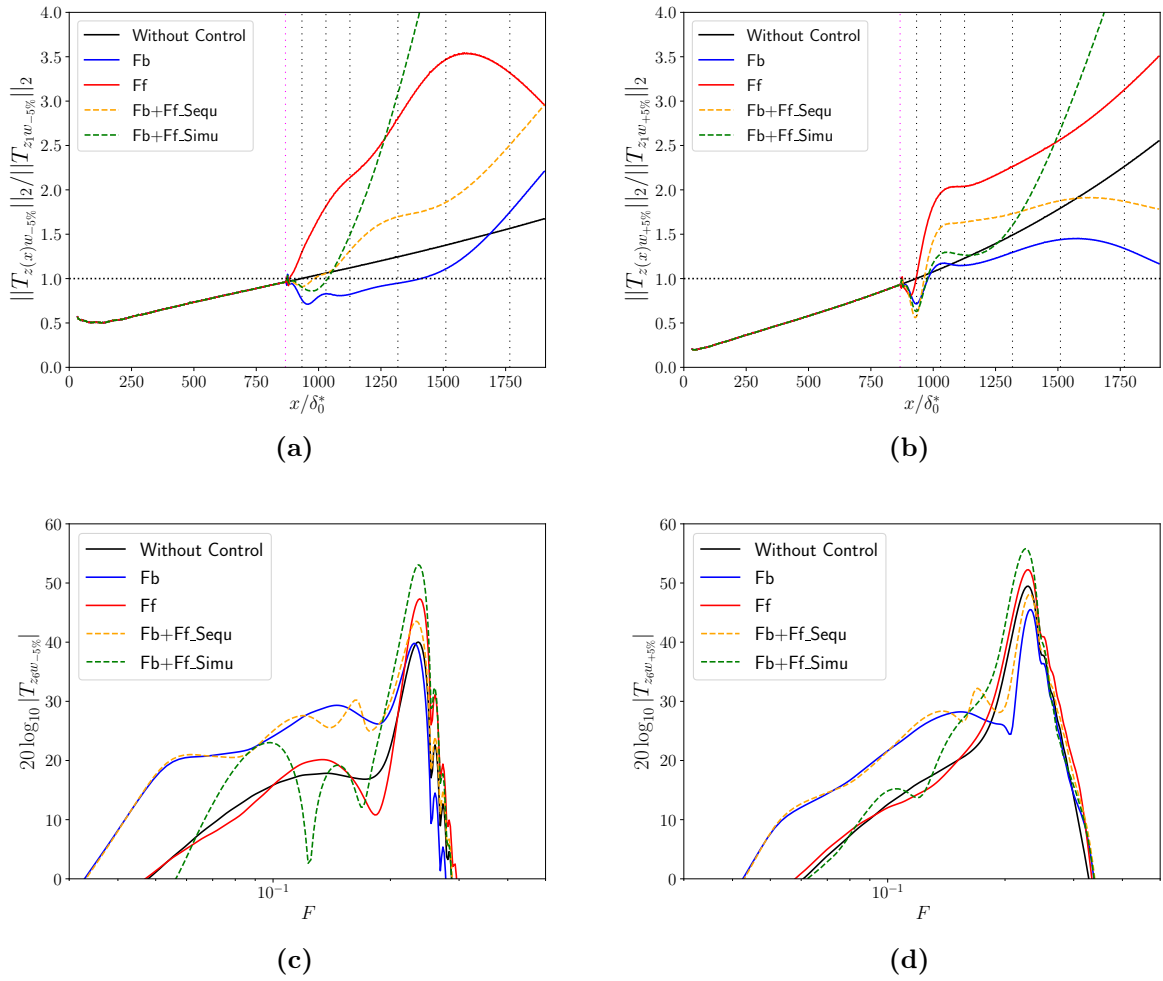


Figure 5.6: Evolution of the local H_2 norm of $T_{z(x)w}$ for the (a) -5% and (b) $+5\%$ cases. For vertical and horizontal dotted lines, same caption as in figure 4.14c. Gain of T_{z_6w} for the (c) -5% and (d) $+5\%$ cases.

5.3 Multi-model synthesis

Contrary to the previous syntheses which included in the CMPs only the ROMs of the nominal case and checked performance robustness a posteriori, the multi-model synthesis (see section 2.7) uses the ROMs at the three operating conditions (*i.e.* the nominal and $\pm 5\%$ cases) to maintain the performance over the entire range of free-stream velocities. Hence, performance robustness is now explicitly taken into account during the synthesis step and an improvement can be expected for both feedforward and feedback designs.

5.3.1 ROMs and synthesis method

5.3.1.1 Identification

Before carrying out the multi-model synthesis, it is necessary to identify $T_{z_i u}$, $T_{y u}$, $T_{z_i \tilde{y}}$ and $W_{\tilde{y}}$ for the $\pm 5\%$ cases. The identification follows the same procedure as for the nominal case (see section 4.5.1): the transfer functions $T_{z_i u}$, $T_{y u}$, $T_{z_i \tilde{y}}$ are identified by the ERA after shifting the time axis of the impulse responses to discard the unnecessary delays whereas $W_{\tilde{y}}$ is identified by vector-fitting method. The figures 5.7(a,b) display some identifications for the feedforward estimation sensor y_{ff} while the figures 5.7(c,d) display some identifications for the

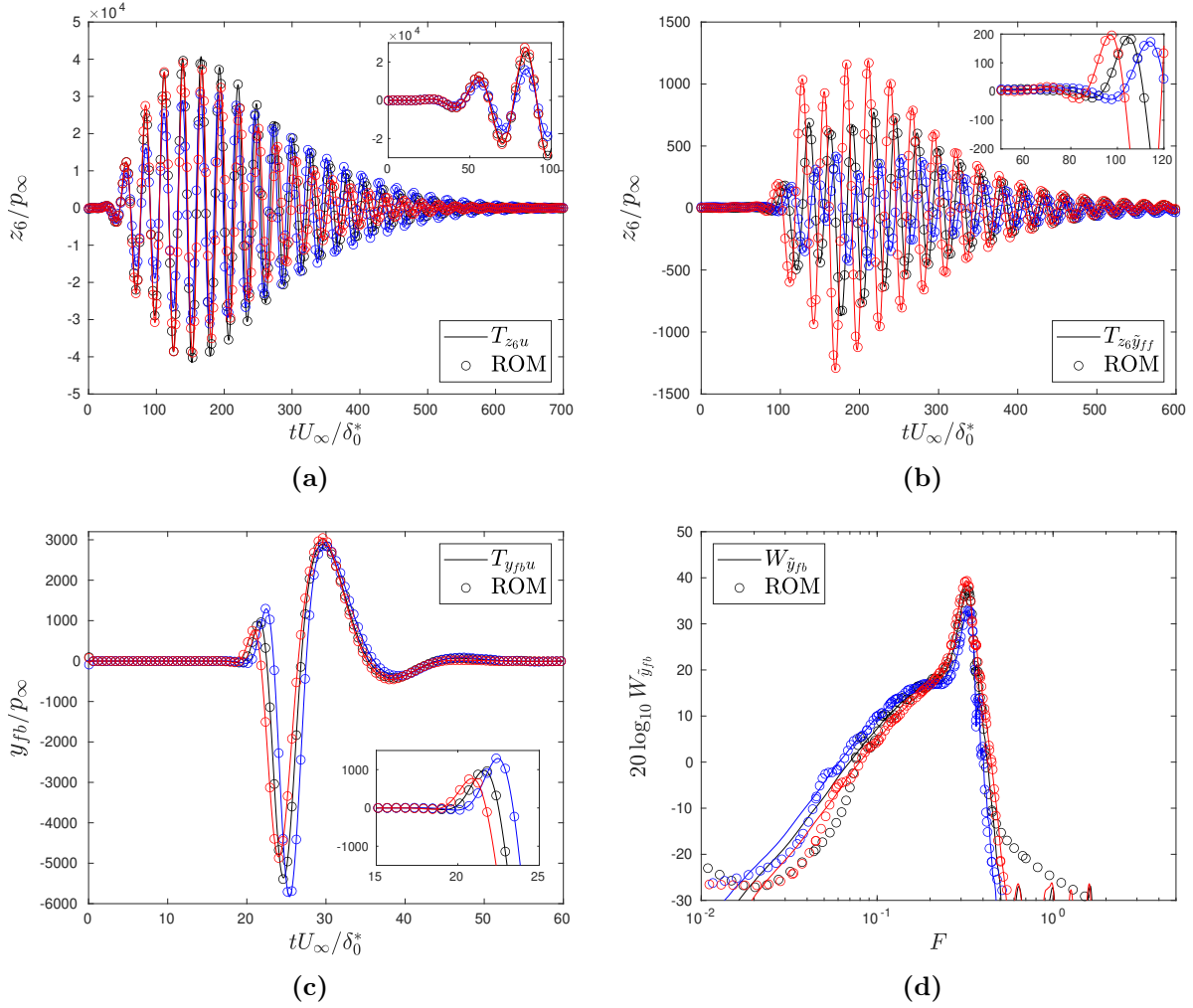


Figure 5.7: Comparison of the ROMs (circles) and impulse/frequency data (solid lines) for the $M_\infty = 4.5$ (in dark), the -5% (in blue) and $+5\%$ (in red) cases. (a) and (b) are displayed for a feedforward estimation sensor (with a shifted time axis for the suppression of the unnecessary dead times) while (c) and (d) stand for a feedback estimation sensor.

feedback estimation sensor y_{fb} . Note that for the transfer $T_{z_i\tilde{y}}$ (see figure 5.7b), the residual delay $e^{-\tau_{uy}s}$ explains that the residual convective times between the three cases differ, contrary to the identification of T_{z_iu} (see figure 5.7a). For the three design points, the sum of the orders of each ROM is 305 for a feedforward setup and 390 for a feedback one (due to the identification of the additional transfer T_{yu}).

5.3.1.2 Constrained minimisation problem

In order to compare the controllers resulting from the multi-model synthesis with the ones designed at a single operating point (the baseline Fb and Ff controllers), the same controller structure and specifications in terms of robustness to stability and robustness to performance despite noisy sensors are conserved. To maintain the performance over the entire range of free-stream velocities, it is sufficient to find a controller which satisfies the Constraint Problem (CP) described in equation 5.3.

of about few hours for a hundred random controller initializations and a parallel computation on 12 CPU cores (Intel(R) Xeon(R) CPU E5-2650 v3 @ 2.30GHz).

5.3.2 Performance on the design points

5.3.2.1 Multi-model feedforward and feedback

Figure 5.8a shows $|KS|$ (for the $M_\infty = 4.5$ case) for the two multi-model controllers and for the two baseline ones. The condition $\|W_{KS}KS\|_\infty < 1$ which was imposed in the CMPs is met as $1/W_{KS}$ (black dashed line) is above $|KS|$ for all frequencies in all designs. All four controllers have a roll-off of -20 dB per decade at high-frequencies due to the strictly-proper structure of all controllers. The quantity $|KS_{\pm 5\%}| = |K \frac{1}{1 - T_{y^u_{\pm 5\%}} K}|$ is not shown here to lighten the figure but it is very similar to the nominal case.

The evolution of the local H_2 norm of $T_{z(x)w}$ for the three design points ($M_\infty = 4.5$ and $\pm 5\%$ cases) of Multi_Fb and Multi_Ff are compared to the results of the baseline Fb and Ff controllers. These results are summarized in Table 5.2 and shown in figures 5.8(b,c,d). For the $M_\infty = 4.5$ case (see figure 5.8b), all multi-model syntheses are below the energy threshold $1.03\|T_{z_1w}\|_2$ (horizontal black dotted line) for the six positions x_i , which is expected because this is required in the CMPs (see equations 5.4 and 5.5). At a few abscissas on the flat plate, the local H_2 norm is found to be very slightly above the energy threshold; therefore, this threshold is not strictly met all along the domain. Nevertheless, the resulting controllers are deemed sufficiently satisfactory that no additional performance sensors are identified and added to the synthesis step.

The Multi_Ff design appears to be more robust in terms of performance compared to the baseline feedforward because it reduces to a larger extent the local H_2 norm after velocity variations (see figures 5.8(c,d)). Nevertheless, despite this improvement, the Multi_Ff setup amplifies the local H_2 norm compared to the uncontrolled case. This amplification of the local H_2 norm arises from the amplification of the dominant frequencies (see figures 5.8(e,f)). We notice that the low magnitude frequencies of $|T_{z_6w_{\pm 5\%}}|$ are not amplified in the Ff and Multi_Ff designs. The fact that the Multi_Ff amplifies the dominant frequencies less than the Ff results from the minimization of $\|T_{z_iw_{\pm 5\%}}^c\|_2$ for $i=1,2,3$. This minimization appears to mitigate the

poor performance of the feedforward structure for the $\pm 5\%$ cases and it even has a positive effect downstream of the domain even though only the three most upstream z_i were used in the CMP. Hence, it is possible to robustify a little a LTI feedforward controller thanks to

| Case | $\max_{x_1 < x < x_6} \left(\frac{\ T_{z(x)w}^c\ _2}{\ T_{z_1w}\ _2} \right)$ | $\max_{x_1 < x < x_6} \left(\frac{\ T_{z(x)w_{\pm 5\%}}^c\ _2}{\ T_{z_1w_{\pm 5\%}}\ _2} \right)$ |
|-----------------|--|--|
| Without control | 1.96 | 2.26 |
| Multi_Fb | 1.05 | 1.60 |
| Fb | 0.92 | 1.74 |
| Multi_Ff | 1.04 | 2.52 |
| Ff | 0.73 | 3.54 |

Table 5.2: Comparison of performance for the different cases. As the energy threshold imposed in the multi-model syntheses is considered satisfied for the $M_\infty = 4.5$ case for all control configurations

(*i.e.* $\max_{x_1 < x < x_6} \left(\frac{\|T_{z(x)w}^c\|_2}{\|T_{z_1w}\|_2} \right) \lesssim 1.03$), they are ranked from best to worst according to the performance metric $\max_{x_1 < x < x_6} \left(\frac{\|T_{z(x)w_{\pm 5\%}}^c\|_2}{\|T_{z_1w_{\pm 5\%}}\|_2} \right)$.

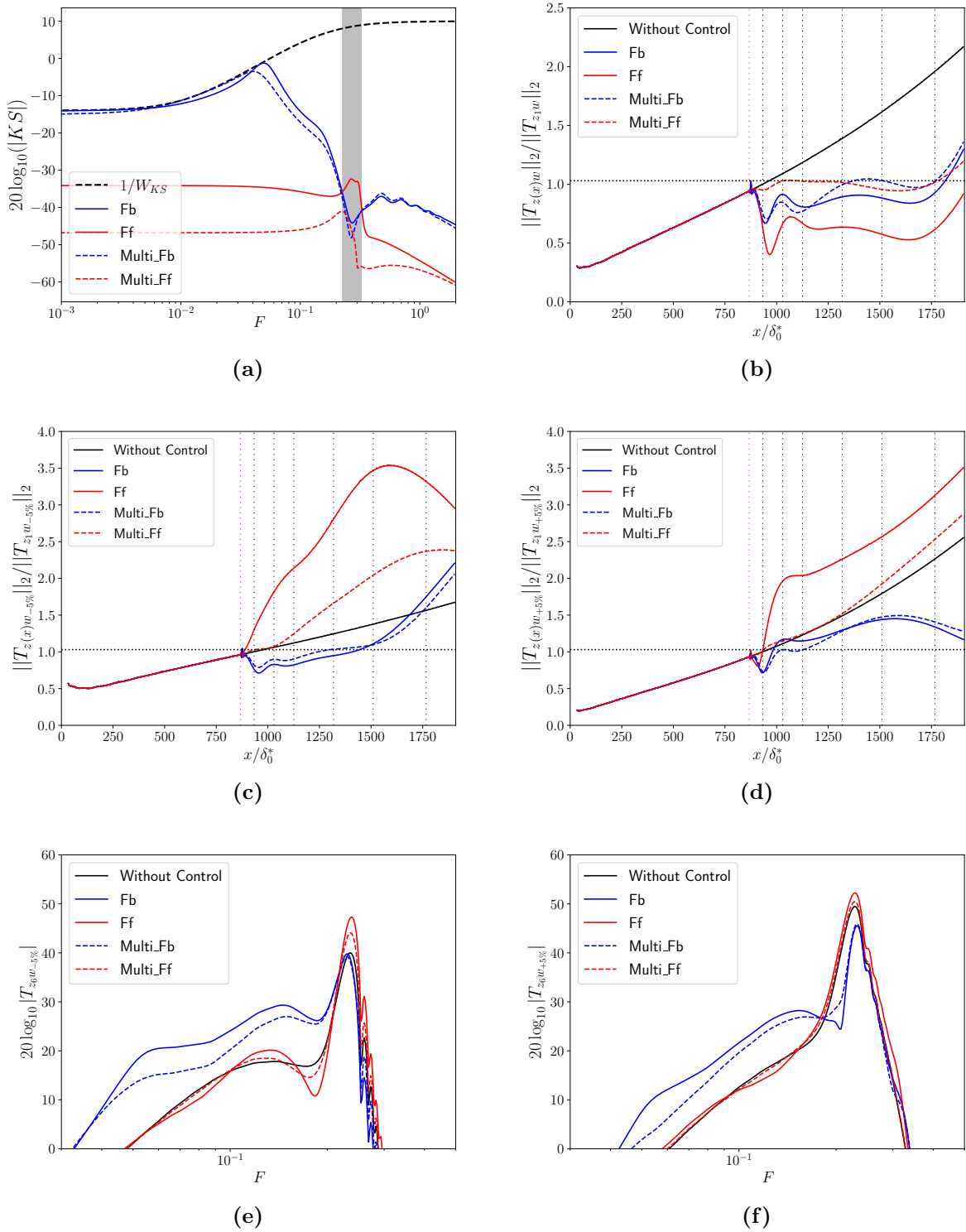


Figure 5.8: (a) Gain of KS and of the constraint $1/W_{KS}$ for the $M_\infty = 4.5$ case. The grey shaded area represents the frequency range to control from the actuator to the end of the domain. Evolution of the local H_2 norm of $T_{z(x)w}$ for (b) the nominal $M_\infty = 4.5$, (c) the -5% and (d) the $+5\%$ cases. The horizontal black dotted lines show the energy thresholds $1.03\|T_{z_1w}\|_2$ imposed in the multi-model syntheses for some sensors z_i . Same caption as figure 4.14c for vertical lines. Gain of T_{z_6w} for (e) the -5% and (f) the $+5\%$ cases.

multi-model synthesis. Nevertheless, asking to maintain performance over this wide free-stream velocity variations of $\pm 5\%$ appears to be too demanding for a LTI feedforward configuration, even with multi-model synthesis. The Multi_Fb controller avoids exceeding the energy of the uncontrolled system near the actuator for the $+5\%$ case contrary to the baseline Fb (see figure 5.8d) thanks to the constraint $\|T_{z_i w_{\pm 5\%}}^c\|_2 < 1.03 \|T_{z_1 w_{\pm 5\%}}\|_2$. The multi-model synthesis enables shaping precisely the evolution of the energy near the actuator. Moreover, thanks to the minimization of $\max_{i=4,5,6} (\|T_{z_i w_{\pm 5\%}}^c\|_2)$, the energy at the position x_6 in the -5% case is more strongly attenuated compared to the baseline feedback (see figure 5.8c). Compared to the Fb controller, the Multi_Fb case decreases $\max_{x_1 < x < x_6} \left(\frac{\|T_{z(x) w_{\pm 5\%}}^c\|_2}{\|T_{z_1 w_{\pm 5\%}}\|_2} \right)$ from 1.74 to 1.60 (see Table 5.2), which represents a relative improvement of 8%. The Multi_Fb configuration amplifies less the low magnitude frequencies of $|T_{z_6 w_{\pm 5\%}}|$ compared to the Fb setup; both controllers lead to similar values of $|T_{z_6 w_{\pm 5\%}}^c|$ for the dominant frequencies. Even with the Multi_Fb design, the amplitude of the perturbations at x_6 is almost not reduced compared to the uncontrolled configuration for the -5% case (see figures 5.8(c,e)).

5.3.2.2 Multi-model combined configuration

A multi-model synthesis on a configuration combining both a feedback and a feedforward controller is also tested (see figure 5.4). The constraint $\|W_{KS} K_{ff}\|_\infty < 1$ is added to the CMP in equation 5.4 which is solved with the two controller structure (labelled ‘Multi_Fb+Ff’). The K_{ff} and K_{fb} controllers of the combined configuration are only optimized simultaneously and not sequentially. This choice to focus only on the simultaneous configuration is explained by the fact that from the strict point of view of the specifications of the CMP in equation 5.2, the Fb+Ff_Simu case has obtained better results than the Fb+Ff_Sequ one (see section 5.2.2).

The Multi_Fb+Ff design obeys the threshold $1.03 \|T_{z_1 w}\|_2$ all along the domain for the nominal case (see figure 5.9a). The use of the ROMs at the $\pm 5\%$ cases in the synthesis step allows to keep the disturbance amplitude below the uncontrolled case over a fairly long distance along the plate for these cases (see figures 5.9(b,c)); thus, a certain performance robustness is obtained for this combined configuration, contrary to the combined configurations of the section 5.2 where only the ROMs at the $M_\infty = 4.5$ case were employed in the synthesis step. Nevertheless, compared to the Multi_Fb setup, the Multi_Fb+Ff configuration decreases $\max_{x_1 < x < x_6} \left(\frac{\|T_{z(x) w_{\pm 5\%}}^c\|_2}{\|T_{z_1 w_{\pm 5\%}}\|_2} \right)$ from 1.60 to 1.51, which represents a relative improvement of only 5.6%. This small improvement confirms the low added value of K_{ff} in the combined configuration when velocity fluctuations are considered.

As the combined configuration requires more effort to perform (need of two estimation sensors, more complex synthesis scheme, longer synthesis time) and brings only few gain, it is no longer considered in the rest of the manuscript.

5.3.2.3 Effect of controller order

A controller order of 5 was selected for multi-model syntheses in order to be consistent with the baseline cases. This choice of order 5 controller for the baseline cases came from preliminary tests performed for a very simplified CMP (see equation 4.13); the CMPs of the multi-model syntheses being richer, the controller order for the CMPs in equations 5.4 and 5.5 is raised up to 15 to increase the number of decision variables in order to improve the ability of the controllers to maintain performance over the wide free-stream velocity variations.

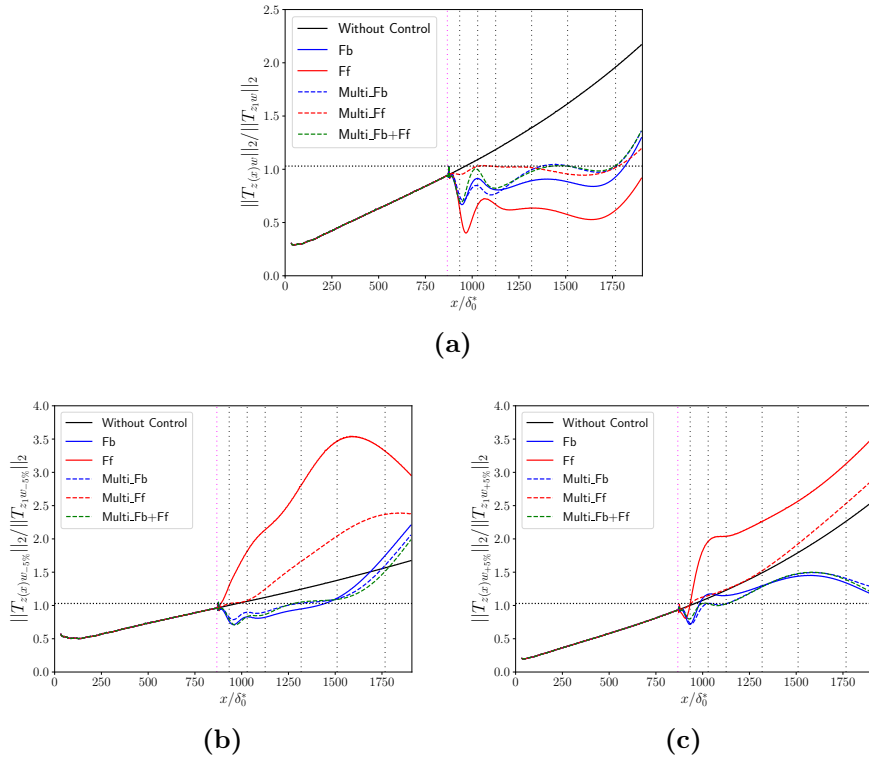


Figure 5.9: Evolution of the local H_2 norm of $T_{z(x)w}$ for the (a) $M_\infty = 4.5$, (b) -5% and (c) $+5\%$ cases. For vertical and horizontal dotted lines, same caption as in figure 5.8.

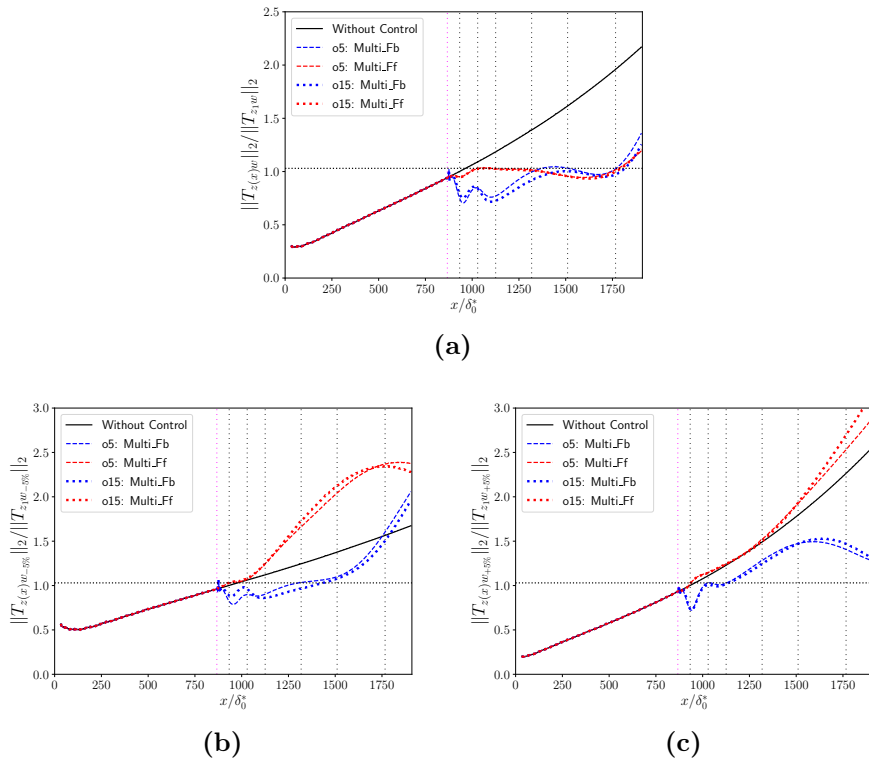


Figure 5.10: Same caption as in figure 5.9. Order 5 controllers and order 15 controllers are in dashed and dotted lines, respectively.

For the $M_\infty = 4.5$ case (see figure 5.10a), all the controlled cases satisfy the $1.03\|T_{z_1 w}\|_2$ threshold (because it is required in the CMPs). For the $\pm 5\%$ cases (see figures 5.10(b,c)), the order 15 controller does not bring any improvement for a feedforward structure. For the Multi_Fb configuration, the quantity $\max_{x_1 < x < x_6} \left(\frac{\|T_{z(x)w \pm 5\%}^c\|_2}{\|T_{z_1 w \pm 5\%}\|_2} \right)$ decreases from 1.60 for an order 5 controller to 1.53 for an order 15 controller (relative improvement of 4.3%).

As increasing the controller order marginally improves the results of the feedback structure and does not bring any improvement for the feedforward configuration, only the order 5 controller Multi_Fb and Multi_Ff are retained for further analysis.

5.3.3 Performance robustness

The previous section has shown that multi-model syntheses improve the results in terms of maintaining performance over the three design points ($M_\infty = 4.5$ and $\pm 5\%$ cases), but not sufficiently for the feedforward and only slightly for the feedback. Performance robustness of these order 5 Multi_Fb and Multi_Ff controllers is assessed by looking at the evolution of performance: i) between the design points, so in off-design conditions and ii) when gain/phase uncertainties are added to the ROMs to analyse in more detail the root cause of performance loss.

5.3.3.1 Off-design operating points

Controllers are tested at $U_\infty^{\pm 2.5\%} = U_\infty \pm 0.025U_\infty$ to check if the multi-model designs improve/deteriorate performance in off-design conditions compared to the baseline Fb and Ff controllers. Contrary to the $\pm 5\%$ cases, the Multi_Ff control is below the uncontrolled curves

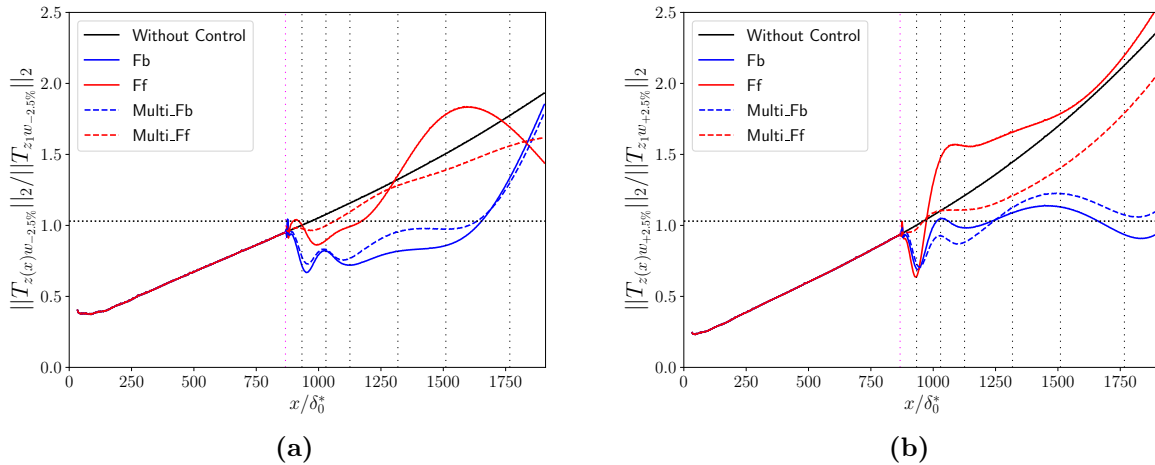


Figure 5.11: Evolution of the local H_2 norm of $T_{z(x)w}$ for (a) the -2.5% and (b) the $+2.5\%$ cases. The horizontal black dotted lines show the energy threshold $1.03\|T_{z_1 w \pm 2.5\%}\|_2$. Same caption as in figure 4.14c for vertical lines.

for both $\pm 2.5\%$ cases (see figure 5.11) and improves significantly the results compared to the Ff configuration. Therefore, the minimization in the CMP of $\|T_{z_i w \pm 5\%}^c\|_2$ was also beneficial for the $\pm 2.5\%$ cases. By working directly on the ROMs of the $\pm 2.5\%$ cases, even better results could be achieved. Hence, it would be possible to maintain performance over smaller free-stream velocity variations thanks to a LTI multi-model feedforward setup, which would remain impossible with

a simple feedforward structure designed at a single operating point. The Multi_Fb controller does not improve the results compared to the Fb controller for the $\pm 2.5\%$ cases: although both feedback control syntheses exceed the energy threshold at some abscissa of the domain, they both manage to significantly reduce the local H_2 norm along the entire domain. The multi-model feedback design therefore improves the results slightly on the on-design cases, but not between the design points as a simple feedback structure already has a natural ability to maintain performance around the nominal case.

5.3.3.2 Gain versus phase uncertainties

All the previous results were obtained using linearized DNS from the *elsA* solver. Changing the free-stream velocity impacts both convective time-delays and growth rates, which is reflected respectively in phase and gain changes. The aim of this section is to disentangle these two effects by modifying them independently. This analysis is performed only for z_6 , which plays a central role as it is the most downstream performance sensor and a substantial energy reduction must occur at its location to meet the energy threshold.

Assuming that all the nominal $M_\infty = 4.5$ ROMs are altered by a multiplicative factor $a_g \in \mathbb{R}$ on the gain (respectively a multiplicative factor $a_\tau \in \mathbb{R}$ on the delay) as if all noise/actuator induced perturbations are subject to the same amplitude variations (respectively convective time variations, *i.e.* phase variations), the transfer functions may be written as $T_{z_6u} = a_g T'_{z_6u} e^{-a_\tau \tau_{z_6u} s}$, $T_{yu} = a_g T'_{yu} e^{-a_\tau \tau_{yu} s}$, $T_{z_6\tilde{y}} = \frac{a_g T'_{z_6w} e^{-a_\tau \tau_{zw} s}}{a_g T'_{yw} e^{-a_\tau \tau_{yw} s}} = T'_{z_6\tilde{y}} e^{-a_\tau \tau_{z_6\tilde{y}} s}$. For the quantity $W_{\tilde{y}}$, it is not modified as it is just a frequency template and its phase/gain variations do not impact the results of the synthesis. For the gain and delay variations, from the equation 4.10, we obtain for a feedback design:

$$\frac{\|T_{z_6w}^c\|_2}{\|T_{z_6w}\|_2} = \frac{\|W_{\tilde{y}}(T'_{z_6\tilde{y}} + a_g e^{-a_\tau \tau_{yu} s} T'_{z_6u} K (1 - a_g e^{-a_\tau \tau_{yu} s} T'_{yu} K)^{-1})\|_2}{\|W_{\tilde{y}} T'_{z_6\tilde{y}}\|_2}. \quad (5.6)$$

For a feedforward design, from the equation 4.11, the relation is:

$$\frac{\|T_{z_6w}^c\|_2}{\|T_{z_6w}\|_2} = \frac{\|W_{\tilde{y}}(e^{-a_\tau \tau_{yu} s} T'_{z_6\tilde{y}} + a_g T'_{z_6u} K)\|_2}{\|W_{\tilde{y}} T'_{z_6\tilde{y}}\|_2}. \quad (5.7)$$

Hence, for the phase variations and a feedback design, only the ROMs of T_{z_6u} and T_{yu} are modified and can impact the result of the ratio $\frac{\|T_{z_6w}^c\|_2}{\|T_{z_6w}\|_2}$; for the feedforward design, only the ROM of $T_{z_6\tilde{y}}$ is modified when phase variations are considered. For the gain variations and both feedforward and feedback designs, only the ROMs of T_{z_6u} and T_{yu} are modified and can impact the result. In the following, the gain and delay variations are applied independently to decouple the effects: when a_g (respectively a_τ) varies, $a_\tau = 1$ (respectively $a_g = 1$). The case $a_g = a_\tau = 1$ corresponds to the ROMs of the nominal $M_\infty = 4.5$ case. The modules of $a_g T'_{z_6u}$ and $a_g T'_{yu}$ are displayed in figure 5.12a for some values of a_g . The phase of $e^{-a_\tau \tau_{yu} s} T'_{z_6u}$ and $e^{-a_\tau \tau_{yu} s} T'_{yu}$ for the feedback case and the phase of $e^{-a_\tau \tau_{yu} s} T'_{z_6\tilde{y}}$ for the feedforward one are displayed in figure 5.12b for some values of a_τ .

Performance robustness with respect to gain variations is evaluated in figure 5.12c. The Ff controller manages to reduce the H_2 norm over a wide range of $0 \leq a_g \leq 1.92$. Therefore, the feedforward controller is robust in performance despite gain errors/variations. The Fb controller is also robust despite gain variations but it yields better performance than the Ff case only far away from the nominal case ($a_g \gtrsim 1.7$). For $a_g > 2.53$, the Fb controller is unstable as this value corresponds to the GM of this controller (see figure 4.19d). The Multi_Fb appears slightly more robust in terms of maintaining performance than the Fb for large values of a_g and

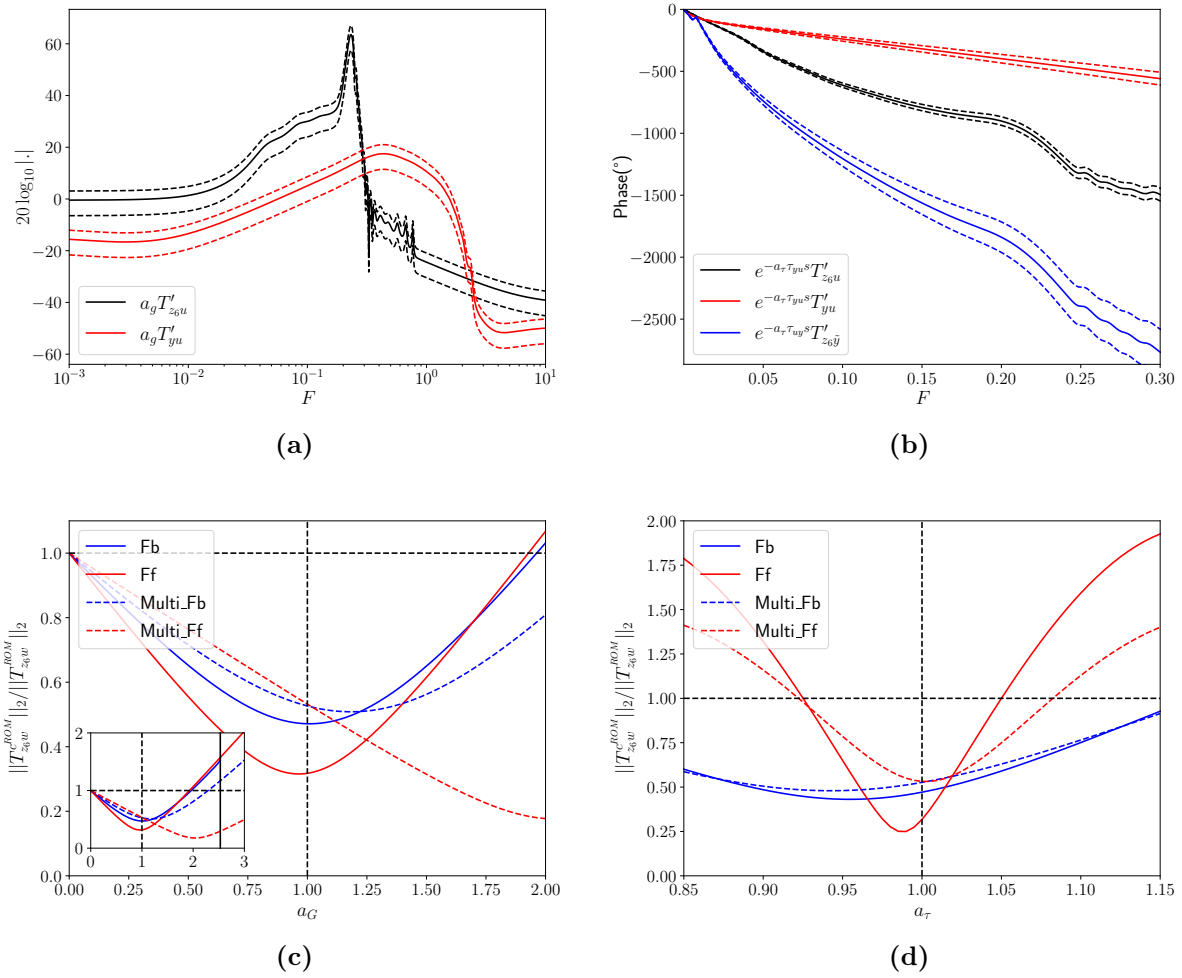


Figure 5.12: (a) Gain of the ROMs for $a_g = 1$ (solid lines), $a_g = 0.5$ and $a_g = 1.5$ (dashed lines). (b) Phase of the ROMs for $a_\tau = 1$ (solid lines), $a_\tau = 0.85$ and $a_\tau = 1.15$ (dashed lines). Evolution of the performance of the ROM at x_6 as a function of (c) gain variations a_g and (d) phase variations a_τ . Vertical dashed lines represent the performance on the nominal $M_\infty = 4.5$ ROM. Below (respectively above) the horizontal dashed lines, the control action reduces (respectively increases) the amplitude of perturbations. The vertical solid line in (c) displays the stability limit of the Fb controller for gain variations.

it is stable up to $a_g = 3.16$. The Multi_Ff presents an optimal point in terms of disturbance amplitude reduction for $a_g \sim 2$ (whereas the design point corresponds to $a_g = 1$). For $a_g < 1$, it reduces a bit less the H_2 norm compared to the other controllers. Consequently, the main point to note is that the feedforward controllers are robust in performance to gain variations and can perform better in terms of amplitude reduction than the feedback controllers over a wide range of a_g .

The performance robustness according to the phase variations is evaluated in figure 5.12d. The Multi_Fb configuration marginally improves performance robustness to phase variations compared to the baseline Fb, which is consistent with the results in section 5.3.2.1. As soon as we move away from the nominal case $a_\tau = 1$, the performance of the Ff setup deteriorates very sharply and is outperformed by the two feedback controllers and also by the Multi_Ff controller. Therefore, the robustness problem to maintain performance over the wide free-stream velocity variations of $\pm 5\%$ around $M_\infty = 4.5$ for the Ff case is mainly due to the variations of convective delays. The Multi_Ff controller appears more robust in performance to phase variations than

the Ff one, but the performance continues to deteriorate rapidly compared to feedback designs.

In summary, the feedforward controllers are robust to significant gain variations; if they are not able to maintain performance over wide free-stream velocity variations, it is mainly due to phase variations (thus convective delays). The feedback controller designed at one operating point has already a natural performance robustness over wide phase variations, which explains why multi-model feedback design only slightly improves the results.

5.4 Gain scheduling

As the single set of controller parameters provided by multi-model synthesis (*i.e.* one LTI controller) only enhances slightly the results in terms of maintaining performance over the three design points (due to the wide free-stream velocity operating range), gain scheduling is tested for this issue. Gain scheduling is a standard method to design controllers for dynamical systems over a wide range of operating points (see section 2.7). The gain scheduling method also uses the ROMs at different operating points as the multi-model synthesis, but the controllers parameters vary with the operating point considered because the gain scheduled control law is built from a family of LTI controllers, contrary to the multi-model synthesis where a single LTI controller is exploited for the entire operating range. One could be tempted to employ an adaptive controller structure where the parametrisation of the control law according to the scheduled variable is not known a priori, but this technique remains subject to the convergence of the steepest-descent method from one operating point to another contrary to the gain scheduling method.

5.4.1 Synthesis method

The gain scheduled control law is obtained by interpolating from a set of LTI controllers synthesized at various operating points. For one scheduling variable η , the polynomial interpolant of order $i - 1$ is:

$$K(\eta) = K_0 + K_1\eta + K_2\eta^2 + \dots + K_{i-1}\eta^{i-1}, \quad (5.8)$$

and the method consists in optimizing K_0, K_1, \dots, K_{i-1} for a set of i operating points (with i not necessarily equal to the number n of available models). A subset i (such as $i < n$) is used generally to simplify the synthesis and the results are checked a posteriori on the complete design point mesh. If the results are not satisfactory, the subset i is augmented and the critical cases are added in the synthesis.

In this study, we have three operating points; the selected subset of operating points is composed of the two extreme points corresponding to the $\pm 5\%$ cases and a linear relation is chosen:

$$K(\eta) = K_{-5\%}(1 - \eta) + K_{+5\%}\eta, \quad (5.9)$$

with $\eta = \frac{U_\infty^{\text{op}} - U_\infty^{-5\%}}{U_\infty^{+5\%} - U_\infty^{-5\%}} \in [0, 1]$ and U_∞^{op} the free-stream velocity of the operating point considered. The family of LTI controllers is composed of $K_{-5\%}$ and $K_{+5\%}$ which are feedforward/feedback controllers resulting of the CMP in equation 4.12 (with the six performance sensors z_i) for the -5% and $+5\%$ cases, respectively. Thus these two controllers will minimize disturbances while ensuring substantial stability margins and performance robustness despite noisy sensors on their respective cases. Between the end points $\eta = 0$ and $\eta = 1$, there is no guarantee on the behaviour of the closed-loop and the a posteriori checks will be done on the last operating point, the nominal $M_\infty = 4.5$ case (*i.e.* $\eta = 0.5$). The interpolation law is done directly from the transfer functions $K_{-5\%}(s)$ and $K_{+5\%}(s)$; it is not the different matrices of their state-space representation that are interpolated between them. The gain scheduled feedback and feedforward control laws will be labelled ‘GS_Fb’ and ‘GS_Ff’, respectively.

5.4.2 Performance on the design points

For the two design points (the $\pm 5\%$ cases) on which $K(\eta)$ is based, the evolution of the local H_2 norm along the flat plate is shown in figures 5.13(a,b) (dotted lines). It is compared to the performance of the baseline Fb and Ff controllers (solid lines, also referenced as $K_{0\%}$ for clarity in the following). Both GS_Fb and GS_Ff configurations remain below the $\|T_{z_1 w_{\pm 5\%}}\|_2$ threshold until the most downstream sensor position x_6 thanks to the minimization of $\|T_{z_i w_{\pm 5\%}}^c\|_2$ in the gain scheduling CMPs. As a reminder, this threshold was raised to $1.03\|T_{z_1 w_{\pm 5\%}}\|_2$ in the

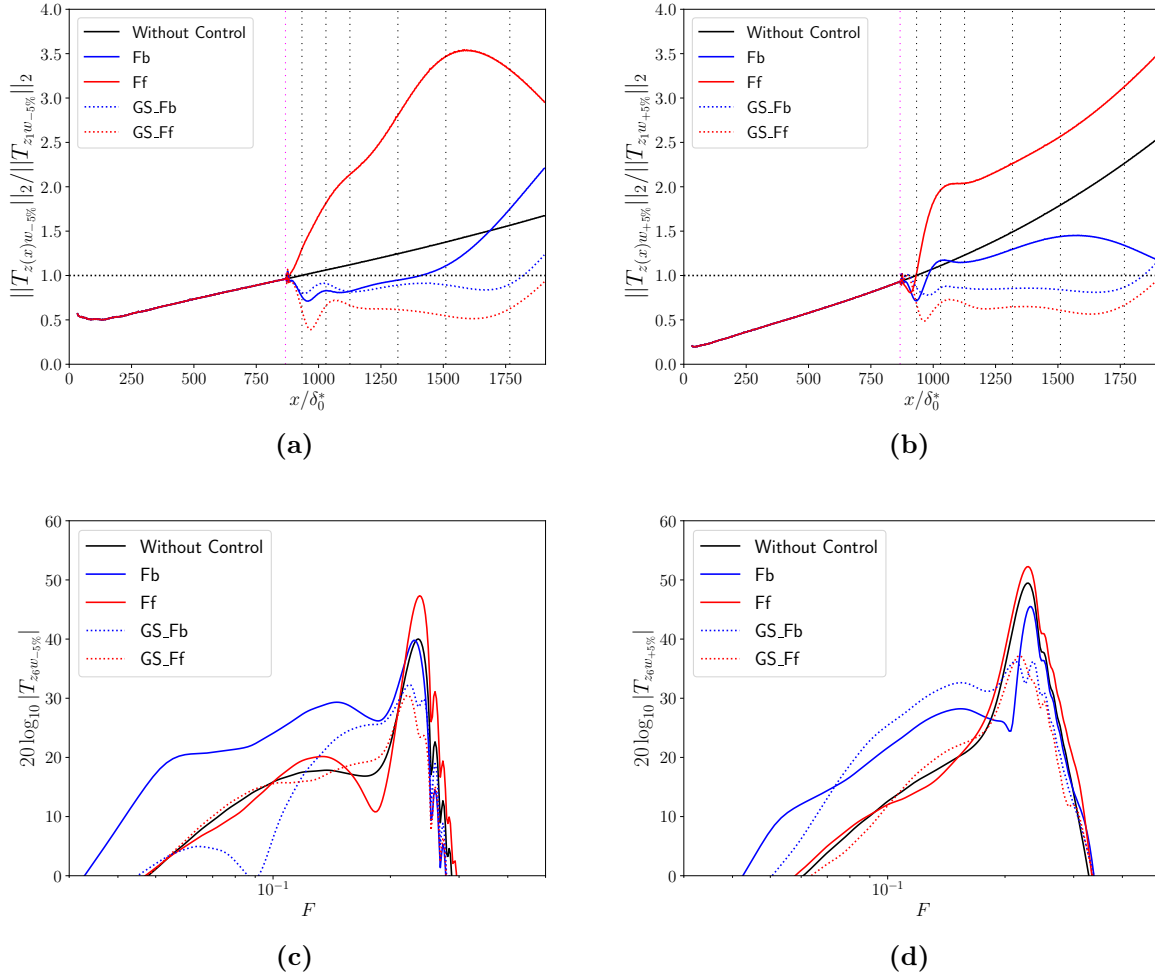


Figure 5.13: Evolution of the local H_2 norm of $T_{z(x)w}$ for the two gain scheduling design points: (a) the -5% and (b) the $+5\%$ cases. The baseline Fb/Ff controllers $K_{0\%}$ are in solid lines for comparison. For vertical and horizontal dotted lines, same caption as in figure 4.14c. Gain of $T_{z_6 w}$ for (c) the -5% and (d) the $+5\%$ cases.

multi-model feedback synthesis (to make the CMP feasible) and the $1.03\|T_{z_1 w_{\pm 5\%}}\|_2$ threshold could not even be met for the three most downstream z_i (and for none of the z_i in the multi-model feedforward design). The GS_Ff controllers are optimal in terms of amplitude reduction for the $\pm 5\%$ cases as these cases correspond to the design points, contrary to the Ff controller which worked in off-design conditions for these configurations and amplified the disturbances. Thus, the dominant frequencies at x_6 which were amplified in the Ff due to the out-of-phase action (so a phase problem) are drastically reduced with the gain scheduling (see figures 5.13(c,d)). This out-of-phase action is illustrated in figure 5.14 which compares the actuator signals u following an impulse of w for the -5% case. The signal of the GS_Ff controller

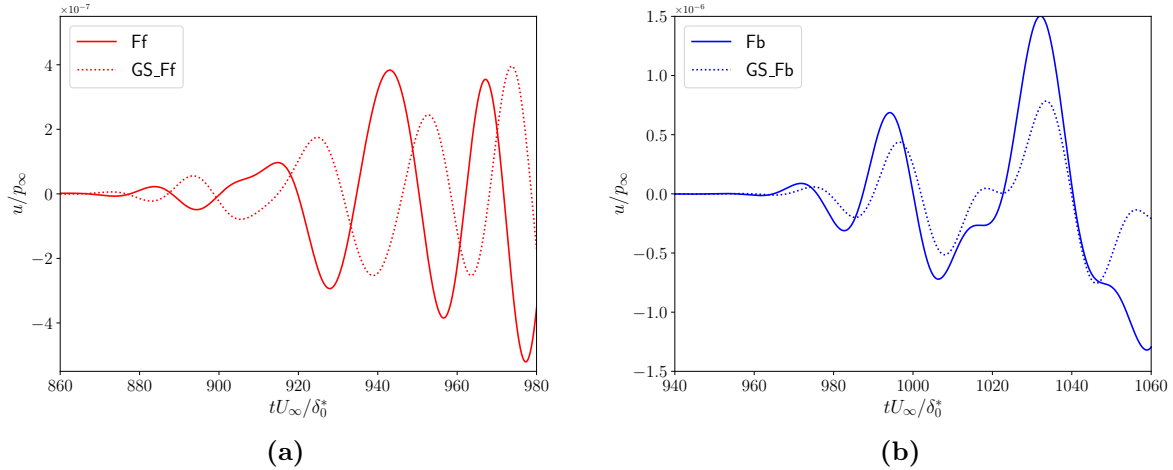


Figure 5.14: Actuator signals u following an impulse of w for the -5% case. The impulse of w defines the origin of time. (a) Feedforward controllers. (b) Feedback controllers. Ff and Fb designate baseline controllers $K_{0\%}$.

(see figure 5.14a) represents the optimal actuator-signal to cancel noise-induced perturbations as this controller is in on-design condition, whereas the Ff controller (designed at $M_\infty = 4.5$) is in off-design condition. The signal u of the Ff controller appears to be in phase opposition with respect to the signal u of the GS_Ff controller and induces constructive rather than destructive interference. In comparison, the signals u of the Fb and GS_Fb controllers are not in phase opposition and are rather similar, which illustrates the natural performance robustness of the baseline Fb controller with regard to phase variations.

5.4.3 Performance robustness

Both GS_Ff and GS_Fb controllers managed to meet the energetic threshold up to the most downstream sensor position x_6 for the $\pm 5\%$ cases. For the off-design operating conditions, we focus on the operating point $\eta = 0.5$ which corresponds to the $M_\infty = 4.5$ case. The gain scheduled controllers implemented derive from the interpolation of $K_{-5\%}$ and $K_{+5\%}$ such that $K(0.5) = 0.5(K_{-5\%} + K_{+5\%})$. The quantity $|K|$ resulting from this interpolation is shown in figure 5.15a in dotted lines (with in dashed lines $|K_{\pm 5\%}|$). For the interpolating controllers, we verify that we satisfy $\|W_S S\|_\infty < 1$ (see figure 5.15b) and $\|W_{KS} K S\|_\infty < 1$ (see figure 5.15c); this verification is mandatory because the gain scheduled controller at $\eta = 0.5$ does not immediately derive from a synthesis but from an interpolation and does not necessarily respect the constraints that we would like to enforce. The gain scheduled controllers at $\eta = 0.5$ are as robust in stability and performance despite noisy estimation sensors as the baseline $K_{0\%}$ Fb/Ff controllers (solid lines). In terms of performance, the GS_Ff law at $\eta = 0.5$ is unable to reduce the disturbance amplitude (see figure 5.15d), contrary to the GS_Fb law which performs close to the optimal Fb case specifically designed for this operating point. The GS_Fb setup almost satisfies the $\|T_{z_1 w}\|_2$ energy threshold until the last performance sensor z_6 used in the syntheses of $K_{-5\%}$ and $K_{+5\%}$. Therefore, the gain scheduling associated to a feedback design manages to maintain performance over the $M_\infty \in [4.275, 4.725]$ range whereas the GS_Ff controller is not robust in off-design conditions.

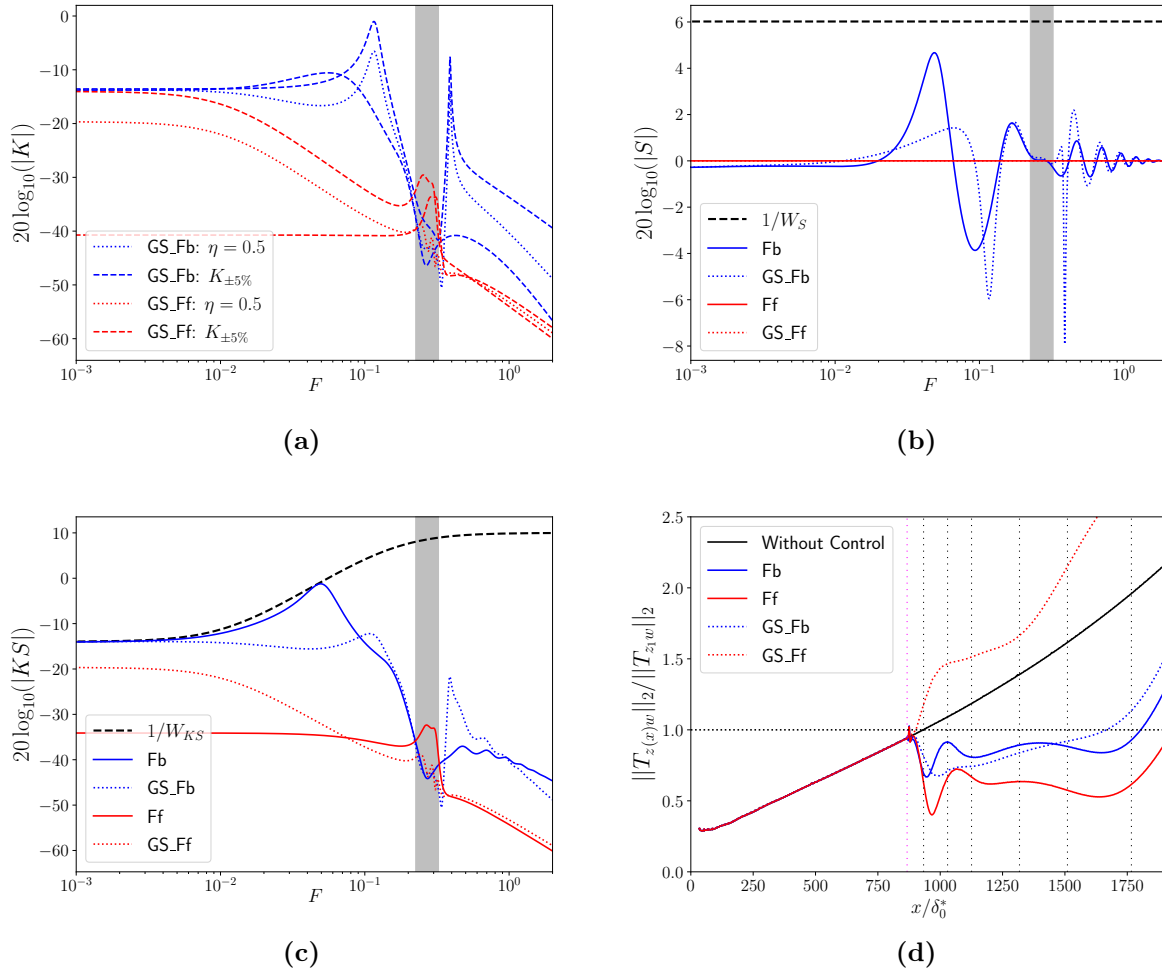


Figure 5.15: The baseline $K_{0\%}$ Fb/Ff controllers and the gain scheduled laws are in solid and dotted lines, respectively. Gain of (a) K (with in dashed lines $|K_{\pm 5\%}|$), (b) $|S|$ and (c) KS for the $M_\infty = 4.5$ case. (d) Evolution of the local H_2 norm for the $M_\infty = 4.5$ case (*i.e.* $\eta = 0.5$). At this point, the gain scheduled laws are off-design and the baseline $K_{0\%}$ Fb/Ff controllers are on-design. For (d), same caption as in figure 4.14c for vertical and horizontal dotted lines.

5.4.4 Piecewise gain scheduled law

As the results are not satisfactory for the GS_Ff, the operating point subset used to design the gain scheduled law is increased. The critical case $\eta = 0.5$ is considered and the baseline Fb and Ff controllers are employed in the interpolation, forming a piecewise gain scheduled law:

$$K(\eta) = \begin{cases} 2(K_{0\%} - K_{-5\%})\eta + K_{-5\%}, & \eta \in [0, 0.5] \\ 2(K_{+5\%} - K_{0\%})\eta + 2K_{0\%} - K_{+5\%}, & \eta \in [0.5, 1] \end{cases} \quad (5.10)$$

where a first sub-function uses the controller $K_{-5\%}$ and $K_{0\%}$ while a second one uses the controller $K_{0\%}$ and $K_{+5\%}$. For this piecewise laws, the performance on the design point $M_\infty = 4.5$ (*i.e.* $\eta = 0.5$) corresponds to the on-design performance of the baseline Fb and Ff. For the two other design points ($\pm 5\%$ cases), the performance of the piecewise law corresponds to the one described in section 5.4.2. So for these new GS_Fb and GS_Ff piecewise law, only the performance robustness is assessed here.

For the off-design operating conditions, we focus on the operating points $\eta = 0.25$ and $\eta = 0.75$ which correspond to the $\pm 2.5\%$ cases. For these two operating points, the controllers

implemented in *elsA* are $K(0.25) = 0.5(K_{0\%} + K_{-5\%})$ and $K(0.75) = 0.5(K_{0\%} + K_{+5\%})$, respectively. Both piecewise GS_Fb and GS_Ff configurations remain below the $\|T_{z_1 w_{\pm 2.5\%}}\|_2$

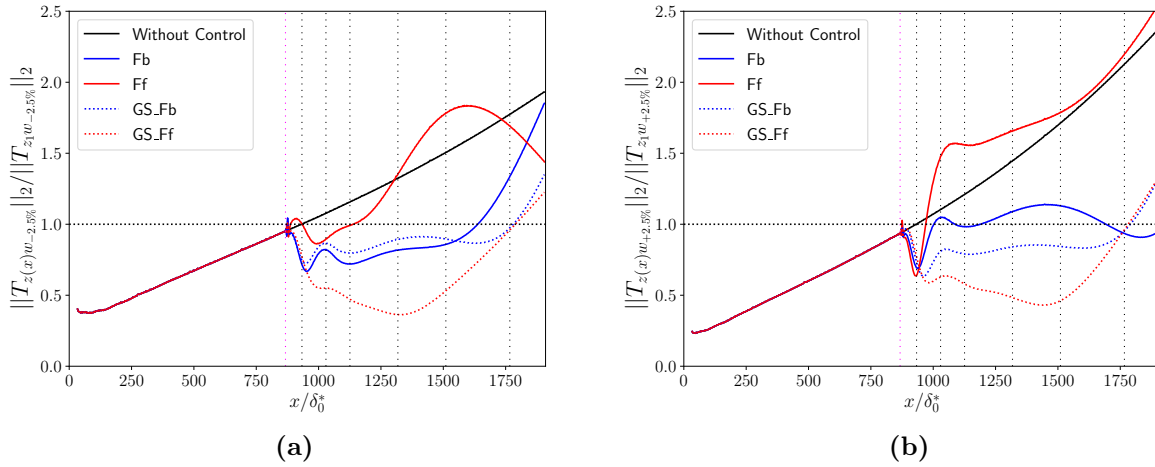


Figure 5.16: Evolution of the local H_2 norm of $T_{z(x)w}$ for two off-design points of the piecewise gain scheduled law: (a) the -2.5% and (b) the $+2.5\%$ cases. The baseline Fb/Ff controllers $K_{0\%}$ are in solid lines for comparison. For vertical and horizontal dotted lines, same caption as in figure 4.14c.

threshold until the most downstream sensor position x_6 , contrary to the previous baseline Fb and Ff controllers (see figure 5.16). Hence both piecewise gain scheduled feedforward and feedback laws allow to maintain performance in terms of amplitude reduction over the entire operating range $M_\infty \in [4.275, 4.725]$, contrary to the previous section where only the GS_Fb succeeded for this issue.

The performance robustness is also assessed by employing a scheduled parameter η that does not correspond to the real free-stream velocity condition; in realistic application, this amounts to consider an imperfect scheduling sensor that does correctly measure the free-stream velocity. The free-stream condition is at $\eta = 0.75$ (*i.e.* the $+2.5\%$ case) while the controllers implemented

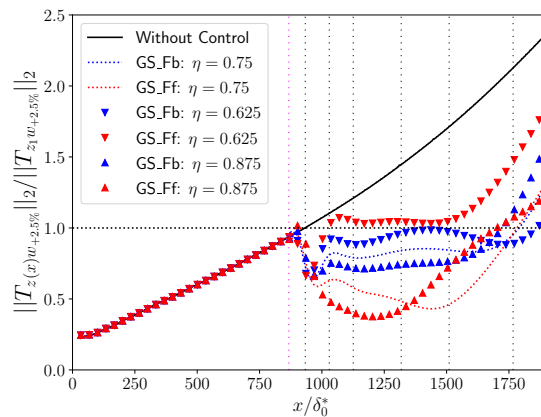


Figure 5.17: Evolution of the local H_2 norm of $T_{z(x)w}$ for the $+2.5\%$ case (*i.e.* $\eta = 0.75$). The gain scheduled cases with no error on η are in dotted lines while the cases with an imperfect scheduling sensor are plotted by triangular symbols. For vertical and horizontal dotted lines, same caption as in figure 4.14c.

in the *elsA* DNS are those corresponding to $\eta = 0.625$ (*i.e.* $K(0.625) = 0.75K_{0\%} + 0.25K_{+5\%}$) and $\eta = 0.875$ (*i.e.* $K(0.875) = 0.25K_{0\%} + 0.75K_{+5\%}$). A relative error of $\pm 1.22\%$ is thus

made on the value of the free-stream velocity. For this relatively low amount of errors, the GS_Ff still manages to reduce the disturbance amplitude compared to the uncontrolled case but it does not respect anymore the $\|T_{z_1 w_{\pm 2.5\%}}\|_2$ threshold if the scheduling variable is measured as $\eta = 0.625$ instead of $\eta = 0.75$ (see figure 5.17). Conversely, the GS_Fb cases with imperfect scheduling sensor maintain a performance close to the one of the GS_Fb at $\eta = 0.75$ (*i.e.* without measuring error) and almost satisfy the energy threshold up to x_6 . Note that if the scheduling variable error was higher (*e.g.* $\pm 5\%$), we would recover similar results that those in section 4.7.3.2 and the GS_Ff would not be robust in performance because it would amplify the amplitude of the disturbances compared to the uncontrolled case, contrary to the GS_Fb. Besides, one could imagine additional uncertainties such as free-stream density variations in addition of low scheduling variable errors and the feedback setup would far outweigh the feedforward one as it is more robust also for these density variations (see section 4.7.3.2).

In summary, in the frame of gain scheduled linear laws, one way to maintain performance over the entire operating range $M_\infty \in [4.275, 4.725]$ with a feedforward structure is to increase the operating point subset. In the case of a wider Mach range, representative of flight conditions, a feedback gain scheduled law could be built with a coarser design point mesh (and less sub-functions) than a feedforward gain scheduled law. Moreover, the feedback structure is more robust than the feedforward one in case of additional uncertainties/errors (*e.g.* free-stream density variations or the scheduled parameter η that does not correspond to the real free-stream velocity). Thus, the feedback gain scheduled law is the most suitable configuration to control instabilities over a wide range of operating conditions despite uncertainties/errors.

Chapter outcome summary:

Several synthesis methods have been investigated to obtain optimized laws to reduce the linear growth of second Mack mode instabilities in a 2D boundary layer over free-stream velocity variations of $\pm 5\%$ around $M_\infty = 4.5$. These variations lead to important changes on the input/output dynamics and are therefore considered wide from a control point of view. The controllers are obtained by combination of a feedforward and a feedback controller, by multi-model synthesis and by gain scheduling methods, that are all based on the structured mixed H_2/H_∞ synthesis. To compare these controllers with those designed at a single operating point (called baseline controllers), the same controller structure is imposed with similar specifications in terms of stability robustness and performance robustness despite noisy estimation sensors.

Combined feedforward/feedback does not bring satisfaction because adding a feedforward controller to a feedback one, although improving the nominal performance, deteriorates the natural robustness provided by the feedback when only the ROMs of the nominal case are used in the synthesis step.

Multi-model synthesis results in a single LTI controller based on ROMs corresponding to three distinct operating conditions. This methodology falls short in outperforming significantly the baseline designs. The multi-model feedforward, although more robust than the simple LTI feedforward controller designed at a single operating point, still amplifies the disturbances compared to the uncontrolled case due to the poor ability of a feedforward setup to be robust to phase variations. Conversely, the multi-model feedback significantly reduces the local H_2 norm along the domain and slightly improves the results on the $\pm 5\%$ cases compared to the baseline feedback controller. Indeed, multi-model synthesis makes possible to shape more precisely the evolution of the energy during velocity variations compared to synthesis with a single operating point. Nevertheless, meeting an energy threshold along the entire domain for all operating points remains impossible, even by using a multi-model combination structure (which presents similar results as the multi-model feedback) or by increasing the controller order.

Contrary to the multi-model method, gain scheduling does not result in a single control law but in a parameterized control law interpolating controllers synthesized at few design points. Gain scheduling does not improve the results in a feedforward setup when interpolation points are too far apart; adding interpolation points allows to maintain the performance over the free-stream velocity range considered but small errors on the scheduling variable measurement lead to a significant loss of performance. Gain scheduling yields significant enhancement in the feedback setup and makes possible to almost respect an energy threshold all along the domain over the entire operating range $M_\infty \in [4.275, 4.725]$ by using only two design points, while still being robust to additional uncertainties/errors. This gain scheduling feedback methodology could be extended to an even wider Mach range without any particular technical limit by simply adding more interpolation points.

In summary, the best trade-off between nominal performance and performance robustness for noise-amplifier flows necessarily requires a feedback configuration. As soon as a simple feedback controller does not provide desired performance throughout the different operating points, a gain scheduled feedback law is required.

Robust control of 3D instabilities in a supersonic boundary layer

| | | |
|------------|---|------------|
| 6.1 | 3D Flow configuration | 119 |
| 6.2 | Control setup | 120 |
| 6.2.1 | MIMO transfers: centralized problem | 120 |
| 6.2.2 | SISO transfers: decentralized problem | 121 |
| 6.3 | Control settings | 124 |
| 6.3.1 | Input disturbances | 124 |
| 6.3.2 | Actuators | 129 |
| 6.3.3 | Sensors for the synthesis | 131 |
| 6.4 | Identification and synthesis methods | 134 |
| 6.4.1 | Reduced-order models | 134 |
| 6.4.2 | Constrained minimization problems | 137 |
| 6.5 | Analysis of the controlled flow in the linear regime | 138 |
| 6.5.1 | Performance on the ROMs | 138 |
| 6.5.2 | Performance on the full system | 140 |
| 6.5.3 | Performance robustness | 144 |
| 6.5.3.1 | Noisy estimation sensors | 144 |
| 6.5.3.2 | Off-design operating conditions | 146 |
| 6.6 | Robustness to non-linearities | 148 |
| 6.7 | Transition to turbulence | 150 |

Chapter foreword:

In the present chapter, we will consider a 3D supersonic boundary layer at $M_\infty = 4.5$ and focus on obtaining a robust law to control finite-amplitude 3D instabilities and delay transition to turbulence. Hence, this chapter is an extension of the two previous ones where only spanwise invariant and linear perturbations were considered. One key question we wish to address is how to extend to the 3D case the methodology developed along the two previous chapters leading to a robust reactive control law in the 2D configurations? How does the control law, constructed from linear tools (ERA and structured mixed H_2/H_∞ synthesis) and targeting the linear growth of both first and second Mack modes, behave on a non-linear case of transition to turbulence? Answering these questions will show whether a methodology based on data-driven identification and robust synthesis on a feedback setup is relevant for the issue of delaying transition to turbulence of a supersonic boundary layer.

The chapter is organized as follows. Firstly, the 3D flow configuration is described. Secondly, the control setup and settings are provided, as well as the characterization of the noise-amplifier behaviour of this 3D configuration. Then the identification of the ROMs and the several CMPs solved are presented. The efficacy of control in the linear regime on and off-design is then analysed. Finally, robustness to non-linearities and transition delay are assessed.

6.1 3D Flow configuration

A three-dimensional compressible flow of air (modelled as a perfect gas) over a flat plate is considered. The parameters of Sutherland's law, the thermodynamic properties of air as well as the free-stream conditions are those of the chapters 4 and 5: $\mu_{\text{ref}} = 1.716 \times 10^{-5}$ Pa.s, $T_{\text{ref}} = 273.15$ K, $S = 110.4$ K, $\gamma = 1.4$, $r = 287$ J.K⁻¹.kg⁻¹, $Pr = 0.725$, $T_{\infty} = 65.149$ K, $U_{\infty} = 728.191$ m.s⁻¹, $p_{\infty} = 728.312$ Pa. The 3D computational domain used for the linearized DNS (where perturbations remain in the linear regime) is represented in figure 6.1: it consists of the 2D numerical domain used in the previous chapters and extruded of $L_z = 116.4\delta_0^*$ in the spanwise direction (with $\delta_0^* = 3.2656 \times 10^{-4}$ m the compressible displacement thickness at the inlet of the domain as in the 2D studies). The boundary conditions are periodic in the spanwise direction. A far-field, a no-slip adiabatic, a supersonic inlet and a supersonic outlet conditions are respectively applied at the top, at the bottom, at the inlet and at the outlet of the computational domain. Beyond the periodic conditions, the only difference in terms of boundary conditions compared to the 2D *elsA* DNS lies in the fact that the sponge zone is no more present in the far-field boundary and that the sponge zone is only constituted by the stretching of the mesh in the longitudinal direction for the downstream boundary (30 cells in the streamwise direction, *i.e.* $L_{\text{sponge}} = 91.9\delta_0^*$). Indeed, for the 3D calculations, we changed software and the option to add a source term in the sponge zone was no longer present. It was checked that the stretching alone is sufficient to avoid reflections that would impact the results in the useful domain.

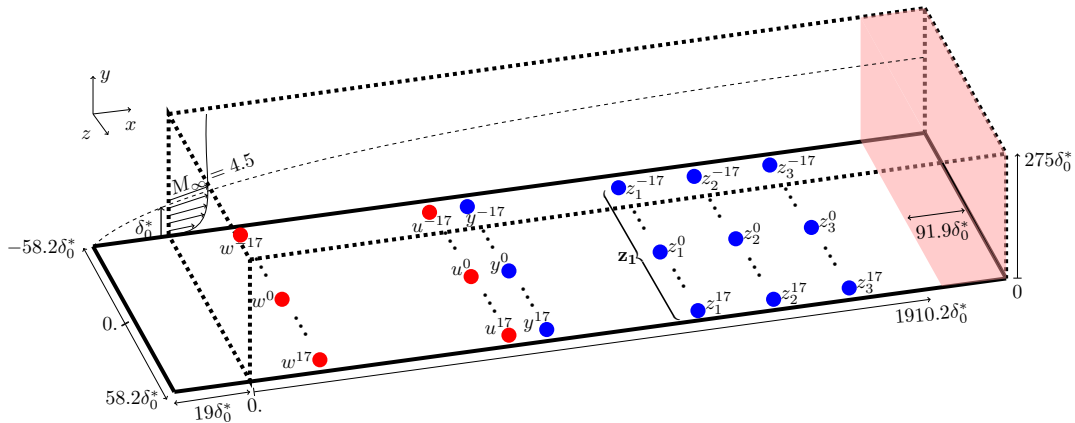


Figure 6.1: Diagram of the 3D computational domain used for linearized DNS. The red shaded region represents the sponge zone. Inputs and outputs of the control problem are in red and blue, respectively.

DNS are performed using the finite volume code *FastS* (see <https://w3.onera.fr/FAST/> and section 3.1.1). A resolution of $3200 \times 220 \times 176$ cells for the useful domain (*i.e.* not including the downstream sponge zone) is chosen with a uniform mesh in the x and z directions and a geometric law in the y direction. The resolution in the x and y directions is the one used in the 2D configuration. Convergence tests for grid and time-step independence are reported in appendix B. The 3D laminar base flow corresponds to the 2D simulation (see figure 4.1c) as the free-stream conditions are the same and the flow is homogeneous in the z -direction. For the DNS of transition to turbulence (see section 6.7), the length and the number of grid points of the previously described 3D domain will be doubled in the longitudinal direction in order to reach transition at the downstream end of the computational domain while remaining weakly non-linear at the streamwise position of the estimation sensors.

6.2 Control setup

6.2.1 MIMO transfers: centralized problem

Contrary to the 2D case, inputs and outputs are now also placed along the spanwise direction (see figure 6.1). The input/output are no longer scalars (associated with SISO transfer functions) but are now vectors (associated with MIMO transfer functions). In the following, we will suppose that the different elements constituting a input/output vector have the same streamwise and wall-normal positions; only their spanwise positions differ. The MIMO transfers $T_{\mathbf{y}\mathbf{w}}$ and $T_{\mathbf{z}_i\mathbf{w}}$ represent the impact of the disturbances \mathbf{w} on the estimation sensors \mathbf{y} and the performance sensors \mathbf{z}_i used in the synthesis, respectively. The impact of the actuators on the sensors is represented by the MIMO transfers $T_{\mathbf{y}\mathbf{u}}$ and $T_{\mathbf{z}_i\mathbf{u}}$. The controlled transfer from \mathbf{w} to \mathbf{z}_i (see section 2.4) is:

$$T_{\mathbf{z}_i\mathbf{w}}^c = T_{\mathbf{z}_i\mathbf{w}} + T_{\mathbf{z}_i\mathbf{u}}K(\mathcal{I} - T_{\mathbf{y}\mathbf{u}}K)^{-1}T_{\mathbf{y}\mathbf{w}}. \quad (6.1)$$

For a particular streamwise position associated with the performance vector $\mathbf{z}_i = [z_i^{-m}, \dots, z_i^j, \dots, z_i^m]^T$, the reduction of the r.m.s. value of each signal z_i^j along the spanwise direction following its excitation by the unitary zero-mean uncorrelated Gaussian white noise sources w^j translates into the reduction of:

$$\|T_{\mathbf{z}_i\mathbf{w}}^c\|_2 = \left(\frac{1}{2\pi} \int_{-\infty}^{+\infty} \text{Tr}(T_{\mathbf{z}_i\mathbf{w}}^{c*} T_{\mathbf{z}_i\mathbf{w}}^c) d\omega \right)^{1/2}, \quad (6.2)$$

with Tr the trace operator. Indeed, for unitary uncorrelated exogenous noises, we have:

$$\begin{aligned} \text{Tr}(T_{\mathbf{z}_i\mathbf{w}}^{c*} T_{\mathbf{z}_i\mathbf{w}}^c) &= \sum_{j=-m}^m \sum_{k=-m}^m |T_{z_i^j w^k}^c|^2, \\ &= \sum_{j=-m}^m \text{PSD}_{z_i^j}^c, \end{aligned} \quad (6.3)$$

with $T_{z_i^j w^k}^c$ the SISO transfer corresponding to the j th row and the k th column of $T_{\mathbf{z}_i\mathbf{w}}^c$. Hence, by using Parseval's identity [61, 180], we obtain $\|T_{\mathbf{z}_i\mathbf{w}}^c\|_2^2 = \lim_{T \rightarrow \infty} \frac{1}{T} \int_0^T \|\mathbf{z}_i(t)\|^2 dt$.

As in the 2D configuration, both $T_{\mathbf{y}\mathbf{w}}$ and $T_{\mathbf{z}_i\mathbf{w}}$ cannot be determined in a realistic setup as they are related to the unknown exogenous vector \mathbf{w} . In order to use only experimentally obtainable transfers in the identification and synthesis steps, the performance measurements are inferred from the estimation measurements in absence of control (denoted $\tilde{\mathbf{y}}$) with the MIMO "artificial" transfer $T_{\mathbf{z}_i\tilde{\mathbf{y}}}$, such as:

$$\mathbf{z}_i = T_{\mathbf{z}_i\tilde{\mathbf{y}}}\tilde{\mathbf{y}} + \mathbf{r}, \quad (6.4)$$

with \mathbf{r} a residual term corresponding to the part of the information in \mathbf{z}_i which is not seen by the measurements $\tilde{\mathbf{y}}$ (*e.g.* non-linearities, noise on \mathbf{z}_i , spectral leakage, linear contributions from other unmeasured inputs, etc.) [15, 126]. For this "artificial" input $\tilde{\mathbf{y}}$, the MIMO controlled transfer function of the new system is:

$$T_{\mathbf{z}_i\tilde{\mathbf{y}}}^c = T_{\mathbf{z}_i\tilde{\mathbf{y}}} + T_{\mathbf{z}_i\mathbf{u}}K(\mathcal{I} - T_{\mathbf{y}\mathbf{u}}K)^{-1}. \quad (6.5)$$

The MIMO transfer $T_{\mathbf{z}_i\tilde{\mathbf{y}}}$ is defined as:

$$T_{\mathbf{z}_i\tilde{\mathbf{y}}} = E[\hat{\mathbf{z}}_i(\omega)\hat{\tilde{\mathbf{y}}}(\omega)^*](E[\hat{\tilde{\mathbf{y}}}(\omega)\hat{\tilde{\mathbf{y}}}(\omega)^*])^{-1}, \quad (6.6)$$

with $E[\hat{\mathbf{z}}_i(\omega)\hat{\tilde{\mathbf{y}}}(\omega)^*]$ and $E[\hat{\tilde{\mathbf{y}}}(\omega)\hat{\tilde{\mathbf{y}}}(\omega)^*]$ the cross-power spectral density (CPSD) matrices [66] and $\hat{\mathbf{z}}_i/\hat{\tilde{\mathbf{y}}}$ the Fourier transforms of the vector of records. This way to estimate $T_{\mathbf{z}_i\tilde{\mathbf{y}}}$ minimizes the error due to noisy \mathbf{z}_i and assumes that the noise \mathbf{r} is not correlated with the measurements $\tilde{\mathbf{y}}$ [15, 126, 155, 156]. To estimate $\|T_{\mathbf{z}_i\mathbf{w}}^c\|_2$, which is the quantity one seeks to reduce, a weighting matrix $W_{\tilde{\mathbf{y}}}$ is also introduced by taking the square root of the CPSD matrix of $\tilde{\mathbf{y}}$:

$$W_{\tilde{\mathbf{y}}}W_{\tilde{\mathbf{y}}}^* = E[\hat{\tilde{\mathbf{y}}}(\omega)\hat{\tilde{\mathbf{y}}}(\omega)^*]. \quad (6.7)$$

Indeed, as soon as the residual term \mathbf{r} is negligible (*i.e.* $\text{PSD}_{\mathbf{r}} \sim 0$), reducing $\|T_{\mathbf{z}_i\mathbf{w}}^c\|_2$ or $\|T_{\mathbf{z}_i\tilde{\mathbf{y}}}^c W_{\tilde{\mathbf{y}}}\|_2$ is equivalent because:

$$\begin{aligned} \text{Tr}((T_{\mathbf{z}_i\tilde{\mathbf{y}}}^c W_{\tilde{\mathbf{y}}})^* T_{\mathbf{z}_i\tilde{\mathbf{y}}}^c W_{\tilde{\mathbf{y}}}) &= \text{Tr}(W_{\tilde{\mathbf{y}}} W_{\tilde{\mathbf{y}}}^* T_{\mathbf{z}_i\tilde{\mathbf{y}}}^{c*} T_{\mathbf{z}_i\tilde{\mathbf{y}}}^c), \\ &= \sum_{p,k} (W_{\tilde{\mathbf{y}}} W_{\tilde{\mathbf{y}}}^*)_{pk} (T_{\mathbf{z}_i\tilde{\mathbf{y}}}^{c*} T_{\mathbf{z}_i\tilde{\mathbf{y}}}^c)_{kp}, \\ &= \sum_{p,k} \text{CPSD}_{\tilde{\mathbf{y}}^p, \tilde{\mathbf{y}}^k} \left(\sum_{j=-m}^m T_{z_i^j \tilde{\mathbf{y}}^k}^{c*} T_{z_i^j \tilde{\mathbf{y}}^p}^c \right), \\ &= \sum_{j=-m}^m \left(\sum_{p,k} \text{CPSD}_{\tilde{\mathbf{y}}^p, \tilde{\mathbf{y}}^k} T_{z_i^j \tilde{\mathbf{y}}^k}^{c*} T_{z_i^j \tilde{\mathbf{y}}^p}^c \right), \quad \left. \begin{array}{l} \text{from 6.4 with} \\ \text{PSD}_{\mathbf{r}} \sim 0, \text{ see [15]} \end{array} \right\} \\ &= \sum_{j=-m}^m \text{PSD}_{z_i^j}^c, \\ &= \text{Tr}(T_{\mathbf{z}_i\mathbf{w}}^{c*} T_{\mathbf{z}_i\mathbf{w}}^c). \end{aligned} \quad (6.8)$$

In addition to minimizing $\|T_{\mathbf{z}_i\tilde{\mathbf{y}}}^c W_{\tilde{\mathbf{y}}}\|_2$, the stability of the closed-loop has to be guaranteed, which is realized by constraining H_∞ norms according to the small gain theorem (see section 2.4.2). The choice of the closed-loop transfer subject to the H_∞ constraint depends on the type of uncertainty considered and that can impact the stability of the MIMO system. As for the 2D study, it is chosen to constrain the H_∞ norm of the sensitivity function:

$$S = (\mathcal{I} - T_{\mathbf{y}\mathbf{u}}K)^{-1}. \quad (6.9)$$

Finally, one can seek to reduce the H_2 norm of the MIMO transfer KS . Indeed, the quantity KS may represent the transfer from noise \mathbf{n} (corrupting \mathbf{y}) to \mathbf{u} . Minimizing $\|KS\|_2$ means reducing the r.m.s. value of $\mathbf{u}(t)$ (*i.e.* the power spent by the control) in case of white noise \mathbf{n} on estimation sensors \mathbf{y} . Minimizing $\|KS\|_2$ appears as the most general way to limit actuator activity when the noise \mathbf{n} is unknown; if one seeks to desensitize the controller on a particular frequency range or if the properties of \mathbf{n} (*e.g.* frequency spectrum) are known, it may be of interest to constrain $\|W_{KS}KS\|_\infty$, with a well-chosen frequency template W_{KS} .

In summary and as for the 2D case, H_2 and H_∞ norms could be used to minimize/constrain $T_{\mathbf{z}_i\tilde{\mathbf{y}}}^c W_{\tilde{\mathbf{y}}}$, S and KS which are respectively associated with nominal performance, stability robustness and performance robustness despite noisy estimation sensors. Note that $T_{\mathbf{z}_i\tilde{\mathbf{y}}}$, $T_{\mathbf{z}_i\mathbf{u}}$, $T_{\mathbf{y}\mathbf{u}}$ and $W_{\tilde{\mathbf{y}}}$ which are required in these specifications can all be obtained in a realistic setup as the temporal data of \mathbf{z}_i , \mathbf{u} and \mathbf{y} would be available.

6.2.2 SISO transfers: decentralized problem

The question of working with MIMO centralized configuration, where all the inputs are connected to all the outputs, or with decentralized configuration, where only a subset of inputs are connected to the outputs, had already been raised in the case of incompressible boundary layer control [38, 168, 169]. Working with a decentralized approach allows to limit the interconnection between inputs and outputs in order to reduce the complexity of the synthesis in cases where the number of parameters becomes too large. Semeraro et al. [168, 169] used decentralized SISO system where one sensor y^j was connected to only one actuator u^j .

Their decentralized approach for the control of TS waves yielded unstable closed-loop while their decentralized approach led to similar results than the full centralized approach for the control of streaks. This was due to the strong cross-coupling among the input/output for TS waves, unlike streaks which were weakly dynamical coupled in the spanwise direction. In the same way, Dadfar et al. [38] connected only a subset of the actuators to sensors to reduce the controller complexity without compromising the efficiency. They realized this decentralized approach based on spanwise scale of the wavepacket but still remaining in the physical space (*i.e.* without using spanwise Fourier transform). Li and Gaster [101] were among the first to mention the need to have a spanwise spacing of each sensor/actuator smaller than half the minimum spanwise wavelength found in the wavenumber spectrum to resolve and cancel the three-dimensional characteristics of any growing disturbances. This way of working directly in the wavenumber space to avoid interconnections has been employed recently for the incompressible boundary layer control [126, 153, 156]. Yet, these studies synthesised controllers in the wavenumber space with an inverse feedforward method which raises the problem of performance robustness of their controllers. In our study, we will employ the modern synthesis tools leading to robust control laws to design the different controllers for each wavenumber that one seeks to control.

The flow is periodic in the spanwise direction and this direction is a statistically homogeneous one. Moreover, by considering that the objects composing an input/output vector are equispaced in the spanwise direction and have the same type (*i.e.* same type of sensors/actuators), all the MIMO transfers appear as circulant matrix (even $W_{\tilde{y}}$ as the square root of a circulant matrix is circulant [105]). A circulant matrix \mathcal{C} is fully specified by one vector (corresponding to first column or row of the circulant matrix) and the remaining columns/rows are cyclic permutations of this vector. Consequently, by introducing the new input and output variables $\hat{\mathbf{I}}$ and $\hat{\mathbf{O}}$

$$\hat{\mathbf{I}} = D_{\text{DFT}}\mathbf{I}, \quad (6.10a)$$

$$\hat{\mathbf{O}} = D_{\text{DFT}}\mathbf{O}, \quad (6.10b)$$

with \mathbf{I}/\mathbf{O} the input/output vectors associated with a MIMO circulant transfer $\mathcal{C}(s)$ and D_{DFT} the unitary discrete Fourier transform (DFT) matrix

$$D_{\text{DFT}_{jk}} = \frac{(e^{-2i\pi/(2m+1)})^{jk}}{\sqrt{2m+1}}, \quad 0 \leq j, k \leq 2m, \quad (6.11)$$

we obtain:

$$\begin{aligned} \mathbf{O}(s) &= \mathcal{C}(s)\mathbf{I}(s) \\ D_{\text{DFT}}^{-1}\hat{\mathbf{O}}(s) &= \mathcal{C}(s)D_{\text{DFT}}^{-1}\hat{\mathbf{I}}(s) \\ \hat{\mathbf{O}}(s) &= \underbrace{D_{\text{DFT}}\mathcal{C}(s)D_{\text{DFT}}^{-1}}_{\hat{\mathcal{C}}(s)}\hat{\mathbf{I}}(s). \end{aligned} \quad (6.12)$$

The matrix $\hat{\mathcal{C}}(s)$ is diagonal and it represents a MIMO transfer function in the frequency-wavenumber domain. As the DFT is a unitary transform, both H_2 and H_∞ norms are conserved such that $\|\hat{\mathcal{C}}(s)\|_{2,\infty} = \|\mathcal{C}(s)\|_{2,\infty}$. Moreover, as each dimensionless wavenumber $B_k = \frac{2\pi k}{L_z}\delta_0^*$ is

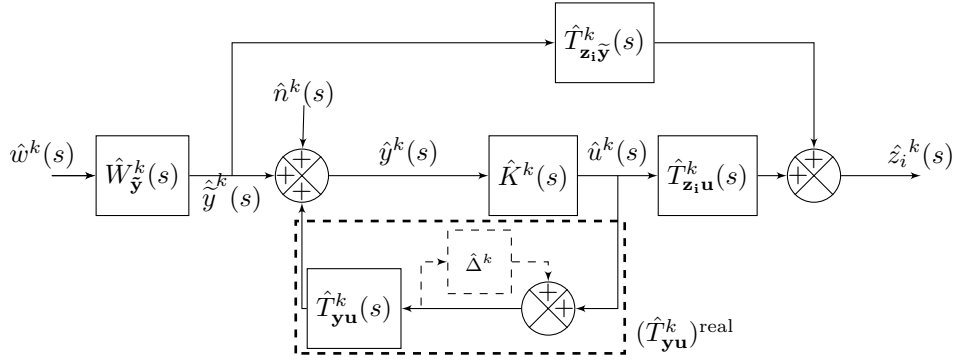


Figure 6.2: Block diagram of the 3D supersonic boundary layer system for a spanwise mode k as $B_k = \frac{2\pi k}{L_z} \delta_0^*$.

independent of the others (for linear perturbations), we have:

$$\begin{aligned}
 \text{minimize } \|\hat{\mathcal{C}}(s)\|_2 &= \text{minimize } \left(\frac{1}{2\pi} \int_{-\infty}^{+\infty} \sum_{k=-m}^{k=m} |\hat{\mathcal{C}}^k(i\omega)|^2 d\omega \right)^{1/2} \\
 &= \sum_{k=-m}^{k=m} \text{minimize } \left(\frac{1}{2\pi} \int_{-\infty}^{+\infty} |\hat{\mathcal{C}}^k(i\omega)|^2 d\omega \right)^{1/2} \\
 &= \sum_{k=-m}^{k=m} \text{minimize } \|\hat{\mathcal{C}}^k(s)\|_2,
 \end{aligned} \tag{6.13}$$

with $\hat{\mathcal{C}}^k(s)$ one of the elements of the diagonal of the MIMO transfer $\hat{\mathcal{C}}(s)$. The element $\hat{\mathcal{C}}^k(s)$ corresponds to the SISO transfer associated with the particular spanwise mode k . In the same way, as $\hat{\mathcal{C}}(s)$ is diagonal, imposing an H_∞ constraint turns to:

$$\begin{aligned}
 \|\hat{\mathcal{C}}(s)\|_\infty &< \text{Constraint} \\
 &\Leftrightarrow \\
 \sup_{\omega \in \mathbb{R}} \sigma_{\max}(\hat{\mathcal{C}}(i\omega)) &< \text{Constraint} \\
 &\Leftrightarrow \\
 \forall k, \sup_{\omega \in \mathbb{R}} |\hat{\mathcal{C}}^k(i\omega)| &< \text{Constraint},
 \end{aligned} \tag{6.14}$$

with σ a singular value.

In summary, the centralized MIMO problem where all the inputs are connected to all the outputs is transformed to several SISO decentralized problems in the wavenumber space where the interconnection of the different spanwise modes is impossible. These problems are equivalent but using the wavenumber space allows to solve multiple low order problems instead of only one high order problem. Indeed, the structured mixed H_2/H_∞ synthesis uses non-smooth/non-convex optimization techniques that are not suitable for large systems. Therefore, although the centralized and decentralized problems are mathematically equivalent, their numerical resolution may differ when the number of decision variables to optimize simultaneously is important while the decision variables can be optimized independently in the wavenumber space. Moreover, with the multiple SISO decentralized problems, different CMPs could be used depending on the spanwise mode: one could seek to increase performance robustness only for the spanwise modes that would imply the largest performance variations, one could seek to increase stability

margins for the spanwise modes where the uncertainty is the greatest, etc. Working with the several SISO CMPs is a flexible approach and makes it easier to understand the phenomena involved as well as the results (*e.g.* the controller obtained for each wavenumber).

The SISO block diagram of the 3D supersonic boundary layer for a spanwise mode is depicted in figure 6.2. It is composed of the four quantities required for the identification and the synthesis which are now associated with a particular spanwise mode k : $\hat{W}_{\hat{\mathbf{y}}}^k$, $\hat{T}_{\mathbf{y}\mathbf{u}}^k$, $\hat{T}_{\mathbf{z}\mathbf{u}}^k$ and $\hat{T}_{\mathbf{z}\mathbf{i}\hat{\mathbf{y}}}^k$. For each spanwise mode k that one seeks to control, a controller $\hat{K}^k(s)$ has to be synthesised. The uncertainty $\hat{\Delta}^k$ models a relative error on $\hat{T}_{\mathbf{y}\mathbf{u}}^k$, which may not correspond to the real transfer $(\hat{T}_{\mathbf{y}\mathbf{u}}^k)^{\text{real}}$ due to modelling errors or inflow condition variations. In the same way, \hat{n}^k corresponds to noise corrupting the input \hat{y}^k in the wavenumber space. As for the MIMO centralized problem, $(\hat{T}_{\mathbf{z}\mathbf{i}\hat{\mathbf{y}}}^k)^c \hat{W}_{\hat{\mathbf{y}}}^k$, $\hat{S}^k = (1 - \hat{T}_{\mathbf{y}\mathbf{u}}^k \hat{K}^k)^{-1}$ and $\hat{K}^k \hat{S}^k$ are related in the wavenumber space to nominal performance, stability robustness and performance robustness despite noisy estimation sensors, respectively. The identifications and the CMPs of our specific study will be respectively presented in sections 6.4.1 and 6.4.2.

6.3 Control settings

6.3.1 Input disturbances

To create the perturbations that will be developed along the flat plate, 35 independent exogenous noise sources are used (see figure 6.1). Each exogenous noise source is modelled using a white-noise signal $w^j(t)$ that multiplies a time-independent volume force field $\mathbf{B}_{w^j}(x, y, z)$ in the right-hand-side of the momentum equations. The field $\mathbf{B}_{w^j}(x, y, z)$ of each exogenous noise source w^j is divergence free and because of periodicity along z :

$$\mathbf{B}_{w^j} = \sum_{p=-\infty}^{p=+\infty} \mathbf{h}_w \delta(z - \Delta z j + pL_z), \quad (6.15)$$

with δ the Dirac delta distribution, $\Delta z = 3.32\delta_0^*$ and \mathbf{h}_w such as:

$$\mathbf{h}_w = A_h \begin{pmatrix} (y - y_0)\sigma_x/\sigma_y \\ -(x - x_0)\sigma_y/\sigma_x \\ 0 \end{pmatrix} \exp^{-\left(\frac{x-x_0}{\sigma_x}\right)^2 - \left(\frac{y-y_0}{\sigma_y}\right)^2}, \quad (6.16)$$

with $A_h = \frac{10.66}{\delta_0^{*2}}$, $x_0 = 4.1\delta_0^*$, $y_0 = \delta_0^*$, $\sigma_x = 1.5\delta_0^*$, $\sigma_y = 0.15\delta_0^*$. The spatial support \mathbf{B}_{w^j} forces only the momentum in the streamwise and wall-normal directions. This spatial support amounts to apply the forcing used in the 2D study (see chapters 4 and 5) in 35 cell centers in the spanwise direction in the length L_z ; the lines of force of such a noise source form also a vortex. The position of \mathbf{B}_{w^j} in the streamwise and wall-normal directions is nearby the inlet boundary condition and the generalized inflection point, respectively. This type of forcing is not intended to be realistic but is just used to excite the boundary layer and to generate perturbations; each spatial support of an exogenous noise source being based on Dirac comb, no wavenumber is privileged and each exogenous noise source $w^j \mathbf{B}_{w^j}$ has equal intensity for each frequency and wavenumber, which avoids favouring some amplification mechanisms. By forcing only the momentum in the x and y directions and localizing \mathbf{B}_{w^j} around the generalized inflection point, one can consider that the receptivity process favors the growth of the 2D second Mack mode [24]. Indeed, maximizing the receptivity process of the oblique first Mack mode also needs a forcing localized around the generalized inflection point but additionally requires forcing the momentum in the spanwise direction [24], which is not realized in this study. For the linearized

DNS necessary for the controller synthesis, the amplitude of each volume force $w^j \mathbf{B}_{w^j}$ is chosen sufficiently small to ensure that the induced perturbations remain in the linear regime until the end of the computational domain. The non-linear and transition DNS will be realized only in the sections 6.6 and 6.7; all other sections correspond only to linearized DNS.

The evolution of the velocity wavepacket at the generalized inflection point y_g and the pressure wavepacket near the wall, both generated by an impulse of w^0 (the exogenous noise source at the center spanwise position of the domain of length L_z , see figure 6.1) is plotted in figure 6.3. Both wavepackets are convected downstream with the same group velocity of approximately $0.92U_\infty$ and grow in amplitude. Additionally, both wavepackets spread in the streamwise and spanwise directions and each wavepacket is symmetrical with respect to the spanwise position $z = 0$. The two wavepackets have different structures: the velocity wavepacket at y_g has an oblique structure while the pressure wavepacket near the wall is elongated in the spanwise direction and has a more 2D structure. As the amplification rates of the first Mack mode and second Mack mode are respectively maximal for oblique perturbations and 2D perturbations (see section 1.4.2), the velocity wavepacket at y_g and the pressure wavepacket near the wall can be associated with the first and second Mack modes, respectively. This assumption is justified in more detail in the following.

Linearized DNS when the 3D boundary layer is excited simultaneously by the 35 uncorrelated white-noise signals w^j is also performed. The profiles at $x = 1766.7\delta_0^*$ of the root-mean-square fluctuations averaged in the spanwise direction are plotted in figure 6.4a. The highest fluctuations are for thermodynamic quantities (density and temperature fluctuations) which peak near the generalized inflection point (dashed line); the velocity profile also takes its highest value nearby y_g while the pressure profile has two peaks: the highest one at the wall and a second one at y_g . These results for the position of the profile peaks at $x = 1766.7\delta_0^*$ are verified all along the domain (see figure 6.4b) meaning that for a given primitive variable, the dominant mechanism associated with the growth of this variable will be the same along the domain. Note that upstream of the domain, the maxima along wall-normal direction of the pressure is not located at the wall; the excitation by the exogenous noise sources creates an acoustic wave exiting the boundary layer.

Although the velocity peaks near the generalized inflection point and can therefore be associated with a predominance of the first Mack mode according to the input/output analysis of Bugeat et al. [24], it is not possible to determine the dominant mechanism based solely on the r.m.s. profiles for density and temperature because both the first and second Mack modes lead to a peak around y_g [24]. Hence, in order to classify more precisely the dominant linear mechanisms involved in our 3D linearized DNS, the frequency spectra at y_g and near the wall are analysed (see figure 6.5) as the dominant values of the primitive variables are located at these positions. The frequency spectra of the primitive variables are normalized by their respective maximal values for comparison purposes and $F = 2\pi f\delta_0^*/U_\infty$ (with f in Hz) represents dimensionless frequency. At the generalized inflection point (see figure 6.5a), all the primitive variables are dominated by low-frequencies associated with the first Mack mode according to our 2D study (see chapter 4) and [24]. Near the wall (see figure 6.5b) all the primitive variables are dominated by higher frequencies associated with the second Mack mode. Hence, the highest r.m.s. values of the velocity, density and temperature are mainly due to first Mack mode while the highest r.m.s. value of the pressure is due to the second Mack mode; concerning the second peak of the r.m.s. profile for the pressure (near y_g), it is associated with the first Mack mode. The chosen exogenous noise sources $w^j \mathbf{B}_{w^j}$ thus trigger the amplification mechanisms of both the first and second Mack modes that coexist in the boundary layer and dominate successively as a function of the wall-normal location and the considered variable.

In view of synthesis where we will seek to control the linear growth of both the first and

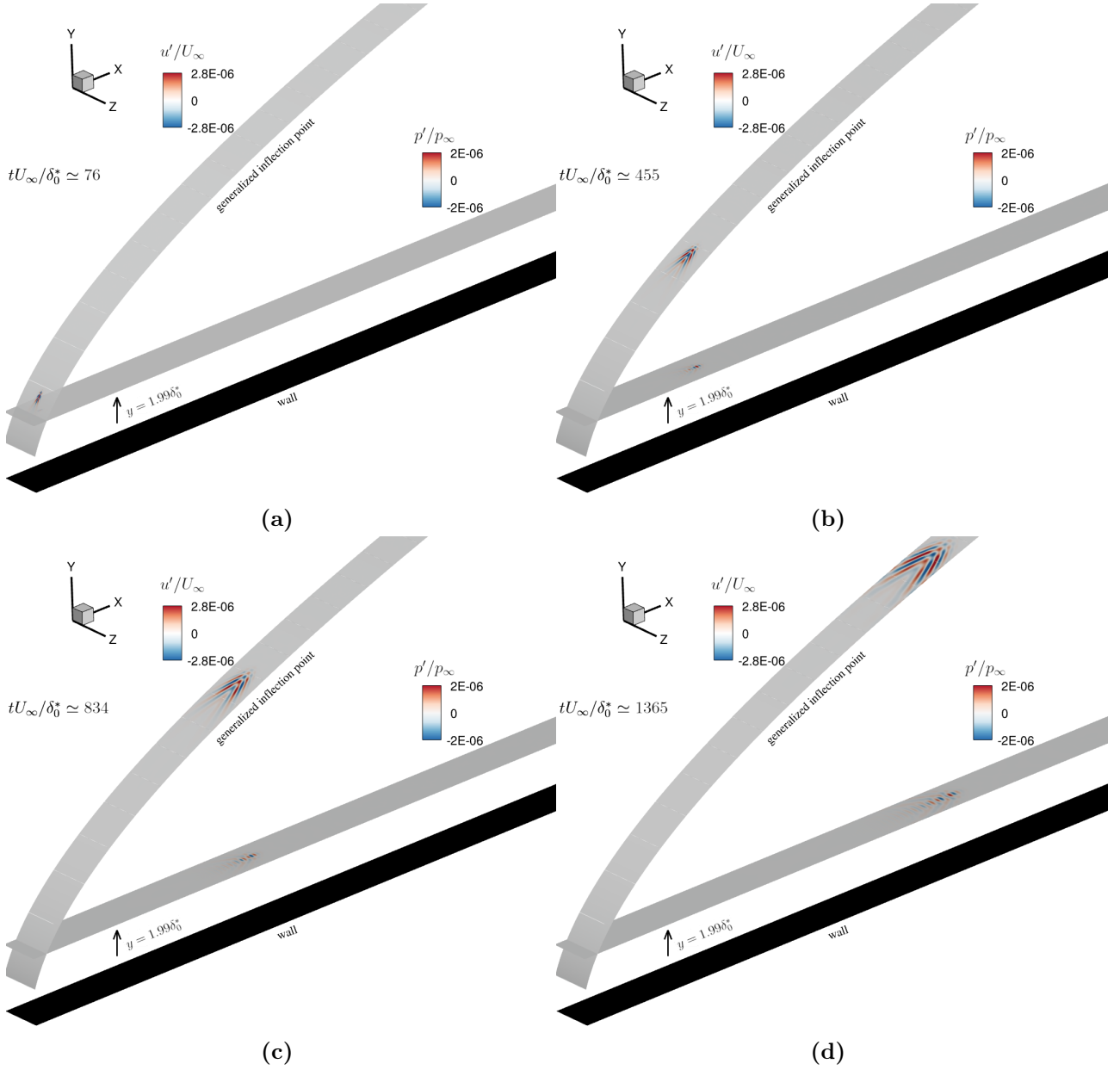


Figure 6.3: Velocity and pressure wavepackets generated by an impulse of the exogenous input w^0 at times $tU_\infty/\delta_0^* = 76$ (a), 455 (b), 834 (c) and 1365 (d).

the second Mack modes, performance sensors with the transverse separation of $\Delta z = 3.32\delta_0^*$ are chosen as wall-pressure fluctuation sensors (denoted $\mathbf{z}_p(x)$) and velocity fluctuation sensors at the generalized inflection point (denoted $\mathbf{z}_u(x)$) to have strong observability of both modes. Taking into account both Mack modes in the synthesis step is important to avoid an unwanted waterbed effect that can lead to change the breakdown scenario without delaying transition to turbulence (see appendix E). As the frequency contents of the near-wall primitive variables are very close (except a difference at low-frequencies for the velocity fluctuations), reducing the r.m.s. values of $\mathbf{z}_p(x)$ will also attenuate the near-wall velocity, density and temperature fluctuations. In the same way, reducing the r.m.s. values of $\mathbf{z}_u(x)$ will also attenuate the pressure, density and temperature fluctuations at y_g as the frequency contents of primitive variables are similar (except for a less pronounced high-frequency jump for the velocity and a more pronounced one for pressure than for density and temperature). The module of the transfer functions $\hat{T}_{\mathbf{z}(x)\mathbf{w}}^k$, obtained by Fourier transforms of the signals from impulse responses,

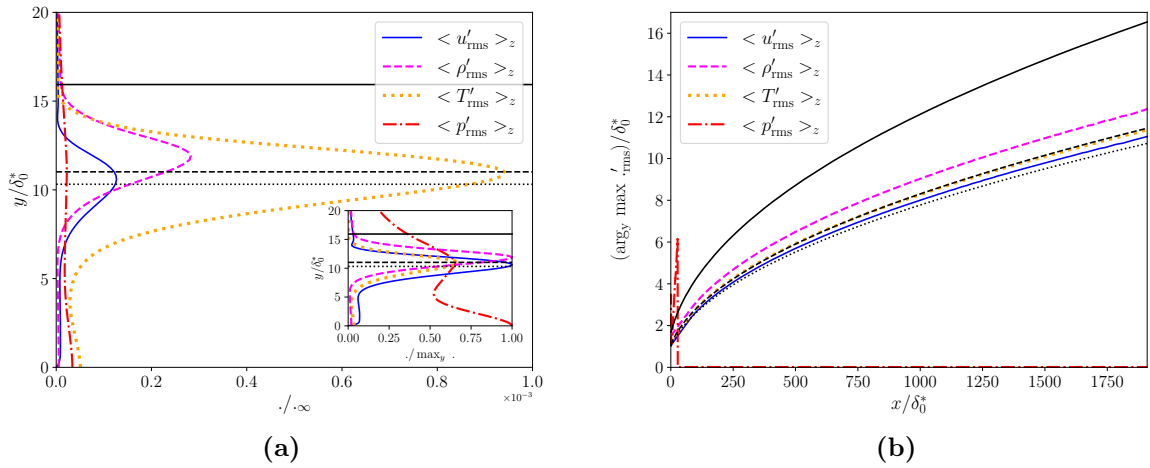


Figure 6.4: (a) Profiles at $x = 1766.7\delta_0^*$ of r.m.s. variables averaged in the spanwise direction. (b) Evolution of $\arg_y \max$ of the r.m.s. variables averaged in the spanwise direction. Black solid, dashed and dotted lines represent the boundary layer thickness, the generalized inflection point and the compressible displacement thickness, respectively.

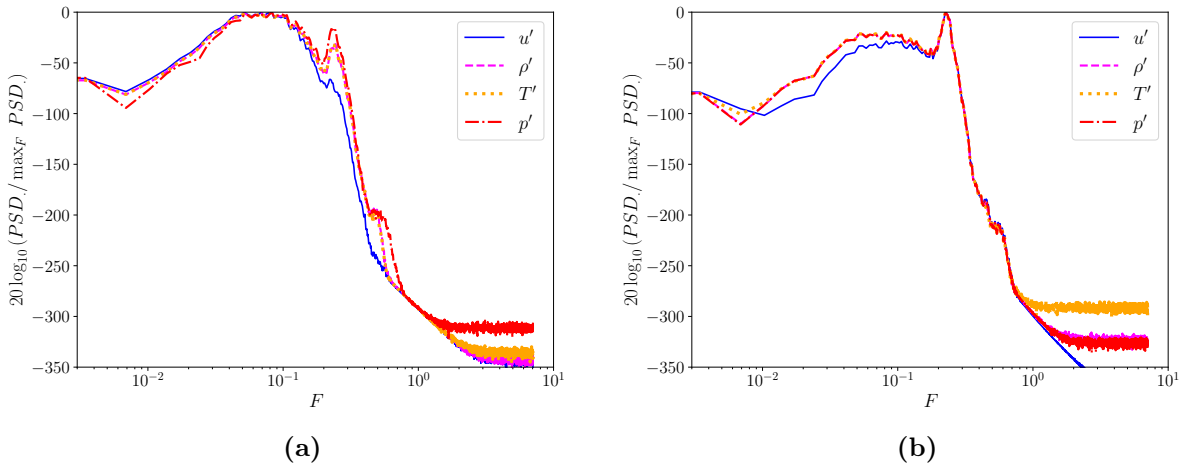


Figure 6.5: Normalized PSD of fluctuating variables at $x = 1775\delta_0^*$, $z = 0$, (a) y_g and (b) $y = 0.015\delta_0^*$ when the 3D boundary layer is excited simultaneously by the 35 uncorrelated white-noise signals w^j .

is plotted in figure 6.6. In the rest of the chapter, transfers related to \mathbf{z}_u are made dimensionless by p_∞/U_∞ ; all other transfers are already dimensionless because \mathbf{z}_p , \mathbf{y} and \mathbf{u} are homogeneous to a pressure. Note that $|\hat{T}_{\mathbf{z}(x)\mathbf{w}}^k|$ is plotted to illustrate more easily the amplification mechanisms but that it is $\hat{T}_{\mathbf{z}_i\tilde{\mathbf{y}}}^k$ and $\hat{W}_{\tilde{\mathbf{y}}}^k$ which will be used for identification and synthesis in sections 6.4.1 and 6.4.2 (as they can be obtained in an experimental configuration). Downstream of the domain, the energy contribution is only due to a certain frequency-wavenumber range. The highest values of $|\hat{T}_{\mathbf{z}_u(x)\mathbf{w}}^k|$ at each abscissa of the domain are for $k \neq 0$ (so oblique first Mack modes) and lower frequencies F dominate compared to $|\hat{T}_{\mathbf{z}_p(x)\mathbf{w}}^k|$. For the wall-pressure performance sensors, the highest values at each abscissa of the domain are for $k = 0$ (so 2D second Mack modes). It might be possible to do without \mathbf{z}_u in the synthesis because the first oblique Mack mode has a significant energy contribution even in the wall-pressure performance sensors. With a suitable frequency template, we could therefore reduce the amplitude of both the first and second Mack modes through H_2 norm minimization only from the wall-pressure

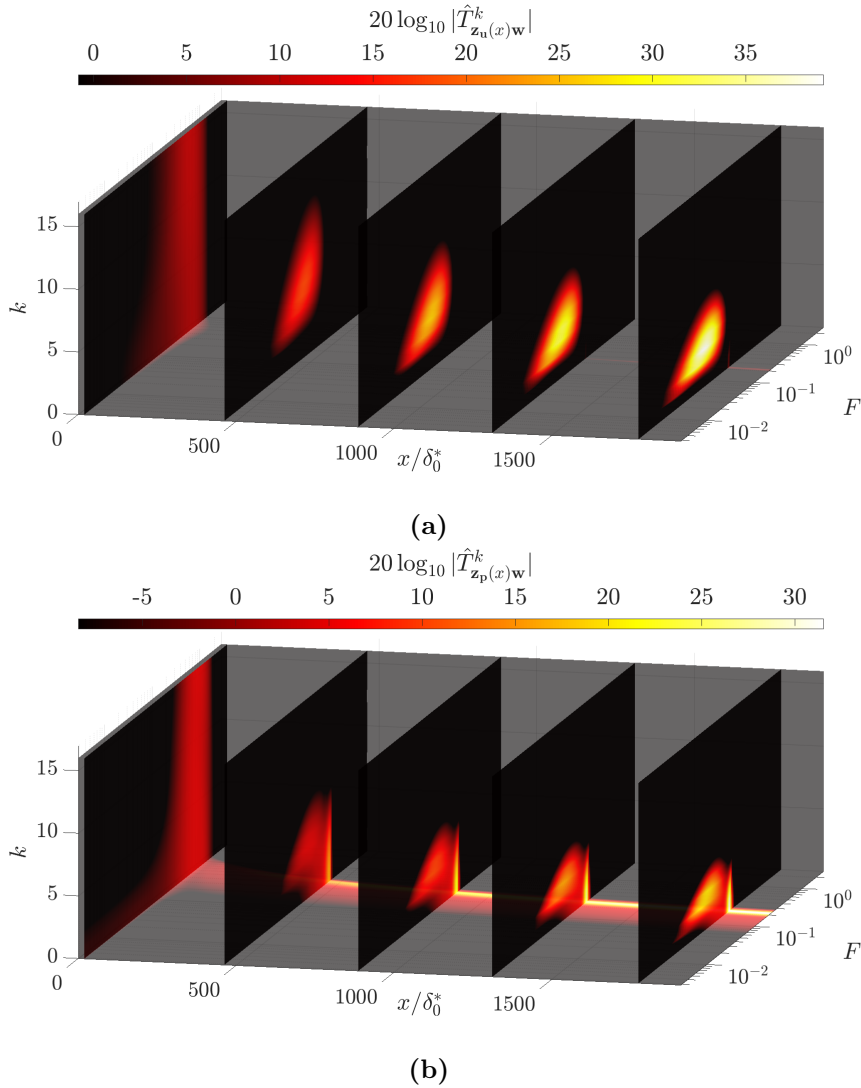


Figure 6.6: Modules of $\hat{T}_{\mathbf{z}(x)\mathbf{w}}^k$ for (a) velocity fluctuation performance sensors at the generalized inflection point and (b) wall-pressure fluctuation performance sensors.

sensors. Nevertheless, for ease of analysis and synthesis, we will use both \mathbf{z}_u and \mathbf{z}_p . For both types of performance sensors, the further downstream in the domain, the more low-frequencies dominate. The evolution of $\|\hat{T}_{\mathbf{z}(x)\mathbf{w}}^k\|_\infty = \sup_{F \in \mathbb{R}} |\hat{T}_{\mathbf{z}(x)\mathbf{w}}^k(iF)|$ for some spanwise modes k is shown in figures 6.7(a,b). After reaching a peak, the magnitude associated with a particular mode k decreases for the highest modes. For the velocity sensors at y_g , spanwise modes that have a negligible energy contribution upstream of the domain are dominant downstream and the most energetic spanwise mode varies as a function of the plate abscissa, contrary to the wall-pressure performance sensors which are continuously dominated by $k = 0$. The number of modes k necessary to capture at each abscissa of the domain $0.9\|T_{\mathbf{z}(x)\mathbf{w}}\|_2$ is depicted in figures 6.7(c,d): only a limited portion of spanwise modes is needed to describe the perturbation energy at each abscissa of the domain and the further downstream in the domain, the more the number of modes k needed decreases. The streamwise position of the actuators \mathbf{u} will be $x_u = 867.2\delta_0^*$ (see section 6.3.2) as for the 2D study (see table 4.1); thus, we will consider for the identification and synthesis only modes up to $k = 5$ (symbolized by horizontal dotted line) because trying to control higher spanwise modes would have a negligible effect on the r.m.s. values of the performance sensors. The minimum number of independent sensors in the spanwise direction

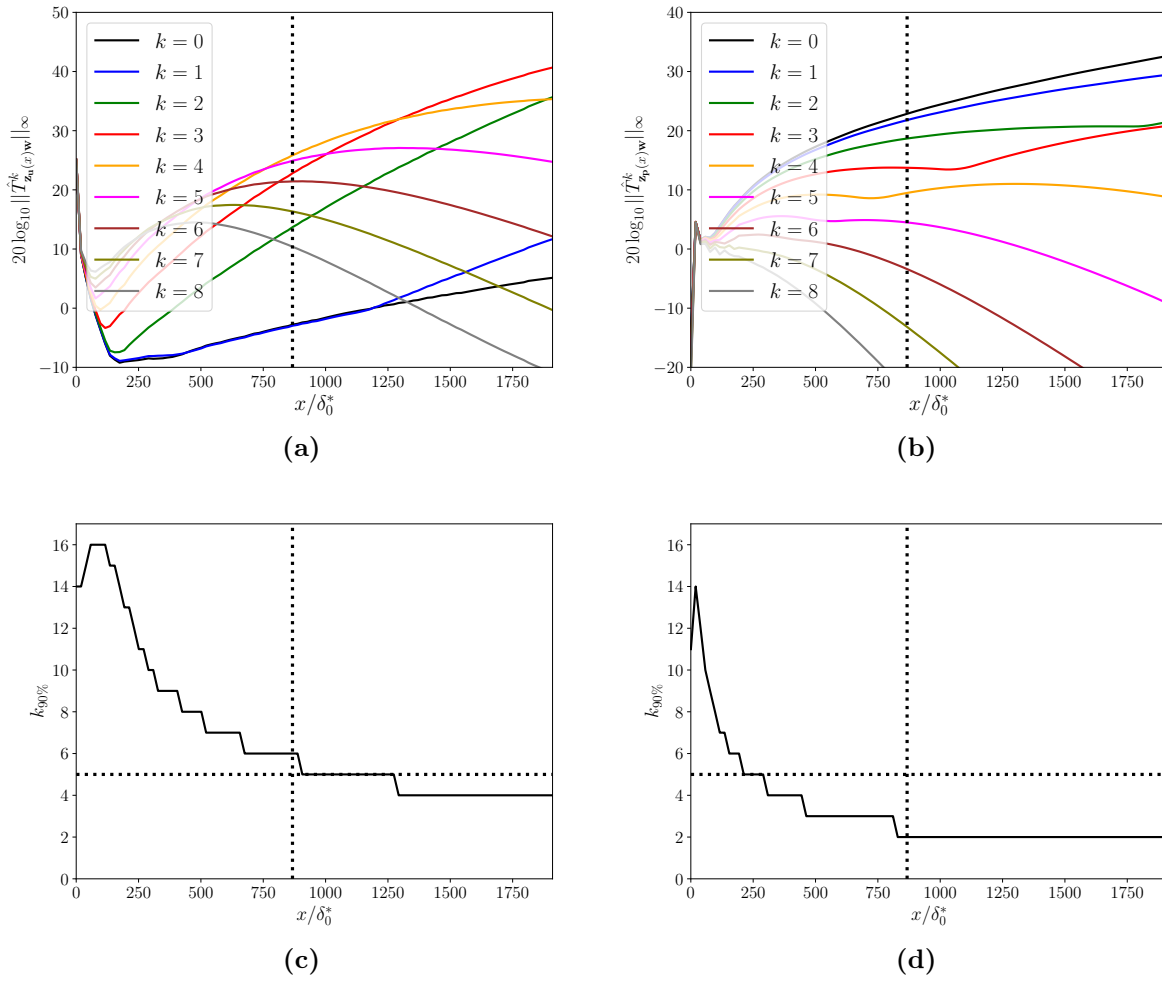


Figure 6.7: Evolution of $\|\hat{T}_{\mathbf{z}(x)\mathbf{w}}^k\|_\infty$ for some k (a,b) and number of spanwise modes k necessary to contain at least 90% of $\|T_{\mathbf{z}(x)\mathbf{w}}\|_2$ (c,d) for velocity fluctuation performance sensors at the generalized inflection point (a,c) and wall-pressure fluctuation performance sensors (b,d). The vertical dotted line represents the streamwise position $x_{\mathbf{u}}$ of the actuators. The spanwise modes equal or lower than $k = 5$ (below the horizontal dotted line in (c,d)) are those used in the identification and synthesis step.

is set by not aliasing the noise-induced perturbation spectrum but also by not aliasing the actuator-induced perturbation spectrum. So even if we will only control spanwise modes up to $k = 5$, the limitation on the actuator-induced perturbations will impose to have 35 independent actuators and performance/estimation sensors (see section 6.3.3).

6.3.2 Actuators

In the same way as for the exogenous noise sources, 35 independent actuators are used. Each actuator is modelled by a volume forcing $u^j(t)\mathbf{B}_{u^j}(x, y, z)$ in the right-hand-side of the momentum equations. Because of the periodic boundary conditions, the spatial support \mathbf{B}_{u^j} of each actuator u^j is:

$$\mathbf{B}_{u^j} = \sum_{p=-\infty}^{p=+\infty} \mathbf{h}_u(z - \Delta z j + pL_z), \quad (6.17)$$

with $\Delta z = 3.32\delta_0^*$ and $\mathbf{h}_u(z)$ such as:

$$\mathbf{h}_u(z) = A_h \begin{pmatrix} (y - y_0)\sigma_x/\sigma_y \\ -(x - x_0)\sigma_y/\sigma_x \\ 0 \end{pmatrix} \exp^{-\left(\frac{x-x_0}{\sigma_x}\right)^2 - \left(\frac{y-y_0}{\sigma_y}\right)^2 - \left(\frac{z}{\sigma_z}\right)^2}, \quad (6.18)$$

with $A_h = \frac{10.66}{\delta_0^{*2}}$, $x_0 = 867.2\delta_0^*$, $y_0 = 7.79\delta_0^*$, $\sigma_x = 1.5\delta_0^*$, $\sigma_y = 0.5\delta_0^*$, $\sigma_z = 7.04\delta_0^*$. The pattern

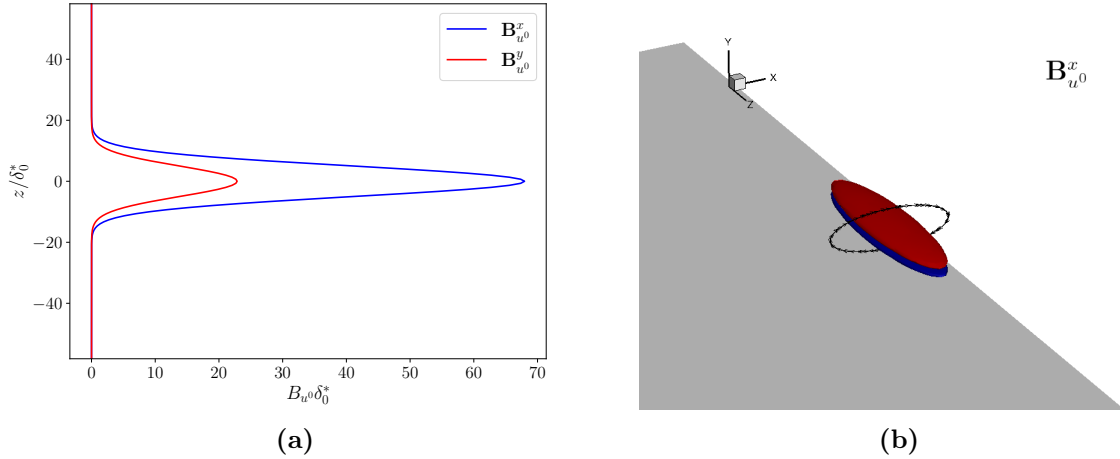


Figure 6.8: (a) Profiles of the streamwise (in blue) and wall-normal components (in red) of \mathbf{B}_{u^0} at (x,y) coordinates associated with their respective maximum values. (b) Iso-surfaces of the streamwise component $B_{u^0}^x$ at -10% (blue) and $+10\%$ (red) of the maximum absolute value. Both figures display \mathbf{B}_{u^0} only on the length L_z of the domain.

that is periodized and that composes \mathbf{B}_{u^j} is the one used in the 2D study but adding a Gaussian in the spanwise direction (see figure 6.8a). The forcing is thus divergence-free and the lines of force form a vortex (see figure 6.8b). Each forcing field of the actuators is centered around the generalized inflection point and this will maximize the receptivity process of the second Mack mode. The receptivity process of the first Mack mode is not optimal as the momentum quantity in the spanwise direction is not forced. The streamwise position of the actuators $x_{\mathbf{u}} = 867.2\delta_0^*$ is a compromise between controlling a sufficiently long domain representative of experimental configurations and restricting the complexity of the control problem by limiting the frequency-wavenumber range to control; an upstream position should have controlled more spanwise modes and higher bandwidth (see figure 6.7).

The figure 6.9 compares the modules of $\hat{T}_{\mathbf{z}(x)\mathbf{u}}^k$ with those of $\hat{T}_{\mathbf{z}(x)\mathbf{w}}^k$ at $x = 1775\delta_0^*$ for both $\mathbf{z}_{\mathbf{p}}$ and $\mathbf{z}_{\mathbf{u}}$. For velocity performance sensors at y_g (see figures 6.9(a,b)), the actuators create in low-frequency range similar oblique structures to those obtained by exogenous noise sources but 2D structures of the second Mack mode are present in $|\hat{T}_{\mathbf{z}_{\mathbf{u}}(x)\mathbf{u}}^k|$ while they are negligible in $|\hat{T}_{\mathbf{z}_{\mathbf{p}}(x)\mathbf{w}}^k|$. For wall-pressure performance sensors (see figures 6.9(c,d)), only second Mack mode is present in $|\hat{T}_{\mathbf{z}_{\mathbf{p}}(x)\mathbf{u}}^k|$ while oblique first Mack mode contains a non negligible amount of energy in $|\hat{T}_{\mathbf{z}_{\mathbf{p}}(x)\mathbf{w}}^k|$. This is mainly due to the fact that the disturbances generated by the actuators do not take advantage of the full length of the instability domain (starting for each wavenumber from the branch I) contrary to the disturbances generated by the noise sources and therefore the first Mack mode appears less dominant for $\hat{T}_{\mathbf{z}(x)\mathbf{u}}^k$ than for $\hat{T}_{\mathbf{z}(x)\mathbf{w}}^k$ because part of its amplification area is not used. The actuator-induced structures being different from the noise-induced structures, it may limit the efficiency of the control which works by destructive

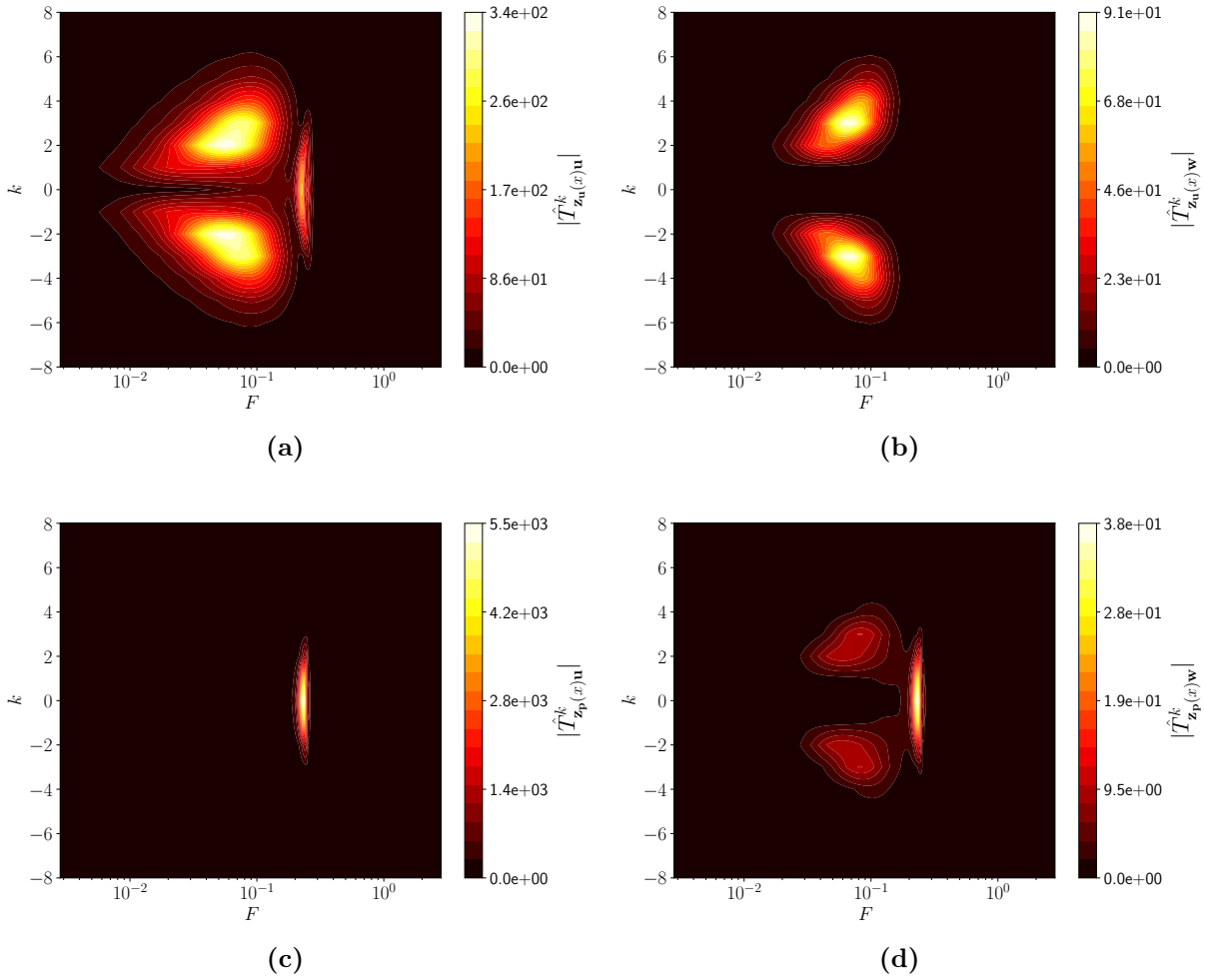


Figure 6.9: Comparison of the modules of (a,c) $\hat{T}_{z(x)u}^k$ and (b,d) $\hat{T}_{z(x)w}^k$ at $x = 1775\delta_0^*$ for velocity fluctuation performance sensors at the generalized inflection point (a,b) and wall-pressure fluctuation performance sensors (c,d).

interference. One could optimize the spatial support $\mathbf{B}_{u,j}$ to improve the control of both the first and the second Mack modes while minimizing the energy cost (*e.g.* by modifying the spreading in the spanwise direction to target only the spanwise modes we need to control or by forcing the momentum in the spanwise direction) but this is outside the scope of this study. One could also seek to constrain the spatial support in the near wall region and not at y_g to get closer to a realistic implementation.

6.3.3 Sensors for the synthesis

Only a few positions in the longitudinal direction for the performance sensors $\mathbf{z}(x)$ should be chosen for the synthesis to limit the model size and simplify the synthesis. The set of performance sensors \mathbf{z}_i used in the synthesis must be representative of the dynamics to be controlled from the actuators to the end of the numerical domain. In figure 6.10, the quantity $F \times \text{PSD}_{z(x)}$ is plotted for different streamwise positions for performance sensors at the center of the spanwise position. For the velocity sensors at y_g , the frequencies F contributing the most to the energy of a sensor close to the actuators ($x = 1022.6\delta_0^*$) are also frequencies that have a non-negligible contribution close to the end of the numerical domain used for linearized DNS ($x = 1775\delta_0^*$). Minimizing the r.m.s. values of a single row of velocity sensors downstream

of the domain $\mathbf{z}_{3,u}$ at $x_{\mathbf{z}_{3,u}} = 1775\delta_0^*$ should therefore also have a positive effect on the rows of sensors further upstream. Choosing a row of sensors sufficiently far downstream also makes sense because the energy of the disturbances increases as they are convected, so the control must reduce consequently the energy downstream. This allows not to trigger non-linearities which appear from a certain energy threshold: the further downstream the disturbances are from the actuators, the more their energy must be reduced (see section 4.2.1). For the wall-pressure

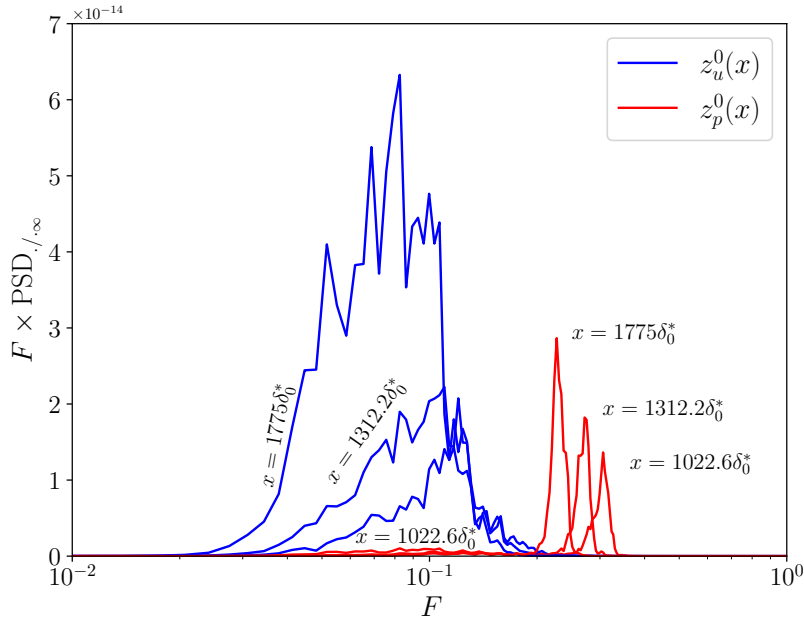


Figure 6.10: Evolution of $F \times \text{PSD}_{z(x)}$ for sensors at the center of the spanwise direction.

sensors, $F \times \text{PSD}_{z(x)}$ is more narrow at each abscissa and the frequencies contributing to the energy near the actuators have a negligible impact downstream of the domain. To cover the entire amplified bandwidth from the actuators to the end of the domain, it is necessary to use several sensors $\mathbf{z}_{i,p}$. Indeed, if all the dominant frequencies from the actuators to the end of the domain are not taken into account in the synthesis step, a harmful waterbed effect may occur: some frequencies can be amplified by the controller whereas they could be predominate in some abscissa of the plate (see section 4.6.2). Three rows of wall-pressure sensors $\mathbf{z}_{1,p}$, $\mathbf{z}_{2,p}$ and $\mathbf{z}_{3,p}$ are used for the synthesis, respectively at $x_{\mathbf{z}_{1,p}} = 1022.6\delta_0^*$, $x_{\mathbf{z}_{2,p}} = 1312.2\delta_0^*$ and $x_{\mathbf{z}_{3,p}} = 1775\delta_0^*$. These positions are close to the ones that allowed to obtain an efficient control in terms of disturbance amplitude reduction in the 2D configuration (see table 4.1).

The estimation sensors \mathbf{y} are wall-pressure fluctuation sensors. This choice is supported by the fact that both Mack modes are observable by this type of sensor (see figure 6.6b) and not only the oblique first Mack mode as with the velocity sensors at y_g (see figure 6.6a). In addition, unlike performance sensors \mathbf{z}_i which are only used during synthesis and whose associated transfer functions could be modeled (*e.g.* by numerical calculations), estimation sensors \mathbf{y} need to be physically implementable in realistic setups to compute the actuator signal $\mathbf{u}(t)$ from K . Wall-pressure sensors are indeed commonly used in hypersonic experimental setups [106]. Only a feedback setup where the estimation sensors are downstream of the actuators will be employed in this 3D study as performance robustness requires first and foremost this kind of configuration. Indeed, a feedforward setup where the estimation sensors are upstream of the actuators is unable to ensure performance robustness when free-stream velocity variations are considered (see chapter 4) even with multi-model or gain scheduling methods (see chapter 5).

To control the high-frequencies of the second Mack mode, the convection delay $\tau_{\mathbf{y}\mathbf{u}}$ of the disturbances from \mathbf{u} to \mathbf{y} has to be limited. Considering that frequencies up to $F \sim 0.3$ must be controlled (see figure 6.10), the actuator/estimation sensor distance $U_\infty \tau_{\mathbf{y}\mathbf{u}}$ must be less than $U_\infty / f_c = 2\pi\delta_0^* / F \sim 21\delta_0^*$ with f_c the controllable bandwidth [66]. Then, the estimation sensors are placed at a distance of $20.4\delta_0^*$ from the streamwise position of the actuators ($x_{\mathbf{y}} = 887.6\delta_0^*$), which is similar to that of the 2D study. Although only spanwise modes up to $k = 5$ will be

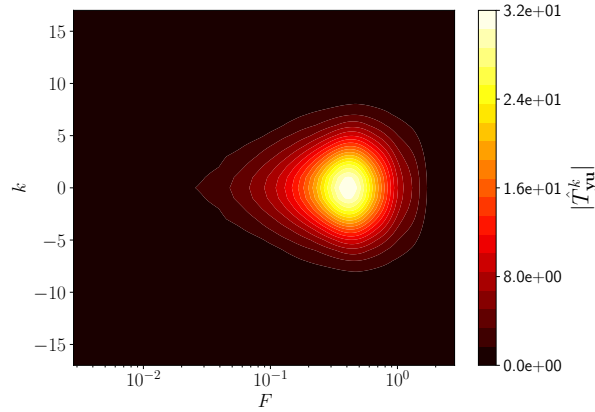


Figure 6.11: Module of $\hat{T}_{\mathbf{y}\mathbf{u}}^k$.

controlled, 35 equispaced independent objects with the transverse separation of $\Delta z = 3.32\delta_0^*$ are necessary to avoid aliasing. Indeed, the frequency spectrum of $\hat{T}_{\mathbf{y}\mathbf{u}}^k$ contains energy up to $k \sim 9$ (see figure 6.11); taking 2 times less sensors would lead to detect only spanwise modes up to $k_{\max} = 8$ and the spectrum would risk to be aliased. Therefore, the minimum number of independent actuator/sensor in the spanwise direction is actually set by not aliasing the actuator-induced and noise-induced perturbation spectra. One could seek to optimize the actuator forcing field to have only energy up to the mode $k = 5$ on the estimation sensors, which would reduce the number of actuators and sensors to use, but this is outside the scope of this study.

The control settings of the 3D configuration (exogenous noise sources, actuators, estimation sensors and performance sensors used in synthesis) are summarized in table 6.1.

| | w | u | y | z_i |
|--|----------------------------------|------------------------------------|------------------------------------|--|
| Streamwise position | $x_{\mathbf{w}} = 4.1\delta_0^*$ | $x_{\mathbf{u}} = 867.2\delta_0^*$ | $x_{\mathbf{y}} = 887.6\delta_0^*$ | $x_{\mathbf{z}_{3,\mathbf{u}}} = 1775.0\delta_0^*$ $x_{\mathbf{z}_{1,\mathbf{p}}} = 1022.6\delta_0^*$ $x_{\mathbf{z}_{2,\mathbf{p}}} = 1312.2\delta_0^*$ $x_{\mathbf{z}_{3,\mathbf{p}}} = 1775.0\delta_0^*$ |
| Wall-normal position | $y_{\mathbf{w}} = \delta_0^*$ | $y_{\mathbf{u}} = y_g$ | $y_{\mathbf{y}} = 0$ | $y_{\mathbf{z}_{\mathbf{u}}} = y_g$ $y_{\mathbf{z}_{\mathbf{p}}} = 0$ |
| Number of independent objects per streamwise position | 35 | 35 | 35 | 35 |
| Spanwise spacing | $\Delta z = 3.32\delta_0^*$ | $\Delta z = 3.32\delta_0^*$ | $\Delta z = 3.32\delta_0^*$ | $\Delta z = 3.32\delta_0^*$ |

Table 6.1: Summary of the control settings: exogenous noises **w**, actuators **u**, feedback estimation sensors **y** and performance sensors **z_i** used in identification and synthesis.

6.4 Identification and synthesis methods

Both identification and synthesis methods used in this 3D study employ state-space representations. In such representations, the system matrices are real implying that the transfer functions must respect the frequency Hermitian symmetry $\hat{\mathcal{C}}^k(i\omega) = \hat{\mathcal{C}}^{k*}(-i\omega)$. In the general case, the problem with the new transfer functions $\hat{\mathcal{C}}^k$ is that the frequency Hermitian symmetry is not guaranteed for complex inputs/outputs $\hat{\mathbf{I}}(t)/\hat{\mathbf{O}}(t)$. These variables should be decomposed to real and imaginary parts and several MIMO CMPs (instead of several SISO CMPs) of size 2×2 should be solved to guarantee the Hermitian symmetry.

However, due to the even nature of our actuators/sensors (see equations 6.15 and 6.17 for instance) and the type of forcing chosen, a symmetry plane for the streamwise velocity/pressure disturbance responses exists (see figure 6.3), thus we have

$$\forall \omega \quad \hat{\mathcal{C}}^k(i\omega) = \hat{\mathcal{C}}^{-k}(i\omega), \quad (6.19)$$

implying that the frequency Hermitian symmetry is respected. This enables in our specific case to work on several independent SISO CMPs: we will identify $\hat{T}_{\mathbf{z}_i\tilde{\mathbf{y}}}^k$, $\hat{T}_{\mathbf{z}_i\mathbf{u}}^k$, $\hat{T}_{\mathbf{y}\mathbf{u}}^k$ and $\hat{W}_{\tilde{\mathbf{y}}}^k$ and synthesized \hat{K}^k only for the spanwise modes $k \geq 0$. The SISO controllers \hat{K}^k for $k \geq 1$ will be duplicated to obtain \hat{K}^{-k} and fill properly the diagonal matrix \hat{K} .

6.4.1 Reduced-order models

For the quantities $T_{\mathbf{z}_i\tilde{\mathbf{y}}}$ and $W_{\tilde{\mathbf{y}}}W_{\tilde{\mathbf{y}}}^*$ (see equations 6.6 and 6.7) from which $\hat{T}_{\mathbf{z}_i\tilde{\mathbf{y}}}^k$ and $\hat{W}_{\tilde{\mathbf{y}}}^k$ are derived, they are calculated by means of Welch's method [198]. Then, an ensemble averaging is performed on the different rows to obtain perfectly circulant matrices. The quantity $W_{\tilde{\mathbf{y}}}$ is defined as the square root of the matrix $W_{\tilde{\mathbf{y}}}W_{\tilde{\mathbf{y}}}^*$ to be also circulant [105]. For the quantity $T_{\mathbf{z}_i\tilde{\mathbf{y}}}$ built from the inverse of a CPSD matrix, a Moore-Penrose pseudoinverse [124, 138] is in fact realized to get rid of too low singular values and ill-conditioned matrix. A Savitzky-Golay [157] and low/high pass filters [26] are also applied on $T_{\mathbf{z}_i\tilde{\mathbf{y}}}$ to smooth the frequency spectrum and to focus only on the dominant frequencies of the Mack modes, respectively. For the quantities $T_{\mathbf{z}_i\mathbf{u}}$ and $T_{\mathbf{y}\mathbf{u}}$ from which $\hat{T}_{\mathbf{z}_i\mathbf{u}}^k$ and $\hat{T}_{\mathbf{y}\mathbf{u}}^k$ are derived, they are calculated by Fourier transform of the responses obtained from an impulse of one of the actuator (as the circulant matrix is fully specified from one column).

For each transfer function, 6 SISO systems have to be identified as we have to control spanwise modes until $k = 5$. The identification of $\hat{T}_{\mathbf{z}_i\tilde{\mathbf{y}}}^k$, $\hat{T}_{\mathbf{z}_i\mathbf{u}}^k$, $\hat{T}_{\mathbf{y}\mathbf{u}}^k$ and $\hat{W}_{\tilde{\mathbf{y}}}^k$ is carried out with the ERA which requires impulse responses. These impulse responses are obtained by inverse Fourier transform of the different quantities. Following the procedure developed in the 2D study (see section 4.5.1), the ERA is applied after shifting the time axis of the impulses from $\hat{\mathbf{y}}^k$ and $\hat{\mathbf{u}}^k$ to $\hat{\mathbf{z}}_i^k$ by $\tau_{\mathbf{z}_i\tilde{\mathbf{y}}}$ (the delay of the perturbations from the row of estimation sensors to the row of performance sensors in absence of control) to discard the unnecessary delays. This eases the identification by reducing the size of the ROMs without impacting the results of the synthesis. The comparison of the ROMs (circles) and frequency/impulse data (solid lines) for the $\hat{T}_{\mathbf{z}_i\tilde{\mathbf{y}}}^k$, $\hat{T}_{\mathbf{z}_i\mathbf{u}}^k$, $\hat{T}_{\mathbf{y}\mathbf{u}}^k$ and $\hat{W}_{\tilde{\mathbf{y}}}^k$ used in the synthesis step is plotted in figure 6.12. A good agreement is obtained and the ROMs capture most of the important dynamics. For a particular spanwise mode k , the sum of the orders of each SISO ROM is ~ 160 ; as we have to control modes up to $k = 5$, this would amount to working on a MIMO system potentially of order ~ 960 (common states could be in fact shared between the modes lowering this potential order of ~ 960) which illustrates the need to work on multiple decentralized SISO problems in the wavenumber space.

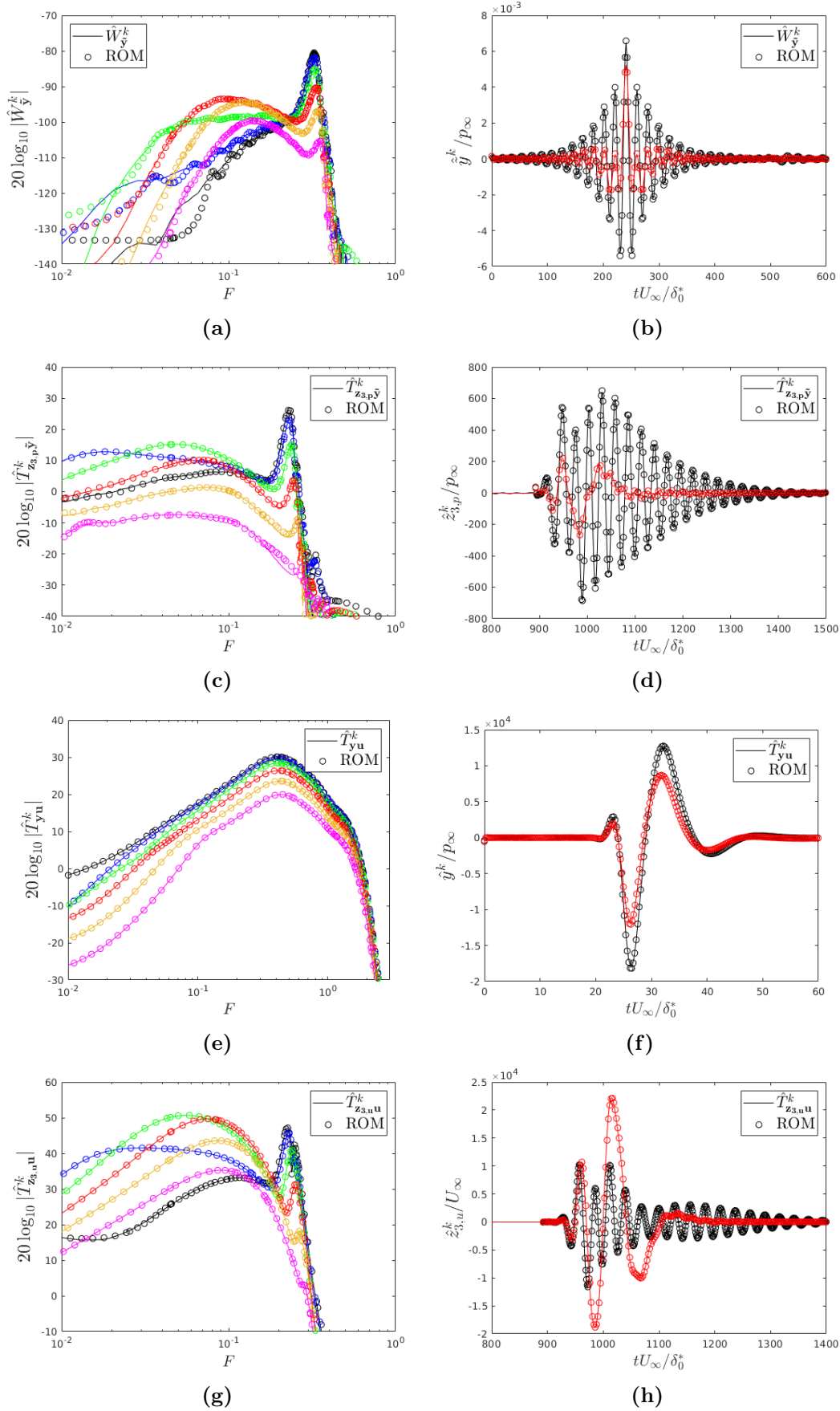


Figure 6.12: Comparison of the ROMs (circles) and frequency/impulse data (solid lines) for the $\hat{T}_{\mathbf{z}_i\tilde{y}}^k$, $\hat{T}_{\mathbf{z}_i\mathbf{u}}^k$, $\hat{T}_{\mathbf{y}u}^k$ and $\hat{W}_{\tilde{y}}^k$ used in the synthesis. Black, blue, green, red, orange and magenta colors correspond to quantities associated with a spanwise mode $k = 0$, $k = 1$, $k = 2$, $k = 3$, $k = 4$ and $k = 5$, respectively. Figures (c,d) are plotted for the wall-pressure performance sensors $\mathbf{z}_{3,p}$ while figures (g,h) are plotted for the velocity sensors $\mathbf{z}_{3,u}$. For the ROMs of $\hat{T}_{\mathbf{z}_{3,p}\tilde{y}}^k$ and $\hat{T}_{\mathbf{z}_{3,u}u}^k$, the time axis of the impulse responses are shifted by $\tau_{\mathbf{z}_i\tilde{y}}U_\infty/\delta_0^* \simeq 892$ which corresponds to the suppression of unnecessary dead times.

6.4.2 Constrained minimization problems

The structure of the six controllers \hat{K}^k is imposed in the following way: each controller \hat{K}^k is searched in a state-space form with a strictly-proper structure (inducing a roll-off of -20 dB per decade at high-frequencies allowing to be robust to high-frequency noisy estimation sensors) and a tridiagonal state matrix; each controller \hat{K}^k is stable with a controller order equal to 6, which is similar to what was imposed for the controllers in the 2D study (see section 4.5.2).

For each controller \hat{K}^k with the structure imposed above, the *systune* algorithm solves the following mixed H_2/H_∞ problem:

$$\begin{aligned}
 \text{Step 1: minimize } & \max(\|(\hat{T}_{\mathbf{z}_3, \mathbf{u}\hat{\mathbf{y}}}^k)^c \hat{W}_{\hat{\mathbf{y}}}^k\|_2, \|(\hat{T}_{\mathbf{z}_p^{\text{All}}\hat{\mathbf{y}}}^k)^c \hat{W}_{\hat{\mathbf{y}}}^k\|_2) \\
 & \text{subject to } \|W_{\hat{S}^k} \hat{S}^k\|_\infty < 1 \text{ and } \|W_{(\hat{K}\hat{S})^k} (\hat{K}\hat{S})^k\|_\infty < 1, \\
 \\
 \text{Step 2: minimize } & \|(\hat{K}\hat{S})^k\|_2 \\
 & \text{subject to } \|W_{\hat{S}^k} \hat{S}^k\|_\infty < 1, \|(\hat{T}_{\mathbf{z}_3, \mathbf{u}\hat{\mathbf{y}}}^k)^c \hat{W}_{\hat{\mathbf{y}}}^k\|_2 < 1.01 \|(\hat{T}_{\mathbf{z}_3, \mathbf{u}\hat{\mathbf{y}}}^k)^c \hat{W}_{\hat{\mathbf{y}}}^k\|_2^{\text{Step1}} \\
 & \text{and } \|(\hat{T}_{\mathbf{z}_p^{\text{All}}\hat{\mathbf{y}}}^k)^c \hat{W}_{\hat{\mathbf{y}}}^k\|_2 < 1.01 \|(\hat{T}_{\mathbf{z}_p^{\text{All}}\hat{\mathbf{y}}}^k)^c \hat{W}_{\hat{\mathbf{y}}}^k\|_2^{\text{Step1}},
 \end{aligned} \tag{6.20}$$

with $\hat{K}^k \hat{S}^k$ denoted $(\hat{K}\hat{S})^k$ to lighten the notation and $\mathbf{z}_p^{\text{All}}$ a vector such as $\mathbf{z}_p^{\text{All}} = [\mathbf{z}_{1,p}, \mathbf{z}_{2,p}, \mathbf{z}_{3,p}]^T$. Hence, for a spanwise mode k , $(\hat{T}_{\mathbf{z}_p^{\text{All}}\hat{\mathbf{y}}}^k)^c$ is a SIMO (one input and three outputs) transfer function. This two step CMP is the transcription of the fluidic specifications established in sections 6.2.1 and 6.2.2 and is explained in the following.

In the step 1 of the CMP, the minimization of $\|(\hat{T}_{\mathbf{z}_3, \mathbf{u}\hat{\mathbf{y}}}^k)^c \hat{W}_{\hat{\mathbf{y}}}^k\|_2$ and $\|(\hat{T}_{\mathbf{z}_p^{\text{All}}\hat{\mathbf{y}}}^k)^c \hat{W}_{\hat{\mathbf{y}}}^k\|_2$ allows the reduction of r.m.s. values of both velocity sensors at the generalized inflection point and wall-pressure fluctuation sensors. To be able to compare these two types of sensors in the "minimize max" formulation, their H_2 norms are normalized by their respective uncontrolled values $\|T_{\mathbf{z}\mathbf{w}}\|_2$ approximated by the six spanwise modes k used in the synthesis. The results are therefore weighted by the importance that a spanwise mode has in the total energy. The H_∞ constraint on $W_{\hat{S}^k} \hat{S}^k$ maintains adequate stability margins. Different stability margins could be imposed for each mode depending on the uncertainty on $\hat{T}_{\mathbf{y}\mathbf{u}}^k$. As no additional study has been carried out in our case on the modelling errors or the variations of $\hat{T}_{\mathbf{y}\mathbf{u}}^k$ after inflow variations, a constant frequency template $W_{\hat{S}^k} = 0.5$ involving $\|\hat{S}^k\|_\infty < 2$ is chosen independently of the spanwise mode considered. This template provided substantial margins despite variation of $\pm 5\%$ of the free-stream velocity in the 2D case (*i.e.* for the case $k = 0$, see section 4.7.2) and one can hope that it will be the same for the other modes. With this template, each SISO system associated with a spanwise mode k will be guaranteed stable up to 50% of relative model errors $\hat{\Delta}^k$ on $\hat{T}_{\mathbf{y}\mathbf{u}}^k$ (see section 4.3). The frequency template $|1/W_{(\hat{K}\hat{S})^k}| = 80$ dB linked to the H_∞ constraint on $W_{(\hat{K}\hat{S})^k} (\hat{K}\hat{S})^k$ is just chosen as a very large constant so as not to constrain too much the actuator activity while rejecting ill-conditioned controller \hat{K}^k with infinite norms; the constraint of performance robustness despite noisy estimation sensors is thus very weakly active in this step. In summary, this first algorithmic step returns controller \hat{K}^k reducing as much as possible the H_2 norms of the transfers related to the velocity and pressure performance sensors while ensuring the stability robustness of the feedback loop.

In the step 2 of the CMP, a minimization of $\|(\hat{K}\hat{S})^k\|_2$ is realized under the constraint of recovering similar results to step 1 in terms of pressure/velocity disturbance rejection. The same minimal stability margins than in the step 1 are required through the frequency template $W_{\hat{S}^k} = 0.5$. This two-step resolution is explained by the fact that it is difficult to find

weighting functions to compare H_2 norms related to nominal performance and H_2 norms related to performance robustness despite noisy sensors in order to solve a single minimization problem. By minimizing $\|(\hat{K}\hat{S})^k\|_2$, the controller is desensitized as much as possible to white noise corrupting the estimation sensors. This minimization completes the strictly-proper structure of \hat{K}^k which brings natural robustness to high-frequency noise. This approach is more straightforward than the one used in the 2D study, where the actuator activity had been progressively constrained in low-frequency range to be robust to a signal-to-noise ratio of 2 at the estimation sensor (see section 4.7.3.1), because the actuator activity is here directly minimized. The optimal results of the step 1 in terms of disturbance rejection (*i.e.* $\|(\hat{T}_{\mathbf{z}_3, \mathbf{u}, \hat{\mathbf{y}}}^k)^c \hat{W}_{\hat{\mathbf{y}}}^k\|_2^{\text{Step1}}$ and $\|(\hat{T}_{\mathbf{z}_p, \mathbf{u}, \hat{\mathbf{y}}}^k)^c \hat{W}_{\hat{\mathbf{y}}}^k\|_2^{\text{Step1}}$) are raised by a factor 1.01 in the step 2 in order to obtain several controllers that respect these constraints before that the algorithm starts the minimization procedure of $\|(\hat{K}\hat{S})^k\|_2$. In summary, the second algorithmic step is a trivial way to obtain controller \hat{K}^k reducing as much as possible both H_2 norm related to velocity/pressure disturbance rejection and H_2 norm related to actuator activity in case of white noises corrupting the estimation signals, while ensuring stability robustness.

In the step 1 and 2, a dozen and a hundred random controller initializations are respectively performed to deal with the non-convex nature of the optimisation problem. With the non-smooth algorithm employed and a parallel computation on 12 CPU cores (Intel(R) Xeon(R) CPU E5-2650 v3 @ 2.30GHz), the six controllers \hat{K}^k at the end of the step 2 are obtained in approximately 2 hours (so around twenty minutes per controller \hat{K}^k), which seems very reasonable for the control of a 3D configuration.

6.5 Analysis of the controlled flow in the linear regime

6.5.1 Performance on the ROMs

The results of the six controllers \hat{K}^k on the ROMs are analysed in this section. The figure 6.13a shows the magnitude of $(\hat{K}\hat{S})^k$ for the two steps of the algorithmic procedure. Note that the frequency template $1/|W_{(\hat{K}\hat{S})^k}| = 80$ dB used in the step 1 is located well above the maximum of $(\hat{K}\hat{S})^k$. Thanks to the minimization of $\|(\hat{K}\hat{S})^k\|_2$ at the step 2, the actuator activity is considerably reduced at low and high-frequencies for most controllers compared to those resulting of the step 1. In the bandwidth of the first Mack mode ($F \sim [0.02, 0.2]$) and second Mack mode ($F \sim [0.2, 0.3]$), the actuator activities resulting from step 1 and 2 are equivalent. All the controllers have the roll-off of -20 dB per decade at high-frequencies due to

their strictly-proper structure. The quantity $\sqrt{\sum_{k=0}^5 \|(\hat{K}\hat{S})^k\|_2^2}$ at the end of the step 2 is about 1.89 times lower than after the step 1 which allows a stronger performance robustness to white noise corrupting estimation sensors, and this without impacting the nominal performance and stability robustness. The Nyquist plots of the SISO loop gains $-(\hat{T}_{\mathbf{y}\mathbf{u}}\hat{K})^k$ after the step 2 is plotted in figure 6.13b. The minimal distance between the Nyquist plots and the critical point $(-1, 0)$ (red cross) after which a closed-loop becomes unstable, representing by the modulus margin $\|\hat{S}^k\|_\infty^{-1}$, is higher than 0.5 for all loop gains $-(\hat{T}_{\mathbf{y}\mathbf{u}}\hat{K})^k$, which obeys logically the constraint $\|W_{\hat{S}^k}\hat{S}^k\|_\infty < 1$ imposed in the CMPs. Some controllers are even further away from the critical point and would be guaranteed stable for a relative error on $\hat{T}_{\mathbf{y}\mathbf{u}}^k$ greater than 50%: for example $\|\hat{S}^1\|_\infty^{-1} = 0.82$ which means that the controller \hat{K}^1 associated with the spanwise mode $k = 1$ will be guaranteed stable up to 82% of relative model error $\hat{\Delta}^1$ on $\hat{T}_{\mathbf{y}\mathbf{u}}^1$. Concerning the nominal performance evaluated on the ROMs, it is summarized in table 6.2 and plotted in figure

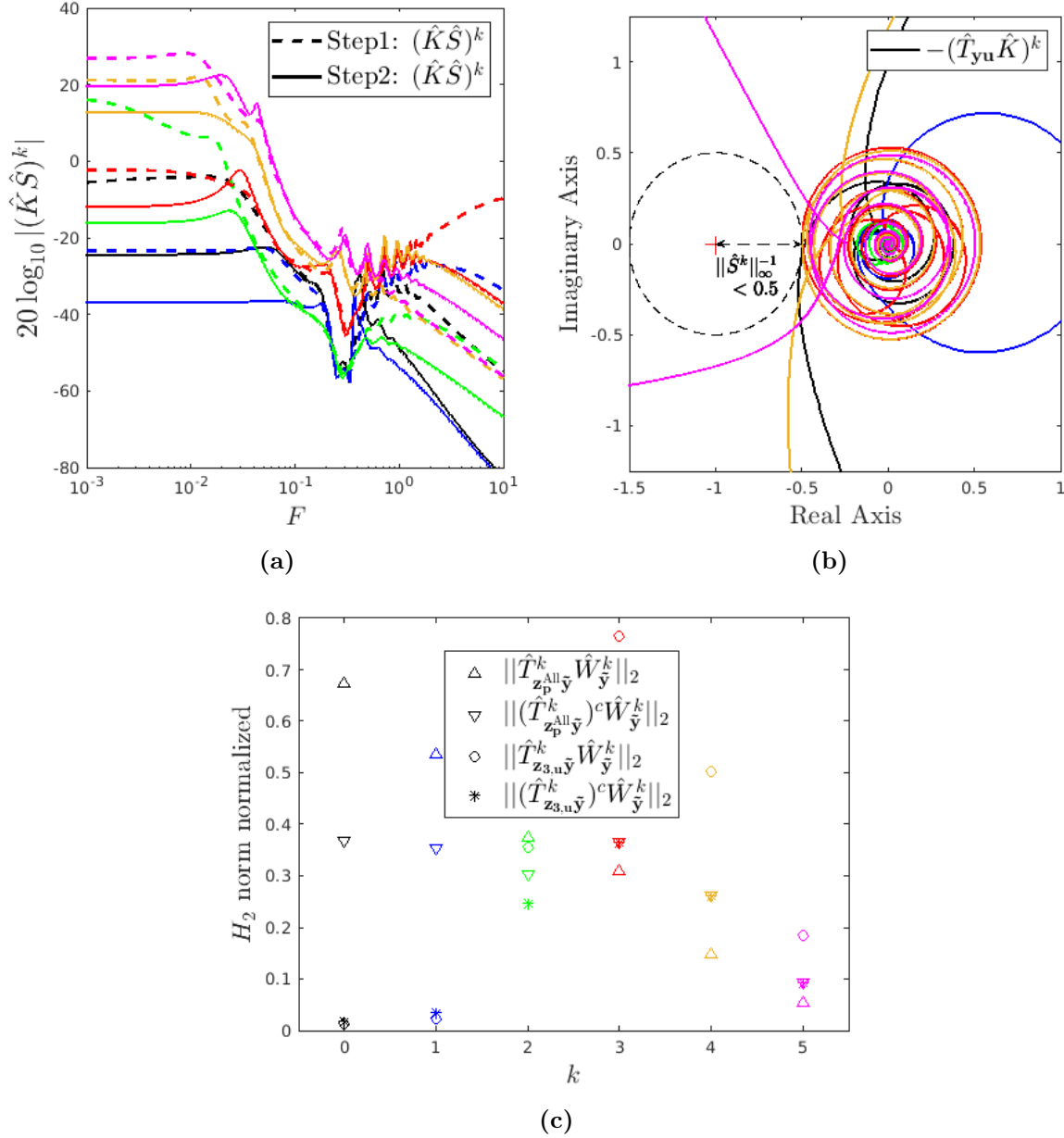


Figure 6.13: For colors, same caption as in figure 6.12. (a) Gain of $(\hat{K}\hat{S})^k$ for the two minimization steps. (b) Nyquist plot of the loop gain $-(\hat{T}_{yu}\hat{K})^k$. (c) Comparison for controlled and uncontrolled cases of $\|\hat{T}_{z_{3,u}\hat{y}}^k \hat{W}_{\hat{y}}^k\|_2$ and $\|\hat{T}_{z_p^{All}\hat{y}}^k \hat{W}_{\hat{y}}^k\|_2$ normalized by their respective uncontrolled values $\|T_{zw}\|_2$ approximated by the six spanwise modes used in the synthesis.

6.13c. The weightings lead to privilege pressure disturbance rejection over velocity disturbance rejection for the first two modes $k = 0$ and $k = 1$ as $\|(\hat{T}_{z_p^{All}\hat{y}}^k)^c \hat{W}_{\hat{y}}^k\|_2 > \|(\hat{T}_{z_{3,u}\hat{y}}^k)^c \hat{W}_{\hat{y}}^k\|_2$; the algorithm therefore seeks in priority to minimize the pressure perturbations and even amplifies the velocity perturbations compared to the uncontrolled case for these first two spanwise modes. Hence, an effect similar to the waterbed effect appears as the reduction of the amplitude of some frequencies leads to the amplification of other ones. Both pressure and velocity disturbances are reduced for $k = 2$. For the last three modes $k = 3$, $k = 4$ and $k = 5$, the weightings lead to privilege velocity disturbance rejection while the pressure perturbations are amplified until reaching a Pareto front $\|(\hat{T}_{z_p^{All}\hat{y}}^k)^c \hat{W}_{\hat{y}}^k\|_2 \simeq \|(\hat{T}_{z_{3,u}\hat{y}}^k)^c \hat{W}_{\hat{y}}^k\|_2$ where it is no longer possible to reduce one without degrading the other.

| | $k = 0$ | $k = 1$ | $k = 2$ | $k = 3$ | $k = 4$ | $k = 5$ |
|---|---------|---------|---------|---------|---------|---------|
| $\ \hat{T}_{\mathbf{z}_p, \mathbf{u}}^k \hat{W}_{\tilde{\mathbf{y}}}^k\ _2$ | 0.67 | 0.54 | 0.37 | 0.31 | 0.15 | 0.05 |
| $\ (\hat{T}_{\mathbf{z}_p, \mathbf{u}}^k)^c \hat{W}_{\tilde{\mathbf{y}}}^k\ _2$ | 0.37 | 0.35 | 0.30 | 0.36 | 0.26 | 0.09 |
| $\ \hat{T}_{\mathbf{z}_3, \mathbf{u}}^k \hat{W}_{\tilde{\mathbf{y}}}^k\ _2$ | 0.01 | 0.02 | 0.36 | 0.76 | 0.50 | 0.18 |
| $\ (\hat{T}_{\mathbf{z}_3, \mathbf{u}}^k)^c \hat{W}_{\tilde{\mathbf{y}}}^k\ _2$ | 0.02 | 0.04 | 0.25 | 0.36 | 0.26 | 0.09 |

Table 6.2: Nominal performance on the ROMs for each spanwise mode k normalized by the weightings used in step 1 of the algorithmic procedure: their respective uncontrolled values $\|T_{\mathbf{z}\mathbf{w}}\|_2$ approximated by the six spanwise modes used in the synthesis.

6.5.2 Performance on the full system

The six controllers \hat{K}^k are used to form the diagonal matrix $\hat{K}(s)$. The controller matrix $\hat{K}(s)$ is of order $6 + 5 \times 6 \times 2 = 66$ as each \hat{K}^k is of order 6 and \hat{K}^k appears twice in the matrix when $k \geq 1$. For $k \geq 6$, $\hat{K}^k = 0$. Then, the MIMO centralized controller used in the physical space is obtained as $K(s) = D_{DFT}^{-1} \hat{K}(s) D_{DFT}$ and implemented in the CFD solver *FastS* where the control signal vector \mathbf{u} is updated from the estimation signal vector \mathbf{y} by solving the first-order differential equations of the controller state-space representation.

The spatio-temporal responses and frequency spectra of the spanwise modes for the performance sensors $\mathbf{z}_{3,\mathbf{u}}$ and $\mathbf{z}_{3,\mathbf{p}}$ after an impulse of the exogenous noise w^0 (at the center spanwise position) are represented in figure 6.14. With the control action, the oblique structure of the velocity wavepacket at the generalized inflection point is conserved but its amplitude is lower compared to the uncontrolled case (see figures 6.14(a,c)) as the amplitude of the dominant frequencies and spanwise modes of the first Mack mode have been reduced (see figures 6.14(b,d)). The amplitude of the wall-pressure wavepacket is also decreased (see figures 6.14(e,g)) thanks to the control which targets also the dominant frequencies and spanwise modes of the second Mack mode (see figures 6.14(f,h)). As the dominant frequencies and modes between the controlled and uncontrolled cases are still the same, the 2D structure of the wall-pressure wavepacket is weakly impacted. The amplitude of the dominant spanwise modes are reduced at each abscissa of the plate and control does not modify modes higher than $k = 5$ (see figure 6.15) because we focused only on smaller modes in our synthesis. The quantity $\max_{x > x_{\mathbf{u}}, k} \ln \|\hat{T}_{\mathbf{z}(x)\mathbf{w}}^k\|_{\infty} - \max_{x > x_{\mathbf{u}}, k} \ln \|(\hat{T}_{\mathbf{z}(x)\mathbf{w}}^k)^c\|_{\infty}$ from the streamwise position of the actuators $x_{\mathbf{u}}$ until the end of the domain is equal to ~ 0.9 and ~ 0.85 for the velocity and pressure performance sensors, respectively. From the LLST point of view, this quantity may akin to $\max_{x > x_{\mathbf{u}}} \tilde{N} - \max_{x > x_{\mathbf{u}}} \tilde{N}^c$ with \tilde{N} and \tilde{N}^c the N -factor envelope of the uncontrolled and controlled cases, respectively.

Beyond these results for the performance sensors, the performance is also evaluated by considering the r.m.s. values averaged in the spanwise direction when the 3D boundary layer is excited simultaneously by the 35 uncorrelated white-noise signals w^j . For the r.m.s. velocity field (see figure 6.16), whose high values are located around the generalized inflection point due to the predominance of the first Mack mode, the control reduces the amplitude of the perturbations. For the r.m.s. pressure field (see figure 6.17), the high values are located both close to the generalized inflection point and close to the wall due to the first Mack mode and second Mack mode, respectively. The reactive law controls simultaneously these two modes but an acoustic wave is generated at the location of the actuators. This acoustic wave is almost not present on the density and temperature fields (see figures 6.18(a,b)) whose perturbations are considerably mitigated thanks to the control. The quantitative results for the quantity $\max_y \langle u'_{\text{rms}} \rangle_z$ are depicted in figure 6.18c and only one row of velocity performance sensors

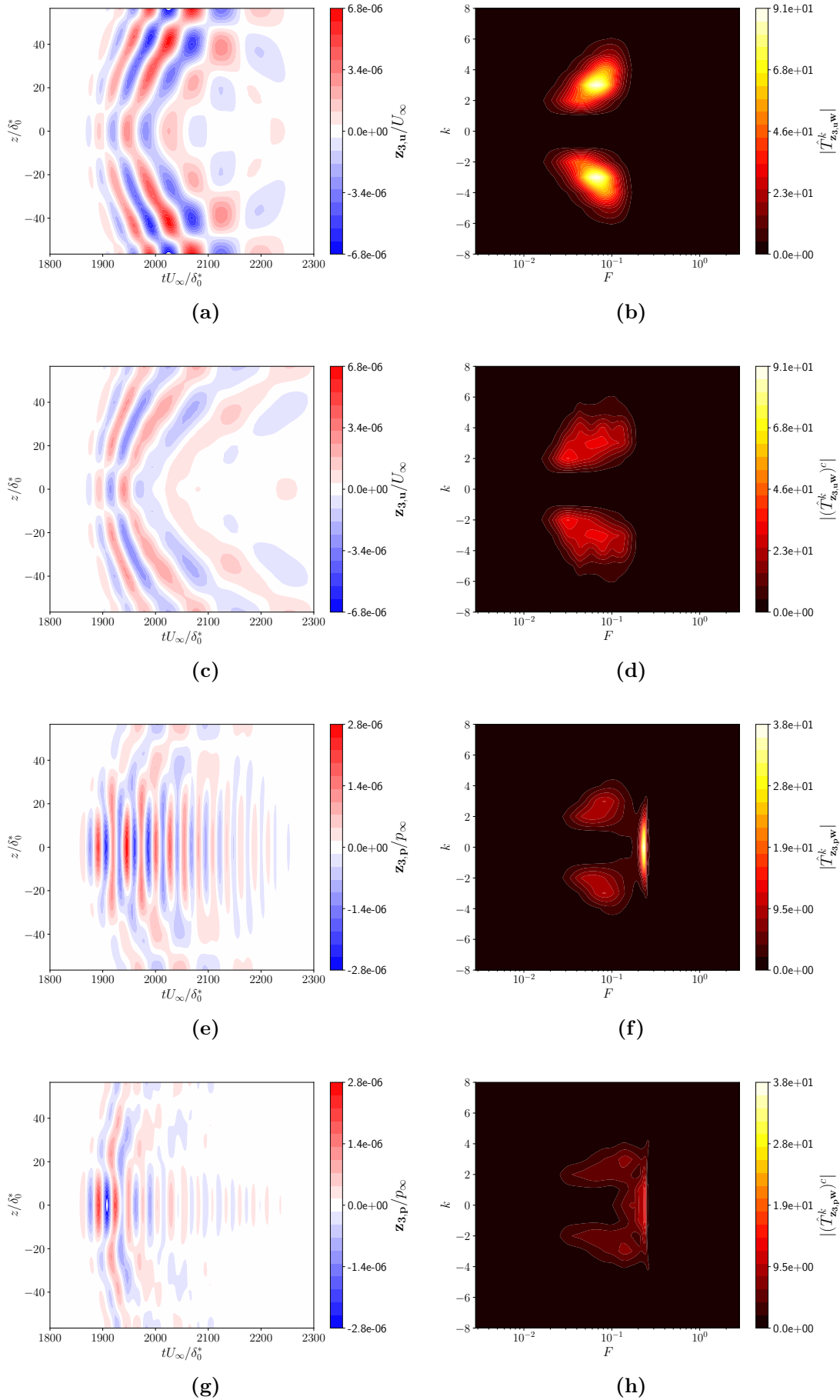


Figure 6.14: Spatio-temporal responses and frequency spectra of the spanwise modes are in the first and second columns, respectively. The uncontrolled case for the performance sensors $\mathbf{z}_{3,u}$ (resp. $\mathbf{z}_{3,p}$) is plotted in (a,b) (resp. (e,f)). The controlled case for the performance sensor $\mathbf{z}_{3,u}$ (resp. $\mathbf{z}_{3,p}$) is plotted in (c,d) (resp. (g,h)).

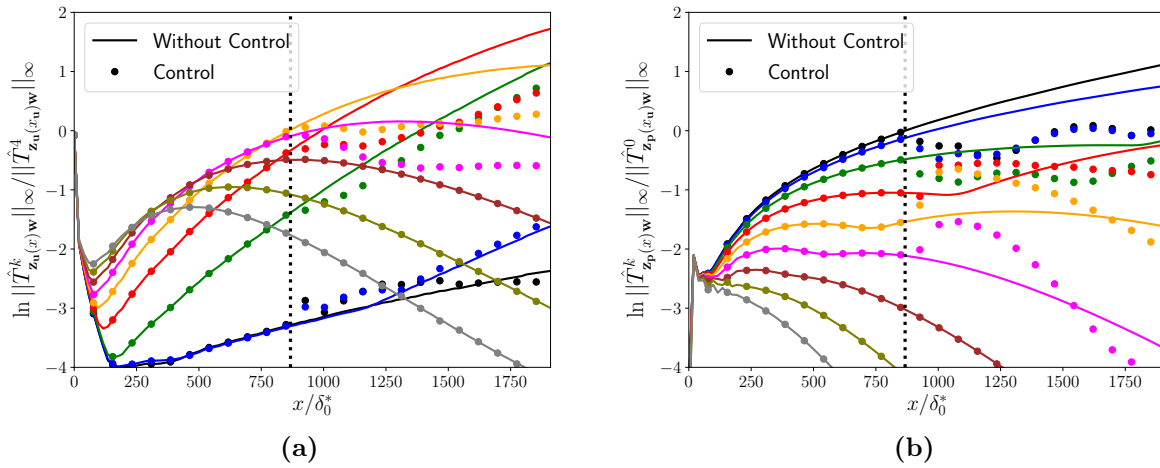


Figure 6.15: Evolution of $\|\hat{T}_{\mathbf{z}(x)\mathbf{w}}^k\|_{\infty}$ for some k for (a) velocity fluctuation performance sensors at the generalized inflection point and (b) wall-pressure fluctuation performance sensors. The vertical dotted line represents the streamwise position of the actuators. For colors, same legend as in figures 6.7(a,b).

at y_g in the synthesis step has allowed to reduce the amplitude of the disturbances all along the numerical domain. The quantity $\max_y \langle p'_{\text{rms}} \rangle_z$ bumps immediately after $x_{\mathbf{u}}$ (see figure

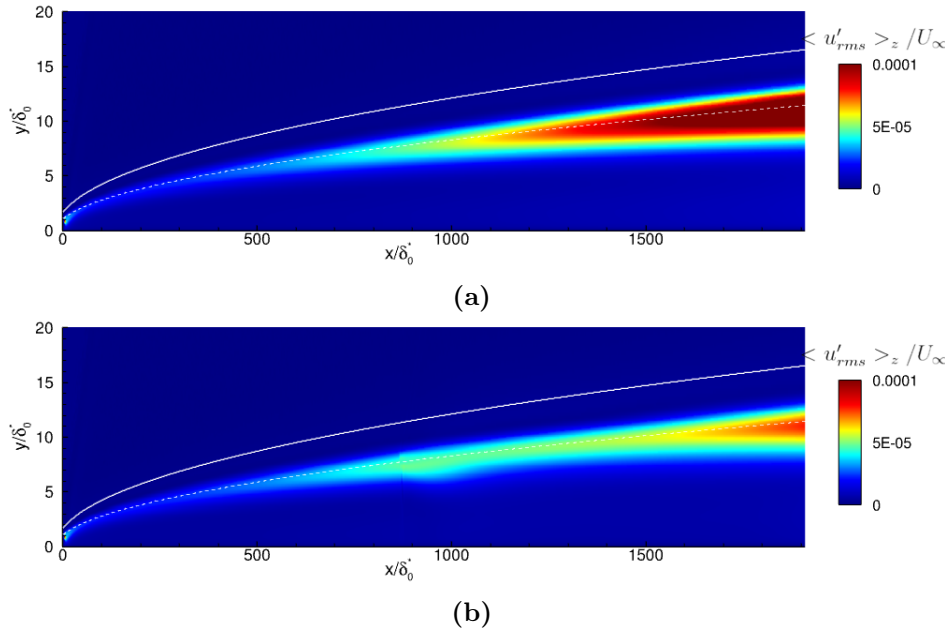


Figure 6.16: Contours of u'_{rms} averaged in the spanwise direction for the uncontrolled (a) and controlled (b) cases. The white solid and dashed lines represent the boundary layer thickness δ and the generalized inflection point position y_g , respectively.

6.18d) before decreasing as the acoustic wave is attenuated when exiting the boundary layer.

One could seek to further reduce the actuator activity, add performance sensors capable of detecting this acoustic wave or change the forcing field of the actuators to avoid this pressure bump. Yet, we will see in section 6.7 that this wave does not prevent delaying the transition to turbulence so the resulting controller is deemed sufficiently satisfactory and performance robustness is addressed next.

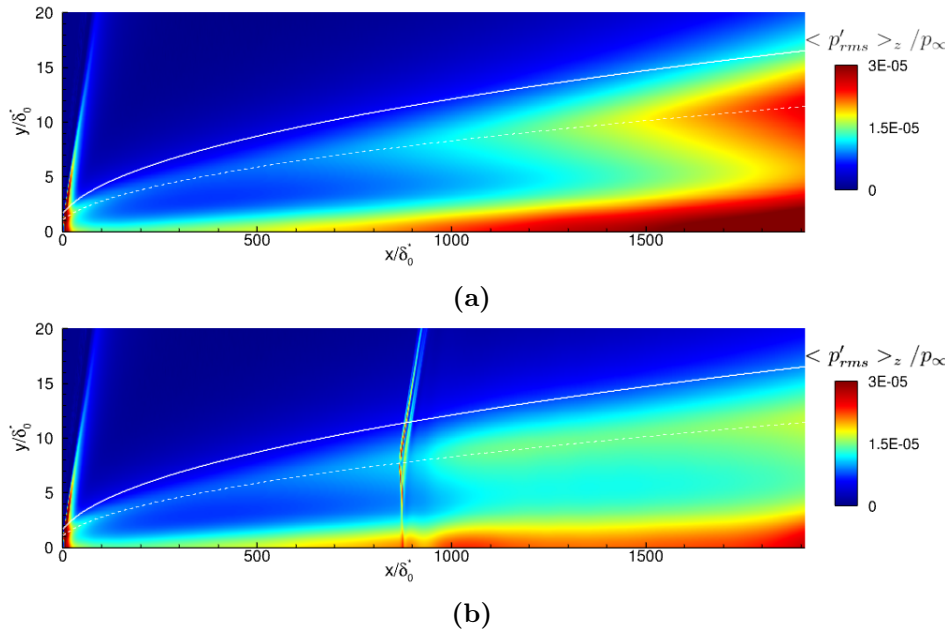


Figure 6.17: Contours of $\langle p'_{rms} \rangle_z$ averaged in the spanwise direction for the uncontrolled (a) and controlled (b) cases. The white solid and dashed lines represent the boundary layer thickness δ and the generalized inflection point position y_g , respectively.

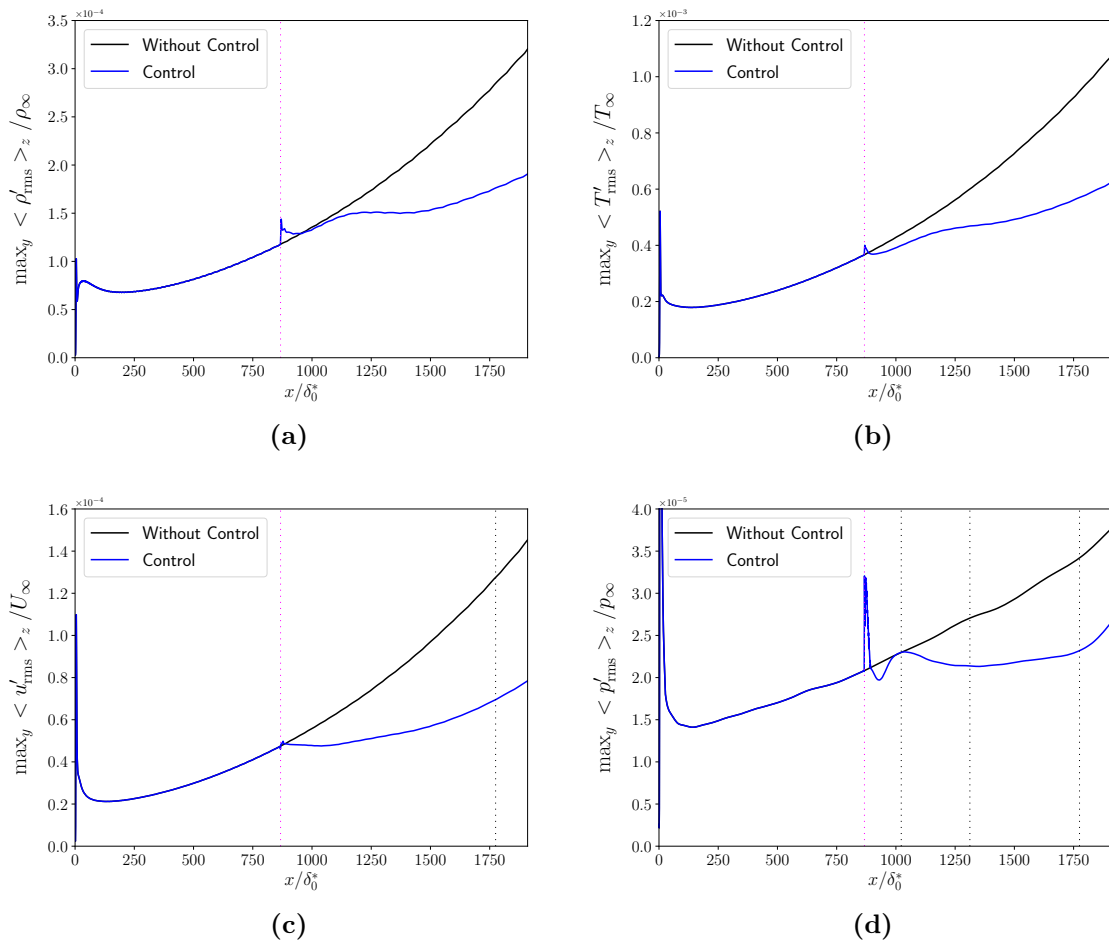


Figure 6.18: Evolution of $\max_y \langle \cdot \rangle_z$ for (a) ρ' , (b) T' , (c) u' and (d) p' . The vertical magenta and black dotted lines represent, respectively, the streamwise positions of the actuators (with the sensors \mathbf{y} nearby) and the performance sensors \mathbf{z}_i used for synthesis.

6.5.3 Performance robustness

Performance robustness is evaluated by checking the performance in terms of disturbance rejection despite noisy estimation sensors and off-design operating conditions when free-stream velocity variations are considered, as in the 2D study (see section 4.7.3).

6.5.3.1 Noisy estimation sensors

Firstly, all the estimation sensors y^j are corrupted by uncorrelated white Gaussian noises n^j and by the same amount of noise (50% of the r.m.s. value without control of y^j , *i.e.* ideal signal-to-noise ratio of 2), which models an intrinsic defect of the wall-pressure estimation sensors. The PSD of the noisy estimations sensors y^j (red line) is very far from that of the ideal sensors (blue line) in low and high frequencies (see figure 6.19a) because as n^j is a white noise, the gain of the ratio $y^j(iF)/n^j(iF)$ is low where the ideal signal power is low. Conversely,

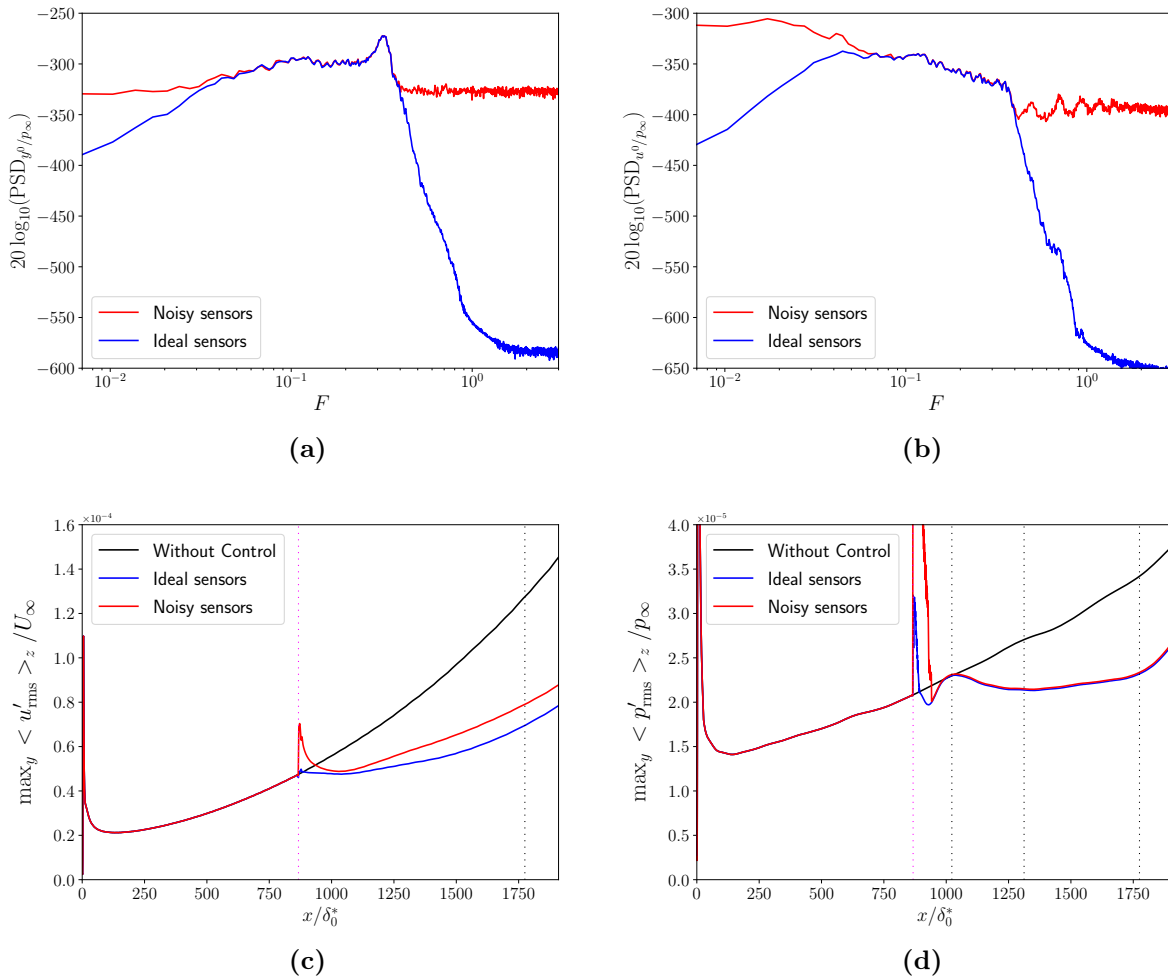


Figure 6.19: In all subplots, controlled systems with ideal and noisy estimation sensors \mathbf{y} are represented by blue and red lines, respectively. PSD of (a) y^0 and (b) u^0 . Evolution of (c) $\max_y \langle u'_{\text{rms}} \rangle_z$ and (d) $\max_y \langle p'_{\text{rms}} \rangle_z$. For vertical lines in (c,d), same caption as in figure 6.18.

the ratio $y^j(iF)/n^j(iF)$ is large where the ideal signal power is large ($F \sim [0.06, 0.35]$) and the PSD of the noisy sensors is similar to that of the ideal sensors. The PSD of the actuator signals for corrupted \mathbf{y} differs from that from ideal \mathbf{y} also in low and high frequencies because $\mathbf{u}(iF) = K(iF)\mathbf{y}(iF)$ (see figure 6.19b). The maximum along the wall-normal direction of

$\langle u'_{\text{rms}} \rangle_z$ slightly differs between the ideal and noisy estimation sensor cases (see figure 6.19c). Yet, except a bump near the streamwise actuator position due to the higher energy injection in

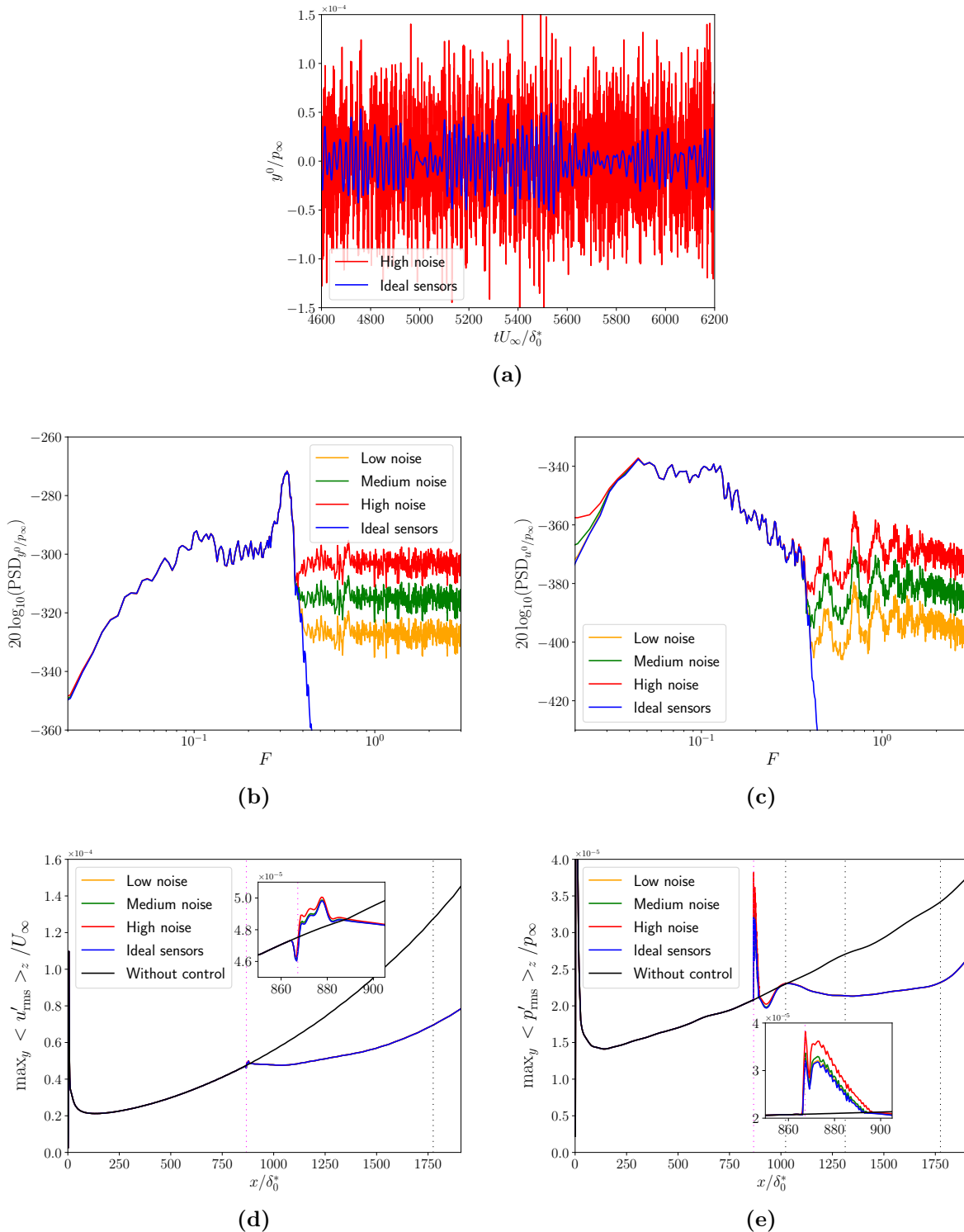


Figure 6.20: Estimation sensors \mathbf{y} are corrupted by different levels of colored noises. (a) Short sequence of y^0 . PSD of (b) y^0 and (c) u^0 . Evolution of (d) $\max_y \langle u'_{\text{rms}} \rangle_z$ and (e) $\max_y \langle p'_{\text{rms}} \rangle_z$. For vertical lines in (d,e), same caption as in figure 6.18.

low-frequencies, the quantity $\max_y \langle u'_{\text{rms}} \rangle_z$ stays below the uncontrolled curve all along the domain. For the quantity $\max_y \langle p'_{\text{rms}} \rangle_z$, the noisy sensors lead to a stronger acoustic wave

(see figure 6.19d). Downstream of this acoustic wave, the attenuation of disturbances with noisy sensors is equal to that with ideal ones. This is because the frequencies of the second Mack mode to be controlled ($F \sim [0.2, 0.3]$) are not impacted by the white noises \mathbf{n} as the ratio $y^j(iF)/n^j(iF)$ is the most important in this bandwidth, unlike the frequencies of the first Mack mode to be controlled ($F \sim [0.02, 0.2]$) where this ratio is weaker involving higher variations between the ideal and noisy cases for the quantities related to this first mode (*e.g.* the velocity field at y_g). The variations between the ideal and noisy cases for density and temperature fields (not shown here) follow the same trend as for velocity field. Note that if a strictly-proper structure for \hat{K}^k had not been imposed in the synthesis and the minimization of $\|(\hat{K}\hat{S})^k\|_2$ not realized in the step 2 of the CMPs, the power of the actuator signals would be much higher in high and low-frequencies and the intensities of the velocity bump and the acoustic wave would have been even more important.

Considering white noises \mathbf{n} is the most conservative approach when we do not know what kind of noise corrupts the sensors \mathbf{y} . Some sensors may be noisy only in high-frequencies in realistic setup [106]. A high-pass filter of order 12 with a cut-off frequency $F = 0.38$ is applied to the white Gaussian noises n^j . Hence, the estimation sensors are now corrupted by colored noises outside the bandwidth of the first and second Mack modes to be controlled. Different ideal signal-to-noise ratios (SNR) for these colored noises are evaluated: $\text{SNR}_1 \simeq 2.08$ (denoted "Low noise"), $\text{SNR}_2 \simeq 1.04$ (denoted "Medium noise") and $\text{SNR}_3 \simeq 0.52$ (denoted "High noise"). A temporal sequence of the corrupted sensors for the "High noise" case is depicted in figure 6.20a. The PSD of the estimation and actuator signals is corrupted only in high-frequencies with these colored noises (see figures 6.20(b,c)). The velocity disturbance rejection is as in the ideal sensor case even in the high noise $\text{SNR}_3 \simeq 0.52$ case (see figure 6.20d). The velocity bump that was present in the case of white noises is no longer present while the SNR is lower in the medium and high noise cases than in the previous white noise case: this velocity bump was clearly due to the low-frequency actuator activity which took important values when estimation sensors were corrupted by white noises. The pressure disturbance rejection is also equivalent to the ideal sensor case except in the acoustic wave region (see figure 6.20e): the acoustic wave intensity increases with the intensity of the colored noise but remains much lower than in the white noise case despite lower SNRs.

In summary, performance robustness despite noisy estimation sensors of our control law depends mostly on which frequencies are noisy. If white Gaussian noises corrupt the estimations sensors, the velocity disturbance rejection linked to first Mack mode is deteriorated as soon as $\text{SNR} = 2$ but the controlled curves stay below the uncontrolled ones over a fairly long distance along the plate. The performance remains that of the ideal case even with much lower SNRs when only high-frequency noisy sensors are considered. If even noisier sensors were used or if the velocity/acoustic bumps prevented delaying transition to turbulence, it would be enough to reduce more the actuator activity $(\hat{K}\hat{S})^k$ in the CMPs (especially in low-frequencies) by relaxing the constraints related to nominal performance.

6.5.3.2 Off-design operating conditions

Performance robustness to off-design operating conditions is assessed when free-stream velocity variations of $\pm 2.5\%$ are considered. These variations appeared to be the most problematic in the 2D study because they change the convective delays involving phase variations in the transfer functions (see chapters 4 and 5). In addition to modifying the hydrodynamic delays, the variations of U_∞ imply variations of $\pm 2.5\%$ of M_∞ and Re_x , since ρ_∞ and T_∞ are kept constant. The stability robustness analysis on these $\pm 2.5\%$ cases is not carried out and the controller is directly implemented on the full 3D system because each Nyquist plot of the SISO loop gain $-(\hat{T}_{\mathbf{y}\mathbf{u}}\hat{K})^k$ was far enough from the critical point (see figure 6.13b) to hope to be

stable after small velocity variations of $\pm 2.5\%$. New boundary layer profiles are used as inlet

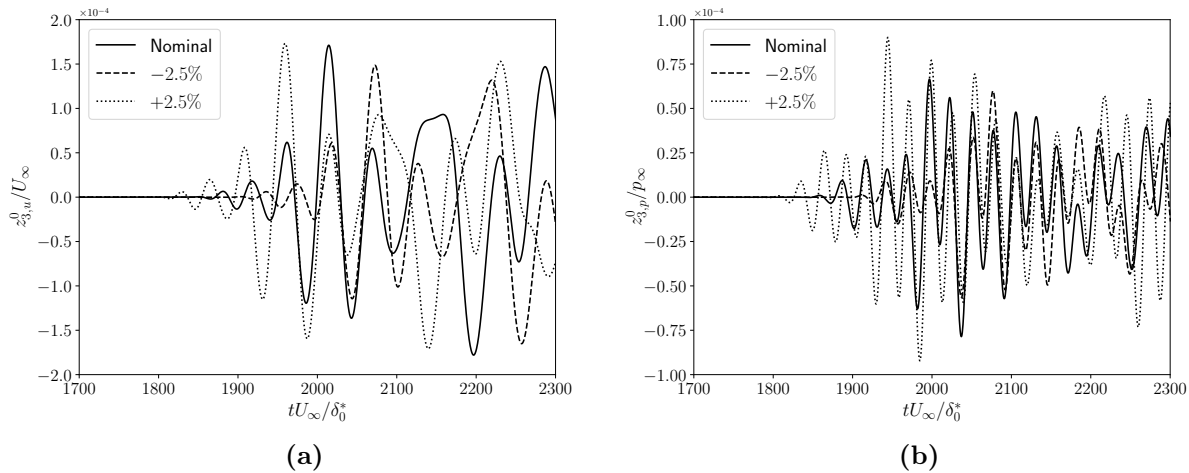


Figure 6.21: Start of the time sequence for (a) $z_{3,u}^0$ and (b) $z_{3,p}^0$ for the on-design case (solid lines) and the $\pm 2.5\%$ (dotted and dashed lines) off-design cases.

conditions. The start of the time sequence for performance sensors when the 3D boundary layer is excited simultaneously by the 35 uncorrelated white noise sources w^j with the same amplitudes as in the $M_\infty = 4.5$ DNS is plotted in figure 6.21: it illustrates the variation of convective delays. The PSD of the performance sensors $z_{3,u}^0$ and $z_{3,p}^0$ at the center spanwise position is represented in figures 6.22a and 6.22b, respectively. For uncontrolled cases (black lines), the dominant frequencies of the first Mack mode are relatively unaffected by the free-stream velocity variations. For the uncontrolled high-frequencies of the second Mack mode, their magnitudes are higher (respectively lower) in the $+2.5\%$ (respectively -2.5%) case than in the nominal $M_\infty = 4.5$ case. The amplitudes of the dominant frequencies of both the first and second Mack modes are reduced in the $\pm 2.5\%$ controlled cases (blue lines). The maxima along the wall-normal direction of $\langle u'_{\text{rms}} \rangle_z$ (see figure 6.22c) and $\langle p'_{\text{rms}} \rangle_z$ (see figure 6.22d) are still reduced in off-design conditions thanks to the feedback setup. Note that the higher the free-stream velocity, the lower the intensity of the acoustic wave generated by the control. For this range of free-stream variations, our simple feedback law is considered to be sufficiently robust in performance so that it is not necessary to further robustify some \hat{K}^k by multi-model synthesis (see chapter 5). For an even wider range of operating points, gain scheduling could be employed where the controller parameters vary with the operating point considered following an interpolating law from a set of LTI SISO controllers \hat{K}^k synthesized at various operating points. The gain scheduled law could be built very easily without any technical limitation in the 3D configuration because the interpolation law could be obtained in the wavenumber space thanks to the decentralized approach by solving the SISO CMPs.

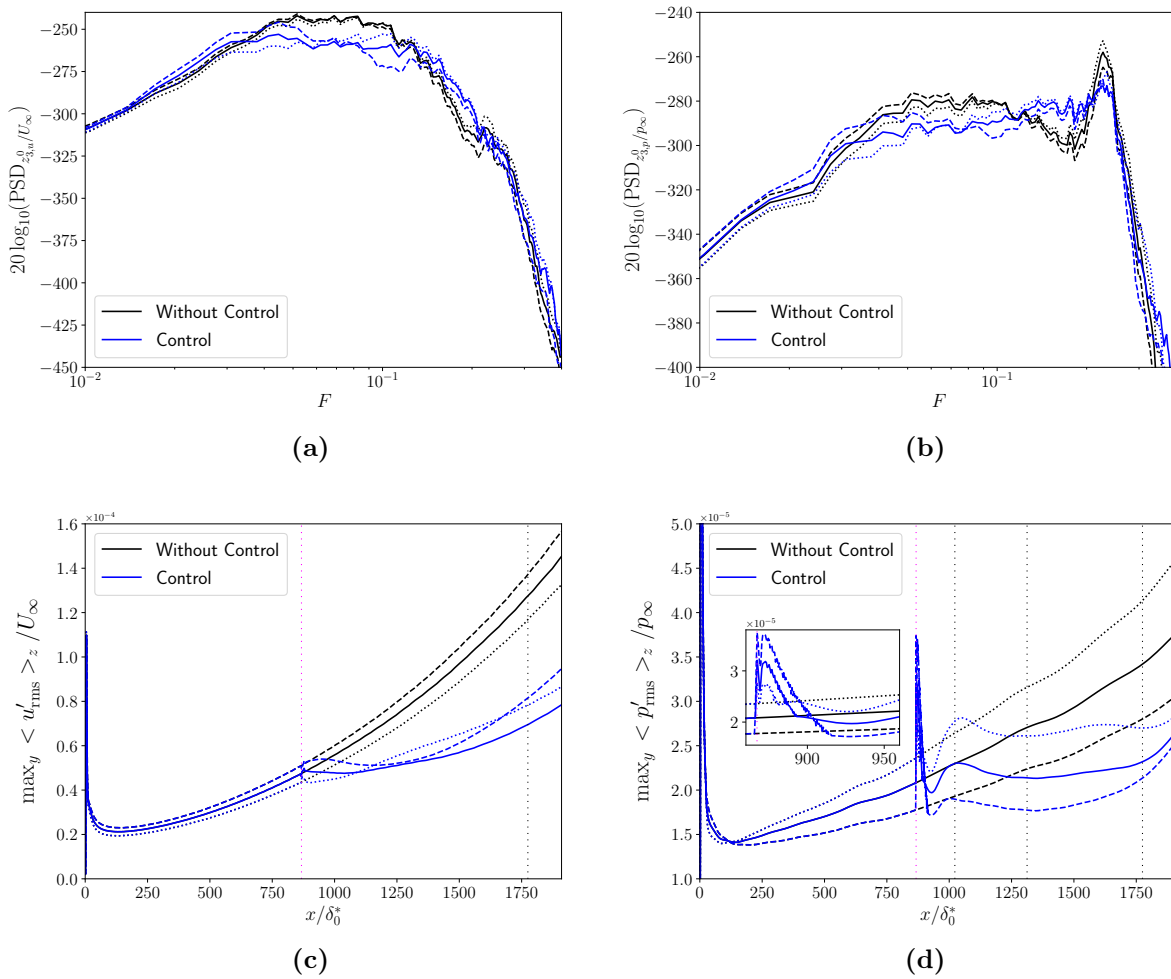


Figure 6.22: Evolution of the PSD of (a) $z_{3,u}^0$ and (b) $z_{3,p}^0$ after a variation of U_∞ of $\pm 2.5\%$. Evolution of (c) $\max_y < u'_{\text{rms}} >_z / U_\infty$ and (d) $\max_y < p'_{\text{rms}} >_z / p_\infty$ after a variation of U_∞ of $\pm 2.5\%$. The nominal cases are in solid lines; the $\pm 2.5\%$ cases are in dotted and dashed lines. For vertical lines in (c,d), same caption as in figure 6.18.

6.6 Robustness to non-linearities

All the results presented so far were for $w^j(t)$ of sufficiently low value to obtain perturbations which remain in the linear regime until the end of the domain as the tools of control theory (identification, synthesis) we used are based on the assumption of linearity. The robustness of the control law to non-linearities is now assessed as the non-linear interactions of secondary growth mechanisms may lead to the vortex breakdown which is a necessary phase to have a turbulent boundary layer (see section 1.5).

Two variances for the exogenous noise sources leading to non-linear growth in the domain are tested: $\text{Var}[w^j] = 1$ and $\text{Var}[w^j] = 25$. For comparison, the variance used in the linearized DNS was $\text{Var}[w_{\text{linear}}^j] = 0.0016$. The fluctuations of the estimation sensors are up to 0.19% and 1% of p_∞ when $\text{Var}[w^j] = 1$ and $\text{Var}[w^j] = 25$, respectively (see figure 6.23). At the streamwise position of the estimation sensors, the velocity fluctuations are up to 0.38% and 2% of U_∞ when $\text{Var}[w^j] = 1$ and $\text{Var}[w^j] = 25$, respectively. The control law still reduces significantly both velocity and pressure disturbances when $\text{Var}[w^j] = 1$, which is considered as a weakly non-linear case as the results are close to the linear ones (see figures 6.24(a,b)). When $\text{Var}[w^j] = 25$ (see figures 6.24(c,d)), the perturbation amplitude is such that the disturbances

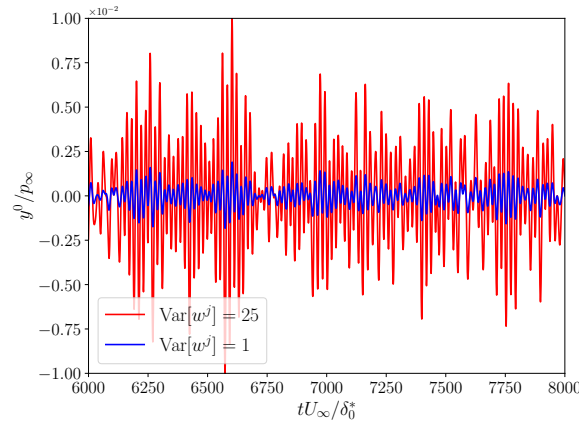


Figure 6.23: Short sequence of y^0 for different intensity levels of exogenous noises w^j in the uncontrolled case.

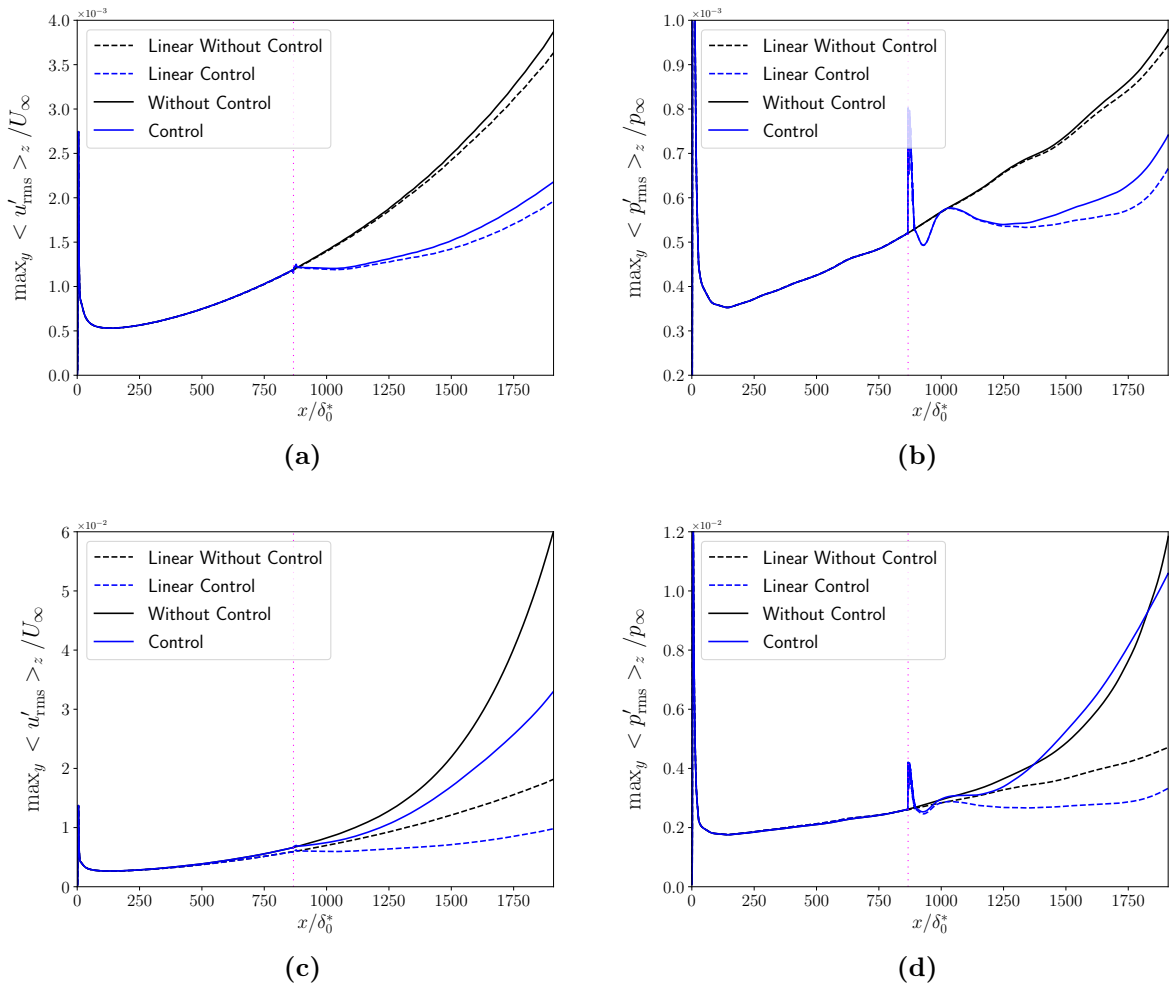


Figure 6.24: For exogenous noise sources with (a,b) $\text{Var}[w^j] = 1$ and (c,d) $\text{Var}[w^j] = 25$, evolution of (a,c) $\max_y \langle u'_{\text{rms}} \rangle_z$ and (b,d) $\max_y \langle p'_{\text{rms}} \rangle_z$. The linear cases (dashed lines) are rescaled by multiplying their results by $\sqrt{\text{Var}[w^j]/\text{Var}[w^j_{\text{linear}}]}$ for comparison. For vertical lines, same caption as in figure 6.18.

are weakly non-linear at $x_{\mathbf{u}}$ before being strongly non-linear at the end of the domain. For this stronger non-linear case, the control law still manages to maintain some performance by staying below $\max_y \langle u'_{\text{rms}} \rangle_z$ of the uncontrolled system all along the domain but the mitigation of pressure disturbances is no longer effective.

In summary, the control law designed from linear tools appears to be robust to non-linearities in terms of velocity perturbation rejection while the performance in terms of pressure perturbation rejection drops when the non-linear effects are too large.

6.7 Transition to turbulence

Finally, the ability of the feedback law to delay transition to turbulence of a supersonic boundary layer is assessed. The length of the previous 3D computational domain is doubled in the streamwise direction in order to obtain transition in the new domain while remaining weakly non-linear from the streamwise position of the actuators to the end of the previous domain used in linearized DNS. Indeed, this allows to mitigate both the pressure and velocity disturbances at least up to $x = 1910.2\delta_0^*$ as the reduction of pressure disturbances drops when non-linear effects are too important. For this new computational domain used for transition to turbulence, the boundary conditions and the wall-normal and spanwise lengths remain unchanged. The new streamwise length is $x \in [0., 3820.4\delta_0^*]$; the sponge zone after this useful domain is still present with the stretching of 30 cells in the streamwise direction and $L_{\text{sponge}} = 91.9\delta_0^*$. A resolution of $6400 \times 220 \times 176$ is adopted (not including the sponge zone) and the spacings in the x , y , z directions are the same as in the previous DNS. This resolution ensures that $\Delta x^+ < 4$, $\Delta z^+ < 3.5$ and $\Delta y_{\text{wall}}^+ < 1$ in the entire domain (dimensionless grid size is defined as $\Delta x_i^+ = \sqrt{\tau_{\text{wall}}\rho_{\text{wall}}} dx_i / \mu_{\text{wall}}$ with x_i corresponding to any direction of the cartesian coordinate system).

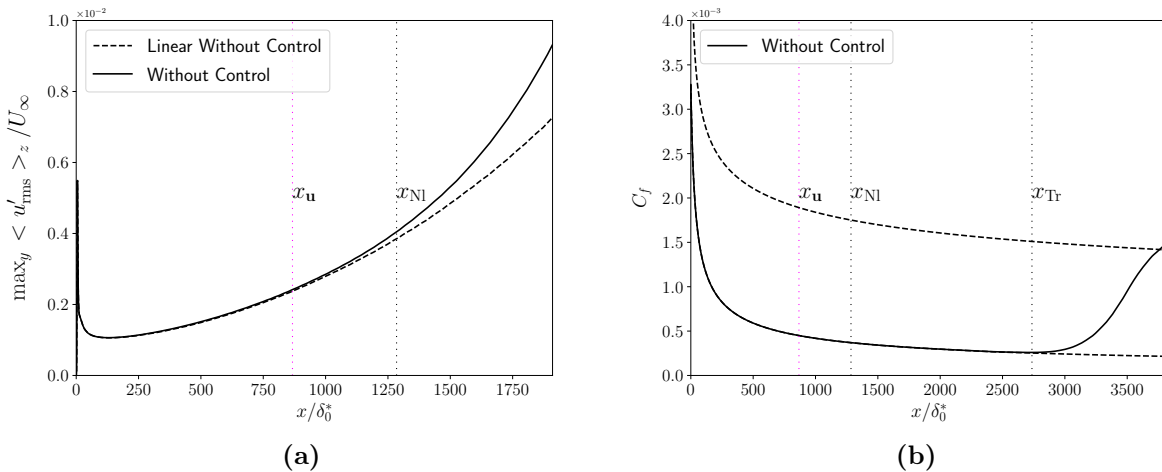


Figure 6.25: For exogenous noise sources with $\text{Var}[w^j] = 4$, evolution of (a) $\max_y \langle u'_{\text{rms}} \rangle_z$ and (b) C_f . The linear case (dashed line) in (a) is rescaled by multiplying its results by $\sqrt{\text{Var}[w^j]/\text{Var}[w_{\text{linear}}^j]}$ for comparison. The magenta vertical line represents the streamwise position of the actuators. The first and second black vertical dotted lines represent the streamwise position from which the non-linear effects are no longer negligible and the beginning of transition to turbulence, respectively. The black dashed curves in (b) represent the evolution of the skin friction coefficient for the fully laminar case (lower curve) and the turbulent case (upper curve).

The DNS of transition to turbulence is performed with exogenous noise sources with $\text{Var}[w^j] =$

4. With this noise intensity, the non-linear effects are no longer negligible from $x_{\text{NI}} = 1284.6\delta_0^*$ (see figure 6.25a, first vertical black dotted line); this position is defined in this study when the relative difference between $\max_y \langle u'_{\text{rms}} \rangle_z$ of linearized DNS and non-linear DNS is higher than 5%. At $x = 1910.2\delta_0^*$ (*i.e.* the end of the previous domain used for linearized DNS), the results differ by about 30%. In the uncontrolled case, the start of transition to turbulence, defined by $\arg_x \min C_f$ (with $C_f = \frac{\langle \tau_{\text{wall}} \rangle_{z,t}}{0.5\rho_\infty U_\infty^2}$), is at $x_{\text{Tr}} = 2736.0\delta_0^*$ (see figure 6.25b, second vertical black dotted line). The threshold curves that represent the skin friction of a laminar and a fully turbulent flat-plate boundary layer are also presented in this figure: the laminar and turbulent thresholds come from the DNS without exogenous noise sources and the results of [77] with a least square fit to obtain a $Re_x^{-1/5}$ correlation law, respectively.

A qualitative description of the transition process for the uncontrolled case is provided in figure 6.26. In the weakly non-linear region ($0 < x < x_{\text{NI}}$), the flow field is

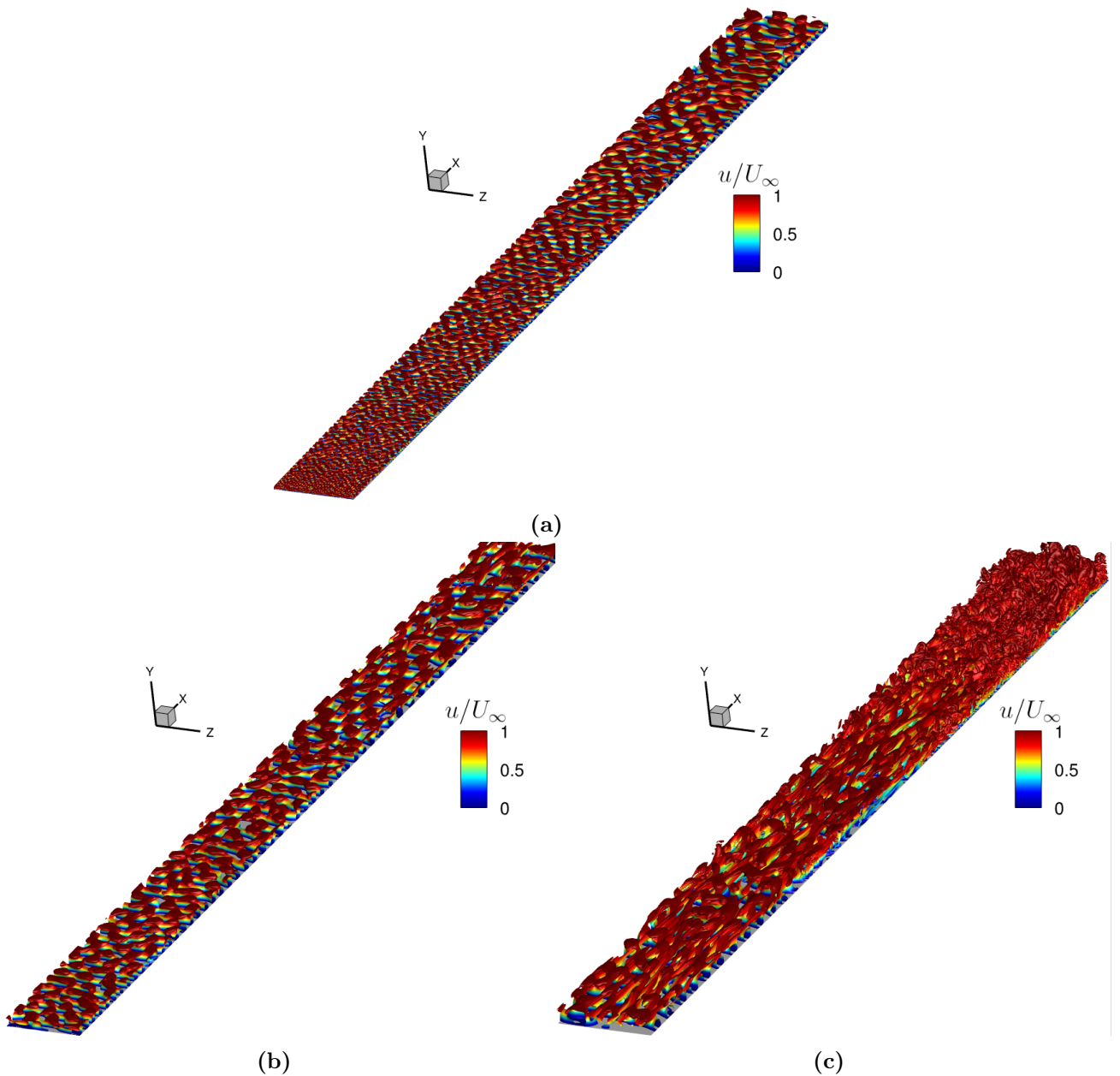


Figure 6.26: Uncontrolled DNS results of transition visualized using a Q-criterion isosurface ($Q = 2 \times 10^{-7} U_\infty^2 / \delta_0^{*2}$) colored by streamwise velocity for different streamwise segments: (a) $0 < x < x_{\text{NI}}$, (b) $x_{\text{NI}} < x < x_{\text{Tr}}$ and (c) $x_{\text{Tr}} < x < 3820.4\delta_0^*$.

dominated by the 2D structures of the second Mack mode near the wall with the oblique structures of the first Mack mode above (see figure 6.26a). Then, for $x_{\text{NI}} < x < x_{\text{Tr}}$ (see figure 6.26b), the 2D structures are still near the wall but the growth of the oblique waves leads to the generation of elongated streaks giving birth to Λ -vortices. Finally, for $x > x_{\text{Tr}}$ (see figure 6.26c), the evolution of the Λ -vortices and streaks results in the formation of hairpin vortices and the destabilization of near-wall structures which indicates a turbulent breakdown of the flow.

For this transition to turbulence scenario, the feedback control drastically reduces the maximum amplitude of disturbances all along the new numerical domain (see figure 6.27). At the end of the domain for $x = 3820.4\delta_0^*$, the quantity $\max_y \langle \cdot \rangle_z$ is reduced by approximately 42%, 53%, 61% and 27% for ρ' , T' , u' and p' , respectively. Note that the intensity of the acoustic wave generated by the control near x_{u} is negligible compared to the values of the pressure fluctuations further downstream of the domain and this acoustic wave does not prevent mitigation of the disturbance growth further downstream (see figure 6.27d). The reduction in disturbance

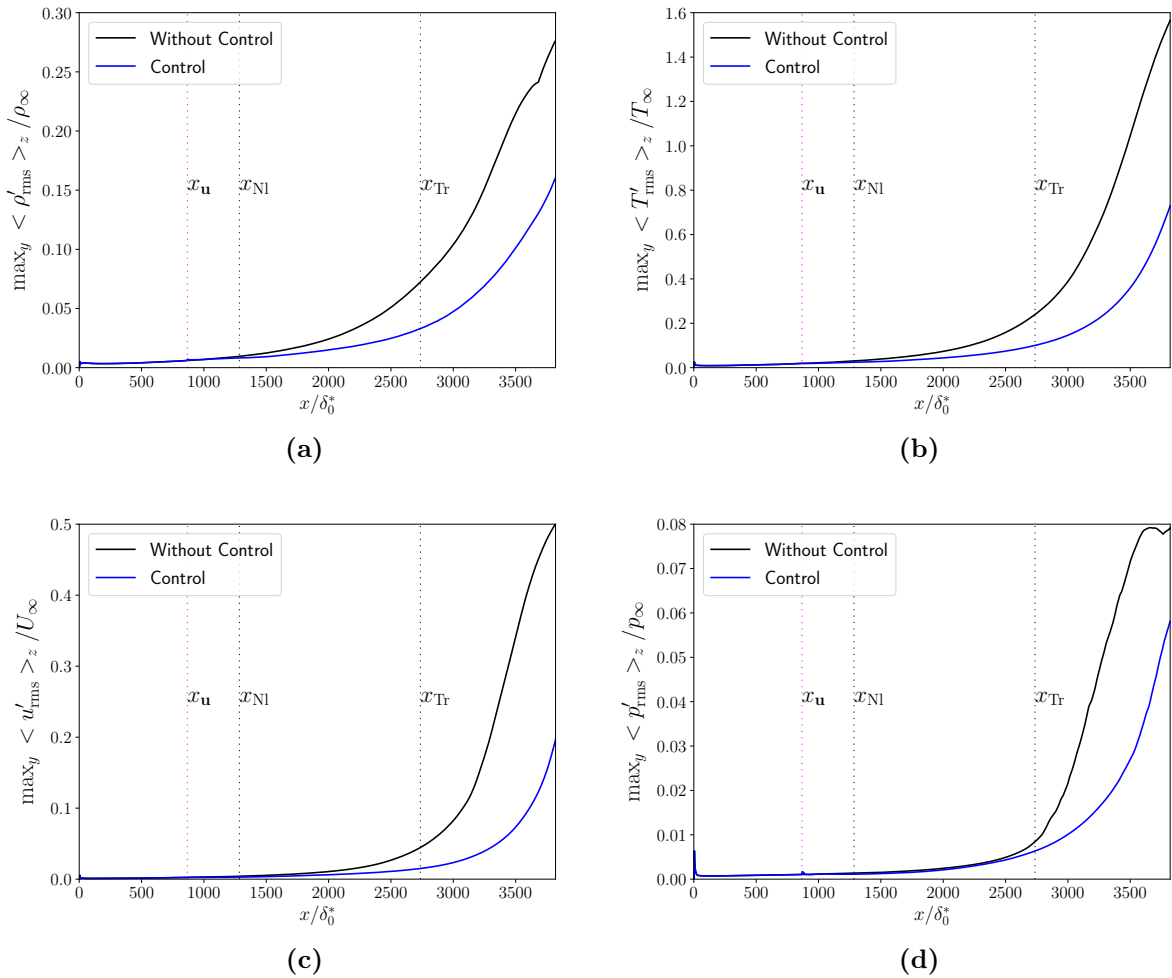


Figure 6.27: Evolution of $\max_y \langle \cdot \rangle_z$ for (a) ρ' , (b) T' , (c) u' and (d) p' for the transition case. For vertical lines, same caption as in figure 6.25.

amplitude is also illustrated by short timeseries in figure 6.28 for both the velocity and pressure fluctuations. The profiles of $\langle u'_{\text{rms}} \rangle_z$ at different streamwise locations are plotted in figure 6.29. In the weakly non-linear region (see figure 6.29a), the controlled r.m.s. profile takes lower values than the uncontrolled r.m.s. profile on the whole wall-normal direction thanks to the control of both the first and the second Mack modes. Even at a more downstream position

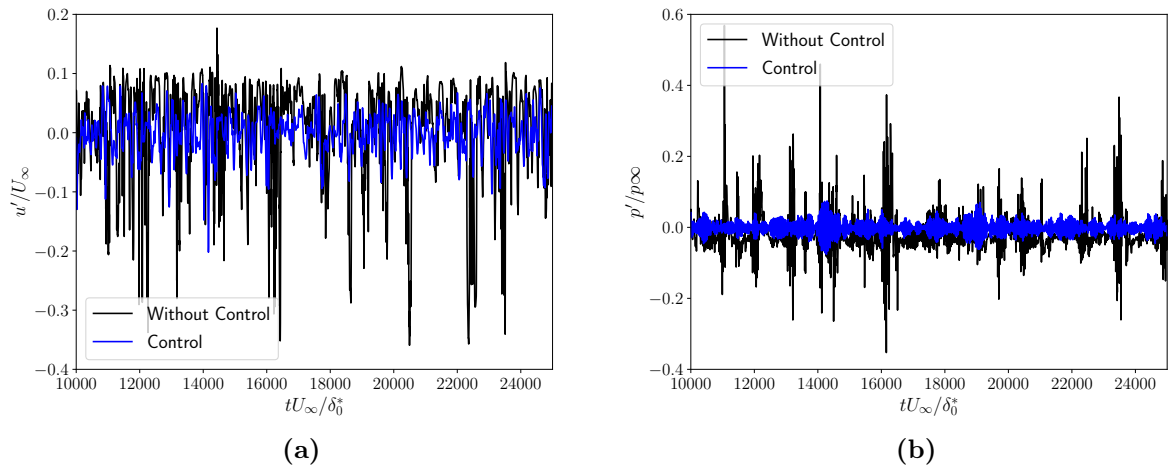


Figure 6.28: Short sequence of u' (a) and p' (b) at $(x, y, z) = (3281.6\delta_0^*, 15.1\delta_0^*, 0.)$ and $(x, y, z) = (3281.6\delta_0^*, 0., 0.)$, respectively.

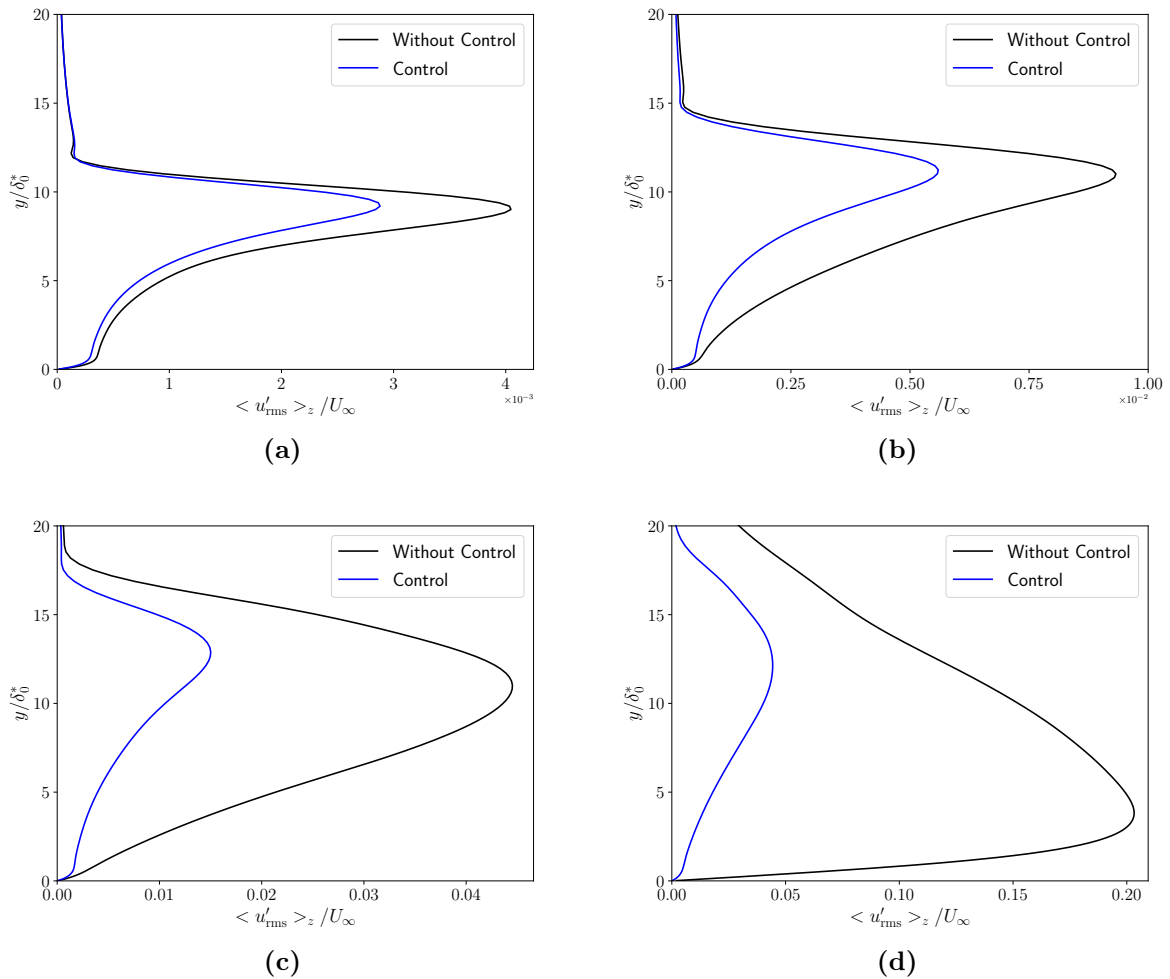


Figure 6.29: Profiles of $\langle u'_{\text{rms}} \rangle_z$ at (a) $x = x_{N1}$, (b) $x = 1910.2\delta_0^*$, (c) $x = x_{Tr}$ and (d) $x = 3300.5\delta_0^*$.

where the non-linear effects are much more important (see figure 6.29b), the maxima of the profiles are still located near the generalized inflection point as long as the boundary layer remains laminar. At the beginning of transition to turbulence (see figure 6.29c), the uncontrolled

profile $\langle u'_{\text{rms}} \rangle_z$ starts to collapse downwards while the maximum of the controlled profile is still near y_g . Finally, at $x = 3300.5\delta_0^*$ (see figure 6.29d), the maximum of the uncontrolled profile is located close to the wall while it remains further above in the controlled profile, with much lower r.m.s. values. The fact that the collapse of the velocity profile is delayed in the controlled case is due to the delay of the breakdown stage. Indeed, the non-linear interactions of the oblique first Mack modes near y_g lead to structures with wavenumbers twice as large (see figure 6.30a). This results in structures having these wavenumbers twice larger but at

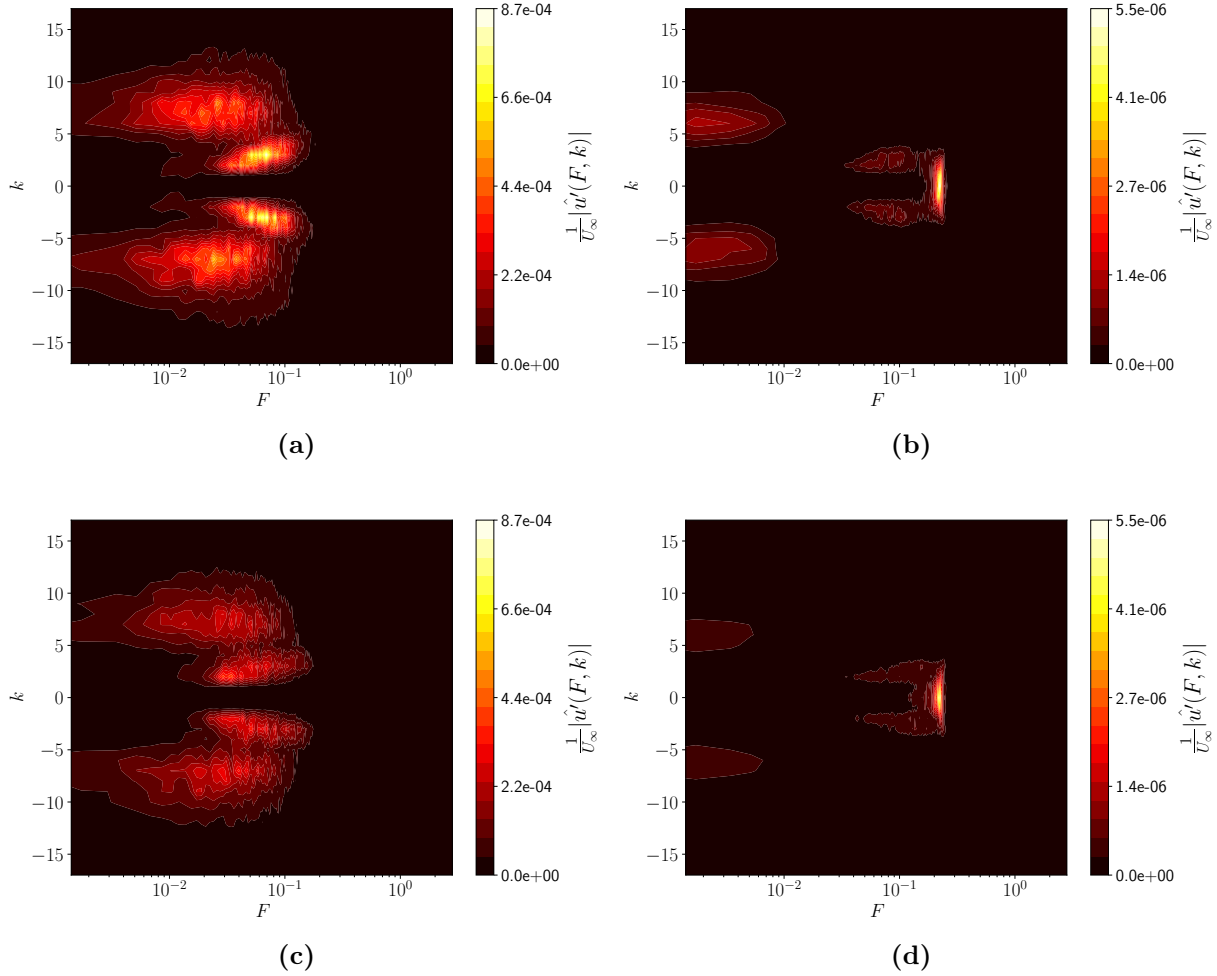


Figure 6.30: 2D spectrum $|\hat{u}'(F, k)|$ of the (a,b) uncontrolled and (c,d) controlled cases at (a,c) $(x, y) = (1904.8\delta_0^*, 11.5\delta_0^*)$ and (b,d) $(x, y) = (1904.8\delta_0^*, 0.015\delta_0^*)$.

zero frequency near the wall (see figure 6.30b): these steady vortices are pushed upward in the boundary layer by the lift-up effect resulting in streaks and in the first Mack mode oblique breakdown in the uncontrolled case. Even if the controller has only impact up to $k = 5$ in the linear case, the amplitude reduction of the modes up to $k = 5$ in the controlled case allows to have weaker non-linear interactions and thus to have weaker amplitudes for the structures with twice the wavenumbers of the oblique first Mack mode (see figure 6.30c). Hence, the amplitude of the steady vortices near the wall is decreased (see figure 6.30d) resulting in a delay of the first Mack mode oblique breakdown in the controlled case.

The instantaneous contours of streamwise velocity and numerical Schlieren visualisation are shown in figure 6.31. The uncontrolled flow presents wiggles and chaotic structures while the controlled flow appears smoother and the turbulent structures are clearly delayed thanks to the lower amplitude of the steady streak structures. The laminar region is extended in the

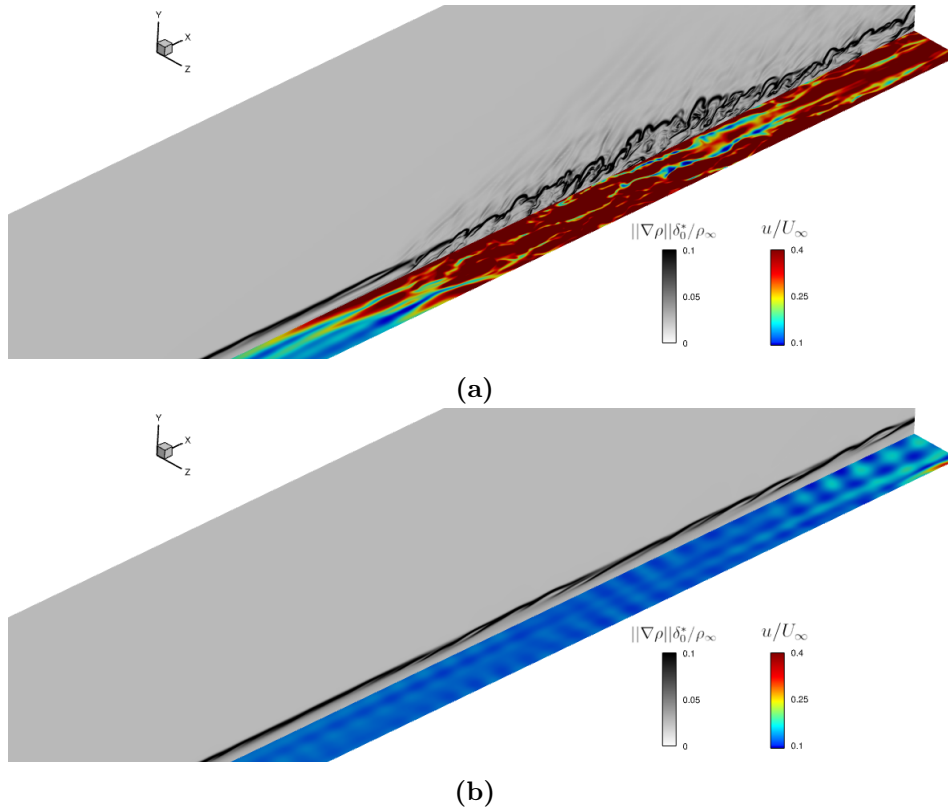


Figure 6.31: Instantaneous contours of streamwise velocity (xz -plane at $y = 1.99\delta_0^*$) and numerical Schlieren visualisation (xy -plane at $z = 0$) between $2939.7\delta_0^* < x < 3820.4\delta_0^*$ for the (a) uncontrolled and (b) controlled cases.

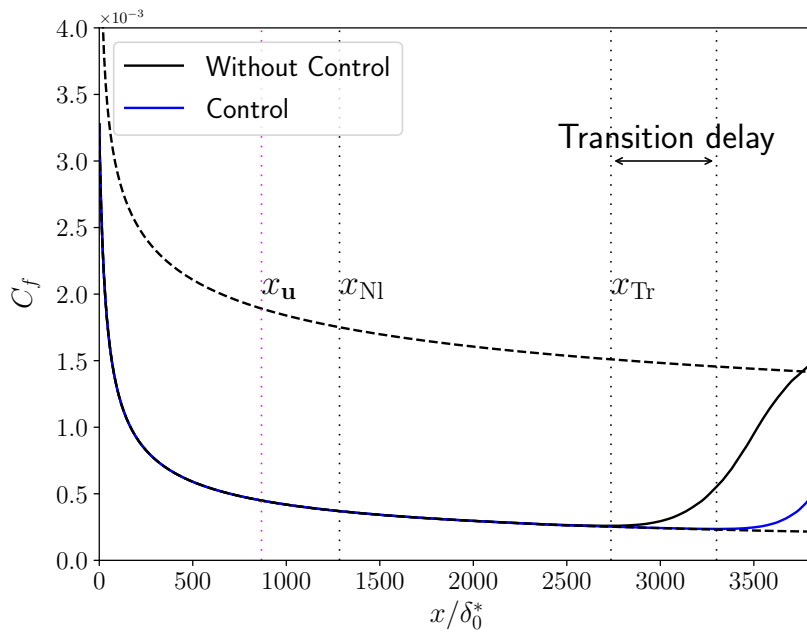


Figure 6.32: Evolution of the friction coefficient C_f for the transition to turbulence case. The third black vertical dotted line represents the beginning of transition to turbulence for the controlled case. For other vertical lines, same caption as in figure 6.25.

controlled case and transition to turbulence is delayed by $\Delta x_{\text{Tr}} = 564.4\delta_0^*$ (see figure 6.32); this distance represents $\sim 20\%$ of the distance from the leading edge of the flat plate to abscissa of transition in the uncontrolled case (*i.e.* $19\delta_0^* + 2736\delta_0^*$). The delay in terms of Re_x is $\Delta Re_x = 1.2 \times 10^6$. This result will be discussed and put in perspective in the next chapter.

Chapter outcome summary:

A robust reactive law has been developed to control both the linear growth of first and second Mack modes in a 3D boundary layer over a flat plate at Mach 4.5 in order to delay transition to turbulence.

The estimation sensors are placed downstream of the actuators to have a feedback setup and take advantage of its natural ability to be robust to free-stream variations and model uncertainties. Performance sensors are wall-pressure fluctuation sensors and velocity fluctuations sensors at the generalized inflection point to have strong observability of the amplification mechanisms of the first and second Mack modes. The MIMO centralized problem where all the inputs are connected to all the outputs is transformed to a SISO decentralized problem in the transverse wavenumber space where only one input is connected to one output. This greatly simplifies model identification and controller synthesis by solving multiple low-order independent problems instead of a single high-order problem and to spend control effort only on the spanwise modes associated with the most energetic structures. Indeed, the interconnection of the different modes is impossible in the linear growth stage.

The control law is built from linear tools where perturbations remain in the linear regime. The ERA is used for the identification procedure after shifting the time axis (removing dead times does not impact system norms) of some impulse responses to reduce the size of the ROMs. Then, structured mixed H_2/H_∞ synthesis is employed to impose the controller structure upfront and to obtain simultaneously in an optimal way nominal performance, stability robustness and performance robustness despite noisy estimation sensors.

The resulting controller, implemented in the *FastS* solver, is firstly tested on linear configurations. The control drastically reduces the amplitude of both first and second Mack modes although it leads to the creation of an acoustic wave. Performance robustness to noisy estimation sensors depends mostly on the noise spectrum but whether the estimation sensors are corrupted by white noise or high-frequency colored noise, the perturbation amplitude is reduced over a fairly long distance along the plate thanks to the CMPs solved. The performance robustness despite free-stream velocity variations, which are the most problematic variations due to the variations of the convective delays preventing to generate destructive interferences, is also ensured for variations of $\pm 2.5\%$ of U_∞ thanks to the feedback setup employed. The closed-loop is obviously stable on these off-design conditions thanks to the large stability margins imposed in the synthesis.

The robustness to non-linearities and the ability of the control law to delay transition to turbulence are also assessed. The perturbations have to be weakly non-linear at the streamwise position of the actuators to avoid a drop of the performance in terms of pressure perturbation rejection. For a transition to turbulence case, the control reduces the non-linear interactions as the amplitude of the steady structures near the wall is decreased, resulting in delaying the first Mack mode oblique breakdown of a distance representing $\sim 20\%$ increase in the laminar zone from the upstream edge of the plate.

Conclusions and outlook

Conclusions

The whole process of this thesis is dedicated to obtain a robust reactive control law to delay transition to turbulence of a supersonic boundary layer. This thesis has been divided into three main axes detailed below which allow to reach the objective.

Control of 2D instabilities with modern robust synthesis tools: feedforward vs feedback

The first step is dedicated to the control of 2D linear perturbations in a supersonic boundary layer at Mach 4.5 and to the comparison of the feedforward and feedback setups. Starting with a two-dimensional configuration simplifies the problem and allows probing new synthesis tools for tackling the issues of stability and performance robustness in closed-loop.

After linear input-output reduced-order models have been identified with special emphasis on the problem of time-delays in such noise-amplifier flow, multi-criteria structured mixed H_2/H_∞ synthesis is used to select beforehand the controller structure and to minimize appropriate norms of various closed-loop transfer functions: the H_2 norm is used to guarantee nominal performance (reduction of perturbation amplification) and the H_∞ norm is used to maintain performance robustness (with respect to noisy estimation sensor) and stability robustness (with respect to uncertain free-stream velocity/density variations).

Two control configurations are tested: one where the estimation sensor is placed upstream of the actuator (called *feedforward*) and one where the estimation sensor is placed downstream of the actuator (called *feedback*). Both feedforward and feedback setups maintain the local perturbation energy below a given threshold over a significant distance downstream of the actuator in the nominal case. Moreover, the stability robustness for the feedback design is not a problem thanks to the robust synthesis and the constraints imposed. Regarding performance robustness, both setups manage to reduce the amplitude of disturbances compared to the uncontrolled case despite noisy estimation sensors or inflow density variations of $\pm 5\%$. However, the feedforward setup becomes completely ineffective when free-stream velocity variations of $\pm 5\%$ are considered, which highlights the strong relevance of the feedback setup for performance robustness in convectively unstable flows when LTI controllers are built from a single operating point.

Maintaining low disturbances over a range of free-stream velocity variations

While stability robustness in a feedback configuration is not an issue thanks to modern synthesis methods, performance robustness, through velocity variations, has emerged as the major issue for noise-amplifier flows. In order to maintain performance in terms of perturbation amplitude reduction over a wide range of free-stream velocity variations, different techniques are employed (all based on the structured mixed H_2/H_∞ synthesis) for the control of the 2D supersonic boundary layer to improve the performance robustness of the baseline feedback-/feedforward controllers designed at a single operating point.

The first approach consisted in taking advantage of both the nominal performance of the feedforward configuration and the robust performance of the feedback configuration by combining the two in a single synthesis scheme to achieve optimal control over both aspects. Yet, this combined approach has no performance robustness when it is designed at a single operating point because the feedforward controller deteriorates the natural ability of the feedback controller to be robust to free-stream velocity variations.

Then, a multi-model synthesis was used which explicitly takes into account the performance robustness in the synthesis problem by optimizing a single controller over multiple operating points at once. The multi-model feedforward controller still amplifies more the disturbance amplitude than the uncontrolled case over the range of considered operating points due to the poor ability of a feedforward setup to be robust to phase variations which is equivalent to convective delay variations. Keeping the local perturbation energy below a constant threshold downstream of the actuator, for free-stream velocity variations of $\pm 5\%$, is found to be impossible using a unique feedback controller, even with multi-model synthesis. Multi-model synthesis slightly improves off-design performance over single-model synthesis indeed, but the gain is clearly insufficient for such a wide range of free-stream velocity variations and a different approach is required.

A gain scheduling method was therefore employed which results in a parametrized control law interpolating several controllers designed at different operating points. In the feedforward case, significant performance loss is observed in off-design conditions if interpolation points are too far apart. In the feedback case, gain scheduling allows to maintain low disturbances over the entire operating range $M_\infty \in [4.275, 4.725]$ with only two design points in the interpolation law.

In summary, when free-stream velocity variations are considered, the most effective control strategy requires first and foremost a feedback configuration. If a simple feedback controller does not provide desired performance over the entire range of operating points considered, then a gain scheduled feedback law needs may be employed.

Robust control of 3D instabilities in a supersonic boundary layer

The last step is dedicated to the robust control of 3D instabilities in order to delay transition to turbulence in the Mach 4.5 supersonic boundary layer. Based on the previous results, only a feedback controller designed from the structured mixed H_2/H_∞ synthesis is used in this 3D study to have the best trade-off between nominal performance and robustness to performance.

The control law is built from linear tools: data-driven identification with the ERA is performed after removing the unnecessary dead times and a decentralized method (where one input is connected to only one output) in the wavenumber space is exploited to build the controller as the interconnection of the different wavenumbers is impossible in the linear growth stage. This decentralized approach leads to solve with the structured mixed H_2/H_∞ synthesis several

constrained minimization problems with low complexity for each spanwise mode that one seeks to control, instead of one complex centralized problem of very high order.

The linear growth of both the first and second Mack modes is drastically reduced by the control. The performance is robust to noisy estimation sensors or free-stream velocity variations. In a case of transition to turbulence where the perturbations are weakly non-linear at the streamwise position of the estimation sensors, the laminar region is extended in the controlled case of a distance representing $\sim 20\%$ increase in the laminar zone from the upstream edge of the plate. Hence, a robust reactive control law delaying transition to turbulence due to the first Mack mode oblique breakdown has been obtained.

Outlook

A robust reactive control law delaying transition to turbulence at Mach 4.5 has been obtained but many research tracks remain to be investigated and some suggestions are given.

Direct continuation of this work would be:

- To check the control efficiency of the 3D configuration by comparing the mean power spent by the control (*i.e.* $\int_{\Omega} < (\sum_j u^j(t) \mathbf{B}_{u^j}) \cdot \mathbf{u}^c >_t \, d\Omega$) to the power saved by drag reduction (*i.e.* $U_{\infty} L_z \int_0^{L_x} < \tau_{\text{wall}} - \tau_{\text{wall}}^c >_{t,z} \, dx$) [56, 183]. If the control efficiency is less than 1, the implementation of the control law might not be worth it and a balance should be found between control cost and transition delay.
- To verify that transition can effectively be delayed for different uncontrolled transition positions. Indeed, our control law delays transition to turbulence for a certain uncontrolled transition position so different levels of exogenous noise sources should be tested. This is in the essence the problem of robustness to non-linearity, which is unfortunately not embedded in the LTI framework of robust control.
- To try different breakdown scenarios. Even if both the first and second Mack modes are present in the DNS, the transition scenario in the uncontrolled case is related to the first Mack mode oblique breakdown. Even if our law controls the linear growth of both modes, it could be interesting to check if our control law is able to delay the second Mack mode fundamental/sub-harmonic breakdown by exciting with the exogenous noise sources only the high-frequencies of the second Mack mode. In case of a transition generated by linear growth of streaks, our control law would surely be inefficient because this has not been taken into account in the synthesis.

None of these ideas require the synthesis of a new control law based on a different performance goal or a different control setup (actuators and sensors), but this may be beneficial for further transition delay:

- The control law of the 3D study is based on velocity and pressure disturbance rejection; one could investigate what is the best performance metric to minimize in terms of linear growth (*e.g.* POD mode coefficients based on Chu's or kinetic energy, temperature sensors, etc.) to delay transition as much as possible. It seems also possible to dispense with the velocity sensors at the generalized inflection point, because the wall-pressure fluctuation sensors are also sensitive to the first oblique Mack mode. This would allow to have only sensors at the wall, which would facilitate the experimental implementation.

- One might ask which is the most effective setup for delaying transition, between minimizing an H_2 norm (an integrated gain over all frequencies) or an H_∞ norm (maximum gain over all frequencies, somewhat to the N -factor envelope).
- One could seek to optimize the spatial support of the actuators (size of the Gaussian supports, the weight given to the different components of the forcing, which components to force, etc.) to target the spanwise modes to be controlled and thus improve the rejection of disturbances or reduce the energy cost. It might be worth to make this optimization under feasibility constraints.
- In the present study, each spanwise mode is controlled by an order 6 controller, but it is possible that increasing the controller order may lead to improved performance.
- It would be very interesting to try an idea proposed by Barbagallo et al. [13] where several actuators, estimation sensors, performance sensors triplets are used along the streamwise direction. Indeed, given the very large range of unstable frequencies developing along the plate, the impact of a single triplet is necessarily limited in the streamwise direction. Distributing multiple triplets in the streamwise direction would potentially push transition to turbulence even further downstream. Downstream triplets would take care of lower and lower frequencies. As soon as the non-linearities start to become too important, a new triplet is employed to keep perpetually disturbances in a linear regime and avoid transition to turbulence.

Open questions remain regarding multi-model synthesis and gain scheduling for maintaining performance robustness over a wide range of free-stream velocities:

- Multi-model synthesis has not been assessed for oblique modes developing in 3D. This method may provide satisfactory performance robustness to free-stream velocity variations, despite the weak effect on the second Mack mode in 2D.
- Gain scheduling could be pivotal to delay transition to turbulence over a large Mach range representative of flight conditions as soon as a simple feedback controller does not provide satisfactory performance for the different operating points. Nevertheless, the ability of a gain scheduled law to maintain performance has only been assessed for quasi-static variations of the free-stream velocity and it seems essential to verify the behaviour of the gain scheduled law (stability, overshoot, etc.) at short time scale. This may be achieved by progressively varying the free-stream conditions while keeping the controller active and parametrized by the scheduled variable and watch the behaviour of the controlled flow.

Finally, some orders of magnitude for the application of a control law on experimental/realistic configurations at Mach 4.5 are given. In table 6.3, the free-stream conditions of the experiments of Kendall [84] in a wind tunnel are provided, as well as the free-stream conditions at different altitudes from U.S. Standard Atmosphere Air Properties [194]. Critical quantities associated with our 3D study are computed for each operating point in table 6.4, leading to the following remarks:

- Controlling instabilities from $Re_{x_u} \sim 1.9 \times 10^6$ involves frequencies of the second Mack mode up to 50 kHz at 30 km of altitude, and it gets even worse at lower altitude (up to 1000 kHz at 10 km of altitude). Plasma actuator appears to be the only technology capable of reaching such high frequencies while being able to steer the input signal $\mathbf{u}(t)$ in real time according to sensor measurements [28]. More specifically, nanopulsed dielectric barrier discharge (NDBD) could be a promising lead although it is unclear whether the

| | ρ_∞ (kg/m ³) | T_∞ (K) | U_∞ (m/s) | μ_∞ (Pa.s) |
|----------------|------------------------------------|----------------|------------------|-----------------------------|
| Wind tunnel | ~ 0.03895 | ~ 65.15 | ~ 728 | $\sim 0.437 \times 10^{-5}$ |
| Altitude 0 km | ~ 1.225 | ~ 288.15 | ~ 1530 | $\sim 1.789 \times 10^{-5}$ |
| Altitude 10 km | ~ 0.4135 | ~ 223.25 | ~ 1348 | $\sim 1.458 \times 10^{-5}$ |
| Altitude 20 km | ~ 0.08891 | ~ 216.65 | ~ 1328 | $\sim 1.422 \times 10^{-5}$ |
| Altitude 30 km | ~ 0.01841 | ~ 226.51 | ~ 1358 | $\sim 1.476 \times 10^{-5}$ |

Table 6.3: Wind tunnel and typical free-stream conditions for different altitudes.

| | Frequencies to be controlled up to | y_g at x_u | Transition delay | Uncontrolled $x_{Tr} + 19\delta_0^*$ position |
|----------------|------------------------------------|----------------------------------|------------------------------------|---|
| Dimensionless | $F \sim 0.3$ | $Re_{y_g} \sim 1.6 \times 10^4$ | $\Delta Re_x \sim 1.2 \times 10^6$ | $Re_x \sim 5.8 \times 10^6$ |
| Wind tunnel | $f \sim 1.0 \times 10^5$ Hz | $y_g \sim 2.5 \times 10^{-3}$ m | $\Delta x \sim 0.18$ m | $x \sim 0.90$ m |
| Altitude 0 km | $f \sim 36 \times 10^5$ Hz | $y_g \sim 0.16 \times 10^{-3}$ m | $\Delta x \sim 0.011$ m | $x \sim 0.055$ m |
| Altitude 10 km | $f \sim 12 \times 10^5$ Hz | $y_g \sim 0.43 \times 10^{-3}$ m | $\Delta x \sim 0.030$ m | $x \sim 0.15$ m |
| Altitude 20 km | $f \sim 2.5 \times 10^5$ Hz | $y_g \sim 2.0 \times 10^{-3}$ m | $\Delta x \sim 0.14$ m | $x \sim 0.70$ m |
| Altitude 30 km | $f \sim 0.52 \times 10^5$ Hz | $y_g \sim 9.7 \times 10^{-3}$ m | $\Delta x \sim 0.70$ m | $x \sim 3.45$ m |

Table 6.4: Requirements and performance of the control law for a 3D supersonic boundary layer at Mach 4.5 for different free-stream conditions.

actuator authority would be sufficient to produce destructive interference. The power output may be too weak and it may difficult to hit the generalized inflection point to maximize receptivity, as we shall see in a later bullet point.

- In addition to having actuators capable of controlling these frequencies, the digital data acquisition system must have an even higher sampling frequency as well as the computational system to calculate the actuator signals.
- The forcing field of the actuators in our DNS was centered around the generalized inflection point y_g to maximize the receptivity process. Even if Shahriari et al. [171] showed that the body force of a ring-type plasma actuator in an experimental setup (obtained from the velocity field induced) can act up to few millimeters above the wall in their incompressible boundary layer case, y_g at the streamwise position of the actuators is almost located at 1 cm from the wall at 30 km of altitude. This position is probably unreachable with realistic DBD technology, but the situation is less critical at lower altitude: y_g is of the order of 0.5 mm at 10 km of altitude. Since receptivity is so critical to control authority, it would be interesting to optimize the design of a plasma actuator to specifically target the generalized inflection point for a given flight altitude.
- It is also unclear how an array of independent DBD actuators would behave if the actuators are very close to each other. Indeed, controlling oblique modes with high transverse wavenumber imposes a constraint on the minimal spacing between the various electrodes, which may induce undesired transverse streamers. In any case, designing actuators for closed-loop control of high-speed flows remains an immense technological challenge, which likely is the bottleneck to real implementation.
- Delaying transition by $\sim 20\%$ in the wind tunnel amounts to an extra 18 cm added to an 90 cm laminar zone without control. On the other hand, at 10 km of altitude, transition occurs very quickly over the first 15 cm without control and the benefit of

control is only 3 cm: this is clearly not enough for a missile of a few meters long. Placing multiple actuators/estimation sensors/performance sensors in this case probably becomes mandatory. The gain of laminarity is much greater at 20-30 km of altitude, of the order of 14-70 cm for an uncontrolled laminar zone of 70 cm-3.45 m. These orders of magnitude indicate the direct relevance of the closed-loop technology to surface-to-air missiles (MIM-104 Patriot, Aster 30, S-400 Triumpf, etc.). Some air-to-air missiles also fly at $M = 4.5$ (R-27, Meteor, MICA, AIM-120 AMRAAM) but not as high as 20-30 km of altitude.

- The proposed H_2/H_∞ framework for feedback control of boundary layer instabilities is quite generic and may be implemented at lower Mach numbers, where unstable frequencies are lower. It is therefore likely that an experimental proof-of-concept of the present methodology will be carried out at a lower Mach number than 4.5.

Appendices

Inner product matrices

The explicit expressions of \mathcal{Q}_f and \mathcal{Q}_e used for the different global stability analyses performed in this thesis are given in this section. The inner product matrix $\|\tilde{\mathbf{f}}\|_F^2 = \tilde{\mathbf{f}}^* \mathcal{Q}_f \tilde{\mathbf{f}}$ corresponds to the energy of the momentum forcing and the positive-definite matrix \mathcal{Q}_f is a block diagonal matrix where one block is defined as:

$$\mathcal{Q}_f^{\text{block}} = \mathcal{P}^* d\Omega \begin{pmatrix} 1 & 0 & 0 & 0 & 0 \\ 0 & 1 & 0 & 0 & 0 \\ 0 & 0 & 1 & 0 & 0 \\ 0 & 0 & 0 & 1 & 0 \\ 0 & 0 & 0 & 0 & 1 \end{pmatrix} \mathcal{P}, \quad (\text{A.1})$$

with $d\Omega$ the elementary volume of a grid cell and $\mathcal{P} = \begin{pmatrix} 0 & 0 & 0 \\ 1 & 0 & 0 \\ 0 & 1 & 0 \\ 0 & 0 & 1 \\ 0 & 0 & 0 \end{pmatrix}$ the prolongation operator

that transforms the momentum forcing $\tilde{\mathbf{f}}$ into a full state-vector forcing by adding zero components. The inner product matrix $\|\tilde{\mathbf{q}}\|_E^2 = \tilde{\mathbf{q}}^* \mathcal{Q}_e \tilde{\mathbf{q}}$ corresponds to the kinetic perturbation energy or the Chu's energy. For the kinetic perturbation energy, the semi-definite-positive matrix \mathcal{Q}_e is a block diagonal matrix where one block is defined as:

$$\mathcal{Q}_e^{\text{Kinetic, block}} = \frac{1}{2} d\Omega \begin{pmatrix} \frac{\|\tilde{\mathbf{u}}\|^2}{\bar{\rho}} & -\frac{\tilde{u}}{\bar{\rho}} & -\frac{\tilde{v}}{\bar{\rho}} & -\frac{\tilde{w}}{\bar{\rho}} & 0 \\ -\frac{\tilde{u}}{\bar{\rho}} & \frac{1}{\bar{\rho}} & 0 & 0 & 0 \\ -\frac{\tilde{v}}{\bar{\rho}} & 0 & \frac{1}{\bar{\rho}} & 0 & 0 \\ -\frac{\tilde{w}}{\bar{\rho}} & 0 & 0 & \frac{1}{\bar{\rho}} & 0 \\ 0 & 0 & 0 & 0 & 0 \end{pmatrix}. \quad (\text{A.2})$$

For the Chu's energy, the semi-definite-positive matrix \mathcal{Q}_e is a block diagonal matrix where one block is defined as:

$$\mathcal{Q}_e^{\text{Chu, block}} = \frac{1}{2} d\Omega \begin{pmatrix} \frac{\|\bar{\mathbf{u}}\|^2}{\bar{\rho}} + \frac{r\bar{T}}{\bar{\rho}} + a_1 a_2^2 & -\frac{\bar{u}(1+a_1 a_2)}{\bar{\rho}} & -\frac{\bar{v}(1+a_1 a_2)}{\bar{\rho}} & -\frac{\bar{w}(1+a_1 a_2)}{\bar{\rho}} & \frac{a_1 a_2}{\bar{\rho}} \\ -\frac{\bar{u}(1+a_1 a_2)}{\bar{\rho}} & \frac{1}{\bar{\rho}} + \frac{\bar{u}^2 a_1}{\bar{\rho}^2} & \frac{\bar{u}\bar{v} a_1}{\bar{\rho}^2} & \frac{\bar{u}\bar{w} a_1}{\bar{\rho}^2} & -\frac{\bar{u} a_1}{\bar{\rho}^2} \\ -\frac{\bar{v}(1+a_1 a_2)}{\bar{\rho}} & \frac{\bar{u}\bar{v} a_1}{\bar{\rho}^2} & \frac{1}{\bar{\rho}} + \frac{\bar{v}^2 a_1}{\bar{\rho}^2} & \frac{\bar{v}\bar{w} a_1}{\bar{\rho}^2} & -\frac{\bar{v} a_1}{\bar{\rho}^2} \\ -\frac{\bar{w}(1+a_1 a_2)}{\bar{\rho}} & \frac{\bar{u}\bar{w} a_1}{\bar{\rho}^2} & \frac{\bar{v}\bar{w} a_1}{\bar{\rho}^2} & \frac{1}{\bar{\rho}} + \frac{\bar{w}^2 a_1}{\bar{\rho}^2} & -\frac{\bar{w} a_1}{\bar{\rho}^2} \\ \frac{a_1 a_2}{\bar{\rho}} & -\frac{\bar{u} a_1}{\bar{\rho}^2} & -\frac{\bar{v} a_1}{\bar{\rho}^2} & -\frac{\bar{w} a_1}{\bar{\rho}^2} & \frac{a_1}{\bar{\rho}^2} \end{pmatrix}, \quad (\text{A.3})$$

with

$$a_1 = \frac{(\gamma - 1)\bar{\rho}}{r\bar{T}}, \quad (\text{A.4a})$$

$$a_2 = \frac{\frac{1}{2}\|\bar{\mathbf{u}}\|^2 - \bar{e}}{\bar{\rho}}. \quad (\text{A.4b})$$

The quantity e is the internal energy of the flow, defined as:

$$e = \frac{r}{\gamma - 1} T. \quad (\text{A.5})$$

Validation of the temporal and spatial schemes

The validation of the temporal schemes used in the 2D/3D DNS and the spatial schemes for 3D DNS is given in this section.

For the 2D linearized DNS (solver *elsA*) of the chapters 4 and 5, the ability of the spatial schemes used to describe the 2D perturbation field has been validated in section 3.1.4 and only the validation of the temporal scheme is presented here. The transfer functions can be obtained from the resolvent operator as $T_{z(x)w} = \mathbf{C}_{z(x)} \mathcal{R} \mathbf{B}_w$ (see section 2.4). In this formula, the quantities are those defined in the chapters 4 and 5: the performance sensors $z(x)$ are wall-pressure fluctuation sensors, w is the exogenous noise, \mathbf{B}_w is the divergence-free spatial support associated with w and the field $\mathbf{C}_{z(x)}$ extracts from the state vector \mathbf{q}' the wall-pressure measurements. The time step and the number of sub-iterations of the implicit second-order Gear scheme are validated by comparing transfer functions from the linearized DNS (see section 4.4) and those determined from the frequency-domain resolvent approach (see figure B.1). The frequency-domain resolvent approach is independent of the temporal scheme; this method is only dependent on spatial schemes (validated in the 2D case in section 3.1.4) to obtain a converged Jacobian matrix. For the two abscissa $x = 866.6\delta_0^*$ (in blue) and $x = 1766\delta_0^*$ (in red) (which correspond to positions near than those of the actuator u and the last performance sensor z_6 used in the synthesis, respectively), the gain of the transfer $T_{z(x)w}$ computed with the linearized 2D DNS (solid lines) corresponds to the one computed with the resolvent procedure (circles), which allows to validate the temporal scheme employed in the linearized 2D unsteady simulations.

For the 3D case of the chapter 6, no global stability analysis has been performed which prevents the validation of the temporal and spatial schemes by comparison with the resolvent analyses; hence the validation of the schemes for the linearized 3D unsteady simulations (solver *FastS*) is performed by grid and temporal convergences. The transfer function from the exogenous noise at the center spanwise position w^0 (see section 6.3) to the wall-pressure fluctuation sensor at the center spanwise position $z_p^0(x)$ (respectively velocity fluctuation sensor at the generalized inflection point at the center spanwise position $z_u^0(x)$) is plotted in figure B.2a (respectively in figure B.2b) as a function of the mesh grid. The baseline mesh grid (used in the chapter 6) has a resolution of $3200 \times 220 \times 176$ cells (black solid lines); the streamwise and spanwise resolutions are refined independently. A refinement in the streamwise direction (blue dashed lines) slightly modifies the gain of the high-frequencies of the second Mack mode

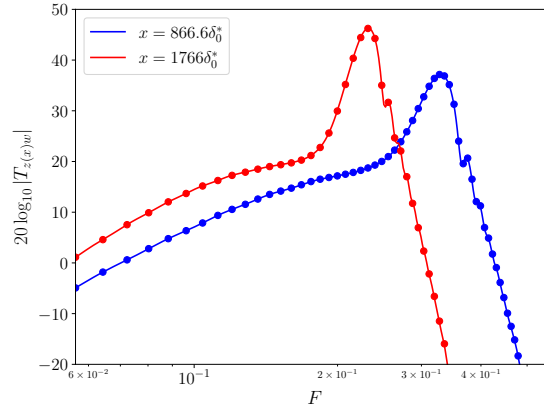


Figure B.1: Comparison of the gain of $T_{z(x)w}$ from the linearized DNS (solid lines) and from the frequency-domain resolvent approach (circles) for $x = 866.6\delta_0^*$ (in blue) and $x = 1766\delta_0^*$ (in red). The quantity $F = 2\pi f\delta_0^*/U_\infty$ represents the dimensionless frequency.

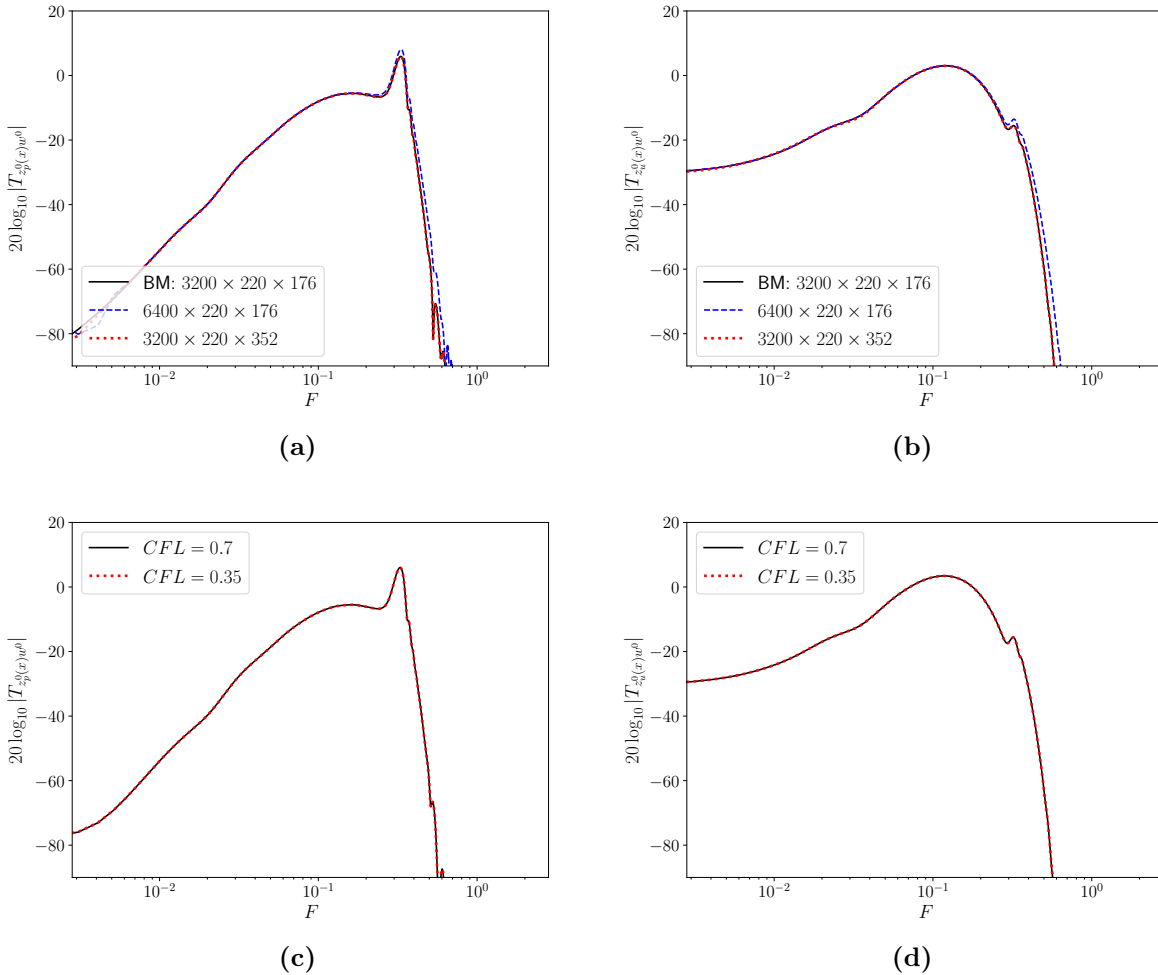


Figure B.2: (a,b) Grid and (c,d) temporal convergences of the gain of $T_{z^0(x)w^0}$ at $x = 868.5\delta_0^*$ for (a,c) wall-pressure performance sensor and (b,d) velocity performance sensor at the generalized inflection point.

(which are the dominant frequencies of the pressure sensor $z_p^0(x)$) while the low-frequencies

of the first Mack mode (which are the dominant frequencies of the velocity sensor $z_u^0(x)$) are not impacted. A refinement in the spanwise direction (red dotted lines) does not modify the results obtained with the baseline mesh. The temporal convergence of the linearized 3D DNS is validated by comparing the previous transfer functions as a function of the CFL number (see figures B.2(c,d)); the same results are obtained for the baseline CFL number lower than 0.7 (black solid lines) than for a CFL number lower than 0.35 (red dotted lines) in the whole 3D domain. According to these results, the temporal and spatial schemes used in the chapter 6 are validated to accurately compute the dynamics of the first and second Mack modes.

Sponge zone

For the 2D linearized DNS (solver *elsA*) of the chapters 4 and 5, a sponge zone is used to minimize reflections. A source term is added to the Navier–Stokes equations in the last 10 cells closest to the downstream and upper boundaries:

$$S = \sigma\beta \left(\frac{L_{max} - x}{L_{max}} \right)^\gamma (\mathbf{q} - \mathbf{q}_{ref}). \quad (\text{C.1})$$

In the equation C.1, L_{max} represents the length of the domain where the source term is applied, x the abscissa in this area ($x = 0$ at the boundary condition and $x = L_{max}$ at the beginning of the area), $\sigma = 2$ the intensity of the source term, $\beta = 0.1$ the intensity of the Gaussian filter, $\gamma = 0.01$ the exponent of the filter and \mathbf{q}_{ref} the reference state as:

$$\begin{aligned} \mathbf{q}_{ref/i,j,k} = & \mathbf{q}_{i,j,k} - \beta \left(\frac{L_{max} - x}{L_{max}} \right)^\gamma \\ & \left(\frac{3}{2} \mathbf{q}_{i,j,k} - \frac{1}{4} (\mathbf{q}_{i+1,j,k} + \mathbf{q}_{i-1,j,k} + \right. \\ & \left. \mathbf{q}_{i,j+1,k} + \mathbf{q}_{i,j-1,k} + \mathbf{q}_{i,j,k+1} + \mathbf{q}_{i,j,k-1}) \right), \end{aligned} \quad (\text{C.2})$$

with i , j and k , respectively the indices of a node in the longitudinal, wall-normal and spanwise direction. In addition to this source term, the mesh is stretched in the longitudinal direction for the downstream boundary ($L_{\text{sponge}} = 91.9\delta_0^*$ and 30 cells in the streamwise direction) from the wall to the top of the domain. The combination of the source term and the stretching allows to rapidly decrease the amplitude of disturbances entering the sponge zone; a wavepacket generated by an impulse of exogenous noise w (defined in the chapter 4) progressively disappears from the beginning of the sponge zone (see figure C.1), thus minimizing reflections.

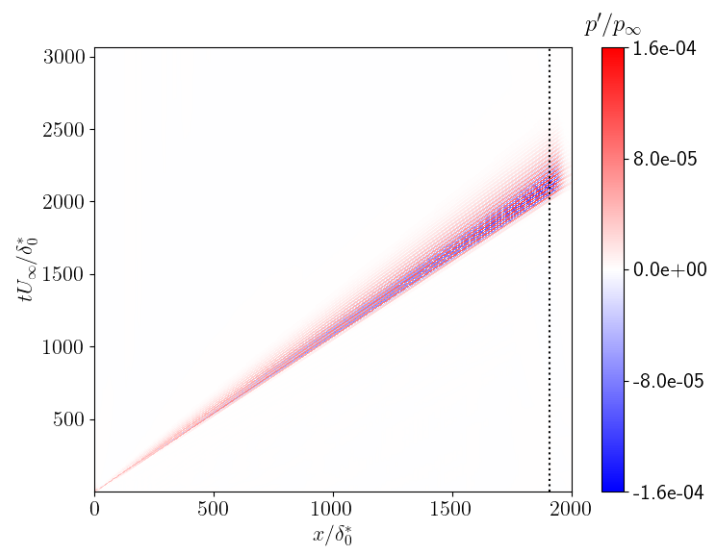


Figure C.1: Spatio-temporal response of wall-pressure fluctuation sensors after an impulse of w . The dashed line represents the sponge zone beginning.

Additional 2D global stability results

The analysis of the results of the first Mack mode at $F = 0.118$ for the 2D supersonic boundary layer (see section 4.2.2) as well as the comparison of the results of both Mack modes depending of the optimisation norm chosen are realized in this appendix.

For the frequency $F = 0.118$ corresponding to the second peak of gain and associated to first Mack mode, the peak of the forcing density $d_{e_f}(x) = \int_0^{y=92\delta_0^*} \|\tilde{\mathbf{f}}\|^2 dy$ is not very far from the position of branch I from LLST (see figure D.1a); the energy of the response is dominated at each abscissa by the thermodynamic quantities $e_{T'}$ and $e_{\rho'}$, while the quantity $e_{u'}$ has a smaller contribution, as it was the case for the second Mack mode at $F = 0.237$ (see section 4.2.2). The forcing field is located around the generalized inflection point (see figures D.1(b,d)) while that of the response depends on the quantity considered (see figures D.1(c,e)). The hydrodynamic perturbations (velocity and pressure) are no more trapped in the region $|\widehat{M}| > 1$ (contrary to the second Mack mode) and take important values close to the generalized inflection point y_g . The thermodynamic quantities (density and temperature) still peak near y_g . As the thermodynamic quantities $e_{T'}$ and $e_{\rho'}$ dominate, the field e_{Chu} is located near y_g (see figures D.2(a,c)) for both $F = 0.118$ (first Mack mode) and $F = 0.237$ (second Mack mode). Yet, the field $e_{u'}$ differs between the two Mack modes (see figures D.2(b,d)) as the velocity is no more trapped in the supersonic instability region for the first Mack mode. Note that the response field is less spread and more localized in the streamwise direction for $F = 0.237$ than for $F = 0.118$, which is related to the fact that the length of the instability domain (*i.e.* the length between the branch I and the branch II) is smaller for $F = 0.237$ than for $F = 0.118$ (see figure 4.2).

The eigenvalue problem solved in the resolvent analysis (see equation 1.19) depends on the quantity that one seeks to optimise. Hence, a kinetic energy norm for the response is now employed for the gain optimisation to check that the main conclusions (dominant frequencies, dominant quantities, eigenvector profiles, etc.) are independent of the norm choice. The optimal energy gain \tilde{g} as a function of the forcing frequency F is represented in figure D.3a for both Chu (solid line) and kinetic (circles) optimisation. Both curves are normalized by their respective \tilde{g}_{max} for comparison purposes. The most amplified frequency according to a Chu or kinetic optimization is similar and the gain evolution of the high-frequencies is the same. The low-frequencies of the first Mack mode have been, in proportion of \tilde{g}_{max} , less amplified in the kinetic optimisation case than in the Chu optimisation one. In other words, a hydrodynamic-based

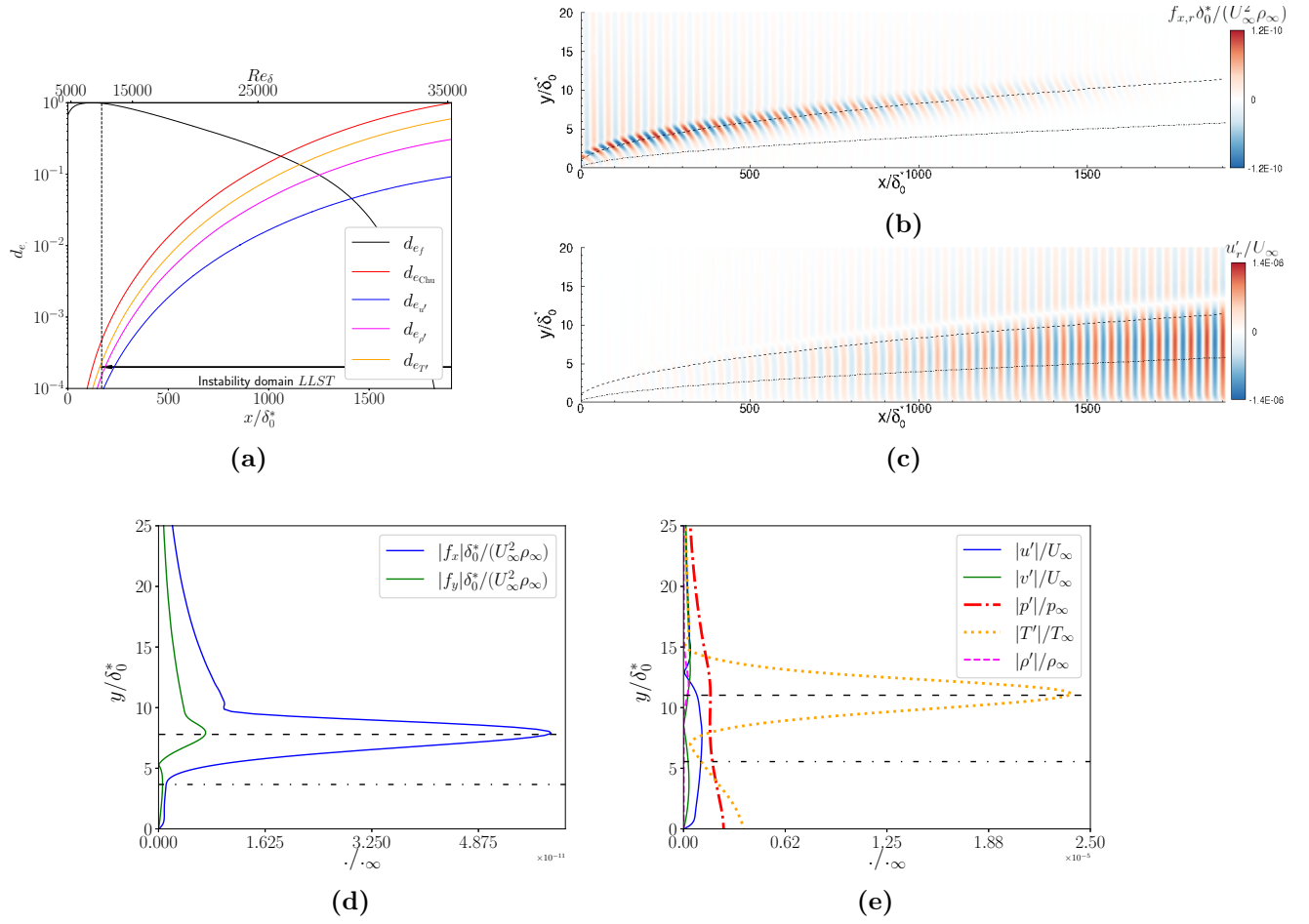


Figure D.1: (a) Evolution at $F = 0.118$ of the forcing density and the different contributions to the Chu's energy density normalized by their maximum values. The position of the branch I from LLST is symbolized by vertical dashed line. Real part of the streamwise component at $F = 0.118$ of the (b) optimal forcing and its associated (c) streamwise velocity response. Profiles of the optimal forcing components at $x = 867.2\delta_0^*$ (d) and response at $x = 1766.7\delta_0^*$ (e) at $F = 0.118$. The black dashed and dashed-dotted lines in (b), (c), (d) and (e) represent respectively the generalised inflection point position and the limit of the region of supersonic instabilities ($|\widehat{M}| > 1$ below this line).

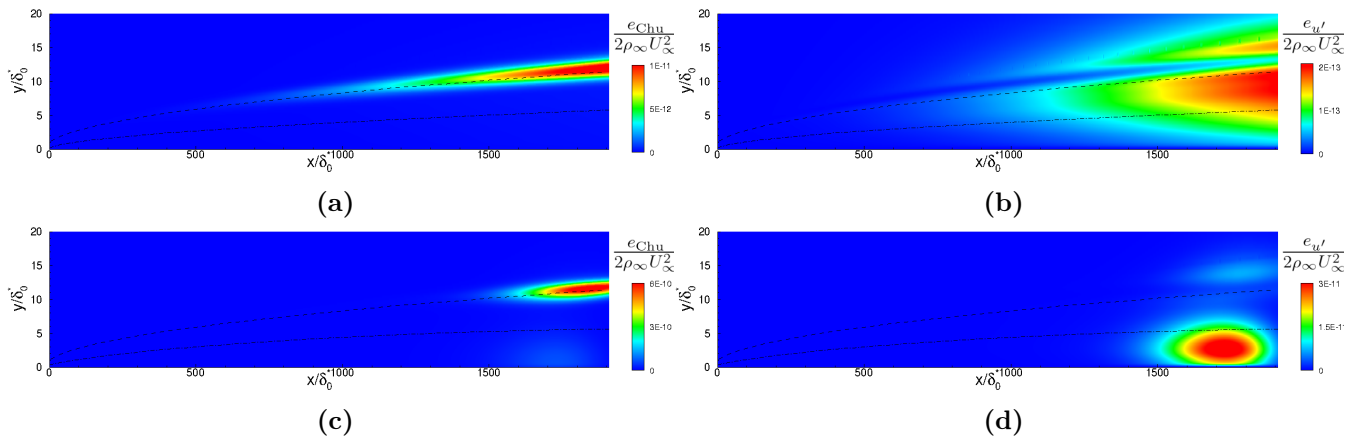


Figure D.2: For $F = 0.118$ (a,b) and $F = 0.237$ (c,d), evolution of e_{Chu} (a,c) and $e_{u'}$ (b,d). The black dashed and dashed-dotted lines represent the generalised inflection point position and the limit of the region of supersonic instabilities ($|\widehat{M}| > 1$ below this line), respectively.

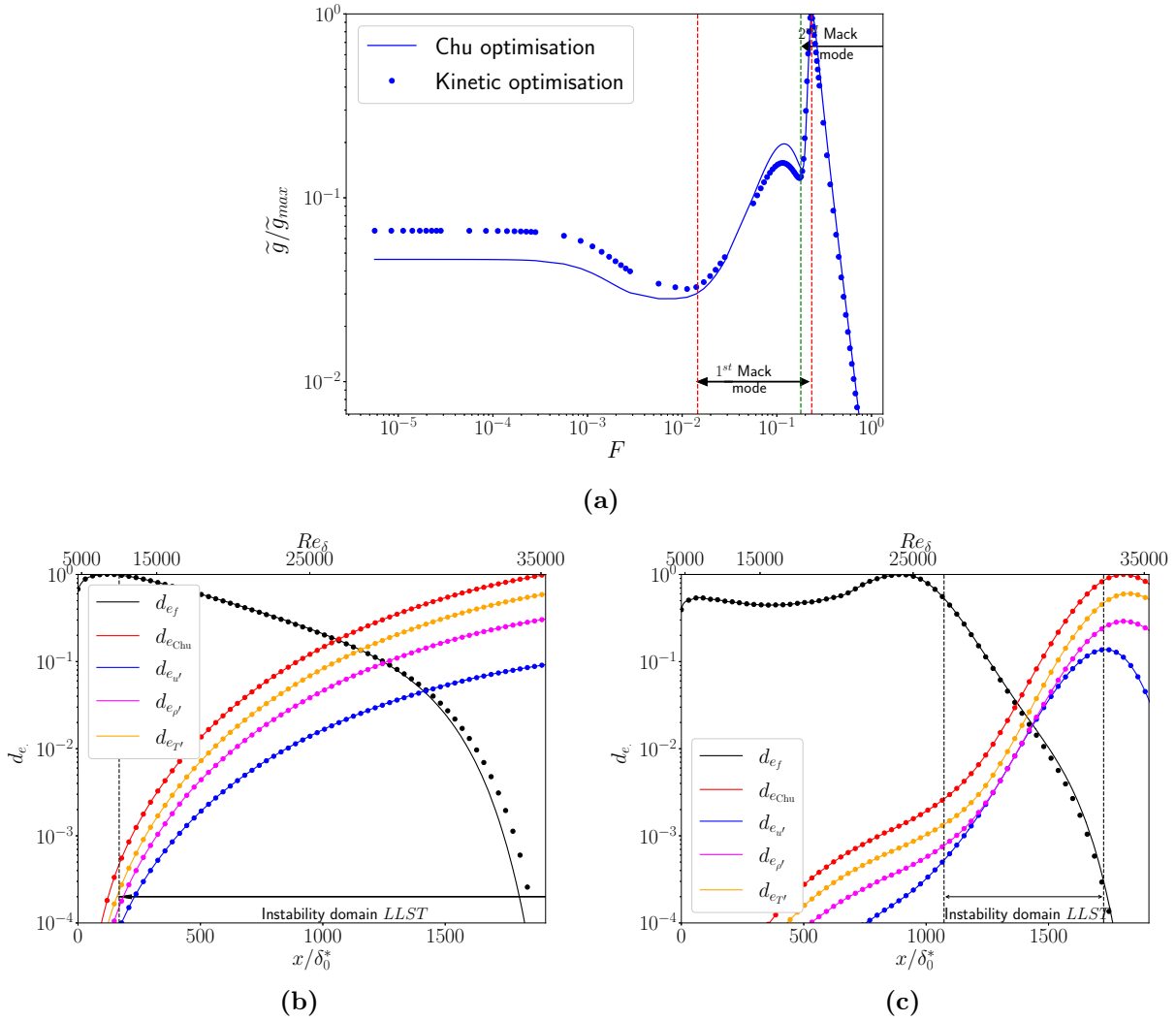


Figure D.3: The results of the gain optimisation based on Chu's energy and kinetic energy are in solid lines and circles, respectively. (a) Optimal resolvent gain as a function of F . Evolution at (b) $F = 0.118$ and (c) $F = 0.237$ of the forcing density and the different contributions to the Chu's energy density normalized by their maximum values. The positions of the branch I and II from LLST are symbolized by vertical dashed lines.

sensor will be less sensitive to the first Mack mode than a thermodynamic-based sensor. Despite this difference in the gain evolution, both forcing density and response density follow the same evolution (see figures D.3(b,c)) and the energy contribution of the different quantities remains the same; only a difference is noted in the low values of the forcing, downstream of the domain. Both forcing and response profiles at $x = 867.2\delta_0^*$ and at $x = 1766.7\delta_0^*$, respectively, are the same whether with an optimization of the Chu's energy or the kinetic energy (see figure D.4). In summary, the main conclusions (most amplified frequencies, contribution of the different energy components, location of the optimal forcing, optimal response profiles) obtained with a Chu's energy optimization remain valid with a kinetic energy optimization. This may seem logical as the convective-type non-normality effects, which depend on modal amplification on the local scale, will not vary with the chosen optimization energy. Only non-modal behaviours (component-type non-normality effects) may change, which is nevertheless not the case here; the non-modal mechanisms (as Orr mechanism) maximizing the Chu's energy are the same than those maximizing the kinetic energy.

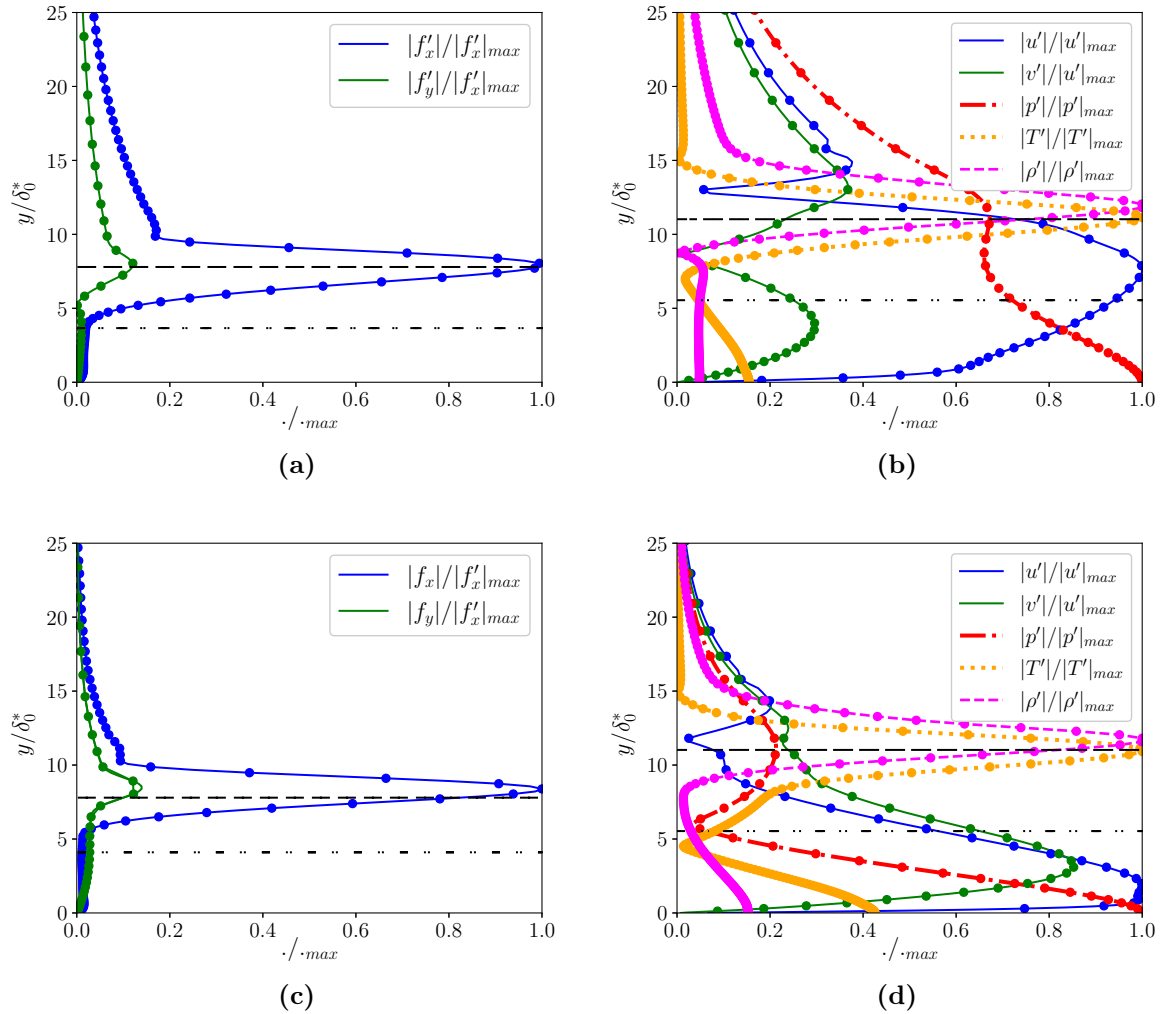


Figure D.4: For $F = 0.118$ (a,b) and $F = 0.237$ (c,d), profiles of the optimal forcing components at $x = 867.2\delta_0^*$ (a,c) and response at $x = 1766.7\delta_0^*$ (b,d). Solid lines and circles represent the results for an optimisation of the Chu'energy and kinetic energy, respectively. The black dashed and dashed-dotted lines represent the generalised inflection point position and the limit of the region of supersonic instabilities ($|\widehat{M}| > 1$ below this line), respectively.

3D: Controller based on velocity performance sensors only

We saw that the transition scenario obtained in section 6.7 is related to the first Mack mode oblique breakdown as the steady structures near the wall have twice the wavenumber of the fundamental oblique Mack mode. One may ask what is the interest of limiting the linear growth of the second Mack mode and therefore of using wall-pressure sensors in the synthesis in order to delay transition. Indeed, reducing the r.m.s. values of these kind of sensors leads to limit the amplitude of the frequencies of the second Mack mode. Hence, we will show in this appendix what happens when we minimize only the r.m.s. values of the velocity at the generalized inflection point (*i.e.* the highest r.m.s. values) and we limit only the amplitude of the frequencies of the first Mack mode.

The CMP in equation 6.20 becomes:

$$\begin{aligned} & \text{minimize } \|(\hat{T}_{\mathbf{z}_{3,\mathbf{u}}\tilde{\mathbf{y}}}^k)^c \hat{W}_{\tilde{\mathbf{y}}}^k\|_2 \\ & \text{subject to } \|W_{\hat{S}^k}\|_\infty < 1 \text{ and } \|W_{(\hat{K}\hat{S})^k}(\hat{K}\hat{S})^k\|_\infty < 1, \end{aligned} \tag{E.1}$$

with the controller structure developed in section 6.4.2. Remember that \hat{K}^k refers to a controller associated with a particular spanwise mode and six controllers are designed (up to the mode $k = 5$). In this new CMP, only a minimization of $\|(\hat{T}_{\mathbf{z}_{3,\mathbf{u}}\tilde{\mathbf{y}}}^k)^c \hat{W}_{\tilde{\mathbf{y}}}^k\|_2$ is realized; the H_∞ constraints have been explained in section 6.4.2. In this appendix, the question of interest is only related to nominal performance and mitigation of the first Mack mode in order to delay transition so the step 2 of the previous CMP in equation 6.20 is no longer required because it was only present for questions of performance robustness with respect to noisy estimation sensors. In summary, the CMP in equation E.1 returns controller \hat{K}^k reducing as much as possible the H_2 norm of the transfer related to the velocity performance sensor in the wavenumber space while ensuring the stability of the feedback loop.

Then the six decentralized controllers \hat{K}^k resulting from this synthesis are used to form the centralized controller in the physical space as explained in section 6.5.2 and this final controller is implemented in the CFD solver *FastS*. Its results are compared to those of the baseline controller of the chapter 6 where the CMPs in the wavenumber space were based on both velocity $\mathbf{z}_{3,\mathbf{u}}$ and pressure $\mathbf{z}_{\mathbf{p}}^{\text{All}} = [\mathbf{z}_{1,\mathbf{p}}, \mathbf{z}_{2,\mathbf{p}}, \mathbf{z}_{3,\mathbf{p}}]^T$ performance sensors.

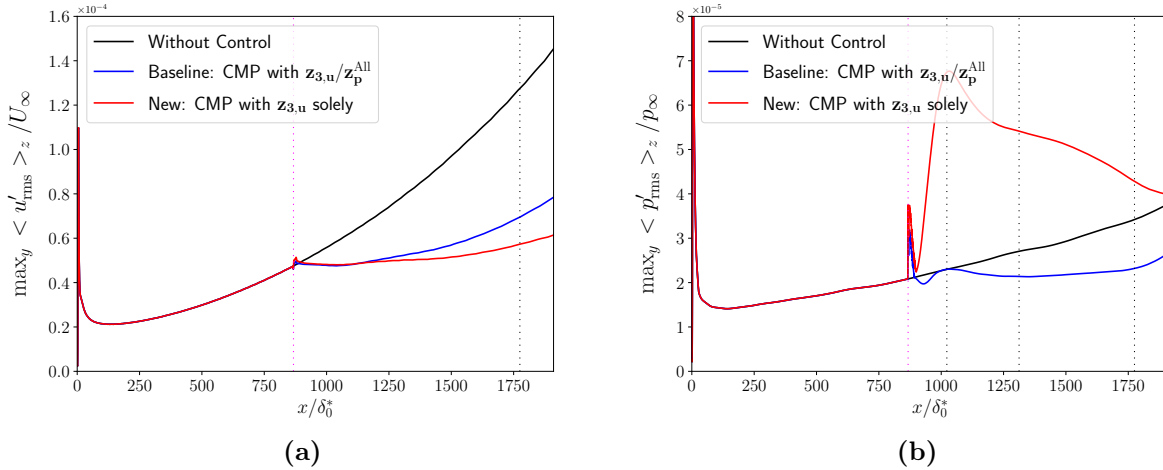


Figure E.1: Evolution of (a) $\max_y \langle u'_{\text{rms}} \rangle_z$ and (b) $\max_y \langle p'_{\text{rms}} \rangle_z$ for the baseline controller (blue line) and the controller based solely on velocity performance sensors $\mathbf{z}_{3,u}$ in the CMP (red line). The vertical magenta and black dotted lines represent, respectively, the streamwise positions of the actuators (with the sensors \mathbf{y} nearby) and the performance sensors \mathbf{z}_i used for the baseline synthesis.

The new controller (in red) reduces even more $\max_y \langle u'_{\text{rms}} \rangle_z$ than the baseline controller (in blue) (see figure E.1a) for the linearized DNS. This is due to the fact the new CMP minimizes the velocity whereas the baseline controller was a trade-off between pressure and velocity. The quantity $\max_y \langle p'_{\text{rms}} \rangle_z$ (see figure E.1b) is no more reduced compared to the uncontrolled case; the amplitude of the pressure disturbances is increased by the control whereas it is decreased with the baseline controller. Near the actuators, the increase of $\max_y \langle p'_{\text{rms}} \rangle_z$ is due to the intensity of the generated acoustic wave but on the rest of the domain, this increase in the new control case is due to the amplification of convective instabilities near the wall (see figure E.2). Indeed, whereas the high values located both close to y_g and close to the wall in the uncontrolled case (see figure E.2a) are reduced by the baseline control, only the high values near y_g are reduced with the new controller (after a transient distance) while the pressure field near the wall is amplified (see figure E.2b). The 2D frequency-wavenumber spectra of wall-pressure fluctuation sensors are plotted in figure E.3. The low-frequency oblique structures of the first Mack mode in the uncontrolled case (see figure E.3a) are reduced in both baseline (see figure E.3b) and new (see figure E.3c) cases. This is due to the minimization in both syntheses of the energy of the velocity sensors at the generalized inflection point which are dominated by these structures. The new controller based solely on velocity performance sensors amplifies the high-frequencies of the second Mack mode compared to the uncontrolled case, contrary to the baseline controller which reduced them. To minimize $\|(\hat{T}_{\mathbf{z}_{3,u},\tilde{\mathbf{y}}}^k)^c \hat{W}_{\tilde{\mathbf{y}}}^k\|_2$ in the new case, the algorithm reduces the amplitude of the dominant frequencies (*i.e* the low-frequencies of the first Mack mode) and amplifies the high-frequencies that do not contribute for $\mathbf{z}_{3,u}$. This effect where reducing the amplitude of disturbances in one part of the frequency spectrum can lead to increasing it in the other part is similar to the waterbed effect [180]. In summary, the new controller mitigates the linear growth of the first Mack mode but amplifies the linear growth of the second Mack mode as no wall-pressure performance sensors (which are dominated by this mode) are used in the synthesis step.

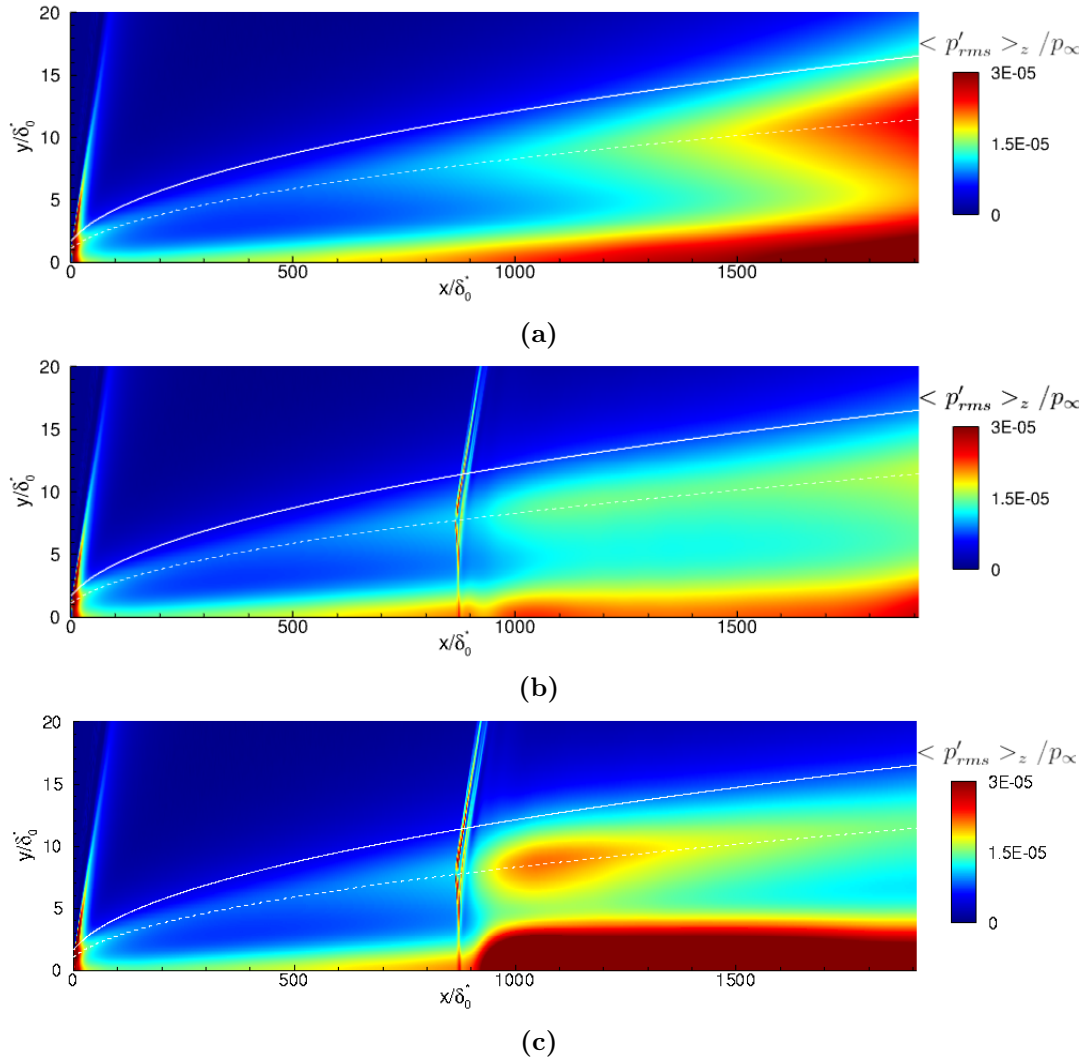


Figure E.2: Contours of p'_{rms} averaged in the spanwise direction for (a) the uncontrolled case, (b) the baseline controller and (c) the controller based solely on velocity performance sensors $\mathbf{z}_{3,u}$ in the CMP. The white solid and dashed lines represent the boundary layer thickness δ and the generalized inflection point position y_g , respectively.

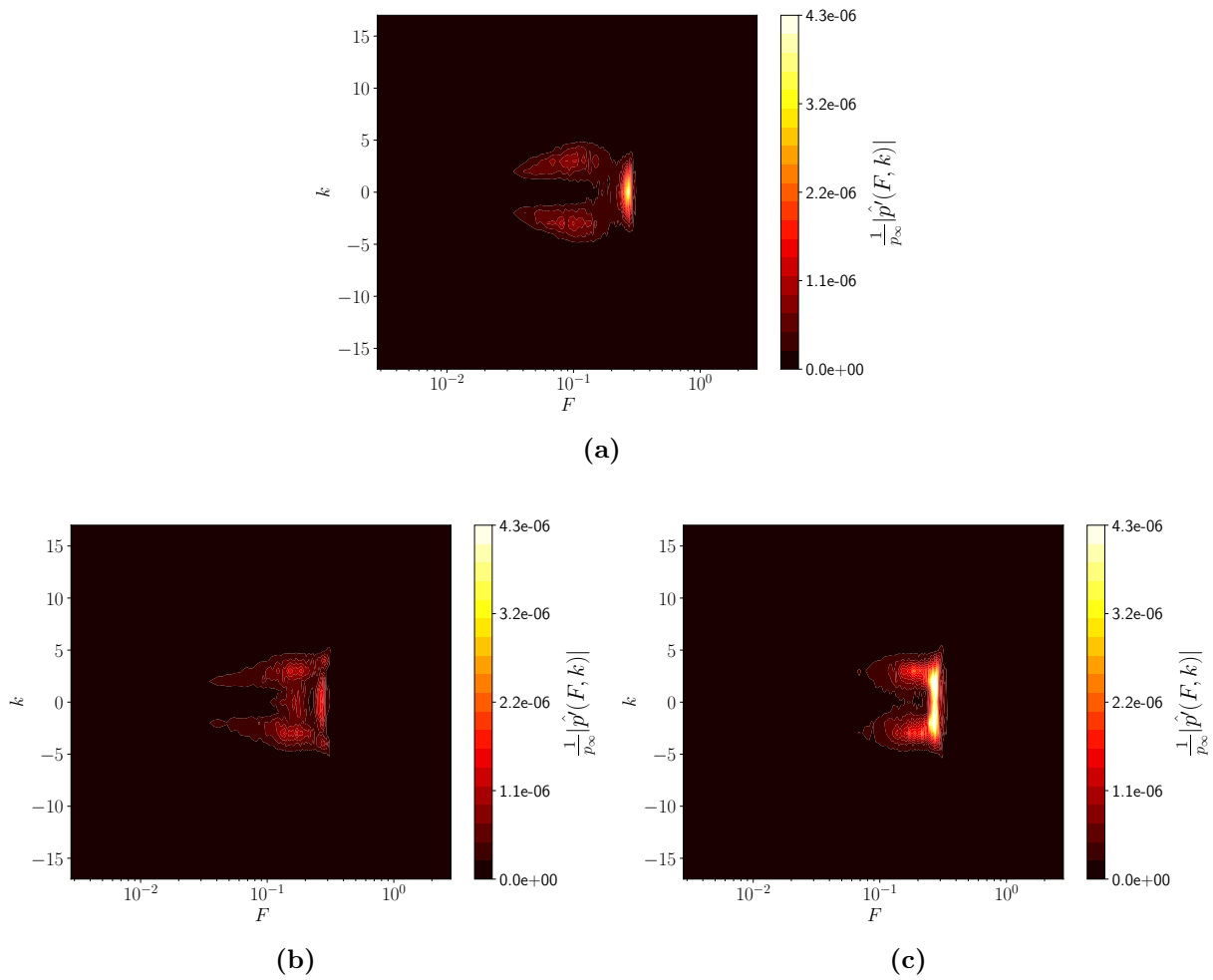


Figure E.3: Comparison of $|\hat{p}(F, k)|$ at $(x, y) = (1312.2\delta_0^*, 0)$ for (a) the uncontrolled case, (b) the baseline controller and (c) the controller based solely on velocity performance sensors $\mathbf{z}_{3,u}$ in the CMP.

The results of the new controller are now analysed when the variances of the exogenous noise sources are $\text{Var}[w^j] = 1$ and $\text{Var}[w^j] = 25$ which lead to non-linear regime in the domain (see section 6.6). The new control law still reduces more the velocity disturbances than the baseline controller when $\text{Var}[w^j] = 1$ but the gap has reduced compared to the linearized DNS (see figure E.4a). Compared to the uncontrolled case, the pressure disturbances at the end of the domain are even more amplified in this weakly non-linear case than in the linear case (see figure E.4b). For the case $\text{Var}[w^j] = 25$ where the non-linearities are more important, the new control law, based on velocity minimization in the linear case, no longer reduces velocity disturbances (see figure E.4c), unlike the previous controller which was based on a velocity/pressure disturbance rejection trade-off. For this fully non-linear case, both controllers fall short to mitigate pressure disturbances (see figure E.4d).

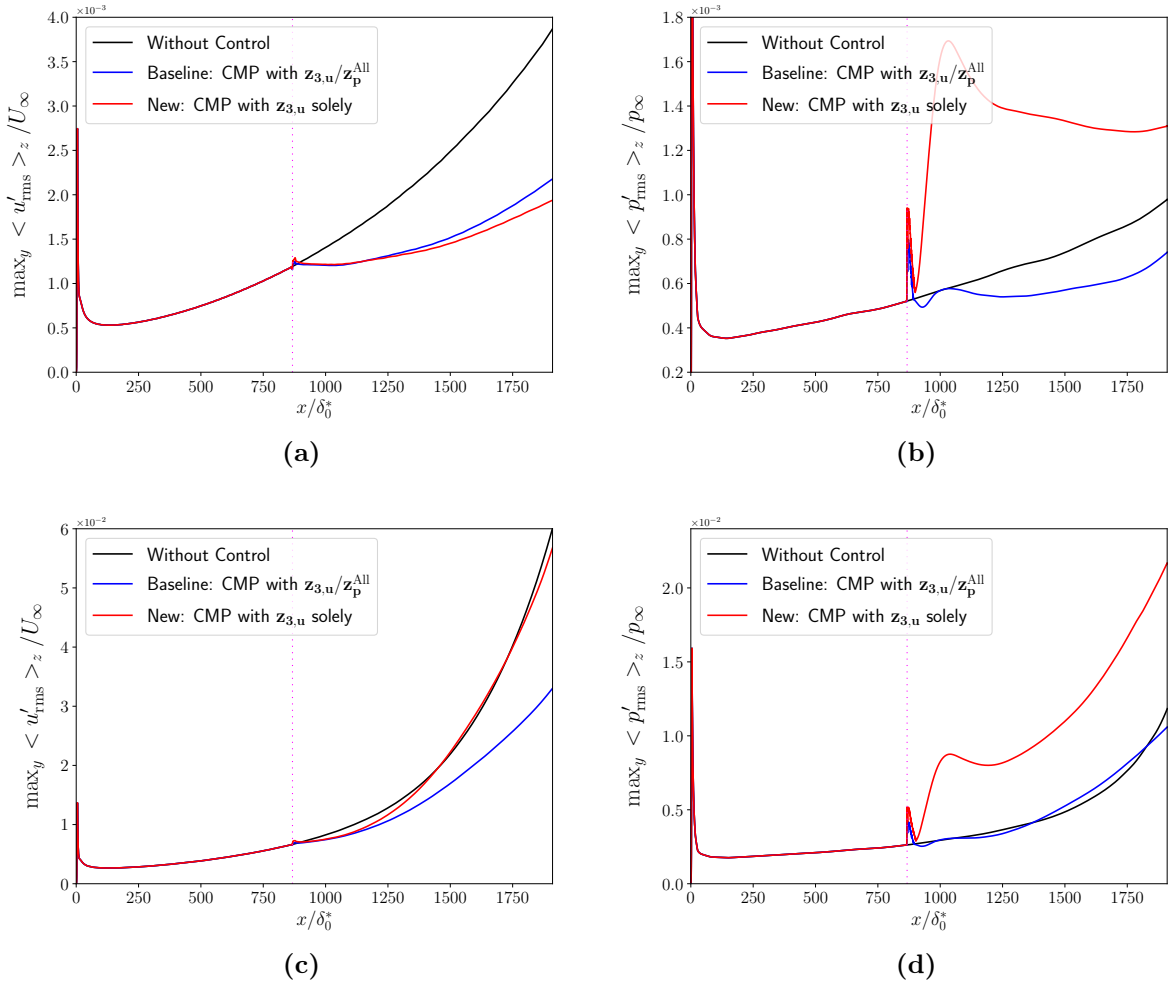


Figure E.4: For exogenous noise sources with $\text{Var}[w^j] = 1$ (a,b) and $\text{Var}[w^j] = 25$ (c,d), evolution of $\max_y \langle u'_{\text{rms}} \rangle_z$ (a,c) and $\max_y \langle p'_{\text{rms}} \rangle_z$ (b,d). For vertical magenta lines, same caption as in figure E.1.

The fact that the velocity is no longer reduced with the new controller when $\text{Var}[w^j] = 25$ (whereas it has been designed for this in the linear case) is explained in the following. In the uncontrolled case (see figure E.5a), steady vortices with twice the wavenumber of the oblique first Mack mode appear near the wall. In the baseline case (see figure E.5b), the amplitude of these steady structures is decreased due to weaker non-linear interactions. In the new control case (see figure E.5c), even if the amplitude of the steady vortices with twice the wavenumber of the oblique first Mack mode is still reduced (but less than in the baseline case), steady vortices

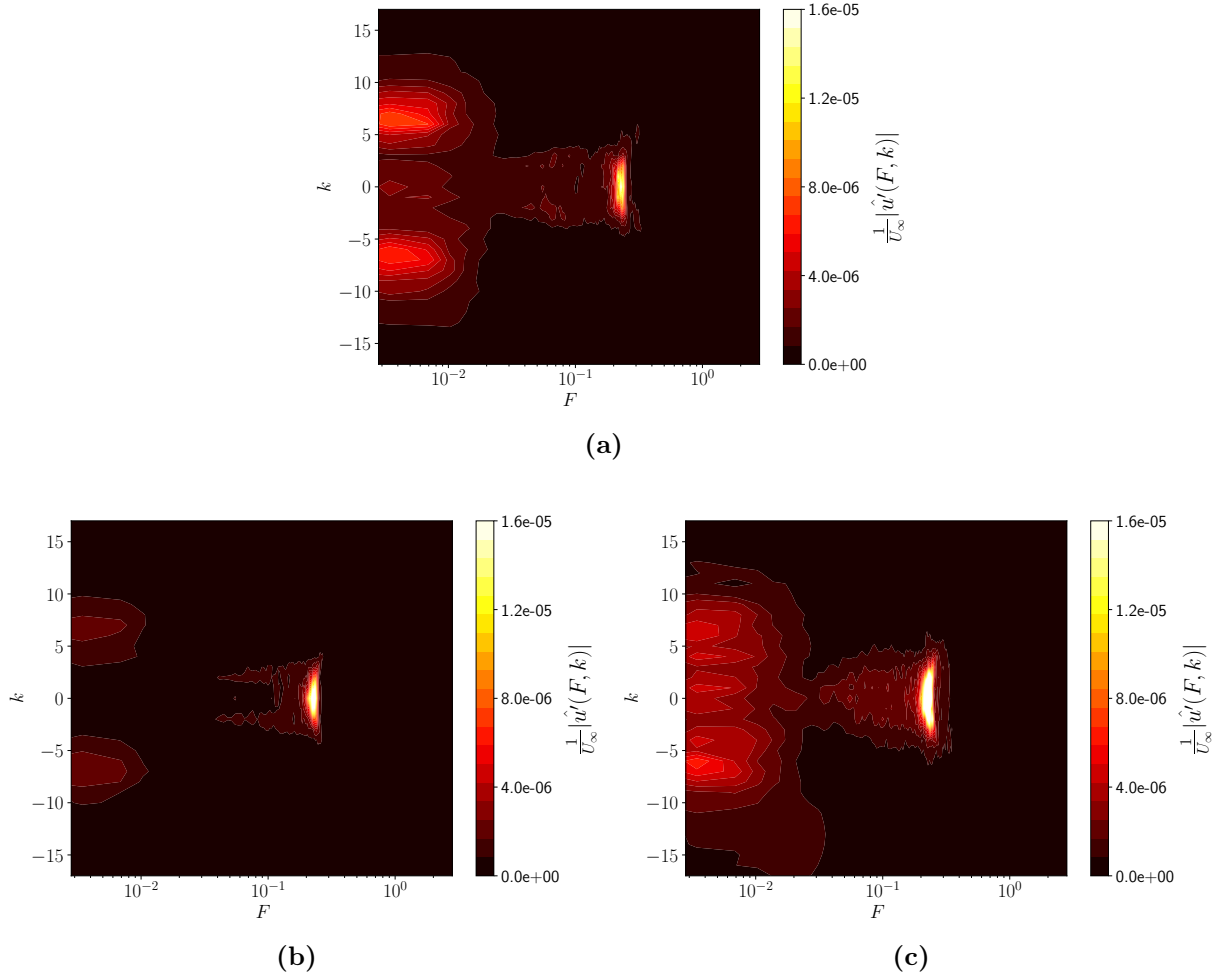


Figure E.5: Comparison of $|\hat{u}(F, k)|$ at $(x, y) = (1775\delta_0^*, 0.015\delta_0^*)$ for exogenous noise sources with $\text{Var}[w^j] = 25$: (a) the uncontrolled case, (b) the baseline controller and (c) the controller based solely on velocity performance sensors $\mathbf{z}_{3,\mathbf{u}}$ in the CMP.

with lower wavenumbers are amplified. These new structures may be associated with the non-linear interactions of a pair of oblique Mack second mode waves which have been amplified by the control action. Indeed, the new controller amplifies the linear growth of the second Mack mode as seen previously, leading to stronger non-linear interactions. While the steady vortices in the uncontrolled case will lead to first Mack mode oblique breakdown, the steady vortices in the new control case may lead to a second Mack mode breakdown. In view of the curves in figure E.4c, we can imagine that the transition will not be delayed in the new controlled case while it could be the case for the baseline controller. Thus, if the two Mack modes are not taken into account in the synthesis step, a too important waterbed effect can lead to change the breakdown scenario without delaying transition to turbulence. It is therefore recommended to take into account both Mack modes in the synthesis (as for the baseline case) to limit all the non-linear interactions by reducing the linear growth of both modes.

References

- [1] N. A. Adams and L. Kleiser. Subharmonic transition to turbulence in a flat-plate boundary layer at Mach number 4.5. *Journal of Fluid Mechanics*, 317:301–335, 1996. [21](#)
- [2] S. Ahuj and C. W. Rowley. Feedback control of unstable steady states of flow past a flat plate using reduced-order estimators. *Journal of Fluid Mechanics*, 645:447–478, 2010. [37](#)
- [3] E. Akervik, J. Hoepffner, U. Ehrenstein, and D. Henningson. Optimal growth, model reduction and control in a separated boundary-layer flow using global eigenmodes. *J. Fluid Mech.*, 579:305–314, 2007. [35](#)
- [4] P. Amestoy, I. Duff, J.-Y. L’Excellent, and J. Koster. A fully asynchronous multifrontal solver using distributed dynamic scheduling. *SIAM*, 23, 2001. [49](#)
- [5] A. Antoulas. *Approximation of Large-Scale Dynamical Systems*. SIAM, 2005. [35](#)
- [6] P. Apkarian. *Éléments de la théorie de la commande robuste*, 2005. [33](#)
- [7] P. Apkarian and D. Noll. Nonsmooth H_∞ synthesis. *IEEE Transactions on Automatic Control*, 51:71–86, 2006. [41](#), [55](#)
- [8] P. Apkarian, D. Noll, and A. Rondepierre. Mixed H_2/H_∞ control via nonsmooth optimization. In *Proceedings of the IEEE Conference on Decision and Control*, volume 47, pages 6460 – 6465, 2010. [41](#)
- [9] P. Apkarian, P. Gahinet, and C. Buhr. Multi-model, multi-objective tuning of fixed-structure controllers. In *2014 European Control Conference (ECC)*, pages 856–861, 2014. [42](#), [55](#)
- [10] S. Bagheri, L. Brandt, and D. Henningson. Input-output analysis, model reduction and control of the flat-plate boundary layer. *J. Fluid Mech.*, 620:263–298, 2009. [2](#), [28](#), [30](#), [34](#), [35](#), [36](#), [38](#), [66](#)
- [11] B. Bamieh and L. Giarré. Lpv models: Identification for gain scheduling control. In *2001 European Control Conference (ECC)*, pages 3092–3097, 2001. [42](#)
- [12] A. Barbagallo, D. Sipp, and P. Schmid. Closed-loop control of an open cavity flow using reduced-order models. *J. Fluid Mech.*, 641:1–50, 2009. [28](#), [35](#)

- [13] A. Barbagallo, G. Dergham, D. Sipp, P. Schmid, and J.-C. Robinet. Closed-loop control of unsteadiness over a rounded backward-facing step. *J. Fluid Mech.*, 703:326–362, 2012. [2](#), [3](#), [28](#), [30](#), [34](#), [35](#), [36](#), [38](#), [74](#), [82](#), [86](#), [161](#)
- [14] B. Belson, O. Semeraro, C. Rowley, and D. Henningson. Feedback control of instabilities in the two-dimensional Blasius boundary layer: The role of sensors and actuators. *Physics of Fluids*, 25:054106, 2013. [3](#), [30](#), [34](#), [35](#), [36](#), [37](#), [39](#), [42](#), [52](#), [65](#), [66](#), [74](#), [75](#), [76](#), [81](#), [196](#)
- [15] J. Bendat and A. Piersol. *Random Data: Analysis and Measurement Procedures*. John Wiley & Son, 1971. [120](#), [121](#)
- [16] S. Beneddine. *Characterization of unsteady flow behavior by linear stability analysis*. PhD thesis, Université Paris-Saclay, 2017. [XI](#), [49](#)
- [17] S. Beneddine, C. Mettot, and D. Sipp. Global stability analysis of underexpanded screeching jets. *European Journal of Mechanics B/Fluids*, 49:392–399, 2015. [48](#), [62](#)
- [18] C. Bett. Gain-scheduled controllers. *The Electrical Engineering Handbook*, pages 1107–1114, 12 2005. [42](#)
- [19] T. Bewley and S. Liu. Optimal and robust control and estimation of linear paths to transition. *J. Fluid Mech.*, 365:305–349, 1998. [35](#), [41](#)
- [20] N. Bitter and J. Shepherd. Transient growth in hypersonic boundary layers. In *7th AIAA Theoretical Fluid Mechanics Conference*, 2014. [25](#)
- [21] J. Bridges and C. Brown. Parametric testing of chevrons on single flow hot jets. In *10th AIAA/CEAS Aeroacoustics Conference*, 2004. [25](#)
- [22] S. Brunton and B. Noack. Closed-loop turbulence control: Progress and challenges. *Applied Mechanics Reviews*, 67, 2015. [1](#), [36](#)
- [23] F. Bruzelius. *LPV-Based Gain Scheduling- An H_∞ -LMI approach*. PhD thesis, Chalmers University of Technology, 2002. [42](#)
- [24] B. Bugeat, J.-C. Chassaing, J.-C. Robinet, and P. Sagaut. 3d global optimal forcing and response of the supersonic boundary layer. *J. Comput. Phys.*, 398:108888, 2019. [X](#), [XI](#), [18](#), [19](#), [45](#), [49](#), [50](#), [56](#), [62](#), [124](#), [125](#)
- [25] K. Butler and B. Farrell. Three-dimensional optimal perturbations in viscous shear flows. *Physics of Fluids*, 4:1637–1650, 1992. [18](#)
- [26] S. Butterworth. On the theory of filter amplifiers. *Experimental Wireless and the Wireless Engineer*, 7:536–541, 1930. [134](#)
- [27] L. Cambier, S. Heib, and S. Plot. The onera elsa cfd software: input from research and feedback from industry. *Mechanics & Industry*, 14:159–174, 2013. [46](#)
- [28] L. N. Cattafesta and M. Sheplak. Actuators for active flow control. *Annual Review of Fluid Mechanics*, 43(1):247–272, 2011. [161](#)
- [29] M. Celep, A. Hadjadj, M. S. Shadloo, S. Sharma, M. Yildiz, and M. J. Kloker. Effect of streak employing control of oblique-breakdown in a supersonic boundary layer with weak wall heating/cooling. *Phys. Rev. Fluids*, 7:053904, 2022. [2](#)

- [30] C.-L. Chang and M. R. Malik. Oblique-mode breakdown and secondary instability in supersonic boundary layers. *Journal of Fluid Mechanics*, 273:323–360, 1994. 20
- [31] X. Chanteux, G. Bégou, H. Deniau, and O. Vermeersch. Construction and application of transition prediction databased method for 2nd mode on sharp cone. In *AIAA AVIATION 2022 Forum*. 47
- [32] F. Charru. *Instabilités hydrodynamiques*. Edp Sciences, 2007. 10
- [33] J. Chen, K. Zhou, and B.-C. Chang. Closed-loop controller reduction by a structured truncation approach. In *Proceedings of 1994 33rd IEEE Conference on Decision and Control*, volume 3, pages 2726–2731, 1994. 41
- [34] H. Choi, P. Moin, and J. Kim. Direct numerical simulation of turbulent flow over riblets. *J. Fluid Mech.*, 255:503–539, 1993. 25
- [35] B. Chu. On the energy transfer to small disturbances in fluid flow (part i). *Acta Mech.*, 3:215–234, 1965. 49
- [36] B. Clement, G. Duc, and S. Mauffrey. Aerospace launch vehicle control: a gain scheduling approach. *Control Engineering Practice*, 13(3):333–347, 2005. 42
- [37] R. Dadfar, O. Semeraro, A. Hanifi, and D. Henningson. Output feedback control of Blasius flow with leading edge using plasma actuator. *AIAA Journal*, 51:2192–2207, 2013. 2, 37, 38
- [38] R. Dadfar, N. Fabbiane, S. Bagheri, and D. Henningson. Centralised versus decentralised active control of boundary layer instabilities. *Flow, Turbulence and Combustion*, 93: 537–553, 2014. 2, 38, 121, 122
- [39] J. Dahan, A. Morgans, and S. Lardeau. Feedback control for form-drag reduction on a bluff body with a blunt trailing edge. *J. Fluid Mech.*, 704:360–387, 2012. 40
- [40] J. Dandois, E. Garnier, and P.-Y. Pamart. Narx modelling of unsteady separation control. *Exp. Fluids*, 54:1445, 2013. 37
- [41] R. Deem and J. Murphy. Flat plate boundary layer transition at hypersonic speeds. In *2nd Aerospace Sciences Meeting*, 1965. 25
- [42] S. Devasia. Should model-based inverse inputs be used as feedforward under plant uncertainty? *IEEE Transactions on Automatic Control*, 47(11):1865–1871, 2002. 39
- [43] J. Doyle. Guaranteed margins for LQG regulators. *IEEE Transactions on Automatic Control*, 23:756–757, 1978. 2, 38, 65
- [44] J. Doyle and G. Stein. Multivariable feedback design: Concepts for a classical/modern synthesis. *IEEE Transactions on Automatic Control*, 26:4–16, 1981. 38
- [45] J. Doyle, K. Glover, P. Khargonekar, and B. Francis. State-space solutions to standard H_2 and H_∞ control problems. *IEEE Transactions on Automatic Control*, 34:831–847, 1989. 3, 40
- [46] Z. Drmac, S. Gugercin, and C. Beattie. Quadrature-based vector fitting for discretized H_2 approximation. *SIAM Journal on Scientific Computing*, 2:A625–52, 2015. 36, 54

- [47] A. Durant, T. André, S. Schneider, and B. Chynoweth. Mach 6 quiet tunnel laminar to turbulent investigation of a generic hypersonic forebody. In *20th AIAA International Space Planes and Hypersonic Systems and Technologies Conference*, 2015. [X](#), [1](#)
- [48] A. Dwivedi, G. Sidharth, G. V. Candler, J. W. Nichols, and M. Jovanovic. Input-output analysis of shock boundary layer interaction. In *2018 Fluid Dynamics Conference*. [50](#)
- [49] A. Dwivedi, G. S. Sidharth, J. W. Nichols, G. V. Candler, and M. R. Jovanović. Reattachment streaks in hypersonic compression ramp flow: an input–output analysis. *Journal of Fluid Mechanics*, 880:113–135, 2019. [50](#)
- [50] U. Ehrenstein, P.-Y. Passaggia, and F. Gallaire. Control of a separated boundary layer: Reduced-order modeling using global modes revisited. *Theor. Comput. Fluid Dyn.*, 25: 195–207, 2011. [35](#)
- [51] T. Ellingsen and E. Palm. Stability of linear flow. *Physics of Fluids*, 18:487–488, 1975. [18](#)
- [52] R. Erdmann, A. Pätzold, M. Engert, I. Peltzer, and W. Nitsche. On active control of laminar–turbulent transition on two-dimensional wings. *Philosophical Transactions of the Royal Society A: Mathematical, Physical and Engineering Sciences*, 369(1940):1382–1395, 2011. [2](#), [41](#)
- [53] N. Fabbiane. *Transition delay in boundary-layer flows via reactive control*. PhD thesis, Royal Institute of Technology, 2016. [34](#)
- [54] N. Fabbiane, O. Semeraro, S. Bagheri, and D. Henningson. Adaptive and model-based control theory applied to convectively unstable flows. *Applied Mechanics Reviews*, 66: 60801, 2014. [2](#), [35](#), [41](#), [42](#), [196](#)
- [55] N. Fabbiane, B. Simon, F. Fischer, S. Grundmann, S. Bagheri, and D. Henningson. On the role of adaptivity for robust laminar flow control. *J. Fluid Mechanics*, 767, 2015. [2](#), [41](#), [42](#), [90](#)
- [56] N. Fabbiane, S. Bagheri, and D. S. Henningson. Energy efficiency and performance limitations of linear adaptive control for transition delay. *Journal of Fluid Mechanics*, 810:60–81, 2017. [82](#), [83](#), [160](#)
- [57] A. Fedorov and A. Tumin. The mack’s amplitude method revisited. *Theor. Comput. Fluid Dyn.*, 36:9–24, 2022. [60](#)
- [58] T. Flinois and A. Morgans. Feedback control of unstable flows: a direct modelling approach using the eigensystem realisation algorithm. *J. Fluid Mech.*, 793:41–78, 2016. [40](#)
- [59] G. Franklin, J. Powell, and M. Workman. *Digital Control of Dynamic Systems-Third Edition*. Prentice Hall, 1997. [54](#)
- [60] K. Franko and S. K. Lele. Breakdown mechanisms and heat transfer overshoot in hypersonic zero pressure gradient boundary layers. *J. Fluid Mech.*, 730:491–532, 2013. [X](#), [20](#), [21](#)
- [61] G. Freire, A. Cavalieri, F. Silvestre, A. Hanifi, and D. Henningson. Actuator and sensor placement for closed-loop control of convective instabilities. *Theor. Comput. Fluid Dyn.*, 34:619–641, 2020. [2](#), [37](#), [38](#), [40](#), [74](#), [75](#), [120](#)

- [62] M. Gad-el Hak. *Flow Control: Passive, Active, and Reactive Flow Management*. Cambridge University Press, 2000. [2](#), [31](#)
- [63] M. Gad-el Hak. Flow control: The future. *Journal of Aircraft*, 38, 2001. [XI](#), [25](#), [196](#)
- [64] S. Gaponov and B. Smorodsky. Supersonic turbulent boundary layer drag control using spanwise wall oscillation. *International Journal of Theoretical and Applied Mechanics*, 1: 97–103, 2016. [2](#), [27](#)
- [65] E. Gillies. Low-dimensional control of the circular cylinder wake. *J. Fluid Mech.*, 371: 157–178, 1998. [36](#)
- [66] T. Glad and L. Ljung. *Control Theory*. Taylor & Francis, 2000. [34](#), [39](#), [121](#), [133](#)
- [67] P. J. Goddard and K. Glover. *Performance-Preserving Controller Approximation*. PhD thesis, University of Cambridge, 1995. [41](#)
- [68] B. Gustavsen and A. Semlyen. Rational approximation of frequency domain responses by vector fitting. *IEEE Transactions on Power Delivery*, 14:1052–1061, 1999. [36](#)
- [69] S. Hachicha, M. Kharrat, and A. Chaari. N4sid and moesp algorithms to highlight the ill-conditioning into subspace identification. *Int. J. Autom. Comput.*, 11:30–38, 2014. [37](#)
- [70] C. Hader and H. F. Fasel. Direct numerical simulations of hypersonic boundary-layer transition for a flared cone: fundamental breakdown. *Journal of Fluid Mechanics*, 869: 341–384, 2019. [21](#)
- [71] A. Hanifi, P. Schmid, and D. Henningson. Transient growth in compressible boundary layer flow. *Physics of Fluids*, 8:826, 1996. [X](#), [18](#), [19](#), [49](#)
- [72] T. Herbert. Secondary instability of boundary layers. *Annual Review of Fluid Mechanics*, 20(1):487–526, 1988. [20](#)
- [73] A. Hervé, D. Sipp, P. Schmid, and M. Samuelides. A physics-based approach to flow control using system identification. *J. Fluid Mech.*, 702:26–58, 2012. [30](#), [34](#), [36](#), [64](#), [68](#)
- [74] S.-C. Huang and J. Kim. Control and system identification of a separated flow. *Physics of Fluids*, 20:101509, 2008. [37](#)
- [75] F. Husmeier and H. Fasel. Numerical investigations of hypersonic boundary layer transition over circular cones. In *18th AIAA Computational Fluid Dynamics Conference*. [21](#)
- [76] M. Högberg, T. Bewley, and D. Henningson. Relaminarization of $Re_\tau = 100$ turbulence using gain scheduling and linear state-feedback control. *Physics of fluids*, 15(11):3572, 2003. [42](#)
- [77] R. Jahanbakhshi and T. Zaki. Nonlinearly most dangerous disturbance for high-speed boundary-layer transition. *J. Fluid Mech.*, 876:87–121, 2019. [151](#)
- [78] R. Jahanbakhshi and T. Zaki. Optimal heat flux for delaying transition to turbulence in a high-speed boundary layer. *J. Fluid Mech.*, 916, 2021. [XI](#), [2](#), [27](#)
- [79] B. Jones, P. Heins, E. Kerrigan, J. Morrison, and A. Sharma. Modelling for robust feedback control of fluid flows. *J. Fluid Mech.*, 769:687–722, 2015. [41](#)

- [80] J.-N. Juang and R. Pappa. An eigensystem realization algorithm for modal parameter identification and model reduction. *J. Guid. Control Dyn.*, 8:620–627, 1985. 37, 52
- [81] F. Juillet, P. Schmid, and P. Huerre. Control of amplifier flows using subspace identification techniques. *J. Fluid Mech.*, 725:522–565, 2013. 2, 30, 34, 37, 74, 75, 81
- [82] T. Juliano, M. Borg, and S. Schneider. Quiet tunnel measurements of hifire-5 boundary-layer transition. *AIAA Journal*, 53:1980–1993, 2015. 1
- [83] R. Kalman. When is a linear control system optimal? *Journal of Basic Engineering*, 86:51–60, 1964. 2, 38
- [84] J. Kendall. Wind tunnel experiments relating to supersonic and hypersonic boundary-layer transition. *AIAA Journal*, 13:290, 1975. 59, 69, 161
- [85] W. Kerstens, J. Pfeiffer, D. Williams, R. King, and T. Colonius. Closed-loop control of lift for longitudinal gust suppression at low reynolds numbers. *AIAA Journal*, 49:1721–1728, 2011. 40
- [86] J. Kim and T. Bewley. A linear systems approach to flow control. *Annual Review of Fluid Mechanics*, 39(1):383–417, 2007. 1, 35
- [87] P. S. Klebanoff, K. D. Tidstrom, and L. M. Sargent. The three-dimensional nature of boundary-layer instability. *Journal of Fluid Mechanics*, 12(1):1–34, 1962. 20
- [88] S. Kolavennu, S. Palanki, and J. C. Cockburn. Robust control of i/o linearizable systems via multi-model h_2/h_∞ synthesis. *Chemical Engineering Science*, 55(9):1583–1589, 2000. 42
- [89] S. Kolavennu, S. Palanki, and J. C. Cockburn. Robust controller design for multivariable nonlinear systems via multi-model h_2/h_∞ synthesis. *Chemical Engineering Science*, 56(14):4339–4349, 2001. 42
- [90] U. Krishnan. Hypersonic boundary layer transition, . URL https://www.youtube.com/watch?v=e6Tdd_7y4oA. X, 16
- [91] U. Krishnan. Hypersonic boundary layer transition, . URL <https://www.youtube.com/watch?v=HjfEjXUXrW8>. X, 16
- [92] H. Kwakernaak. Optimal low-sensitivity linear feedback systems. *Automatica*, 5:279–285, 1969. 38
- [93] A. C. Laible and H. F. Fasel. Continuously forced transient growth in oblique breakdown for supersonic boundary layers. *Journal of Fluid Mechanics*, 804:323–350, 2016. 20
- [94] F. C. Lajús, A. V. Cavalieri, and C. J. Deschamps. Spatial stability characteristics of non-circular jets. In *21st AIAA/CEAS Aeroacoustics Conference*, 2015. 25
- [95] W. Larimore. Canonical variate analysis in identification, filtering, and adaptive control. In *Proceedings of the 29th IEEE Conference on Decision and Control*, 1990. 37
- [96] C. Leclercq, F. Demourant, C. Poussot-Vassal, and D. Sipp. Linear iterative method for closed-loop control of quasiperiodic flows. *J. Fluid Mech.*, 868:22–65, 2019. 28, 41

- [97] B. V. Leer. Towards the Ultimate Conservative Difference Scheme. V. A Second-Order Sequel to Godunov's Method. *J. Comput. Phys.*, 32:101–136, 1979. [46](#)
- [98] B. Lees and C. Lin. *Investigation of the stability of the laminar boundary layer in a compressible fluid*. Technical report for National Advisory Committee for Aeronautics, 1946. [15](#), [16](#)
- [99] J. Lefieux, E. Garnier, and N. Sandham. DNS study of roughness-induced transition at Mach 6. In *AIAA AVIATION*, 2019. [25](#)
- [100] R. Lehoucq, D. Sorensen, and C. Yang. Arpack users' guide: Solution of large scale eigenvalue problems with implicitly restarted arnoldi methods. *SIAM*, 6, 1998. [49](#)
- [101] Y. Li and M. Gaster. Active control of boundary-layer instabilities. *Journal of Fluid Mechanics*, 550:185–205, 2006. [122](#)
- [102] M.-S. Liou. A sequel to ausm, part ii: Ausm⁺-up for all speeds. *J. Comput. Phys.*, 214:137–170, 2006. [46](#)
- [103] M.-S. Liou and J. R. Edwards. Ausm schemes and extensions for low mach and multiphase flows. 1999. [46](#)
- [104] P. Loiseau, P. Chevrel, M. Yagoubi, and J.-M. Duffal. h_∞ multi-objective and multi-model MIMO control design for broadband noise attenuation in an enclosure. In *2016 European Control Conference (ECC)*, pages 643–648, 2016. [42](#)
- [105] C. Lu and C. Gu. The computation of the square roots of circulant matrices. *Applied Mathematics and Computation*, 217:6819–6829, 2011. [122](#), [134](#)
- [106] M. Lugrin, F. Nicolas, N. Severac, J.-P. Tobeli, S. Beneddine, E. Garnier, S. Esquieu, and R. Bur. Transitional shockwave/boundary layer interaction experiments in the R2Ch blowdown wind tunnel. *Experiments in Fluids*, 63, 2022. [66](#), [132](#), [146](#)
- [107] J. Lumley. *Stochastic Tools in Turbulence*. Academic Press, 1970. [35](#)
- [108] A. Lundbladh and A. Johansson. Direct simulation of turbulent spots in plane couette flow. *J. Fluid Mech.*, 229:499–516, 1991. [18](#)
- [109] Y. Ma and X. Zhong. Receptivity of a supersonic boundary layer over a flat plate. Part 1. Wave structures and interactions. *J. Fluid Mech.*, 488:31–78, 2003. [XI](#), [16](#), [45](#), [46](#), [47](#), [48](#), [49](#), [50](#), [51](#), [56](#), [59](#), [60](#), [70](#)
- [110] L. Mack. *Transition and laminar instability*. NASA-CP-153203, 1977. [60](#)
- [111] L. Mack. *Boundary-Layer Linear Stability Theory*. AGARD Report No.709, 1984. [X](#), [2](#), [14](#), [15](#), [16](#), [17](#), [25](#), [47](#), [62](#), [70](#)
- [112] L. Mack. On the inviscid acoustic-mode instability of supersonic shear flows. *Theor. Comput. Fluid Dyn.*, 2:97–123, 1990. [16](#)
- [113] M. Malik. Prediction and control of transition in supersonic and hypersonic boundary layers. *AIAA Journal*, 27:1487, 1989. [XI](#), [16](#), [18](#), [25](#), [26](#)
- [114] E. Martini, A. V. G. Cavalieri, P. Jordan, A. Towne, and L. Lesshafft. Resolvent-based optimal estimation of transitional and turbulent flows. *Journal of Fluid Mechanics*, 900:A2, 2020. doi: 10.1017/jfm.2020.435. [39](#)

- [115] E. Martini, J. Jung, A. V. Cavalieri, P. Jordan, and A. Towne. Resolvent-based tools for optimal estimation and control via the wiener–hopf formalism. *Journal of Fluid Mechanics*, 937:A19, 2022. doi: 10.1017/jfm.2022.102. [39](#)
- [116] J. Masad and R. Abid. On transition in supersonic and hypersonic boundary layers. *Int. J. Engng. Sci.*, 33:1893–1919, 1995. [X](#), [16](#), [17](#), [18](#), [25](#)
- [117] M. Matsubara and P. Alfredsson. Disturbance growth in boundary layers subjected to free-stream turbulence. *J. Fluid Mech.*, 430:149–168, 2001. [X](#), [19](#)
- [118] C. S. J. Mayer, D. A. Von Terzi, and H. F. Fasel. Direct numerical simulation of complete transition to turbulence via oblique breakdown at Mach 3. *Journal of Fluid Mechanics*, 674:5–42, 2011. [20](#)
- [119] D. C. McFarlane and K. Glover. A loop-shaping design procedure using h_∞ synthesis. *IEEE Transactions on Automatic Control*, 37:759–769, 1992. [40](#)
- [120] T. McKelvey and A. Helmersson. State-space parametrizations of multivariable linear systems using tridiagonal matrix forms. In *Proceedings of 35th IEEE Conference on Decision and Control*, volume 4, pages 3654–3659, 1996. [73](#)
- [121] W. Milling. Tollmien-Schlichting wave cancellation. *Physics of Fluids*, 24:979–981, 1981. [29](#)
- [122] A. Monokrousos, E. Akervik, L. Brandt, and D. Henningson. Global three-dimensional optimal disturbances in the Blasius boundary-layer flow using time-steppers. *J. Fluid Mech.*, 650:1–34, 2010. [18](#)
- [123] B. Moore. Principal component analysis in linear systems: Controllability, observability, and model reduction. *IEEE Trans. Auto. Control*, 26:17–32, 1981. [36](#)
- [124] E. Moore. On the reciprocal of the general algebraic matrix. *Bulletin of American Mathematical Society*, 26:394–395, 1920. [134](#)
- [125] M. Morkovin. On the Many Faces of Transition. In C. S. Wells, editor, *Viscous Drag Reduction*. Springer US, 1969. [X](#), [9](#), [10](#), [196](#)
- [126] P. Morra, K. Sasaki, A. Hanifi, A. Cavalieri, and D. Henningson. A realizable data-driven approach to delay bypass transition with control theory. *J. Fluid Mech.*, 883, 2020. [2](#), [30](#), [34](#), [35](#), [38](#), [39](#), [52](#), [64](#), [73](#), [96](#), [120](#), [121](#), [122](#)
- [127] P. Nibourel, C. Leclercq, F. Demourant, E. Garnier, and D. Sipp. Robust control of convective instabilities in a 2d supersonic boundary layer using a feedback setup. In *AERO 2020+1 - 55th 3AF International Conference on Applied Aerodynamics*, online, 2021. [5](#)
- [128] P. Nibourel, C. Leclercq, F. Demourant, E. Garnier, and D. Sipp. Robust reactive control of convective instabilities: application to the 2d supersonic boundary layer. In *GDR 2502 Flow Separation Control*, online, 2021. [5](#)
- [129] P. Nibourel, C. Leclercq, F. Demourant, E. Garnier, and D. Sipp. Extending closed-loop control of 2d supersonic boundary layer instabilities beyond a single operating point. 2022. Submitted in *AIAA Journal*. [5](#)

- [130] P. Nibourel, C. Leclercq, F. Demourant, E. Garnier, and D. Sipp. Robust transition delay in supersonic boundary layer using h_2/h_∞ feedback synthesis. In *14th European Fluid Mechanics Conference-EFMC14*, Athens, Greece, 2022. 5
- [131] P. Nibourel, C. Leclercq, F. Demourant, E. Garnier, and D. Sipp. Reactive control of second mack mode in a supersonic boundary layer with free-stream velocity/density variations. *Journal of Fluid Mechanics*, 954:A20, 2023. 5
- [132] R. Nichols, R. Reichert, and W. Rugh. Gain scheduling for h-infinity controllers: a flight control example. *IEEE Transactions on Control Systems Technology*, 1(2):69–79, 1993. 42
- [133] M. Olazabal-Loumé, F. Danvin, J. Mathiaud, and B. Aupoix. Study on $k-\omega$ shear stress transport model corrections applied to rough wall turbulent hypersonic boundary layers. In *7th European Conference for Aeronautics and Space Sciences*, 2017. 52
- [134] W. Orr. The stability or instability of the steady motions of a perfect liquid and of a viscous liquid. *Proceedings of the Royal Irish Academy.*, 27:9–68, 1907. 18, 62
- [135] P. Overschee and B. D. Moor. N4sid : Subspace algorithms for the identification of combined deterministic-stochastic systems. *Automatica*, 30:75–93, 1994. 37
- [136] S. Ozgen and S. Kiricali. Linear stability analysis in compressible, flat-plate boundary-layers. *Theor. Comput. Fluid Dyn.*, 22:1–20, 2008. XI, 52
- [137] P. Paredes, M. Choudhari, F. Li, and C.-L. Chang. Optimal growth in hypersonic boundary layers. *AIAA Journal*, 54:3050–3061, 2016. 18
- [138] R. Penrose. A generalized inverse for matrices. *Mathematical Proceedings of the Cambridge Philosophical Society*, 51(3):406413, 1955. 134
- [139] S. Peron, T. Renaud, I. Mary, C. Benoit, and M. Terracol. An immersed boundary method for preliminary design aerodynamic studies of complex configurations. In *23rd AIAA Computational Fluid Dynamics Conference*. 46
- [140] F. Picella, M. Bucci, S. Cherubini, and J.-C. Robinet. A synthetic forcing to trigger laminar-turbulent transition in parallel wall bounded flows via receptivity. *J. Comput. Phys.*, 2019. 49
- [141] T. Poinso and S. Lele. Boundary conditions for direct simulations of compressible viscous flows. *Journal of Computational Physics*, 101(1):104–129, 1992. 46
- [142] J. Potter. Review of the influence of cooled walls on boundary-layer transition. *AIAA Journal*, 18:1010, 1980. XI, 25, 26
- [143] L. Prandtl. über Flüssigkeitsbewegung bei sehr kleiner Reibung. In *Verhandl III, Intern. Math. Kongr.*, 1904. 1
- [144] A. V. Ramesh, S. Utku, and J. A. Garba. Computational complexities and storage requirements of some riccati equation solvers. *Journal of Guidance Control and Dynamics*, 12:469–479, 1989. 34
- [145] L. Rayleigh. On the stability, or instability, of certain fluid motions. *Proceedings of the London Mathematical Society*, s1-11:57–72, 1880. 14

- [146] O. Reynolds. An experimental investigation of the circumstances which determine whether the motion of water shall be direct or sinuous, and of the law of resistance in parallel channels. *Phil. Trans. R. Soc. Lon.*, 174:935–982, 1883. [8](#)
- [147] W. J. Rugh and J. S. Shamma. Research on gain scheduling. *Automatica*, 36(10):1401–1425, 2000. [42](#)
- [148] J. Saint-James. *Prévision de la transition laminaire-turbulent dans le code elsA. Extension de la méthode des paraboles aux parois chauffées*. PhD thesis, Institut Supérieur de l’Aéronautique et de l’Espace (ISAE), 2020. [47](#)
- [149] R. Sanator, J. DeCarlo, and D. Torrillo. Hypersonic boundary-layer transition data for a cold-wall slender cone. *AIAA Journal*, 3:758, 1965. [27](#)
- [150] W. Saric, H. Reed, and E. Kerschen. Boundary-layer receptivity to freestream disturbances. *Annu. Rev. Fluid Mech.*, 34:291–319, 2002. [X](#), [10](#)
- [151] F. Sartor, C. Mettot, and D. Sipp. Stability, receptivity, and sensitivity analyses of buffeting transonic flow over a profile. *AIAA Journal*, 53 (7):1980–1993, 2014. [13](#)
- [152] F. Sartor, C. Mettot, R. Bur, and D. Sipp. Unsteadiness in transonic shock-wave/boundary-layer interactions: experimental investigation and global stability analysis. *J. Fluid Mech.*, 781:550–577, 2015. [49](#)
- [153] K. Sasaki, P. Morra, N. Fabbiane, A. Cavalieri, A. Hanifi, and D. Henningson. On the wave-cancelling nature of boundary layer flow control. *Theor. Comput. Fluid Dyn.*, 32: 593–616, 2018. [2](#), [34](#), [38](#), [39](#), [52](#), [64](#), [68](#), [122](#)
- [154] K. Sasaki, G. Tissot, A. Cavalieri, F. Silvestre, P. Jordan, and D. Biau. Closed-loop control of a free shear flow: a framework using the parabolized stability equations. *Theor. Comput. Fluid Dyn.*, 32:765–788, 2018. [37](#), [39](#), [64](#)
- [155] K. Sasaki, R. Vinuesa, A. V. G. Cavalieri, P. Schlatter, and D. S. Henningson. Transfer functions for flow predictions in wall-bounded turbulence. *Journal of Fluid Mechanics*, 864:708–745, 2019. [96](#), [121](#)
- [156] K. Sasaki, P. Morra, A. Cavalieri, A. Hanifi, and D. Henningson. On the role of actuation for the control of streaky structures in boundary layers. *J. Fluid Mech.*, 883:A34, 2020. [2](#), [34](#), [37](#), [38](#), [39](#), [64](#), [96](#), [121](#), [122](#)
- [157] A. Savitzky and M. Golay. Smoothing and differentiation of data by simplified least squares procedures. *Analytical Chemistry*, 36:1627–1637, 1964. [134](#)
- [158] T. Sayadi, C. W. Hamman, and P. Moin. Direct numerical simulation of complete h-type and k-type transitions with implications for the dynamics of turbulent boundary layers. *Journal of Fluid Mechanics*, 724:480–509, 2013. [X](#), [20](#)
- [159] C. Scherer. Mixed h_2/h_∞ control. In *Trends in Control: A European Perspective*, pages 173–216. Springer US, 1995. [40](#), [41](#)
- [160] C. Scherer, P. Gahinet, and M. Chilali. Multiobjective output-feedback control via lmi optimization. *IEEE Transactions on Automatic Control*, 42:896–911, 1997. [41](#)
- [161] H. Schlichting. Zur entstehung der turbulenz bei der plattenstromun. *Nachr. Ges. Wiss. Gottingen, Math.-Phys. Ki.*, pages 181–208, 1933. [X](#), [14](#), [15](#)

- [162] P. Schmid. Nonmodal stability theory. *Annu. Rev. Fluid Mech.*, 39:129–162, 2007. [X](#), [12](#), [18](#)
- [163] P. Schmid and D. Henningson. *Stability and Transition in Shear Flows*. Springer, 2001. [14](#), [15](#)
- [164] P. Schmid and D. Sipp. Linear control of oscillator and amplifier flows. *Physical Review Fluids*, 1, 2016. [28](#), [36](#)
- [165] G. Schrauf. Status and perspectives of laminar flow. *The Aeronautical Journal*, 109:639–644, 2005. [1](#)
- [166] G. Schubauer and H. Skramstad. Laminar boundary-layer oscillations and stability of laminar flow. *Journal of the Aeronautical Sciences*, 14:69–78, 1947. [X](#), [14](#), [15](#)
- [167] G. Scorletti and V. Fromion. Introduction à la commande multivariable des systèmes : méthodes de synthèse fréquentielle \mathcal{H}_∞ , 2007. [XI](#), [31](#), [32](#), [33](#), [40](#)
- [168] O. Semeraro, S. Bagheri, L. Brandt, and D. Henningson. Feedback control of three-dimensional optimal disturbances using reduced-order models. *J. Fluid Mech.*, 677:63–102, 2011. [2](#), [18](#), [30](#), [34](#), [35](#), [36](#), [38](#), [66](#), [121](#)
- [169] O. Semeraro, S. Bagheri, L. Brandt, and D. Henningson. Transition delay in a boundary layer flow using active control. *J. Fluid Mech.*, 731:288–311, 2013. [34](#), [121](#)
- [170] O. Semeraro, J. Pralits, C. Rowley, and D. Henningson. Riccati-less approach for optimal control and estimation: an application to two-dimensional boundary layers. *J. Fluid Mech.*, 731:394–417, 2013. [2](#), [30](#), [34](#), [37](#), [38](#), [81](#)
- [171] N. Shahriari, M. Kollert, and A. Hanifi. Control of a swept-wing boundary layer using ring-type plasma actuators. *J. Fluid Mech.*, 844:36–60, 2018. [162](#)
- [172] T. Shaqarin, P. Oswald, B. Noack, and R. Semaan. Drag reduction of a d-shaped bluff-body using linear parameter varying control. *Physics of Fluids*, 33:077108, 2021. [40](#)
- [173] S. Sharma, M. Shadloo, A. Hadjadj, and M. Kloker. Control of oblique-type breakdown in a supersonic boundary layer employing streaks. *J. Fluid Mech.*, 873:1072–1089, 2019. [2](#), [27](#)
- [174] S. Siegel, J. Seidel, C. Fagley, D. Luchtenburg, K. Cohen, and T. McLaughlin. Low-dimensional modelling of a transient cylinder wake using double proper orthogonal decomposition. *J. Fluid Mech.*, 610:1–42, 2008. [36](#)
- [175] D. Sipp and P. Schmid. Closed-loop control of fluid flow : a review of linear approaches and tools for the stabilization of transitional flows. *AerospaceLab Journal*, pages 1–11, 2013. [35](#)
- [176] D. Sipp and P. Schmid. Linear closed-loop control of fluid instabilities and noise-induced perturbations: A review of approaches and tools. *Appl. Mech. Rev.*, 68:020801, 2016. [32](#), [37](#), [38](#)
- [177] D. Sipp, O. Marquet, P. Meliga, and A. Barbagallo. Dynamics and control of global instabilities in open-flows: A linearized approach. *Appl. Mech. Rev.*, 63:030801, 2010. [13](#), [18](#), [27](#), [28](#), [35](#), [62](#)

- [178] L. Sirovich. Turbulence and the dynamics of coherent structures. *Quart. Appl. Math.*, 45:561–590, 1987. [36](#)
- [179] J. Sivasubramanian and H. F. Fasel. Direct numerical simulation of transition in a sharp cone boundary layer at Mach 6: fundamental breakdown. *Journal of Fluid Mechanics*, 768:175–218, 2015. [21](#)
- [180] S. Skogestad and I. Postlethwaite. *Multivariable Feedback Control: Analysis and Design*. John Wiley & Son, 2005. [3](#), [29](#), [32](#), [33](#), [34](#), [35](#), [38](#), [39](#), [40](#), [55](#), [65](#), [74](#), [79](#), [120](#), [178](#)
- [181] A. Smith and N. Gamberoni. *Transition, Pressure Gradient and Stability Theory*. Douglas Aircraft Company, 1956. [11](#)
- [182] H. Squire. On the stability for three-dimensional disturbances of viscous fluid flow between parallel walls. *Proc. R. Soc. Lond.*, 142:621–628, 1933. [16](#)
- [183] A. Stroh, B. Frohnepfel, P. Schlatter, and Y. Hasegawa. A comparison of opposition control in turbulent boundary layer and turbulent channel flow. *Physics of Fluids*, 27(7):075101, 2015. [83](#), [160](#)
- [184] V. Theofilis. Global linear instability. *Annu. Rev. Fluid Mech.*, 43:319–352, 2011. [11](#)
- [185] X. Tian, R. Zhao, T. Long, and C. Y. Wen. Reverse design of ultrasonic absorptive coating for the stabilization of mack modes. *AIAA Journal*, 57(6):2264–2269, 2019. [2](#)
- [186] X. Tian, T. Liu, T. Wang, J. Zhu, and C. Wen. Double-layer acoustic metasurface for the suppression of the mack second mode in hypersonic boundary-layer flow. *Physics of Fluids*, 34(7):074105, 2022. [XI](#), [2](#), [25](#), [26](#)
- [187] H. Tol, M. Kotsonis, C. D. Visser, and B. Bamieh. Localised estimation and control of linear instabilities in two-dimensional wall-bounded shear flows. *J. Fluid Mech.*, 824:818–865, 2017. doi: 10.1017/jfm.2017.355. [40](#)
- [188] H. Tol, M. Kotsonis, and C. de Visser. Pressure output feedback control of Tollmien-Schlichting waves in Falkner–Skan boundary layers. *AIAA Journal*, 57:1–14, 2019. [2](#), [3](#), [30](#), [34](#), [38](#), [42](#), [81](#), [86](#), [96](#), [99](#)
- [189] W. Tollmien. Über der entstehung der turbulenz. *Nachr. Ges. Wiss. Göttingen, Math.-Phys. Ki.*, pages 21–44, 1929. [X](#), [14](#), [15](#)
- [190] L. Trefethen, A. Trefethen, S. Reddy, and T. Driscoll. Hydrodynamic stability without eigenvalues. *Science*, 261:578–584, 1993. [18](#)
- [191] A. Tumin and E. Reshotko. Spatial theory of optimal disturbances in boundary layers. *Physics of Fluids*, 13:2097, 2001. [18](#)
- [192] S. Unnikrishnan and D. V. Gaitonde. First-mode-induced nonlinear breakdown in a hypersonic boundary layer. *Computers & Fluids*, 191:104249, 2019. [20](#)
- [193] S. Unnikrishnan and D. V. Gaitonde. Linear, nonlinear and transitional regimes of second-mode instability. *Journal of Fluid Mechanics*, 905:A25, 2020. [21](#)
- [194] *U.S. Standard Atmosphere*. U.S. Government Printing Office, 1976. [161](#)

- [195] S. S. Vemuri, R. Bosworth, J. F. Morrison, and E. C. Kerrigan. Real-time feedback control of three-dimensional Tollmien-Schlichting waves using a dual-slot actuator geometry. *Phys. Rev. Fluids*, 3:053903, 2018. [3](#), [30](#), [34](#), [40](#)
- [196] M. Verhaegen. Identification of the deterministic part of MIMO state space models given in innovations form from input-output data. *Automatica*, 30:61–74, 1994. [37](#)
- [197] R. Wang, R. Tóth, and I. R. Manchester. A comparison of LPV gain scheduling and control contraction metrics for nonlinear control. *IFAC-PapersOnLine*, 52(28):44–49, 2019. [42](#)
- [198] P. Welch. The use of fast fourier transform for the estimation of power spectra: A method based on time averaging over short, modified periodograms. *IEEE Transactions on Audio and Electroacoustics*, 15(2):70–73, 1967. [134](#)
- [199] H. Werlé. Transition et décollement: visualisations au tunnel hydrodynamique de l’Onera. *Rech. Aérop*, 5:331–345, 1980. [X](#), [14](#)
- [200] E. White and W. Saric. Application of variable leading-edge roughness for transition control on swept wings. In *38th Aerospace Sciences Meeting and Exhibit*, 2004. [25](#)
- [201] F. White. *Viscous Fluid Flow*. McGraw-Hill, third edition edition, 1991. [X](#), [9](#)
- [202] J. Williamson. Low-storage Runge-Kutta schemes. *Journal of Computational Physics*, 35(1):48–56, 1980. [51](#)
- [203] H. Yao, Y. Sun, T. Mushtaq, and M. S. Hemati. Reducing transient energy growth in a channel flow using static output feedback control. *AIAA Journal*, 60(7):4039–4052, 2022. [37](#)
- [204] J. Yao and F. Hussain. Supersonic turbulent boundary layer drag control using spanwise wall oscillation. *J. Fluid Mech.*, 880:388–429, 2019. [2](#), [27](#)
- [205] Z. Zhang and J. S. Freudenberg. Loop transfer recovery with non-minimum phase zeros. In *26th IEEE Conference on Decision and Control*, volume 26, pages 956–957, 1987. [38](#)
- [206] T. Zhou, Z. Liu, Y. Lu, Y. Wang, and C. Yan. Direct numerical simulation of complete transition to turbulence via first and second-mode oblique breakdown at a high-speed boundary layer. *Physics of Fluids*, 34(7):074101, 2022. [20](#), [21](#)

Résumé en français

La transition à la turbulence d'une couche limite entraîne une augmentation du frottement à la paroi pénalisant la traînée des avions. À très haute vitesse, l'échauffement engendré est significatif et devient même une contrainte majeure pour la conception d'engins supersoniques/hypersoniques. La transition à la turbulence des écoulements pariétaux est initiée par l'amplification de perturbations extérieures de diverses natures (rugosités, ondes sonores, turbulence amont de l'écoulement, etc.) et plusieurs chemins de transition sont possibles en fonction du niveau d'intensité et de la nature des perturbations. Lorsque les perturbations sont de faible intensité, leur croissance est induite par l'instabilité de l'écoulement de base et est décrite par la théorie de la stabilité linéaire. Cependant, la manipulation ciblée de l'écoulement peut limiter l'amplitude de ces perturbations et retarder le passage à la turbulence.

Des études antérieures ont réussi à retarder la transition à la turbulence d'une couche limite supersonique, mais elles ont utilisé des stratégies passives ou actives prédéterminées qui agissent indépendamment de l'état de l'écoulement [63], potentiellement moins efficaces et robustes aux changements de conditions de fonctionnement qu'une stratégie de contrôle réactif où l'action de contrôle est continuellement ajustée en fonction des mesures de capteurs. Des études en écoulement incompressible avec une configuration réactive existent et réussissent à retarder la transition à la turbulence d'une couche limite mais le problème de la robustesse en performance, qui peut être définie comme la capacité de la loi de contrôle à rester efficace en termes de réduction d'amplitude des perturbations malgré des erreurs de modélisation ou des variations des conditions d'écoulement autour du cas de référence, reste un défi majeur pour les écoulements amplificateurs de bruit [125] en raison de leur nature convective. À quelques exceptions notables [14, 54], cette question de la robustesse en performance a été peu abordée dans la littérature en raison des limitations inhérentes à la synthèse *LQG* qui est communément utilisée, laissant la littérature dominée par des configurations peu robustes. Cette étude vise donc à créer une loi de commande réactive robuste pour retarder la transition à la turbulence d'une couche limite supersonique.

Le chapitre 1 est consacré à une revue de la littérature concernant la stabilité et la transition des écoulements de couche limite. Pour un nombre de Mach suffisamment élevé, une couche limite supersonique est caractérisée par la présence de deux modes convectivement instables : le premier et le second mode de Mack. Le premier mode de Mack a des taux d'amplification maximaux pour des perturbations obliques 3D tandis que le second mode de Mack a des taux d'amplification maximaux pour des perturbations 2D invariantes dans le sens de l'envergure. Après cette phase de croissance linéaire, la déstabilisation du premier mode de Mack ou du

second mode de Mack est considérée comme un chemin probable du passage d'un état laminaire à un état turbulent. Par conséquent, nous chercherons à réduire la croissance linéaire des instabilités du premier et du second mode de Mack afin de retarder la transition vers la turbulence.

Le chapitre 2 est dédié à une revue de la littérature concernant le contrôle des écoulements de couche limite. Comme les perturbations de faible amplitude sont à la base de quatre des cinq chemins de la réceptivité à la transition, la stratégie de contrôle réactif, basée sur les outils linéaires classiques de la théorie du contrôle (identification, synthèse, etc.) est parfaitement adaptée pour atténuer la croissance linéaire des perturbations en vue de retarder la transition. Pour l'étape d'identification, nécessaire pour la plupart des méthodes de synthèse, les approches basées données telles que ERA ont l'avantage de construire les modèles uniquement à partir des données temporelles/fréquentielles des entrées/sorties et peuvent être utilisées dans des configurations réalistes contrairement aux méthodes de projection Galerkin. Pour l'étape de synthèse, les outils modernes robustes comme la synthèse structurée mixte H_2/H_∞ permettent de respecter un cahier des charges multi-critères et de traiter simultanément les problèmes de performance nominale, de stabilité et de robustesse des performances, contrairement à la synthèse LQG traditionnellement utilisée. La synthèse structurée mixte H_2/H_∞ semble donc prometteuse pour le contrôle des écoulements amplificateurs de bruit.

Le but du chapitre 3 est de présenter les codes de mécanique des fluides et les méthodes de contrôle employées dans cette thèse. Les solveurs de mécanique des fluides et les schémas spatio-temporels utilisés sont présentés dans ce chapitre. Les codes de stabilité local/global et le code de couche limite utilisés sont également introduits avec des éléments de validation. Les méthodes de contrôle, les algorithmes des méthodes d'identification et de synthèse utilisés sont détaillés dans ce chapitre, ainsi que l'algorithme d'implémentation des contrôleurs dans les solveurs de mécanique des fluides.

Le chapitre 4 est consacré au contrôle de perturbations linéaires 2D dans une couche limite supersonique à Mach 4,5. Ce chapitre permet d'aborder facilement la question de la robustesse en stabilité et de la robustesse en performance des lois de commande car la configuration est 2D, ce qui simplifie la complexité du problème. Après avoir identifié les modèles d'ordre réduit en ayant mis l'accent sur le problème des délais convectifs dans le cas des écoulements amplificateurs de bruit, une synthèse multi-critères structurée mixte H_2/H_∞ est utilisée pour fixer au préalable la structure du contrôleur et pour minimiser/contraindre les normes appropriées de différentes fonctions de transfert : la norme H_2 pour garantir les performances nominales (réduction de l'amplitude des perturbations) et la norme H_∞ pour maintenir la robustesse des performances (en cas de capteur d'estimation bruité) et la robustesse en stabilité (en cas d'incertitudes ou de variations de vitesse/densité de l'écoulement amont). Deux configurations de contrôle sont testées : une où le capteur d'estimation est placé en amont de l'actionneur (appelée *feedforward*) et une où le capteur d'estimation est placé en aval de l'actionneur (appelée *feedback*). Les configurations feedforward et feedback maintiennent l'énergie locale des perturbations en dessous d'un seuil sur une distance significative en aval de l'actionneur dans le cas nominal. De plus, la robustesse en stabilité pour la conception feedback n'est pas un problème grâce à la synthèse robuste et aux contraintes imposées. En ce qui concerne la robustesse des performances, les deux configurations parviennent à réduire l'amplitude des perturbations par rapport au cas non contrôlé malgré des capteurs d'estimation bruités ou des variations de densité de l'écoulement amont de $\pm 5\%$. Cependant, la configuration feedforward devient complètement inefficace lorsque des variations de vitesse de l'écoulement amont de $\pm 5\%$ sont prises en compte, ce qui met en évidence la pertinence de la configuration feedback pour la robustesse des performances dans des écoulements convectivement instables lorsque les contrôleurs sont construits à partir d'un seul point de fonctionnement.

Afin de maintenir les performances en termes de réduction de l'amplitude des perturbations sur une large gamme de variations de vitesse, qui sont apparues comme les variations les plus problématiques, et d'aller plus loin dans la question de la robustesse des performances, des configurations combinées feedforward/feedback, des contrôleurs obtenus par synthèse multi-modèles sur plusieurs points de fonctionnement et des contrôleurs par séquençement de gain sont considérés dans le chapitre 5 pour le cas de la couche limite supersonique 2D. Ces différentes techniques (toutes basées sur la synthèse structurée mixte H_2/H_∞) sont comparées aux contrôleurs feedback et feedforward de référence conçus sur un seul point de fonctionnement. L'approche combinée n'a aucune robustesse en performance lorsqu'elle est conçue sur un seul point de fonctionnement car le contrôleur feedforward détériore la capacité naturelle du contrôleur feedback à être robuste aux variations de vitesse. Le contrôleur multi-modèle feedforward amplifie également l'amplitude des perturbations par rapport au cas non contrôlé sur la plage de points de fonctionnement considérée en raison de la faible capacité d'une configuration feedforward à être robuste aux variations de phases donc aux variations de délais convectifs. Il est impossible de respecter un seuil énergétique pour toute la plage de points de fonctionnement considérée même avec une configuration multi-modèle feedback, qui n'améliore que légèrement les résultats du contrôleur feedback de base conçu sur un seul point de fonctionnement. En ce qui concerne la technique de séquençement de gain, une perte de performance significative est observée dans des conditions hors conception pour le cas feedforward si les points d'interpolation sont trop éloignés. Dans le cas feedback, le séquençement de gain permet de maintenir de faibles perturbations sur toute la plage de fonctionnement $M_\infty \in [4.275, 4.725]$ avec seulement deux points de conception dans la loi d'interpolation. En résumé, lorsque des variations de vitesse sont prises en compte, la stratégie de contrôle la plus efficace nécessite en premier lieu une configuration feedback. Dès qu'un simple contrôleur ne fournit pas les performances souhaitées sur toute la plage de points de fonctionnement considérée, une méthode de séquençement de gain couplée à une configuration feedback doit être utilisée.

Le chapitre 6 est consacré au contrôle robuste d'instabilités 3D afin de retarder la transition à la turbulence de la couche limite supersonique à Mach 4,5. Sur la base des résultats précédemment obtenus, seul un contrôleur feedback conçu à partir de la synthèse structurée mixte H_2/H_∞ est utilisé dans cette étude 3D pour avoir le meilleur compromis entre performance nominale et robustesse en performance. La loi de commande est construite à partir d'outils linéaires : l'identification basée donnée avec ERA est effectuée après avoir supprimé les délais convectifs inutiles et une méthode décentralisée (où une entrée est connectée à une seule sortie) est exploitée pour construire le contrôleur car l'interconnexion des différents nombres d'onde est impossible lors de la phase de croissance linéaire. Cette approche décentralisée conduit à résoudre plusieurs problèmes de minimisation sous contraintes de faible complexité pour chaque nombre d'onde que l'on cherche à contrôler, au lieu d'un seul problème centralisé d'ordre très élevé trop complexe à résoudre. La croissance linéaire des premier et deuxième modes de Mack est considérablement réduite par le contrôle qui présente une certaine robustesse en performance en réduisant toujours l'amplitude des perturbations malgré des capteurs d'estimation bruités ou des variations de vitesse de l'écoulement amont. Pour un cas de transition vers la turbulence où les perturbations sont encore faiblement non linéaires au niveau des actionneurs, la région laminaire est étendue dans le cas contrôlé d'une longueur représentant 19,1% de la distance de la position des actionneurs à la fin du domaine. Ainsi, une loi de commande réactive robuste retardant la transition vers la turbulence a été obtenue.

Titre : Contrôle réactif robuste de la transition à la turbulence d'une couche limite supersonique

Mots clés : Contrôle, Réactif, Robuste, Transition, Couche limite, Supersonique

Résumé : La transition à la turbulence d'une couche limite entraîne une augmentation du frottement à la paroi pénalisant la traînée des avions. À très haute vitesse, l'échauffement engendré est significatif et devient une contrainte majeure pour la conception d'avions supersoniques/hypersoniques. La transition à la turbulence des écoulements pariétaux est initiée par l'amplification de perturbations extérieures.

Lorsque les perturbations sont de faible intensité, il est possible de limiter leurs amplitudes dans l'optique de retarder la transition à la turbulence en se basant sur les outils linéaires classiques de la théorie du contrôle réactif où l'action de contrôle est continuellement ajustée en fonction des mesures de capteurs.

La question de la robustesse en performance, définie comme la capacité de la loi de contrôle à rester efficace en termes de réduction d'amplitude des perturbations malgré des erreurs de modélisation ou des variations des conditions d'écoulement autour du cas de référence, reste un défi majeur pour les écoulements de couche limite en raison de leur nature convective. Le travail de cette thèse consiste donc à obtenir une loi de commande réactive robuste pour retarder la transition vers la turbulence d'une couche limite supersonique. Des simulations numériques di-

rectes ont été réalisées dans des configurations 2D et 3D pour concevoir des lois de contrôle robustes pour une couche limite à Mach 4,5.

Les études 2D, qui permettent de simplifier la complexité du problème et d'aborder facilement la question de la robustesse en stabilité/performance des lois de commande, ont mis en évidence que la stratégie de contrôle la plus efficace consiste à placer le capteur d'estimation en aval de l'actionneur (configuration *feedback*). Dès lors qu'un simple contrôleur ne fournit pas les performances souhaitées sur toute la plage de point de fonctionnement considérée, une méthode de séquençage de gain associée à une configuration *feedback* peut être utilisée.

Dans les simulations 3D, la croissance linéaire des premier et deuxième mode de Mack est considérablement réduite par le contrôle *feedback* qui présente une certaine robustesse en performance en réduisant toujours l'amplitude des perturbations malgré des capteurs d'estimation bruités ou des variations de vitesse de l'écoulement amont. En contrôlant la croissance linéaire des deux modes de Mack, la région laminaire de la couche limite est étendue dans le cas contrôlé et la transition vers la turbulence est retardée.

Title : Robust reactive control of transition to turbulence of a supersonic boundary layer

Keywords : Control, Reactive, Robust, Transition, Boundary layer, Supersonic

Abstract : Transition to turbulence of a boundary layer leads to an increase of the wall friction penalizing aircraft drag. At high speeds, the generated heat is significant and becomes a major concern for the design of supersonic/hypersonic vehicles. Transition to turbulence in boundary layers is initiated by amplification of external disturbances.

With low levels of disturbances, one can seek to limit their amplitudes in order to delay transition to turbulence by relying on classical linear tools of reactive control theory where the control action is continuously adjusted according to sensor measurements.

The issue of performance robustness, defined as the control law's ability to remain efficient in terms of perturbation amplitude reduction despite modelling errors or free-stream condition variations around the reference case, remains a major challenge for boundary layer flows due to their convective nature. This thesis aims to obtain a robust reactive control law to delay transition to turbulence of a supersonic boundary layer. Direct numerical simulations have been perfor-

med in 2D and 3D configurations to design robust control laws for a boundary layer at Mach 4.5.

The 2D studies, which allow to simplify the complexity of the problem and to easily address the issue of stability/performance robustness of the control laws, have shown that the most efficient control strategy is to place the estimation sensor downstream of the actuator (*feedback* configuration). When a simple controller does not provide the desired performance over the entire range of operating points considered, a gain scheduling method associated with a *feedback* configuration can be used.

In 3D simulations, the linear growth of the first and second Mack modes is significantly reduced by the *feedback* control, which has a certain performance robustness by still reducing the disturbance amplitude despite noisy estimation sensors or free-stream velocity variations. By controlling the linear growth of both Mack modes, the laminar region of the boundary layer is extended in the controlled case and the transition to turbulence is delayed.